Spin Dynamics in Doped Semiconductor Quantum Dots

Dissertation
zur Erlangung des Doktorgrades
der Naturwissenschaften
der Fakultät Physik an der
Technischen Universität Dortmund

vorgelegt von

Johannes Hackmann
aus Bergkamen

Juli 2015

Version: September 23, 2015

Erster Gutachter	Prof. Dr. Frithjof B. Anders
Zweiter Gutachter	Prof. Dr. Götz S. Uhrig
Tag der mündlichen Prüfung	15.09.2015

Kontakt zum Autor johannes.hackmann@tu-dortmund.de

Contents

Publication list

- Hackmann, J. ; Anders, F. B.: *Spin noise in the anisotropic central spin model*. In: Phys. Rev. B **89** (2014), Jan, p. 045317. Highlighted as Editors' suggestion.
- Hackmann, J. ; Smirnov, D. S. ; Glazov, M. M. ; Anders, F. B.: *Spin noise in a quantum dot ensemble: From a quantum mechanical to a semi-classical description*. In: Physica Status Solidi (b) **251 (6)** (2014), May, p. 1270-1275.
- Uhrig, G. S. ; Hackmann, J. ; Stanek, D. ; Stolze, J. ; Anders, F. B.: *Conservation laws protect dynamic spin correlations from decay: Limited role of integrability in the central spin model*. In: Phys. Rev. B **90** (2014), Aug, p. 060301.
- Hackmann, J. ; Anders, F. B. ; Glasenapp, P. ; Greilich, A. ; Bayer, M.: *Influcence of the nuclear electric quadrupolar interaction on the coherence time of hole- and electron-spins confined in semiconductor quantum dots*. arXiv:1504.07417. Submitted to PRL.

Chapter 1

Introduction

In the year 1982 Richard P. Feynman asked the question wether a classical computer can simulate the physics of quantum mechanical systems efficiently [1]. Since the Hilbert space dimension of a quantum system containing interacting particles grows exponentially, he came to the conclusion that the boundaries of classical machines will be exceeded rapidly. E.g. for a system of N spin$-1/2$ particles, the Hilbert space dimension is given by $D = 2^N$ and even storing one complex number for each degree of freedom is not managable for a couple of hundred spins. This led Feynman to the conjecture that a suitable quantum computing device might be the most adequate option to simulate quantum dynamics efficiently. In the past couple of decades the vision of such a quantum computer has been subject of various research. As an important confirmation of Feynman's conjecture, Bernstein and Vazirani [2] have, based on a quantum mechanical Turing machine, presented the first proof that a quantum computer is capable of simulating other quantum systems in polynomial instead of exponential time. Also a variety of algorithms, that can be implemented more efficiently on a quantum than on a classical computer, have been put forward [3, 4, 5]. The most prominent of these algorithms is the integer factorization by Shor [6, 7].

With various possible applications of quantum computers around [8], dealing with the obstacles of their realization is unevitable. David DiVincenzo has summarized five requirements [9] for the successful implementation of a quantum computing device, which will not be reviewed in detail here. Of course the central building block of a quantum computer are quantum bits (qubits), which can be represented by any quantum mechanical two level system. Several possible realizations of such qubits have been introduced in the past, including nitrogen-vacancy centers in diamond [10, 11], nuclear spins of molecules in liquids [12, 13], ^{31}phosphorus impurities in silicon [14] and superconducting circuits [15, 16, 17]. The proposal constituting the basis of this work, is the realization of qubits via the spin of electrons or holes that are confined in semiconductor quantum dots (QDs) [18, 19, 20]. All of the mentioned approaches feature different advantages and drawbacks. While the realization of qubits in semiconductor QDs is a promising candidate [21, 22, 23, 24, 25] for quantum computing,

its main problem is the coherence time of the confined spins, which is short compared to other realizations. The scope of this work is the detailed investigation of spin decoherence in such semiconductor QD devices, because an in-depth understanding of the underlying physical mechanisms is the first step to overcome the arising obstacles.

The Fermi contact hyperfine interaction [26] is the dominant mechanism influencing the dynamics of electron spins confined in semiconductor QDs [27, 28]. The isotropic central spin model [29] is usually applied to account for the Fermi contact interaction in theoretical modelings. It consists of one central spin (the electron spin) that interacts with a large bath of spins (of the nuclei forming the QD). The bath spins are not coupled to each other. Due to its relevance for quantum information processing, the central spin model (CSM) has been subject of numerous investigations in the past two decades. The applied methods involve several analytical and numerical approaches. Although exact approaches [19] for the analytical investigation of the model exist, the majority of analytical claims relies on a semi classical treatment of the problem [27, 30, 31]. The variety of numerical studies of the central spin model is manifold. With respect to the model's integrability [29], its exact Bethe Ansatz solution has been evaluated and discussed exactly [32, 33, 34, 35] and stochastically [36, 37], but due to the sophisticated character of the Bethe Ansatz equations these studies were limited to certain initial conditions and bath sizes below 50 spins. A recent time dependent density matrix renormalization group (TD-DMRG) approach to the model [38, 39] managed to push the number of fully quantum mechanically treatable spins to 1000, but is quite limited in its accessible timescales. In certain regimes of the CSM, a perturbative claim is well justified [40] and several master equation approaches for its treatment have been proposed [41, 42, 43]. The success of the semi classical, analytic solution [27], concerning the model's short time dynamics, has justified its semi classical treatment and entailed numerous numerical quasi static approximations [44, 45, 46, 47, 48, 49]. Besides these approaches for the solution of the isotropic CSM, a cluster expansion has been proposed [50, 51, 52, 53], that relies on the separation of the system into smaller pieces that are treatable on short timescales. As the perturbative methods, the cluster expansion works reliably in certain regimes of the CSM, but lacks general validity. In defiance of the large variety of applied methods, the spin dynamics within the isotropic central spin model is not fully understood until the present day and will be revisited and discussed in detail within this work.

While the case of electrons confined in semiconductor QDs has been subject of numerous theoretical investigations, hole spins have not been studied nearly as intensively in the past. Instead of the Fermi contact interaction, a dipole-dipole like interaction between the confined spin and the nuclear spins of the QD is crucial for the hyperfine interaction of holes. This dipole-dipole mechanism acts significantly different when considering light or heavy hole spins. While some studies were limited to the latter case [54, 55], Testelin et al. [56] have demonstrated that both hole species

can be casted into the anisotropic CSM and have discussed an analytic semi classical treatment of the model. Beside further numerical studies of the semi classical picture [57], no investigations concerning the hole doped case exist up to our knowledge. This leaves a detailed discussion on a quantum mechanical level as an open topic. There is experimental evidence [58, 59, 60, 61, 62] that solely considering the hyperfine interaction for electrons and holes yields an incomplete picture of the measured spin dynamics. Namely, similar decoherence times were observed, while the hyperfine interaction alone implies a larger lifetime for holes than for electrons. It has been proposed [63] that this mismatch stems from the coupling of the nuclei to electric field gradients (EFGs) occuring throughout the QDs.

The central goal of this work is to develop a fully quantum mechanical theory, that covers the real time dynamics of electron and hole spins confined in semiconductor QDs. To substantiate the adequacy of the theory, we will compare it to various recent measurements on InGaAs QDs [59, 62, 64, 65] and demonstrate that all the experimental results are in agreement with the established theory, although their findings appear to be contradictory on first sight. With this central goal in mind, this work is structured as follows.

First, the basics of the referenced experiments are discussed. This includes a description of the production process and some properties of self-assembled ensembles of semiconductor QDs, which are the most commonly studied samples with in the addressed experiments. We aim at the investigation of two types of measurements concerning the real time spin dynamics of holes or electrons confined in QDs: (i) pump-probe experiments and (ii) spin noise measurements. The basic ideas and techniques of these two approaches will be reviewed briefly.

Second, the theoretical modeling of the dominant interactions influencing electrons or holes confined in semiconductor QDs will be discussed in detail. In this context the isotropic and anisotropic CSM, which account for the hyperfine interaction influencing electron and hole spins, will be introduced including a short review of their derivation and a realistic model for the entering coupling constants based on the QD geometry will be presented. In prior quantum mechanical studies [19, 32, 36, 39] of the CSM a realistic treatment of these coupling constants has not been applied and instead simplified assumptions have been considered, while we will demonstrate that their choice is crucial for the obtained spin dynamics. We will enhance the CSM by the coupling of the nuclei's quadrupole moment to EFGs throughout the sample and discuss details of the QD's properties influencing the central spin dynamics. The discussion of the investigated model will be completed by introducing the quantity of interest and central properties of the model under study.

Third, the Chebyshev polynomial expansion technique (CET), which is the central numerical tool of this work, will be introduced. While it is originally [66] a numerical method for the propagation of a single quantum state in time, we will discuss

its enhancement to the evaluation of expectation values and the direct calculation of spectral information. For this sake several numerical obstacles need to be treated and benchmarks of the method will be presented. In this context a simplified version of the isotropic CSM, namely the box model, will be discussed in detail.

The core results of this work are divided into four chapters, of which three are entirely based on the CET and various analytical approaches to the model under study. In the fourth chapter, which is the only one that is not directly addressing recent experiments, an approach for the realization of a time dependent numerical renormalization group (TD-NRG) [67, 68, 69] treatment of the isotropic central spin problem is presented. The remainder three chapters are organized as follows. The most prominent special case of the introduced model is the isotropic CSM accounting for the Fermi contact hyperfine interaction, that dominates the spin dynamics of electrons. It is treated in detail in the first of the following chapters, where the numerical results obtained via the CET are compared to various analytical estimates and their agreement to recent experimental findings in a certain regime is illustrated as well as their disagreement in other regimes. After considering a possible implementation of a TD-NRG procedure for the isotropic CSM, the hole spin dynamics within the anisotropic CSM is discussed. The special cases of heavy and light holes are considered as well as heavy and light hole mixing. Namely, a crossover behavior between the two extreme cases will be illustrated and quantified. On top of that, we will demonstrate that the anisotropic CSM is insufficient to reproduce experimentally measured spin noise spectra.

Finally, the influence of the nuclei's quadrupolar couplings (QCs) will be investigated in detail. While the influence of various QD properties onto the resulting central spin dynamics will be initially discussed in general, the scope of the final chapter is to demonstrate the accordance between the presented theory and various experiments on InGaAs QDs. The assumed physical properties of these dots are based on recent microscopic studies [70, 71] and due to the preparatory general discussions, our theory is capable of predicting the spin dynamics in other materials than InGaAs if certain properties of the QDs are known.

Chapter 2

Experimental background

Since this theoretical work is closely related to recent experiments concerning spin noise in semiconductor QDs, we will briefly discuss some of the basic technologies that are related to this type of investigation. The majority of the addressed experiments have been performed on self-assembled ensembles of semiconductor QDs. Accordingly, some details of the production process and the properties for this type of sample will be discussed initially. The most common approach to the measurement of spin dynamics in QDs is probably the pump-probe technique, which is, in contrast to spin noise measurements, an invasive method. Although our focus is on the discussion of spin noise experiments, we will argue in section 3.3 that these two approaches are expected to yield the same physical information of the underlying system and accordingly we will briefly introduce the basics of both methods. Note that a large variety of materials, like Si, CdSe, CdTe, AlGaAs for instance, is on the market, but as proof of principle for our theory we will focus its comparison on experiments on In(Ga)As QDs.

2.1 Semiconductor quantum dots

Most of the investigated QD samples that will be addressed within this work, have been grown via molecular beam epitaxy (MBE) based on the Stranski-Krastanov-mode [72, 73]. Although several different growth procedures, like the more recent stacked submonolayer growth for instance [74], exist, we restrict the following discussions to the widely applied Stranski-Krastanov-method and the special case of InAs/GaAs QDs for brevity. The basic idea is to deposit InAs on top of a GaAs substrate, which is technically realized by MBE, and due to the lattice mismatch [75] of the two materials strain occurs. This strain is on the one hand responsible for the formation of small (few tens of nanometer diameter) InAs islands, i.e. the QDs, and on the other hand it influences the electronic structure within semiconductor QDs, entailing electric field gradients (EFGs). These EFGs are of crucial importance for the studies of this work and will be discussed in greater detail below. Figure 2.1 contains depictions of self-assembled InAs QDs grown via MBE. The excellent resolution of the left picture [76] reveals the

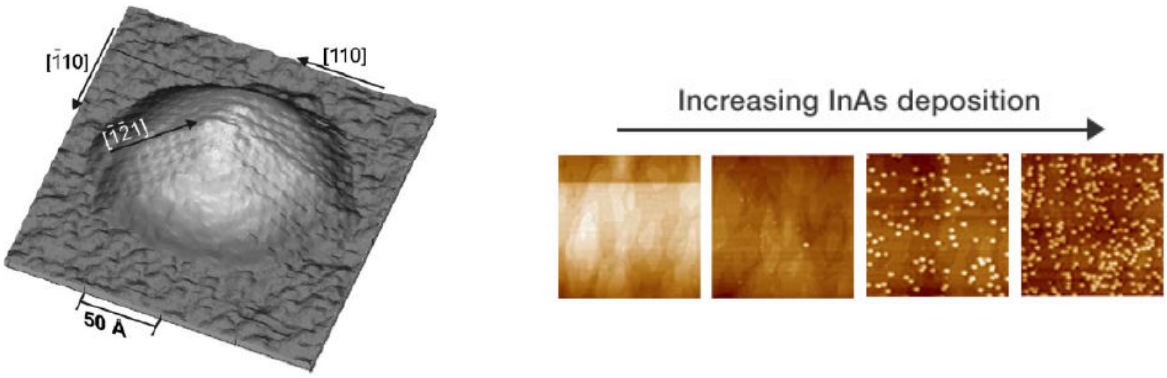

Figure 2.1: The left panel shows an atomically resolved picture of an InAs QD. It has been published in reference [76]. The right panel (picture from [77]) depicts different ensembles of InAs QDs grown on GaAs substrates. By varying the InAs deposition the density of the arising QDs can be well controlled.

detailed structure of an individual dot. The right panel [77] demonstrates how the density of QDs in an ensemble can be controlled by varying the InAs deposition within the MBE. On top of that, the right panel of figure 2.1 reflects the random character of the growth process. Beside the clearly resolved random positioning of the individual dots, it is important to note that also some physical properties, as their characteristic length scale for instance, is varying among the ensemble. We will come back to this aspect in context of the theoretical modeling of a self-assembled QD ensemble.

After the In(Ga)As QDs have been grown on the GaAs substrate, several further monolayers of GaAs are grown on top of the sample. I.e. finally the In(Ga)As film containing the QDs is fully surrounded by GaAs. While the lattice constant of In(Ga)As is approximately 7 % larger than the one of GaAs, its energy gap, which is sketched in k-space in the left panel of figure 2.2, is significantly smaller [78]. Therefore an individual In(Ga)As QD surrounded by GaAs serves as a potential well, as sketched in one dimension in the right panel of figure 2.2, that can be used as confinement potential trapping an individual electron (or hole). The resulting spatial confinement reduces the particle's interaction with the substrate and along with this electronic decoherence mechanisms are suppressed. At the same time the hyperfine interaction of the confined particle with the nuclei forming the QD is enhanced and becomes the main source of decoherence which will be intensively discussed throughout this work. Note that, due to their discrete energy levels that can be populated by the confined particles, QDs are often referred to as artificial atoms.

If an otherwise charge neutral QD is populated by a single electron (hole), it is called n-doped (p-doped). Exemplarily, one possibility to realize an ensemble of n-doped In(Ga)As QDs is to grow a doping layer, e.g. consisting of Si, in a distance of $\approx 20\,\mathrm{nm}$ to the QDs, i.e. underneath the substrate. Electrons from this doping layer can tunnel into the QDs and on average one electron will be trapped permanently in each dot [75]. Another important aspect of the QD fabrication process is the so called annealing

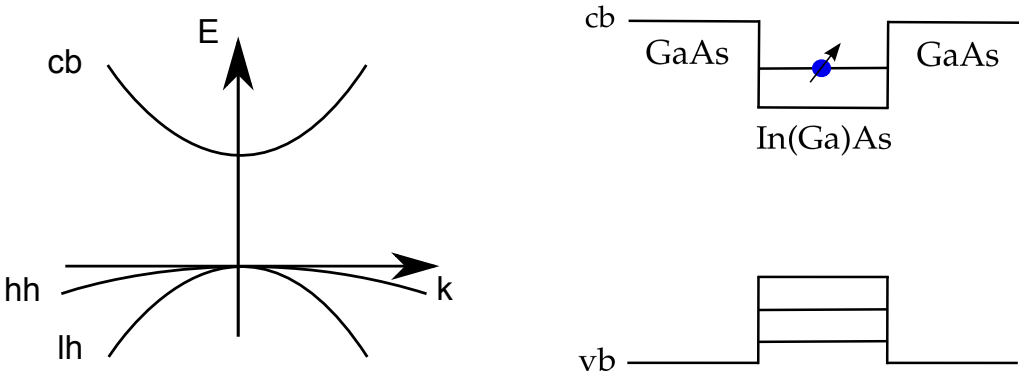

Figure 2.2: In the left panel a sketch of the band structure of a direct semiconductor near its band gap is presented. The acronyms hh and lh account for heavy and light holes. In the right panel the spatial band structure of an In(Ga)As/GaAs QD is depicted. Only the relevant bands for our present studies are shown.

[79, 80]. During this procedure the above described sample is purposefully heated and as a consequence the QD partially diffuses into the substrate and vice versa. This technique is used to influence the physical properties of the QDs selectively. With the basic knowledge of QD fabrication and properties in mind, let us now turn to the description of the experimental realization of spin dynamic measurements.

2.2 Measurement of spin dynamics in semiconductor QDs

The spin dynamics of particles confined in semiconductor QDs is widely studied using the pump-probe technique [81, 82, 83, 84]. While it is often applied to investigate the free time evolution of initially polarized spins, pump protocols can be applied to the sample under study, revealing a lot of further interesting physical effects and details [85, 86, 87, 88]. However, our investigations concern the equilibrium dynamics of electrons or holes trapped in semiconductor QDs. The measurement of spin noise represents, in contrast to the pum-probe procedure, a non-invasive approach to study the addressed spin dynamics in thermal equilibrium [59, 64, 89, 90, 91]. Both mentioned experimental methods are entirely based on optical excitation and detection. In the following we will briefly review the main aspects of their realization.

2.2.1 Pump-probe experiments

The name of the pump-probe technique stems from its composition: first, a pump beam is applied to induce a collective orientation of the spins in the studied sample and second, after a well defined delay time Δt a probe beam is applied to read out the remaining total polarization. The experimental setup for such a measurement is sketched in the left panel of figure 2.3. As indicated in the figure, the pump beam has to be polarized circularly to induce a collective orientation of the confined particles.

The right panel of figure 2.3 needs to be considered to understand the optical polarization mechanism within an ensemble of, e.g. n-doped, semiconductor QDs. The energy of the probe beam is adjusted such that only excitations from the heavy or light hole band (see left panel of figure 2.2) into the lowest lying state of the conduction band are allowed. The resulting six level problem is depicted in figure 2.3 (b). The circularly polarized light can either carry the total angular momentum $+1$ or -1, which is denoted as $\sigma^{\pm}$. As shown in the stated panel, each type of circular light can induce two transitions from the valence into the conduction band. In the following discussion, we exemplarily restrict ourselves to the case σ^{+}. Then, one photon can only excite one valence electron with spin $-3/2$ (from the hh band) into a spin $-1/2$ conduction electron or one spin $-1/2$ valence electron (from the lh band) into a spin $+1/2$ conduction band electron. As indicated in the figure, the latter excitation occurs a factor of 3 less frequent and as a consequence more spin $-1/2$ electrons are excited by a σ^{+} pulse. Since the excitation of a spin $-3/2$ electron from the valence into the conduction band leaves behind a hole with spin $+3/2$ and the lowest conduction band state is permanently occupied by the resident electron, whose spin has to be oriented opposingly to the excited electron, the optical excitation leaves behind three particles, forming a so called trion. Due to a high recombination rate of the hole and the excited electron [92], the trion decays on a very short timescale, leaving behind the polarized resident electron with spin $+1/2$. The polarization process using σ^{-} photons works accordingly.

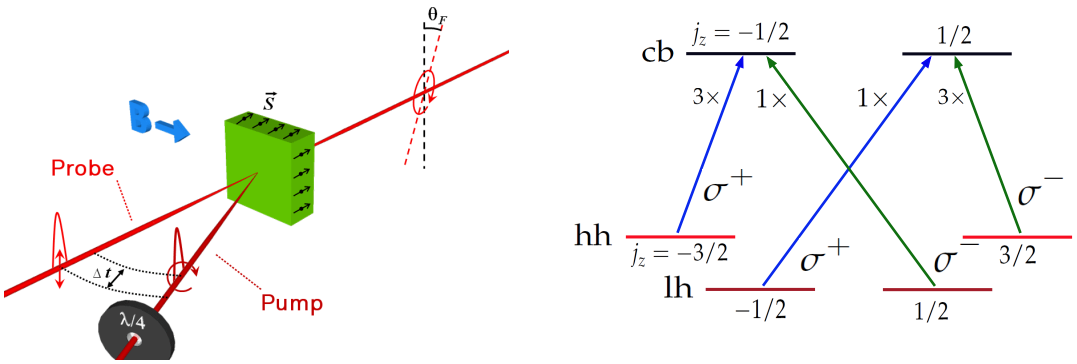

Figure 2.3: The left panel, which has been extracted from reference [93], presents a sketch of the experimental setup for a pump-probe experiment in Voigt-geometry. The right panel is based on reference [94] and shows the optical transitions that are important for the polarization mechanism of an n-doped QD ensemble. The symbols $\sigma^{\pm}$ refer to the circular polarization of the applied pump beam and the added numbers indicate the relative frequency of the different transitions.

After the orientation of the electron spins has been performed, the sample spins evolve freely for the time interval Δt. Then, the probe pulse is applied, which is polarized linearly in a well controlled direction. Due to the spins of the optically oriented electrons, a magnetization arises within the studied sample. This magnetization of the

semiconductor material induces a rotation of the light's polarization axis due to the Faraday effect [94, 95]. The experimentally accessible rotation angle θ_F is proportional to the total magnetization and consequently to the spin orientation. I.e. by building a variable delay line for the probe beam, the real time spin dynamics in n-doped semiconductor QDs can be observed via the described pump-probe method.

2.2.2 Measurement of spin noise

The measurement of spin noise is an alternative approach to gain insight into the spin dynamics of doped semiconductor QDs. In contrast to the pump-probe technique, it is a non-invasive method. I.e. the dynamics of the sample under study is measured in thermal equilibrium and ideally no excitations are induced at any time. The basic setup for a spin noise experiment corresponds to a pump-probe setup, where only a linearly polarized probe beam is applied to the sample and the occuring Faraday rotation angle is measured. Since only a very weak magnetization due to spin fluctuations is present in the sample, the magnitude of the signal in a spin noise measurement is a lot smaller than in a pump-probe experiment. On top of that, a small probe beam intensity, which is unevitable in a spin noise measurement to avoid unpleasant excitations, also entails a small signal and makes a reliable detection of spin noise even more challenging.

In the real time domain a spin noise measurement yields, as indicated by its name, a *noisy* signal, which barely reveals useful information. Thus, a Fourier transformation is applied to the real time measurement and from the obtained spectral function insight into the physical properties of the underlying sample is gained. As we will argue in section 3.3, the investigation of spin noise yields, at least in the limit of high temperature, the same information as a pump-probe measurement, but in contrast to the latter technique a spin noise measurement is not influenced by the above stated trion decay, which might adulterate the pure spin dynamics.

We stress that there are further details that have to be considered for the realization of a spin noise or pump-probe experiment, but their understanding on the discussed level is sufficient in the context of the following theoretical investigations.

Chapter 3

Model

The central step to establish an adequate theory for the spin dynamics of electrons or holes confined in semiconductor QDs is the derivation of a model that covers all the important physical properties of the system under study. The goals of the chapter at hand are (i) to derive a model Hamiltonian H that includes the most relevant interactions influencing the investigated spin dynamics, (ii) to introduce realistic choices of the parameters entering the theory and (iii) to discuss basic properties of the derived Hamiltonian. Finally the quantity of interest, that corresponds to the experimentally measured Faraday or Kerr rotation angles, will be defined in the last section. Let us forestall that the full Hamiltonian has the form

$$H = H_{\mathrm{CSM}} + H_Q, \tag{3.1}$$

where H_Q involves the influence of electric field gradients (EFGs) that couple to the quadrupole moment of the individual nuclei forming a QD and H_{CSM} contains an externally applied magnetic field and the hyperfine interaction, which will be discussed in detail in the following section.

3.1 The anisotropic central spin model (CSM)

In this section the Hamiltonian H_{CSM} is introduced. It describes the dominant interaction for the spin dynamics of both electrons and holes confined in a semiconductor quantum dot. The fact that these two cases of doping can be included in a single model Hamiltonian is noticable, since for electrons the Fermi contact hyperfine interaction and for holes a dipole-dipole like interaction is crucial. In the following the derivation of the full anisotropic CSM is briefly summarized.

3.1.1 Fermi contact hyperfine interaction

E. Fermi has presented [26] a perturbative approach to deduce the hyperfine splitting of a nucleus interacting with an electron, where the electron is considered as a rela-

tivistic particle while the nucleus is treated non-relativistically. In the literature [96] an alternative derivation is presented, that relies on the non-relativistic treatment of the interaction between the electron's spin $\vec{S}$ and the magnetic moment $\vec{\mu}$ of a single nucleus. Since this derivation also provides the dipole-dipole Hamiltonian that is crucial for the description of hole spins, it is briefly summarized in the following and for further details the reader is referred to the original literature [96]. Introducing the spin operator $\vec{I}$ of the nucleus and its gyromagnetic ratio $\gamma = \frac{\mu}{|\vec{I}|} =: \frac{\mu}{I}$, the Hamiltonian of an electron (or hole) in the magnetic field of a single nucleus can, in first order perturbation theory, be written as

$$\mathcal{H}_{\text{e-n}} = 2\mu_B\gamma\frac{\vec{l}\cdot\vec{I}}{r^3} + 2\mu_B\gamma\vec{S}\cdot\text{rot}\left(\text{rot}\left(\frac{\vec{I}}{r}\right)\right), \tag{3.2}$$

where μ_B denotes Bohr's magneton, r is the position operator and $\vec{l}$ is the orbital angular momentum operator. After some considerations concerning the behavior of $\mathcal{H}_{\text{e-n}}$ for $r \to 0$, the Hamiltonian (3.2) might be rewritten as

$$\mathcal{H}_{\text{e-n}} = 2\mu_B\gamma\vec{I}\cdot\left(\frac{\vec{l}}{r^3} - \frac{\vec{S}}{r^3} + 3\frac{\vec{r}\cdot(\vec{S}\cdot\vec{r})}{r^5} + \frac{8}{3}\pi\vec{S}\delta(\vec{r})\right). \tag{3.3}$$

The second and third term represent the usual dipole-dipole interaction and the last term, that only contributes for s-type orbitals, is the Fermi contact hyperfine contact interaction. On top of that setting $l = 0$ causes the first three terms to yield no distribution, i.e. solely the last term contributes in this case. Electrons confined in semiconductor QDs are described by s-type Bloch functions and as a consequence the fermi contact hyperfine interaction is crucial for n-doped QDs. Taking into account that the confined electron interacts with a number of N nuclei instead of a single one, we can rewrite the contact hyperfine term for an n-doped QD as

$$\mathcal{H}_{\text{e-d}} = \frac{16\pi\mu_B}{3}\sum_{k=1}^{N}\frac{\mu_k}{I_k}\left(\vec{S}\cdot\vec{I}_k\right)\delta(\vec{r}-\vec{R}_k). \tag{3.4}$$

$\vec{R}_k$ and $\vec{r}$ denote the position of the k-th nucleus and the electron. Since the energy splitting between two levels of the electrons under study is a lot larger than the energy scale of the hyperfine interaction, the Hamiltonian of an electron confined in a semiconductor QD can be written as [27]

$$H_{\text{hf-contact}} = \sum_{k=1}^{N} J_k\vec{S}\cdot\vec{I}_k, \tag{3.5}$$

$$J_k = \frac{16\pi\mu_B\mu}{3I}\left|\psi_{\text{e}}(\vec{R}_k)\right|^2, \tag{3.6}$$

where $\psi_e(\vec{R}_k)$ is the value of the electron wave function at the k-th nucleus. Note that we assume identical nuclei, i.e. an identical magnetic moment μ and spin I for all bath spins in the system, which is an approximation. For example in an InGaAs QD the nuclei of Ga and As both fullfill $I = 3/2$, while the In atoms carry spin $I = 9/2$ [56]. According to the Bloch theorem the electron wave function can be written as a product $\psi_e(\vec{r}) = u(\vec{r})\psi(\vec{r})$ of the Bloch amplitude $u(\vec{r})$ and the envelope function $\psi(\vec{r})$. The Bloch amplitude describes the behavior of the wave function in the individual unit cells and has maxima at the positions of the nuclei. Typical values of $\eta_k = \left|u(\vec{R}_k)\right|^2$ are of the order $10^3 - 10^4$ [19] and vary among the individual nuclei in a QD. Once again we assume all nuclei to be identical and set $\eta_k = 1$, which coincides with the case of free electrons. Note that the choice of the magnitude of η_k in our model is not crucial for the obtained physics, because we do not aim at constructing a realistic estimate for the energy scale of the total hyperfine coupling $J_s = \sum_k J_k$, but instead want to obtain a detailed picture of the spin dynamics due to the hyperfine interaction and compare the theory to recent experiments by inserting existing data concerning the energy scale of the hyperfine interaction. The envelope function $\psi(\vec{r})$ describes the behavior of $\psi_e(\vec{r})$ among the quantum dot and it is crucial for the distribution of the coupling constants within the model that is introduced here. The assumptions concerning $\psi(\vec{r})$ and their impact on the choice of the coupling constants J_k will be discussed in detail in section 3.1.5. Note that the present work is restricted to the case of antiferromagnetic couplings $J_k > 0$, which is valid for a large variety of semiconductor QDs.

3.1.2 Dipole-dipole interaction

In contrast to conduction electrons, a valence electron or hole that is confined in a semiconductor QD is described by a p-type wave function, which vanishes at the position $\vec{R}_k$ of the nuclei and as a consequence the last term of the Hamiltonian (3.3) does not contribute. C. Testelin et al. [56] calculated the matrix elements of the remainder terms of $\mathcal{H}_{\text{e-n}}$, which describe a dipole-dipole type of interaction between a hole and a given nucleus, in the bases of the heavy holes (hh) and light holes (lh). Applying the resulting Hamiltonians to a hole interacting with N bath spins instead of a single nucleus, one obtains

$$\mathcal{H}_{\text{hh}} = \sum_{k=1}^{N} C_k S^z I_k^z \tag{3.7}$$

$$\mathcal{H}_{\text{lh}} = \sum_{k=1}^{N} \frac{C_k}{3}(S^z I_k^z - 2S^x I_k^x - 2S^y I_k^y) \tag{3.8}$$

$$C_k = \Omega \frac{16\mu_B \mu}{5I} \left\langle \frac{1}{r^3} \right\rangle \left|\psi(\vec{R}_k)\right|^2. \tag{3.9}$$

Several comments are in order: (i) Since heavy holes carry an angular momentum $J_z = \pm 3/2$ the occuring spin operator in $\mathcal{H}_{\mathrm{hh}}$ belongs to a pseudo spin, fullfilling $S^z = \pm 1/2$ as usual. (ii) The negative sign of the last two terms in $\mathcal{H}_{\mathrm{lh}}$ does not make a difference for the obtained spin dynamics in the present considerations and it is for simplicity replaced by a positive sign in the following. (iii) The prefactor Ω is the volume of the semiconductor's unit cell containing two nuclei and $\left\langle \frac{1}{r^3} \right\rangle = \int_\Omega \mathrm{d}r \, \frac{F_x^2(r)}{r^3}$ describes the hole wave function in the individual unit cells, where $F_x(r)$ is the orbital function of p-symmetry. According to reference [56], the bound hole state comprises a superposition of light and heavy hole states and thus the occurence of valence-band mixing is unevitable in self-assembled semiconductor QDs and as a consequence the Hamiltonians (3.7) and (3.8) need to be combined to describe mixed heavy and light hole states. The discussion of the details of valence band mixing is skipped here and instead the combination of the dipole-dipole and fermi contact hyperfine interaction into one Hamiltonian is presented and discussed in the following section.

3.1.3 Hamiltonian of the anisotropic CSM

Piecing together the Hamiltonians (3.5), (3.7) and (3.8) yields the final Hamiltonian describing the hyperfine interaction for both electrons and holes confined in a semiconductor QD, which can be written as

$$H_{\mathrm{hf}} = \sum_{k=1}^{N} A_k \left(S^z I_k^z + \frac{1}{\lambda} (S^x I_k^x + S^y I_k^y) \right). \tag{3.10}$$

The newly introduced coupling constants A_k are given by $A_k = J_k$ for electrons, $A_k = C_k$ for mixed hole states and heavy holes. For the special case of light holes $A_k = C_k/3$ holds. From this point forward the A_k are the only coupling constants that will be referred to and one has to bear in mind that they are of a fundamentally different origin for electrons and holes. Nevertheless these coupling constants are in any case governed by the squared absolute value of the envelope wave function $\left|\psi(\vec{R}_k)\right|^2$ and only differ from each other by their prefactors that are set by the detailed physics of the material at hand:

$$A_k = A_s \Omega \left|\psi(\vec{R}_k)\right|^2, \tag{3.11}$$

where the definition of the prefactor A_s follows from the comparison of A_k to equation (3.6) for electrons and to (3.9) for holes. The envelope wave function $\psi(\vec{r})$ is assumed to vary slowly over the volume Ω of a given unit cell. Therefore the normalization integral of $\psi(\vec{r})$ can be approximated by a sum over its values at the individual nuclei

$$1 = \int \mathrm{d}^3 r \, |\psi(\vec{r})|^2 \approx \sum_k \Omega \left|\psi(\vec{R}_k)\right|^2. \tag{3.12}$$

By applying the sum over all nuclei $\sum_k$ to equation (3.11) and inserting the normalization condition, the energy scale A_s can be identified as

$$A_s = \sum_{k=1}^{N} A_k. \tag{3.13}$$

This energy scale is independent of the electron or hole wave function and therefore independent of the detailed coupling constants distribution. In typical semiconductor QDs A_s is of the order $O(10\,\mu\text{ev})$ [28, 20] for electrons and it is expected to be approximately one order of magnitude smaller for holes [56]. In the Hamiltonian (3.10) the parameter λ has been introduced, which will be referred to as the anisotropy parameter from now on. It takes the values $\lambda = 1$ for electrons, $\lambda = 1/2$ for light holes and $\lambda \to \infty$ for heavy holes. For mixed heavy and light hole states a value in between the latter two extreme cases applies for the anisotropy factor.

The hyperfine interaction is the dominant interaction influencing the spin dynamics of either an electron or hole confined in a semiconductor QD and the Hamiltonian (3.10) fully describes this central effect arising from the confining material. In most experimental setups an external magnetic field $\vec{B}$ is applied to the sample, whose energy scale is usually adjusted to be at least of the same order as the hyperfine interaction. Therefore an arbitrary magnetic field is added to the hyperfine Hamiltonian yielding the full anisotropic central spin model

$$H_{\text{CSM}} = \omega_L \vec{S}\cdot\vec{n}_B + \sum_{k=1}^{N} A_k \left(S^z I_k^z + \frac{1}{\lambda}(S^x I_k^x + S^y I_k^y) \right) =: \omega_L \vec{S}\cdot\vec{n}_B + \sum_{k=1}^{N} H_{hf}^k, \tag{3.14}$$

where $\omega_L = \frac{\mu_B g |\vec{B}|}{\hbar}$ denotes the Larmor frequency of the central spin that is governed by the external field and $\vec{n}_B$ is a unit vector that is directed along the magnetic field direction. The introduced g-factor varies quite significantly for electrons and holes, for example in InGaAs $g_{\text{hole}} \approx 0.16$ and $g_{\text{electron}} \approx 0.54$ has been measured [59]. Note that the external field is assumed to be only acting on the central spin. This approximation is based on the Zeeman energy, which is small for the nuclei compared to the central spin. Especially in the specific scenario of an external field aligned along the z-direction, it can easily be shown that the term stemming from the coupling of the magnetic field to the nuclei only induces a small correction of the field strength acting on the central spin [34]: for $\vec{n}_B = \vec{e}_z$ the total spin z -component $\mathcal{S}^z = S^z + \sum_k I_k^z$ is a conserved quantity, thus the full magnetic contribution $\omega_L S^z + \sum_k \omega_L^{\text{n}} I_k^z$ to the Hamiltonian, where ω_L^{n} denotes the Larmor frequency of the nuclei, can be rewritten as $(\omega_L - \omega_L^{\text{n}})S^z + \omega_L^{\text{n}}\mathcal{S}^z$. The latter term is a constant offset and the Larmor frequency of the nuclei is small compared to ω_L and is therefore negligible. Note that the y-component of the applied magnetic field will always be assumed to be zero, because the presented model contains no contributions that distinguish between the x- and

y-direction in any fashion, i.e. the obtained effects from a certain finite y-component in $\vec{B}$ will always be identical to those stemming from the same absolute value in the x-component.

The first coupling term $S^z I_k^z$ of the central spin to the bath spins in the Hamiltonian (3.14) does not introduce any spin flips and, with respect to its form, it is referred to as the Ising term in the following. In contrast, the last two terms of H_{CSM} can be rewritten as $\frac{1}{2\lambda}(S^+ I_k^- + S^- I_k^+)$, revealing that, in abscence of a magnetic field, the central spin is only able to flip in exchange with a bath spin that flips into the opposite direction. This mechanism is the source of decoherence in the anisotropic central spin model and for obvious reasons it is often referred to as the "flip-flop"-term.

Note that the isotropic ($\lambda = 1$) CSM Hamiltonian H_{CSM} belongs to the class of operators M. Gaudin has proven [29] to be integrable. As a consequence an analytical solution via Bethe Ansatz exists, but its evaluation with the purpose of obtaining the real time dynamics of a central spin interacting with a large bath is very challenging. Such Bethe Ansatz studies of the isotropic CSM have been performed by several groups [36, 37, 32, 33] and are capable of handling large amounts ($N \sim 50$) of bath spins. Anyhow the method is heavily dependent on the initial conditions and lacks the possibility of adding arbitrary further terms to the Hamiltonian (3.14), especially if it breaks its integrability. This lack of variability is decisive for the insufficiency of the Bethe Ansatz method for the investigations that are presented here.

3.1.4 Comments concerning the model's treatment

The central spin operator $\vec{S} = (S^x, S^y, S^z)^T$ refers to a spin-1/2 particle in any investigated scenario, i.e. its components are given by $S^\alpha = \frac{1}{2}\sigma^\alpha$ with $\alpha \in x, y, z$. The introduced matrices σ^α are the well known Pauli matrices

$$\sigma^x = \begin{pmatrix} 0 & 1 \\ 1 & 0 \end{pmatrix}, \qquad \sigma^y = \begin{pmatrix} 0 & -i \\ i & 0 \end{pmatrix}, \qquad \sigma^z = \begin{pmatrix} 1 & 0 \\ 0 & -1 \end{pmatrix}. \tag{3.15}$$

The underlying basis for this representation is given by the eigenstates of σ^z and S^z which is denoted as

$$\sigma^z \left|\frac{1}{2}, \frac{1}{2}\right\rangle = \left|\frac{1}{2}, \frac{1}{2}\right\rangle, \qquad \left|\frac{1}{2}, \frac{1}{2}\right\rangle \hat{=} \begin{pmatrix} 1 \\ 0 \end{pmatrix} \tag{3.16}$$

$$\sigma^z \left|\frac{1}{2}, -\frac{1}{2}\right\rangle = -\left|\frac{1}{2}, -\frac{1}{2}\right\rangle, \qquad \left|\frac{1}{2}, -\frac{1}{2}\right\rangle \hat{=} \begin{pmatrix} 0 \\ 1 \end{pmatrix}. \tag{3.17}$$

For a spin-1/2 particle the eigenstates of S^z are often referred to as spin up $\left|\frac{1}{2}, \frac{1}{2}\right\rangle = |\uparrow\rangle$ and spin down $\left|\frac{1}{2}, -\frac{1}{2}\right\rangle = |\downarrow\rangle$. The spin of the nuclei is not limited to the case $I = 1/2$

and for semiconductor materials that are commonly used for the investigation of spin dynamics in QDs, all values of I from $1/2$ to $9/2$ are represented. Since the size of a single nucleus' Hilbert space is given by $I_{\mathrm{dim}} = 2I + 1$ and the Hilbert space dimension of the full model $D = 2 \cdot I_{\mathrm{dim}}^N$ is the main limiting factor of the numerical investigations presented here, only the cases $I = 1/2$ and $I = 3/2$ are discussed in the present work. In the literature most commonly a restriction to the case $I = 1/2$ is applied, which is exceeded here because the quadrupole coupling (QC) Hamiltonian, that is presented in section 8, does not contribute to the central spin dynamics for spin-1/2 nuclei. As for the central spin operator, the matrix representation of the nuclear spin operators $\vec{I}_k$ is again presented in the eigenbasis of I_k^z. For $I = 1/2$ the nuclear spin operators are identical to the central spin operators and for $I = 3/2$ they take the form

$$I_k^x = \begin{pmatrix} 0 & \sqrt{3}/2 & 0 & 0 \\ \sqrt{3}/2 & 0 & 1 & 0 \\ 0 & 1 & 0 & \sqrt{3}/2 \\ 0 & 0 & \sqrt{3}/2 & 0 \end{pmatrix}, \quad I_k^z = \begin{pmatrix} 3/2 & 0 & 0 & 0 \\ 0 & 1/2 & 0 & 0 \\ 0 & 0 & -1/2 & 0 \\ 0 & 0 & 0 & -3/2 \end{pmatrix},$$
$$I_k^y = \begin{pmatrix} 0 & -\mathrm{i}\sqrt{3}/2 & 0 & 0 \\ \mathrm{i}\sqrt{3}/2 & 0 & -\mathrm{i} & 0 \\ 0 & \mathrm{i} & 0 & -\mathrm{i}\sqrt{3}/2 \\ 0 & 0 & \mathrm{i}\sqrt{3}/2 & 0 \end{pmatrix}. \tag{3.18}$$

Corresponding to the spin-1/2 notation the underlying basis for this representation of the nuclear spin operators I_k^α is denoted as

$$\begin{aligned} \left|\tfrac{3}{2}, \tfrac{3}{2}\right\rangle &\hat{=} (1,0,0,0)^T, \quad \left|\tfrac{3}{2}, \tfrac{1}{2}\right\rangle \hat{=} (0,1,0,0)^T, \\ \left|\tfrac{3}{2}, -\tfrac{1}{2}\right\rangle &\hat{=} (0,0,1,0)^T, \quad \left|\tfrac{3}{2}, -\tfrac{3}{2}\right\rangle \hat{=} (0,0,0,1)^T. \end{aligned} \tag{3.19}$$

The spin operators fullfill a Lie Algebra independently of their irreducible representation: $[S^\alpha, S^\beta] = \mathrm{i}\epsilon_{\alpha\beta\delta} S^\delta$ and $[I_k^\alpha, I_{k'}^\beta] = \mathrm{i}\epsilon_{\alpha\beta\delta} I_k^\delta \delta_{k,k'}$, where $\epsilon_{\alpha\beta\delta}$ is the fully antisymmetric ϵ-tensor that is positive for the case $\alpha = x$, $\beta = y$ and $\delta = z$. All further values of ϵ follow from its definition.

The Hamiltonian (3.14) can be explicitly constructed using the Kronecker product, which is denoted by the symbol "$\otimes$" in the following. For example the explicit form

of the isotropic ($\lambda = 1$) CSM Hamiltonian for $\vec{n}_B = \vec{e}_x$, $N = 2$ and $I = 1/2$ in the eigenbasis of the Operators S^z and I_k^z is given by

$$H_{\mathrm{CSM}} = \omega_L(S^x \otimes \underline{1}_2 \otimes \underline{1}_2) + A_1 \sum_\alpha S^\alpha \otimes I_1^\alpha \otimes \underline{1}_2 + A_2 \sum_\alpha S^\alpha \otimes \underline{1}_2 \otimes I_2^\alpha, \tag{3.20}$$

$$= \frac{1}{4}\begin{pmatrix} A_s & 0 & 0 & 0 & 2\omega_L & 0 & 0 & 0 \\ 0 & \Delta A & 0 & 0 & 2A_2 & 2\omega_L & 0 & 0 \\ 0 & 0 & -\Delta A & 0 & 2A_1 & 0 & 2\omega_L & 0 \\ 0 & 0 & 0 & -A_s & 0 & 2A_1 & 2A_2 & 2\omega_L \\ 2\omega_L & 2A_2 & 2A_1 & 0 & -A_s & 0 & 0 & 0 \\ 0 & 2\omega_L & 0 & 2A_1 & 0 & -\Delta A & 0 & 0 \\ 0 & 0 & 2\omega_L & 2A_2 & 0 & 0 & \Delta A & 0 \\ 0 & 0 & 0 & 2\omega_L & 0 & 0 & 0 & A_s \end{pmatrix}, \tag{3.21}$$

where $\underline{1}_2$ denotes the 2×2 identity matrix. On top of that the quantity $\Delta A = A_1 - A_2$ has been introduced and $A_s = A_1 + A_2$ holds. Obviously the explicit construction of the Hamiltonian H is not an adequate option for the numerical treatment of systems with a significant number of bath spins. For example the storage of H for $N = 17$ spin-1/2 nuclei in double precision would require a memory (assuming only real entries of H_{CSM}) of 500 Gb which exceeds the processing memory of the available machines. Anyhow the explicit matrix form (3.21) of the Hamiltonian H_{CSM} is not very densely occupied, i.e. it features many matrix elements that are zero. Note that the main diagonal includes the contributions of the z-component of the magnetic field and all the terms $\propto S^z I_k^z$ of the hyperfine interaction. The explicit matrix form of H_{CSM} also demonstrates that the contributions from the x-component of the magnetic field always occure on the $D/2$-th diagonal above and below the main diagonal. Also the contributions of each individual flip-flop-term always occure on a certain diagonal next to the main diagonal. Therefore it is possible to store all matrix elements forming the Hamiltonian H_{CSM} as one vector of length D, that represents the main diagonal elements stemming from the Ising terms and the z-component of the external field, and N vectors whose length is guaranteed to be smaller than $D/2$, that represent the N individual flip-flop-terms. There are always D non-zero matrix elements occuring due to the magnetic field component along the x-direction. They are given by $\langle\uparrow, s_\mathrm{b}| S^x |\downarrow, s_\mathrm{b}\rangle = \langle\downarrow, s_\mathrm{b}| S^x |\uparrow, s_\mathrm{b}\rangle$, where s_b represents an arbitrary bath state. Due to their simplicity there is no need to store these matrix elements. This approach for the storage of all matrix elements reduces the demanded process memory from $O(D^2)$ to $O(N \cdot D)$ byte, which is a significant improvement for large systems and it is also advantageous for the computation of the real time dynamics of the central spin.

3.1.5 Distribution of the hyperfine coupling constants

The numerical investigations that are presented in this work are mainly limited by the Hilbert space of the Hamiltonian under study and as a consequence the number of bath spins that can be taken into account is limited to $N \sim O(10)$. In contrast the central spin interacts with $O(10^5)$ nuclei in a realistic QD. The limitations arising from this insufficiency will be discussed in detail in section 5.1.2, while the focus of the section at hand is to develop a distribution of the coupling constants A_k, that is able to mimic the physics of a real QD within a model limited to $O(10)$ bath spins. Note that the coupling constants are treated as dimensionless quantities within the section at hand. The underlying energy scale of the hyperfine interaction will be discussed in detail in section 3.3. The strategy to develop a realistic distribution of the coupling constants A_k is to create n sets of N randomly generated coupling constants A_k with respect to a certain probability distribution, such that the generated couplings are representative for the entire QD. Then the resulting central spin dynamics is calculated individually for each of the n sets of coupling constants and the obtained outputs are averaged to yield a final result that is effectively influenced by a much larger bath than we can handle in a single simulation. The basic idea for the generation of representative sets of coupling constants, is to determine a probability distribution $P(A)$ that yields the probability to find a nucleus associated to the coupling strength A by randomly picking any nucleus from the QD. The derivation of $P(A)$ has been originally presented in reference [97]. It will be reviewed here for more general assumptions concerning the dot geometry and the envelope wave function $\psi(\vec{r})$. For all considerations a d-dimensional spherical QD shape for either $d = 3$ or $d = 2$ is assumed.

While the energy scale of the hyperfine coupling constants (3.11) is governed by the prefactors A_s and Ω, that contain the details of the underlying material and information on its doping, the distribution of the A_k among the QD is solely governed by the squared absolute value of the envelope wave function $|\psi(\vec{r})|^2$ within the presented model. It is assumed to be of the form

$$\psi(\vec{r}) = C(\sqrt{\pi}L_0)^{-d/m}\exp\left(-\frac{r^m}{2L_0^m}\right), \tag{3.22}$$

where L_0 is the characteristic length scale of the considered QD, which is expected to be typically of the order $L_0 \approx 5\,\mathrm{nm}$ [28], and m is restricted to the values $m = 2$, describing a Gaussian envelope wave function, or $m = 1$, corresponding to an exponentially decreasing envelope function. The prefactor $C(\sqrt{\pi}L_0)^{-d/m}$ guarantees the normalization of $\psi(\vec{r})$. For the constant C one obtains $C = 1$ for $m = 2$ independently of the QD dimension d, $C = 1/\sqrt{2}$ for $m = 1, d = 2$ and $C = 1/\sqrt{8}$ for $m = 1, d = 3$.

Basic quantum mechanics teaches us that the central spin's wave function $\psi(\vec{r})$ has a finite value out of the QD and it is technically non-zero even for nuclei from the substrate that are located far from the dot. But obviously these nuclei are associated

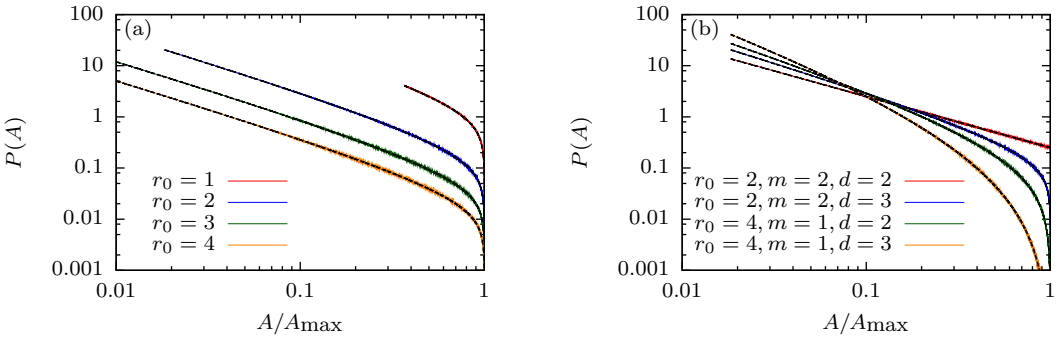

Figure 3.1: Illustration of the probability distribution (3.24). The black dashed lines show $P(A)$ for (a) a variation of the cutoff $r_0 = R/L_0$ assuming a $d = 3$ dimensional QD with a Gaussian envelope wave function ($m = 2$) and (b) all considered choices of the parameters d and m, where the ratio of the largest and smallest coupling constant is set to $A_{\min}/A_{\max} = \mathrm{e}^{-4}$ for all curves. The colored lines depict a histogram generated by 10^8 random picks of $A_k = A_{\max}\exp\left(-r_0^m \gamma_k^{m/d}\right)$, with a uniformly distributed parameter $\gamma_k \in [0:1]$. Panel (a) corresponds to figure 1 of reference [97].

to a very small coupling constant A_k and are not expected to have a noticable impact on the central spin dynamics. On top of that considering all nuclei within a very large radius R around the QD center will yield a divergence of $P(A) \to 0$, because the total number of nuclei within a d-dimensional sphere of radius R is increasing as R^d, while the nuclei associated to a significant coupling constant A_k are expected to be located at maximum a couple of QD length scales L_0 away from the dot center. For this reason we introduce the radius R as a cutoff distance for the nuclei that are taken into account for the calculation of the central spin dynamics. Of course the obtained physics is supposed to be independent of the artificial cutoff R, as long as it is not chosen too small. The probability $P(r)$ to find a nucleus on a surface of radius r, when randomly picking a nucleus with a maximum distance of R to the center of the QD, is given by $P(r) = d \cdot r^{d-1}/R^d$, which is directly associated to the probability of finding a nucleus associated to a certain coupling constant:

$$P(r)\,\mathrm{d}r = P(A)\,\mathrm{d}A. \tag{3.23}$$

By using the relation $A(r) = A_s \Omega\,|\psi(\vec{r})|^2$ with respect to the appropiate assumption for the wave function (3.22), one obtains the probability distribution

$$P(A) = \frac{d}{m}\left(\frac{L_0}{R}\right)^d \frac{1}{A}\left(\ln\left(\frac{A_{\max}}{A}\right)\right)^{d/m-1}, \tag{3.24}$$

where the largest coupling constant, that is located at the center of the QD, is denoted as $A_{\max} = \frac{A_s \Omega C^2}{(\sqrt{\pi} L_0)^d}$. The smallest accessible value of the considered coupling constants is governed by the cutoff parameter $r_0 = R/L_0$ entering the envelope wave function. It is

given by $A_{\min} = A_{\max} \mathrm{e}^{-r_0^m}$. The analytic form (3.24) of the probability distribution $P(A)$ clearly shows its expected divergence for $A \to 0$, that is eliminated by the introduction of the cutoff R. Figure 3.1 illustrates the probability distribution $P(A)$ for a variety of the considered parameters r_0, m and d. Panel (a) treats the case of a $d = 3$ dimensional QD and a Gaussian envelope wave function for various values of r_0. It reflects the rapid decrease of the probability to find a coupling constant $A \sim 0.1 - 1$ near the QD center for an increasing cutoff r_0. Panel (b) compares $P(A)$ for all considered combinations of the parameters $d = 2, 3$ and $m = 1, 2$, based on an identical ratio $A_{\min}/A_{\max} = \mathrm{e}^{-4}$. Since $A_{\min} \propto \mathrm{e}^{-r_0^m}$ applies, the cutoff r_0 has to adjusted appropriately to compare the cases $m = 1$ and $m = 2$. It is observed, that increasing the dimension from $d = 2$ to $d = 3$ always yields an increase of the probability to find a nucleus that is associated to a small coupling constant. This behavior of $P(A)$ is traced back to the number of nuclei within a certain radius r from the dot center, which is proportional to r^d. I.e. the ratio $(r_1/r_2)^d$ of the number of nuclei located in a small shell of radius r_1 around the QD center to those within a larger shell of radius r_2 is decreasing faster in higher dimensions. Comparing $P(A)$ for $m = 1$ and $m = 2$, while keeping the dimension d constant, yields an opposite trend: although the Gaussian envelope function decreases faster than the exponential one, $P(A)$ is larger near $A/A_{\max} \approx 1$ for $m = 2$ than for $m = 1$. This stems from the much larger number of considered nuclei arising from setting $r_0 = 4$ instead of $r_0 = 2$. The underlying argument is the same as it has been put forward for an increase of the dimension.

To produce sets of coupling constants that obey the distribution (3.24), the quantity

$$\gamma(A_k) = \int_{A_k}^{A_{\max}} P(A')\,\mathrm{d}A' \tag{3.25}$$

is introduced. Since $P(A)$ is a monotonically decreasing probability density and only defined on the interval $[A_{\min}, A_{\max}]$, the newly introduced quantity $\gamma(A_k)$ is a bijective function of the form $\gamma : [A_{\min}, A_{\max}] \to [0, 1]$. By inserting $P(A)$ from equation (3.24) into relation (3.25) and calculating the inverse function of $\gamma(A_k)$ one obtains

$$A_k(\gamma) = A_{\max} \exp(-r_0^m \gamma^{m/d}). \tag{3.26}$$

This relation is used for the production of sets of coupling constants A_k that obey $P(A)$, by generating a random value of $\gamma \in [0, 1]$ from a uniform distribution for each individual coupling constant A_k. The colored lines in figure 3.1 depict histograms that have been generated via this procedure for the different sets of parameters as proof of its reliability.

As mentioned above, the obtained physics is supposed to be independent of the choice of the cutoff R as long as the conditions $r_0 > 1$ and $\psi(R) \approx 0$ are satisfied. For the statistical average of an individual coupling constant one easily obtains the value

$$\overline{A} = \int \mathrm{d}A P(A) A \approx A_s / N_d(R), \tag{3.27}$$

where $N_d(R)$ denotes the number of nuclei within the radius R. It is given by $N_2(R) = \pi R^2/\Omega$ or $N_3(R) = 4\pi R^3/3\Omega$. The approximation in equation (3.27) becomes exact for $R \to \infty$. The obtained result is apparently in agreement with the definition of $A_s = \sum_k A_k = N\overline{A}$ and this energy scale is independent of the artificial cutoff R as expected.

3.2 Quadrupole interaction

The formation of QDs grown via molecular beam epitaxy relies on the mismatch of the lattice constants between the substrate and the deposited material, i.e. on the occuring strain that is unevitable when these materials are grown on top of each other. This intrinsic strain is also the source of electric field gradients (EFGs) within such semiconductor QDs, that couple to the quadrupole moment of the nuclei forming the dot. In the following a Hamiltonian is introduced, that involves the influence of this interaction onto the central spin dynamics. C.P. Slichter has derived [98] a Hamiltonian H_q modelling the impact of an arbitrary EFG on a single nucleus, which has a nonzero quadrupole moment. It reads

$$H_q = \frac{eQ}{4I(2I-1)} \left[V_{zz}(3(I^z)^2 - I^2) + (V_{xx} - V_{yy})((I^x)^2 - (I^y)^2) \right], \tag{3.28}$$

where Q denotes the quadrupole moment of the nucleus, e is the elementary charge and $V_{\alpha\alpha}$ is the second partial derivative of the strain induced electric potential V along the α-direction. The quadrupole moment Q arises from the non-spherical shape (see figure 3.2 (a)) of the nucleus under study and its value is determined by the difference between the charge distribution, which is given by the positions of the individual protons within a nucleus, parallel and transverse to the symmetry axis of the nucleus. For simplicity the z-direction is set along this symmetry axis for the representation (3.28) of the Hamiltonian. It is convenient to introduce the asymmetry parameter $\eta = (V_{xx} - V_{yy})/V_{zz}$ as a measure of which term in the Hamiltonian (3.28) is dominant. Concerning the electric potential it is a common [63, 99] approximation to assume axial symmetry, yielding $\eta = 0$. Recent studies by C. Bulutay [70] have shown that this approximation is not necessarily good for self-assembled semiconductor quantum dots. Especially for the alloy InGaAs those studies found values for η of more than 0.5,

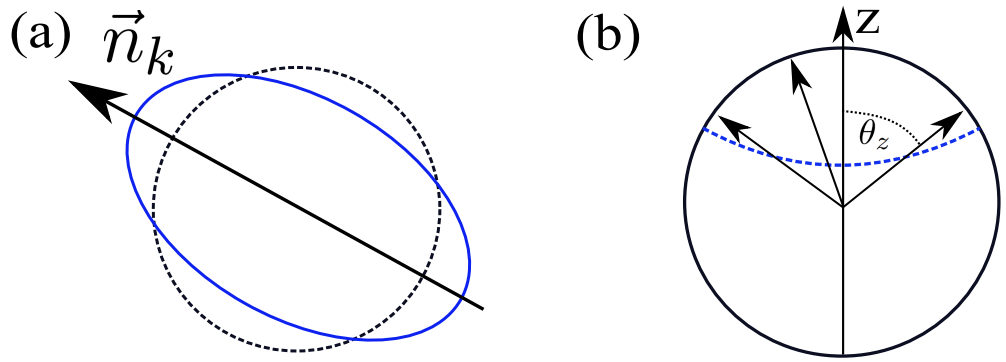

Figure 3.2: (a) Sketch of a nucleus carrying a finite quadrupole moment due to its deviation from a spherical shape. Its symmetry axis is defined as $\vec{n}_k$. (b) Illustration of the random generation process for the orientation vectors $\vec{n}_k$, which are determined randomly within an upper dome of the unit sphere and cover the angle θ_z towards the growth direction of the dot which defines the z-axis.

pointing out that neglecting the latter term of the Hamiltonian (3.28) might not yield a satisfying approximation.

The orientation of the symmetry axis of each individual nucleus within a QD clearly depends on its environment, since it will align according to the EFGs that occure within a self-assembled semiconductor QD. To take an arbitrary orientation of the symmetry axes into account, the normalized vectors $\vec{n}_k$ are introduced according to figure 3.2 (a). They will be referred to as the quadrupole orientation vectors in the following. Defining the prefactor $q_k = \frac{3eQ_k}{4I(2I-1)}V_{zz}^k$, where we restrict ourselves to the case of identical bathspins, and introducing arbitrary quadrupole orientation vectors for each individual nucleus, yields the total quadrupole Hamiltonian

$$H_Q = \sum_{k=1}^{N} q_k \left(\left(\vec{I}_k \cdot \vec{n}_k\right)^2 - \frac{I(I+1)}{3} + \frac{\eta}{3}\left(\vec{I}_k \cdot \vec{n}_k^x\right)^2 - \frac{\eta}{3}\left(\vec{I}_k \cdot \vec{n}_k^y\right)^2 \right) =: \sum_{k=1}^{N} H_q^k, \qquad (3.29)$$

which only yields a non-trivial contribution for nuclei with magnetic moment $I > 1/2$. Note that we have assumed the asymmetry parameter η to be identical for every bath spin, which is an approximation, and that we have introduced the auxilliary vectors $\vec{n}_k^{x/y}$. In the Hamiltonian (3.28) the z-axis was set to be the symmetry axis of the investigated nucleus, which we have set to $\vec{n}_k$. I.e. we have rotated the cartesian unit vector $\vec{e}_z$ onto $\vec{n}_k$ to find a new expression for the operator I_k^z and as a consequence we have to apply the same rotation to $\vec{e}_{x/y}$ to find the representations of $I_k^{x/y}$. Determining the rotation that converts $\vec{e}_z$ into $\vec{n}_k$ is simple: we apply a π-rotation around the axis obtained from the sum of the unit vectors $\vec{e}_z$ and $\vec{n}_k$. Applying this rotation to $\vec{e}_{x/y}$ yields $\vec{n}_k^{x/y}$.

3.2.1 Discussion of the quadrupole parameters

There are three central parameters entering the Hamiltonian H_Q: (i) the quadrupole coupling constants q_k, (ii) the orientation vectors $\vec{n}_k$ and (iii) the asymmetry parameter η. Since the latter is assumed to be identical for each bath spin, its variation among the QD does not have to be considered further. Note that typical values of η in semiconductor QDs are expected to be of the order $O(10^{-1})$ according to reference [70]. The same studies have shown that the distribution of the orientation vectors $\vec{n}_k$ is heavily dependent on the underlying material. Although no explicit spatial distribution of the symmetry axes has been presented, the data concerning the angle θ_z, measuring the deviation of $\vec{n}_k$ from the z-direction as depicted in figure 3.2 (b), indicates that the quadrupole orientation vectors tend to align along the growth direction for InAs, but deviate significantly from this alignment for InGaAs. Numerous studies concerning the distribution of strain within semiconductor QDs have been put forward in the past [100, 101, 102], all reporting an unsteady behavior of the strain, which is crucial for the quadrupole coupling constants. As a consequence, a straight forward and well-grounded derivation for a distribution of neither the couplings q_k nor the orientation vectors $\vec{n}_k$ is possible at the present. As an alternative a stochastical approach is applied to account for the relevant physics within the system: according to the work of Sinitsyn et al. [63] the quadrupole coupling constants are determined randomly from a uniform distribution $q_k \in [0.5 : 1]$. The influence of various claims for this distribution will be discussed in section 8.2.2, pointing out that the intuitive approach put forward by Sinitsyn et al. is supposed to be able to cover the crucial physical effects. Since the orientation of the vectors $\vec{n}_k$ among the QD is not known and expected to be correlated to the EFGs, a stochastical procedure reproducing the average deviation angles θ_z found in reference [70] is applied here. Although a more recent work [71] treats the distribution of the deviation angles θ_z in greater detail, it is to complex to be reproduced within a model consisting of only ~ 10 nuclei. As a consequence we stick to reproducing the reported average angle from reference [70]. This is realised by the generation of a set of isotropically oriented vectors $\vec{n}_k$ on the unit sphere, of which only those vectors within a certain dome at the top of the unit sphere are kept, as sketched in figure 3.2 (b). The angle $\theta_{\max}$ determining the size of this dome is dictated by the deviation angle θ_z of the addressed material. For example in $In_{0.4}Ga_{0.6}As$ the deviation angle varies significantly for the different components: $\theta_z \approx 42^\circ$ for As, $\theta_z \approx 17^\circ$ for Ga and $\theta_z \approx 12^\circ$ for In. As a consequence the mean deviation angle is given by $\theta_z \approx 23^\circ$ which is reproduced by setting $\theta_{\max} \approx 34^\circ$.

As an intuitive parameter that classifies wether the interactions within the CSM or the quadrupole interaction dominates the energy scale of the full Hamiltonian $H = H_{\mathrm{CSM}} + H_Q$, the ratio $Q_r = A_q / A_s$ is introduced, where $A_q = \sum_k q_k$ denotes the sum over all quadrupole couplings corresponding to $A_s = \sum_k A_k$.

3.3 Spin noise function

The experimental measurement of spin noise is usually performed on ensembles of semiconductor QDs that are doped with either electrons or holes. It relies on fluctuations of either the Faraday or Kerr rotation of a linearly polarized probe beam, that occure due to the arising total magnetization from the spins of the confined particles. The autocorrelation function of the rotation angle is equivalent to the symmetrized fluctuation function

$$S(t) = \frac{1}{2}\left(\left\langle S^z(t)S^z\right\rangle + \left\langle S^z S^z(t)\right\rangle\right) - \left\langle S^z\right\rangle^2. \tag{3.30}$$

The average spin polarisation $\left\langle S^z\right\rangle$ vanishes in the abscence of a magnetic field. The function $S(t)$ will be referred to as the spin noise function in the following and it is the central quantity of interest throughout this work. Note that $S(t)$ is symmetric in time by its definition and as a consequence the spectral spin noise function $S(\omega)$, which is also going to be discussed in detail, can be written as

$$S(\omega) = \int_{-\infty}^{\infty} S(t)\mathrm{e}^{-i\omega t}\,\mathrm{d}t = \int_{-\infty}^{\infty} S(t)\cos(\omega t)\,\mathrm{d}t. \tag{3.31}$$

From the inverse Fourier transformation of $S(\omega)$, it is straight forward to show that the total spectral weight of the spectral spin noise function is determined by the initial value $S(t=0)$:

$$S(0) = \frac{1}{2\pi}\int_{-\infty}^{\infty} S(\omega)\,\mathrm{d}\omega. \tag{3.32}$$

This is an important finding as a benchmark for the adequacy of a given numerical method for the calculation of the spectral spin noise function. For the experimental measurement of spin noise the probe laser is adjusted such that it ideally does not induce any excitations in the sample, i.e. the sample is supposed to be in thermal equilibrium. The experiments [59, 64] addressing spin noise in semiconductor QDs are usually performed at a minimum temperature of $T \approx 5\,\mathrm{K}$ which corresponds to approximately $400\,\mu\mathrm{eV}$. Hence, the energy scale of the temperature is significantly larger than $A_s \sim O(10)\,\mu\mathrm{eV}$ and as a consequence we will assume a high temperature limit for all performed simulations, which yields the equilibrium density operator

$$\rho_0 = \frac{1}{D}\underline{\underline{1}}, \tag{3.33}$$

where $D = 2 \cdot I_{\mathrm{dim}}^N$ is the Hilbert space dimension of the investigated system arising from the partition function Z. Taking this initial condition into account, some simplifications for the spin noise function apply: on the one hand the expectation value $\left\langle S^z\right\rangle$

is 0 independently of the applied external field and on the other hand, due to cyclic permutation under the trace and the commutator $[\rho_0, S^z] = 0$, we can rewrite

$$\begin{aligned} S(t) &= \frac{1}{2}\left(\left\langle S^z(t)S^z\right\rangle_{\rho_0} + \left\langle S^z S^z(t)\right\rangle_{\rho_0}\right) = \frac{1}{2}\mathrm{Tr}\left[\rho_0 S^z(t)S^z + \rho_0 S^z S^z(t)\right] \\ &= \frac{1}{2D}\mathrm{Tr}\left[S^z(t)S^z + S^z(t)S^z\right] = \left\langle S^z(t)S^z\right\rangle_{\rho_0}. \end{aligned} \tag{3.34}$$

Taking this simplified form of $S(t)$ into account, it is straight forward to show that the spin noise function corresponds to the time evolution of the z-component of an initially polarised central spin interacting with an unpolarized bath at infinite temperature. Namely, this initial condition is implemented by the density operator

$$\rho_{\mathrm{pol}} = \frac{1}{D}(\underline{\underline{1}} + 2S^z), \tag{3.35}$$

where the central spin is initially in the $\uparrow$-state. For the resulting dynamics of the central spin

$$\left\langle S^z(t)\right\rangle_{\rho_{\mathrm{pol}}} = \frac{1}{D}\mathrm{Tr}[(\underline{\underline{1}} + 2S^z)S^z(t)] = \frac{2}{D}\mathrm{Tr}[S^z S^z(t)] = 2S(t) \tag{3.36}$$

is obtained. This equivalence of $\left\langle S^z(t)\right\rangle$ and $S(t)$ is an important finding, because it states that all investigations and findings concerning the spin noise function also apply for experiments that induce a polarisation in an ensemble of semiconductor QDs via a pump beam and observe the decay of the obtained collective polarisation. As a consequence we put forward that the measurement of spin noise at temperatures $T > 5\,\mathrm{K}$ is in general equivalent to the observation of the real time dynamics of initially polarized spins confined in semiconductor QDs.

3.3.1 The intrinsic time scale

In the following a systematic derivation of a time scale is presented, that describes the leading order impact of the material, which forms the confinement potential to trap a single electron or hole, on the central spin dynamics. I.e. the full Hamiltonian (3.1) for $\omega_L = 0$ is considered within this derivation. To obtain the leading order contribution to $S(t)$, the Taylor series of the entering time evolution operators are inserted:

$$\begin{aligned} S(t) &= \left\langle \mathrm{e}^{\mathrm{i}Ht} S^z \mathrm{e}^{-\mathrm{i}Ht} S^z \right\rangle = \left\langle \sum_{n=0}^{\infty} \frac{(\mathrm{i}Ht)^n}{n!} S^z \sum_{m=0}^{\infty} \frac{(-\mathrm{i}Ht)^m}{m!} S^z \right\rangle \\ &= \left\langle (S^z)^2 \right\rangle + \mathrm{i}t \left\langle [H, S^z] S^z \right\rangle - \frac{t^2}{2} \left\langle \left[H, [H, S^z]\right] S^z \right\rangle + O(t^3). \end{aligned} \tag{3.37}$$

The evaluation of the occuring commutators shows that the first order term $\propto t$ vanishes and the lowest order contribution is of second order in time. The result reads

$$S(t) = \frac{1}{4} - \frac{t^2}{16}\frac{4I(I+1)}{3\lambda^2}\sum_{k=1}^{N} A_k^2 + O(t^3) =: \frac{1}{4} - \left(\frac{t}{4T_\lambda^*}\right)^2 + O(t^3), \tag{3.38}$$

where the intrinsic time scale $T_\lambda^* = \lambda\left(\frac{4I(I+1)}{3}\sum_k A_k^2\right)^{-1/2}$ has been introduced. This is the central time scale, that will be used throughout this work, to form the dimensionless Hamiltonian $\tilde{H} = HT_\lambda^*$ and accordingly it sets the underlying time scale t/T_λ^* for the presented real time dynamics.

Some very intuitive tendencies concerning the impact of H_{CSM} on $S(t)$ can be directly read off the definition of T_λ^*: (i) the central spin dynamics is expected to be a lot faster for electrons than for holes, because the anisotropy parameter λ enters the intrinsic timescale linearly, while the coupling constants A_k, which are expected to be approximately one order of magnitude larger for electrons than for holes, enter T_λ^* inversely. (ii) An increase of the nuclear moment I of the nuclei forming the QD, yields faster occuring decoherence.

Note that the index of the intrinsic time scale T_1^*, applying for electrons, will be dropped for simplicity in the following, a simplification that defines $T^* \equiv T_1^*$. On top of that, the dimensionless magnetic field $b = \omega_L T^*$ will be used throughout this work. Also note that the quadrupole interaction does not contribute to the central spin dynamics in second order and does therefore not enter the intrinsic time scale. Instead the ratio $Q_r = A_q/A_s$, which is independent of the intrinsic time scale, will be used to characterize the magnitude of the QC. Taking the distribution of the coupling constants introduced in section 3.1.5 into account, one can show that the expectation value of T^* for an infinite number of bath spins, corresponding to an infinite cutoff $R \to \infty$, is governed by

$$(T^*)^{-2} \propto \sum_{k=1} A_k^2 = N(R)\overline{A}^2 = \frac{A_s^2}{3\sqrt{\pi}N(L_0)}. \tag{3.39}$$

This points out that the intrinsic time scale of a given QD is fully determined by the energy scale A_s of the hyperfine interaction and the characteristic length scale L_0 of the dot.

3.3.2 Semi classical approximation

Merkulov et al. [27] have introduced a semi classical approach concerning the short time dynamics of an initially polarised spin within the isotropic CSM without an external field. In this simplified scenario, the Hamiltonian H can be rewritten as

$$H_{\mathrm{OH}} = \vec{S} \cdot \sum_{k=1}^{N} A_k \vec{I}_k. \tag{3.40}$$

In this notation the central spin effectively interacts with a single magnetic field $\vec{B}_{\mathrm{OH}} = \sum_k A_k \vec{I}_k$, that is formed by the weighted sum of all nuclei. This field is usually referred to as the Overhauser field. Since the semi classical approach (SCA) by Merkulov et al. is essential to understand the short time dynamics of the spin noise function $S(t)$, it is briefly reviewed here based on the review from reference [103]. Each nuclear spin is assumed as a classical magnetic moment of length I, which is oriented randomly, according to the assumed high temperature limit. On top of that the nuclei are considered to be frozen. This assumption is based on the fact that the total Overhauser field experienced by the central spin is $O(N)$ times larger than the field each individual nucleus sees. Since the total field $\vec{B}_{\mathrm{OH}}$ consists of a large number of small magnetic moments with random orientation, its magnitude is assumed to obey a Gaussian probability distribution

$$W(|\vec{B}_{\mathrm{OH}}|) = \left(\frac{2}{\pi}\right)^{3/2} (T^*)^3 \mathrm{e}^{-2(\vec{B}_{\mathrm{OH}} T^*)^2}. \tag{3.41}$$

The precession of a given spin $\vec{s}$ within a constant external field, which is applied along the $\vec{n}_B$ direction and associated to the Larmor frequency ω_L, can be written as

$$\begin{aligned} \vec{s}(t) = (\vec{s}_0 \cdot \vec{n}_B) \cdot \vec{n}_B + (\vec{s}_0 - (\vec{s}_0 \cdot \vec{n}_B) \cdot \vec{n}_B)\cos(\omega_L t) \\ + [\vec{n}_B \times (\vec{s}_0 - (\vec{s}_0 \cdot \vec{n}_B) \cdot \vec{n}_B)] \sin(\omega_L t), \end{aligned} \tag{3.42}$$

where $\vec{s}_0$ denotes the initial orientation of the spin $\vec{s}$. The central spin dynamics is obtained by averaging equation (3.42) over all possible orientations of the Overhauser field with respect to the probability distribution $W(|\vec{B}_{\mathrm{OH}}|)$ describing its absolute value:

$$\langle \vec{s}(t) \rangle = \int_0^{2\pi} \mathrm{d}\phi \int_0^{\pi} \sin(\theta)\, \mathrm{d}\theta \int_0^{\infty} B^2\, \mathrm{d}B\, W(|\vec{B}|) \vec{s}(t). \tag{3.43}$$

The infinite upper boundary of the last integral arises from the applied limit of an infinite bath $N \to \infty$. As argued above the spin noise function $S(t)$ is equivalent to the measurement of $\langle S^z(t) \rangle$ for an initially fully polarized central spin. Therefore the

initial condition $\vec{s}_0 = s_0\vec{e}_z$ is assumed, where the absolute value $s_0 = 1/4$ applies for the spin noise function. One obtains

$$S_{\mathrm{SCA}}(t) := \frac{s_0}{3}\left[1 + 2\left(1 - \left(\frac{t}{2T^*}\right)^2\right)\exp\left(-\frac{1}{2}\left(\frac{t}{2T^*}\right)^2\right)\right]. \tag{3.44}$$

The only physical quantity that enters this analytical result is the intrinsic time scale T^*, which underlines its fundamental role within the model at hand. Especially note that no details concerning the distribution of the coupling constants A_k enter $S_{\mathrm{SCA}}(t)$. The semi classical approach predicts a finite value of $S(t)$ at infinite times $S(t \to \infty) = 1/12$, but since it assumes a frozen nuclear spin bath, it is expected to be only viable for the short time dynamics of the spin noise function. The Fourier transformation of the semi classical result $S_{\mathrm{SCA}}(t)$ can be straight forwardly performed analytically, yielding

$$S_{\mathrm{SCA}}(\omega) = \int_{-\infty}^{\infty} \mathrm{d}t\, S_{\mathrm{SCA}}(t)\mathrm{e}^{-\mathrm{i}\omega t} = \frac{s_0}{3}\left[2\pi\delta(\omega) + \omega^2(\sqrt{8}T^*)^3\sqrt{\pi}\mathrm{e}^{-2(\omega T^*)^2}\right]. \tag{3.45}$$

Apparently the contribution $\propto \delta(\omega)$ corresponds to the finite value of $S_{\mathrm{SCA}}(t)$ at infinite times and the spectral weight of $S_{\mathrm{SCA}}(\omega)$ corresponding to the central spin's decay due to the frozen Overhauser field contributes $2/3$ of the full spectral weight, which is set by $S(0)$.

Note that Testelin et al. [56] have also introduced semi classical predictions similar to $S_{\mathrm{SCA}}(t)$ for various special cases of the anisotropic CSM, which will not be reviewed here in detail, but will serve as a reference for some numerical calculations below.

3.4 Ensemble averaging

Experimental measurements addressing spin noise in semiconductor QDs are often performed on ensembles of QDs and therefore the effect of ensemble averaging on the spin noise functions $S(t)$ and $S(\omega)$ needs to be considered. Since the model under study does not include possible interactions between the particles confined in neighboring QDs of an ensemble, only those physical properties that may vary among the individual QDs and have an impact onto the Hamiltonian (3.1) need to be discussed in the context of ensemble averaging here. There are such properties influencing each of the three parts forming the Hamiltonian H, but as discussed above we have limited insight into the details of the strain distribution for each individual QD. Hence, the stochastical approach for the implementation of the quadrupole interaction, which has been presented in section 8, is assumed to hold for each QD of the ensemble.

It is well known [104] that the shape of self-assembled QDs is varying among an ensemble. As indicated by equation (3.39), the characteristic length scale L_0 of a given dot directly influences the intrinsic time scale of the system, which is crucial for the central spin's short time dynamics. To account for this effect, a Gaussian distribution

with a variable standard deviation ΔL_0 is assumed for the characteristic length scale L_0, which enters a given simulation via equation (3.39).

Beside the varying shape of the individual QDs, we take into account that a spread of the g-factor occurs in typical ensembles of semiconductor QDs. For electrons this spread is very small [23] and will be neglected throughout this work. In contrast it has been found [64] to be rather large for hole doped QDs and to account for this observation, once again, a Gaussian distribution of the g-factors among the ensemble is assumed. If not stated otherwise its standard deviation is set to the value $\Delta g/g = 0.2$.

Chapter 4

The Chebyshev Polynomial Expansion Technique

The focus of the chapter at hand is the introduction of an adequate numerical method for the calculation of the spin noise function $S(t)$ in the real time and the spectral regime, based on the Hamiltonian $H = H_{\mathrm{CSM}} + H_Q$. The limit of infinite temperature enters all presented considerations. The Chebyshev polynomial expansion technique (CET) is originally a method that propagates a single quantum state in time by expanding the time evolution operator $\mathrm{e}^{-\mathrm{i}Ht}$, arising in the formal time evolution

$$|\psi(t)\rangle = \mathrm{e}^{-\mathrm{i}Ht} |\psi(0)\rangle , \tag{4.1}$$

in orders of Chebyshev polynomials. As discussed in detail in the following, the CET is an exact method for the propagation of a single quantum state $|\psi(t)\rangle$ in time, but its main advantage compared to exact diagonalisation (ED), is that its runtime scales linearly with the Hilbert space dimension D of the underlying Hamiltonian, while the ED scales with D^3. To apply the CET to the calculation of the spin noise function

$$S(t) = \left\langle S^z(t) S^z \right\rangle_{\rho_0} = \frac{1}{D} \sum_{i=1}^{D} \langle i| \, \mathrm{e}^{\mathrm{i}Ht} S^z \mathrm{e}^{-\mathrm{i}Ht} S^z \, |i\rangle , \tag{4.2}$$

every individual basis state $|i\rangle$ and the modified basis states $S^z |i\rangle$ would have to be propagated in time individually, which implies an enormous numerical effort rapidly exceeding reasonable amounts of resources. Thus, an efficient way for the calculation of traces has to be found, to apply the CET to the spin noise function $S(t)$. On top of that, a direct way to calculate the spectral function $S(\omega)$ is not known a priori.

The remainder of this chapter is structured as follows: first, the definition of the Chebyshev polynomials is given and some of their elementary properties that are crucial for the CET are briefly introduced. Second, the propagation of a single quantum state in time is discussed along with some numerical details. Third, a systematic approach for the numerically efficient treatment of the occurring traces in the spin noise

function $S(t)$ is presented. Fourth, the Fourier transformation of $S(t)$ is performed analytically, based on its expansion in Chebyshev polynomials, to obtain a direct method for the calculation of $S(\omega)$ that does not rely on the transformation of time resolved data. Finally, benchmarks for the CET concerning both $S(t)$ and $S(\omega)$ are performed, to prove the viability of the method. Note that this chapter is based on the discussions concerning the CET from references [97] and [103].

4.1 Definition and properties of the Chebyshev polynomials

For the presented numerical investigations only the Chebyshev polynomials of first kind are of interest. There are two common definitions of these polynomials: (i) the iterative definition, which reads

$$\begin{aligned} T_0(z) &= 1, \qquad T_1(z) = z, \\ T_{n+1}(z) &= 2zT_n(z) - T_{n-1}(z), \end{aligned} \tag{4.3}$$

and (ii) the trigonometric definition, reading

$$T_n(z) = \begin{cases} \cos(n \cdot \arccos(z)), & z \in [-1,1] \\ \cosh(n \cdot \operatorname{arcosh}(z)), & \text{else.} \end{cases} \tag{4.4}$$

The first one will turn out to be useful for the propagation of quantum states, while the latter can be taken into account to show that the Chebyshev polynomials form an orthonormal basis on the interval $z \in [-1:1]$. Starting from the well known orthogonality relation

$$\delta_{n,m}\frac{\pi}{2-\delta_{n,0}} = \frac{1}{2}\int_{-\pi}^{\pi} \mathrm{d}x \cos(nx)\cos(mx) = \int_{0}^{\pi} \mathrm{d}x \cos(nx)\cos(mx), \tag{4.5}$$

where $\delta_{\alpha,\beta}$ denotes the Kronecker symbol, one obtains a corresponding relation occurring for the Chebyshev polynomials by substituting $x \to \arccos(z)$:

$$\langle T_n | T_m \rangle_c := \int_{-1}^{1} \mathrm{d}z \frac{T_n(z)T_m(z)}{\sqrt{1-z^2}} = \frac{\pi}{2-\delta_{n,0}}\delta_{n,m}, \tag{4.6}$$

where the scalar product $\langle\cdot|\cdot\rangle_c$ has been defined. Due to the orthonormality of the Chebyshev polynomials with respect to this scalar product, every function that is defined on the interval $z \in [-1:1]$ can be expanded in Chebyshev polynomials as follows

$$\begin{aligned} g(z) &= \sum_{n=0}^{\infty} b_n T_n(z), \\ b_n &= \frac{2-\delta_{n,0}}{\pi} \int_{-1}^{1} \mathrm{d}x \, \frac{T_n(x) g^*(x)}{\sqrt{1-x^2}}. \end{aligned} \tag{4.7}$$

Another central property, that is crucial for the reliability of the CET, is that the Chebyshev polynomials of first kind are linked to the Bessel functions of first kind via the relation

$$J_n(t) = \frac{(-\mathrm{i})^n}{\pi} \int_{-1}^{1} \mathrm{d}\omega \, \frac{\mathrm{e}^{\mathrm{i}\omega t} T_n(\omega)}{\sqrt{1-\omega^2}}. \tag{4.8}$$

Of course there are several further interesting properties concerning the Chebyshev polynomials, but the introduced repertoire is sufficient for the expansion of the time evolution operator in Chebyshev polynomials, which is of interest here.

4.2 Propagating a quantum state in time

The CET has been originally introduced by H. Tal-Ezer and R. Kosloff [66] and it can be applied to any quantum system whose Hamiltonian has a finite energy spectrum $E_{\min} \leq \omega \leq E_{\max}$. This prerequisite is clearly met for any system that is fully represented by a finite number of spin operators, which is the case for the Hamiltonian H under study. To apply the CET to the enhanced central spin model, its energy spectrum has to be mapped onto the interval $\omega' \in [-1:1]$ on which the Chebyshev polynomials form a complete basis set. This is realised by applying the transformation

$$H' = \frac{H-\alpha}{\beta} \quad \Longleftrightarrow \quad H = \beta H' + \alpha, \tag{4.9}$$

which yields the dimensionless Hamiltonian H', whose energy spectrum is defined on the demanded interval. The introduced quantities α and β are defined as

$$\alpha = \frac{E_{\max} + E_{\min}}{2}, \quad \beta = \frac{E_{\max} - E_{\min}}{2}. \tag{4.10}$$

Taking these definitions into account the time evolution operator can be expanded in Chebyshev polynomials. The expansion reads

$$\mathrm{e}^{-iHt} = \mathrm{e}^{-i\alpha t}\mathrm{e}^{-iH'\beta t} = \sum_{n=0}^{\infty} b_n(t) T_n(H'), \tag{4.11}$$

$$\begin{aligned} b_n(t) &= \mathrm{e}^{-i\alpha t}\frac{2-\delta_{n,0}}{\pi}\int_{-1}^{1} \mathrm{d}\omega' \, \frac{\mathrm{e}^{i\omega'\beta t} T_n(\omega')}{\sqrt{1-\omega'^2}}, \\ &= \mathrm{e}^{-i\alpha t}(2-\delta_{n,0}) i^n J_n(\beta t). \end{aligned} \tag{4.12}$$

Apparently, the Chebyshev expansion of the time evolution operator separates the influence of the Hamiltonian, which only enters the Chebyshev polynomials $T_n(H')$, from the time depedence, wich is fully described by the scalar coefficients $b_n(t)$. Applying the expanded time evolution operator to an arbitrary quantum state $|\psi_0\rangle$ yields the expression

$$\mathrm{e}^{-\mathrm{i}Ht}\,|\psi_0\rangle = \sum_{n=0}^{\infty} b_n(t) T_n(H')\,|\psi_0\rangle =: \sum_{n=0}^{\infty} b_n(t)\,|\phi_n\rangle\,. \tag{4.13}$$

As a consequence the states $|\phi_n\rangle$ can be generated by iteratively applying the Hamiltonian H' to the initial state $|\psi_0\rangle$

$$\begin{aligned} |\phi_0\rangle = |\psi_0\rangle\,, \quad |\phi_1\rangle = H'\,|\psi_0\rangle \\ |\phi_{n+1}\rangle = 2H'\,|\phi_n\rangle - |\phi_{n-1}\rangle \end{aligned} \tag{4.14}$$

before the time evolution of the initial state is calculated. I.e. instead of storing the Hamiltonian H' for the calculation of the real time dynamics $|\psi(t)\rangle$, a set of states $|\phi_n\rangle$ has to be stored. Obviously an infinite number of states can not be treated numerically and the infinite sum entering equation (4.13) has to be truncated after a finite number N_c of elements. In the following a systematic choice for this cutoff N_c is discussed with respect to the convergence properties of the CET. On top of this open topic, the largest and smallest eigenenergies of the Hamiltonian H have to be known to apply the transformation (4.9), which is unevitable for the CET. Of course the full energy spectrum of H is not known a priori and applying an exact diagonalisation of the full Hamiltonian is obviously not an option, because circumventing this step is the whole point of applying the CET instead of an ED procedure to obtain the spin noise function $S(t)$. Pleasently, knowing an upper bound for E_{max} and a lower bound for E_{min} is sufficient to make the CET work, where the deviation of these bounds from the exact values turns out to be crucial for the efficiency of the method.

4.2.1 Convergence of the time dependent CET

The convergence of the CET for the propagation of a single quantum state in time relies on the occurence of the Bessel functions of first kind in the coefficients $b_n(t)$. As demonstrated in figure 4.1 (a), the Bessel functions $J_n(\beta t)$ of large order are approximately zero up to a certain value of their argument, which can be estimated by the asymptotic form $J_n(\beta t) \sim (\mathrm{e}\beta t/2n)^n$ [105, 106] that holds for $n \to \infty$. To determine the number of Chebyshev polynomials N_c, that have to be taken into account to obtain an accurate result for the propagated initial state $|\psi_0\rangle$ at time t, the parameter ϵ is introduced. It is a measure for the accuracy of the CET and by evaluating the smallest N_c fullfilling

$$\epsilon \geq \left(\frac{\mathrm{e}\beta t}{2N_c}\right)^{N_c}, \tag{4.15}$$

a reliable result for $|\psi(t)\rangle$ is obtained by computing equation (4.13), where the infinite sum is truncated after summing up N_c elements. The parameter ϵ is usually set to the value $\epsilon = 10^{-3}$, ensuring an error below 10^{-6} as demonstrated in section 4.5, where general benchmarks concerning the CET are performed. Note that equation (4.15) indicates a quick convergence of the CET as N_c exceeds βt and as a consequence the number of polynomials N_c, that have to be taken into account in a typical simulation, is of the same order as the product of the half spectral width β and the largest time t_{max} that is simulated. In contrast to an ED procedure, whose runtime only depends on the system's Hilbert space, this also implies that the runtime of a simulation based on the CET is proportional to βt. This finding points out that the deviation of the estimate for the largest and smallest eigenvalue of the Hamiltonian H, which will be discussed in the following section, from their exact values enters the runtime of the CET linearly, pointing out that finding a good estimate for E_{min} and E_{max} is worthwhile. For typical setups that will be investigated throughout this work, the number of considered Chebyshev polynomials is of the order $N_c \sim O(100 - 1000)$. This sets the main limitation of the CET, because N_c quantum states of the dimension $D = 2 \cdot I_{\mathrm{dim}}^N$ have to be stored in the active memory at any given time, which limits the number of treatable spin-1/2 nuclei to $N \sim 24$.

4.2.2 Estimating the energy spectrum

As discussed in the previous section, establishing an adequate estimate for the eigenenergies E_{min} and E_{max} is crucial for the runtime optimization of a program that utilizes the CET. The ideal estimate is obviously obtained by exactly diagonalizing the Hamiltonian H, which is not a feasible option, because the diagonalization would consume a lot more time than the whole CET procedure itself. Thus, we have to find a moderate trade off between an estimate that is (i) close to the real extreme eigenvalues of

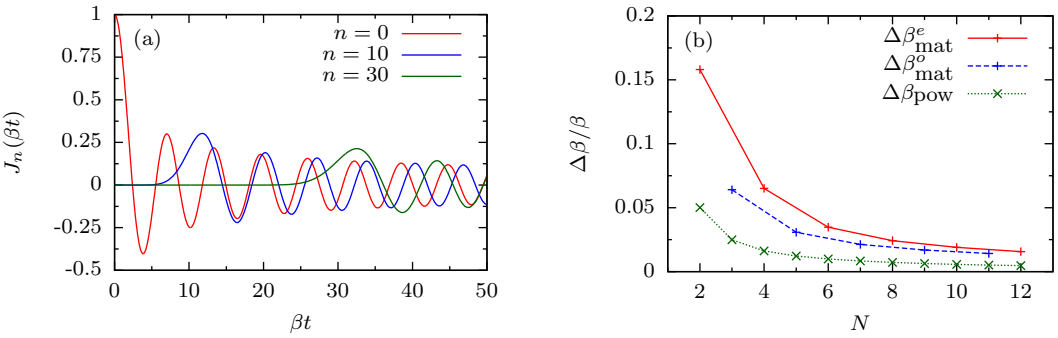

Figure 4.1: Panel (a) illustrates the behavior of the Bessel functions $J_n(\beta t)$ of large order n, which is crucial for the convergence of the CET. Panel (b) shows the relative error of the two presented estimates for the spectral width β of the isotropic CSM with a spin bath of spin-1/2 nuclei, where an external magnetic field strength $b = \omega_L T^* = 2$ applied along the x-direction is considered. Note that the quadrupole term does not contribute for spin-1/2 nuclei. The error of the estimate obtained via the power iteration is referred to as $\Delta\beta_{\text{pow}}$, while $\Delta\beta^{e/o}_{\text{mat}}$ denotes the relative error of the approach based on the triangle inequality, where the even (e) and odd (o) bath sizes N are illustrated seperately.

the Hamiltonian H and (ii) obtained in an adequate amount of time. In the following two approaches for the realization of such an estimate are presented, both featuring different advantages and drawbacks.

Triangle inequality

Since the Hamiltonian H does not include any interactions between the individual bath spins, the triangle inequality [107]

$$||A + B|| \leq ||A|| + ||B|| \tag{4.16}$$

can be applied to gain an estimate for the two extreme eigenenergies E_{min} and E_{max}. For this purpose the triangle inequality is examined with respect to the spectral norm [108]. For a hermitian matrix, as represented by any matrix representation of the Hamiltonian H, the spectral norm is given by the absolute value of the eigenvalue that possesses the largest absolute value. To apply equation (4.16) to the Hamiltonian H, which is given by the relations (3.29) and (3.14), it is split into two parts

$$H = \omega_L \vec{S} \cdot \vec{n}_B + \sum_{k=1}^{N} (H^k_{hf} + H^k_q) = H_1 + H_2 \tag{4.17}$$

$$H_1 = \omega_L \vec{S} \cdot \vec{n}_B + \sum_{k=1}^{m} (H^k_{hf} + H^k_q), \quad H_2 = \sum_{k=m}^{N} (H^k_{hf} + H^k_q). \tag{4.18}$$

Due to this partition of the full Hamiltonian, the two operators H_1 and H_2, whose Hilbert spaces are associated to the dimensions $2 \cdot I^m_{\text{dim}}$ and $2 \cdot I^{N-m}_{\text{dim}}$, can be diagonalised in a moderate amount of time, yielding the sets of eigenvalues $\{E^1_n\}$ and $\{E^2_n\}$. By

examining the triangle inequality with respect to the spectral norm, this procedure straight forwardly provides the upper bound $\left|E^1\right|_{\max} + \left|E^2\right|_{\max}$ for the absolute values of both $E_{\min}$ and $E_{\max}$. Anyhow, the full spectrum of a given matrix can be shifted arbitrarily by adding or substracting a matrix proportional to unity, i.e. one can always set either $E_{\min}$ or $E_{\max}$ to be the eigenenergy with the largest absolute value and the triangle inequality holds in any case. Thus, considering the triangle inequality on basis of the spectral norm is sufficient to show, that the diagonalisation of the two matrices H_1 and H_2 provides the two individual bounds $E_{\min} \geq E^1_{\min} + E^2_{\min}$ and $E_{\max} \leq E^1_{\max} + E^2_{\max}$. Note that the triangle inequality can in principal be generalized to an arbitrary number of summed matrices, but for the Hilbert space dimensions that will be treated with the CET in the following, the separation into two individual parts is sufficient.

Figure 4.1 (b) shows the relative error $\Delta\beta_{\text{mat}} := \Delta\beta/\beta$ of the estimate obtained via the triangle inequality, where $\Delta\beta$ is the absolute deviation of the estimated spectral width from its exact value. The underlying system that has been considered for the shown estimates consists of a nuclear bath of spin $I = 1/2$ particles in the isotropic ($\lambda = 1$) CSM including an external magnetic field along the x-direction. Its strength is given by $b = \omega_L T^* = 2$. For simplicity and comparability the coupling constants are not determined randomly for this benchmark, instead they are increasing linearly: $A_k = k \cdot A_{\min}$. The parameter m, that sets the dimension of the two operators H_1 and H_2, has been set to $N/2$ (rounded up for odd bath sizes) for all calculations. With respect to the shape of the presented curves, the results for even and odd bath sizes are separated from each other. The fact that the relative error $\Delta\beta^o_{\text{mat}}$ for odd bath sizes is significantly smaller than $\Delta\beta^e_{\text{mat}}$ for even bath sizes indicates the tendency that separating the Hamiltonian into two equally large parts is not an optimal choice. A further investigation of this tendency, which is not discussed here in detail, points out that choosing m as large as possible is always ideal. This is an intuitive finding, since setting $m = N$ is obviously the best possible choice. For the numerical investigations that will be presented in the following, the choice of m depends on the numerical effort of the individual calculation. For rather short simulations setting $m = 10$ for spin-1/2 and $m = 5$ for spin-3/2 nuclei is sufficient to quickly obtain a sufficient estimate, while for expensive simulations m is maximally set to 12 or 6 respectively. Note that the error of the presented estimate based on the triangle inequality is decreasing for increasing bath size and already for $N = 12$ and the suboptimal choice $m = N/2$ a relative error of approximately 2 % is achieved, which is expected to be reduced by a factor of approximately $1.5 - 2$ in the typical simulations that will be discussed later. Although the presented estimate based on the triangle inequality is very versatile at a moderate efficiency, a second approach for the estimation of the energy spectrum is presented in the following, that is advantageous in certain scenarios.

Power iteration

The power iteration [109] is a numerical procedure that gives access to the single eigenvalue $\lambda_{\max}$ that possesses the largest absolute value of a given diagonalisable matrix. To obtain this eigenvalue, the matrix is iteratively applied to an arbitrary initial vector a_0, defined in the space that is spanned by the eigenvectors of the matrix under study, until the arising prefactor of the performed matrix vector product converges. The only prerequisite, which is mandatory for the convergence of the method, concerning the vector a_0 is that it needs to have a finite overlap with the subspace spanned by the eigenvectors that are associated to the eigenvalue $\lambda_{\max}$. Note that the vector a_0 has to be normalized after each iteration, to avoid an occurring divergence of the method. Determining $\lambda_{\max}$ for the Hamiltonian H corresponds to the calculation of the series

$$|\varphi_n\rangle = \frac{H^n |\varphi_n\rangle}{\sqrt{\langle\varphi_n| H^n H^n |\varphi_n\rangle}}, \tag{4.19}$$

where $|\varphi_0\rangle$ is usually a randomly generated state. Since the propagation of a quantum state in time via the CET also relies on the iterative application of the Hamiltonian to an initial vector $|\psi_0\rangle$, the power iteration is an obvious candidate for a cheap estimation of the largest eigenenergy according to its absolute value.

For the most general form of the Hamiltonian (3.1) it is unclear wether the power iteration yields the absolute value of $E_{\min}$ or $E_{\max}$ and in general no analytic statement for the other eigenvalue is known. Thus, it is straightforward to determine the eigenvalue $\lambda_{\max}$ of the Hamiltonian H and to set $E_{\min} = -|\lambda_{\max}|$ and $E_{\max} = |\lambda_{\max}|$ afterwards. This clearly yields a valid upper bound for the spectral width β, but apparently not an optimal one. Figure 4.1 (b) shows the relative error $\Delta\beta_{\text{pow}} := \Delta\beta/\beta$ of the estimate obtained via the described power iteration procedure based on the same setup as discussed for the estimation via the triangle inequality. Apparently the relative error obtained via the power iteration is significantly smaller than from the triangle inequality. As described in the context of the estimate via the triangle inequality, it is also possible to shift the entire spectrum of the Hamiltonian and by applying the power iteration, both extreme eigenvalues could be determined exactly this way. Also note that the largest eigenenergy $E_{\max}$ is known a priori for the special case of the isotropic CSM without taking the quadrupole interaction into account ($Q_r = 0$) and it is given by

$$E_{\max} = \frac{\omega_L}{2} + \frac{A_s I}{2}. \tag{4.20}$$

On top of the knowledge of this exact statement, it can be shown that the absolute value of the smallest eigenenergy $E_{\min}$ is always larger than $E_{\max}$ for the pure isotropic CSM.

Hence the power iteration is capable of yielding an exact estimate for the demanded eigenenergies in this special case.

On first sight the power iteration seems to be advantageous compared to an estimation via the triangle inequality. Anyhow, there are two problems associated to this method that are linked to each other: (i) by construction the method always converges towards the largest eigenvalue from below, i.e. aborting the iteration too early yields an underestimation of the energy spectrum, which results in a divergence of the CET. (ii) It turns out that the convergence velocity of the method is heavily dependent on the system parameters and for certain setups the convergence occurs very slowly. For these reasons the estimation based on the triangle inequality is often the better choice, because it is not dependent on the system setup at hand and it therefore yields an adequate result on a timescale that is perfectly predictable. Still the power iteration is the preferred method for certain setups. Especially for the treatment of the isotropic CSM without an external magnetic field and QC, which is a very prominent special scenario of the system under study, the power iteration is the preferred method due to its quick convergence and its exact estimate of the desired energy spectrum.

4.3 Calculation of the spin noise function $S(t)$

As mentioned introductory and shown in equation (4.2), the calculation of the spin noise function $S(t)$ requires the evaluation of a trace, i.e. the propagation of D individual basis states in time, This is clearly not realisable in an adequate amount of time. To circumvent this problem A. Weisse et al. [110] have put forward a stochastical evaluation of traces, which manages to approximate a full trace by considering a small amount N_s of randomly generated states $|r\rangle$. These states are constructed by determining D random coefficients ξ_{ri} fullfilling the relations

$$\langle\langle \xi_{ri} \rangle\rangle = 0, \tag{4.21}$$

$$\left\langle\left\langle \xi_{ri}\xi_{r'j} \right\rangle\right\rangle = \delta_{r,r'}\delta_{i,j}, \tag{4.22}$$

where $\langle\langle \cdots \rangle\rangle$ denotes the statistical average. Equations (4.21) and (4.22) are realized by the generation of real coefficients that obey a Gaussian distribution. To realize such a Gaussian probability distribution, the Box-Muller-method [111] is applied. The coefficients ξ_{ri} are used to construct the random state

$$|r\rangle = \sum_{i=1}^{D} \xi_{ri} |i\rangle , \tag{4.23}$$

which is explicitly not normalized in the process. These states are used to construct the statistical average

$$\left\langle\left\langle \frac{1}{N_s D}\sum_{r=1}^{N_s}\langle r|\,\mathrm{e}^{\mathrm{i}Ht}S^z\mathrm{e}^{-\mathrm{i}Ht}S^z\,|r\rangle\right\rangle\right\rangle = \frac{1}{N_s D}\sum_{r=1}^{N_s}\sum_{i,j=1}^{D}\left\langle\left\langle \xi_{ri}\xi_{rj}\right\rangle\right\rangle\langle i|\,\mathrm{e}^{\mathrm{i}Ht}S^z\mathrm{e}^{-\mathrm{i}Ht}S^z\,|j\rangle$$
$$= \frac{1}{D}\sum_{i=1}^{D}\langle i|\,\mathrm{e}^{\mathrm{i}Ht}S^z\mathrm{e}^{-\mathrm{i}Ht}S^z\,|i\rangle\,. \tag{4.24}$$

Apparently considering a set of N_s random states instead of the D basis states reproduces the spin noise function $S(t)$ in the representation (4.2) on average. As argued by Weisse et al. [110], the error of this stochastical approach is of the order $O(\frac{1}{\sqrt{N_s D}})$. I.e. the number N_s of considered random states, that needs to be taken into account for an adequate approximation of the spin noise function $S(t)$, decreases with the dimension D of the underlying Hilbert space. For example when investigating a system containing a bath of $N = 20$ spin-1/2 nuclei, taking a single random state into account is expected to be sufficient to obtain an error of the order $O(10^{-3})$. In equation (4.2) one time evolution operator is applied to the state $|i\rangle$, while the other acts on the modified state $|i'\rangle = S^z\,|i\rangle$. To avoid the explicit propagation of these two individual states, the relation (3.36) is exploited, where the density operator ρ_{pol} fullfills $\rho_{\mathrm{pol}}^2 = \frac{2}{D}\rho_{\mathrm{pol}}$. Inserting this into the spin noise function yields

$$S(t) \approx \frac{1}{2N_s}\sum_{r=1}^{N_s}\langle r|\,\rho_{\mathrm{pol}}\mathrm{e}^{\mathrm{i}Ht}S^z\mathrm{e}^{-\mathrm{i}Ht}\,|r\rangle = \frac{D}{4N_s}\sum_{r=1}^{N_s}\langle r|\,\rho_{\mathrm{pol}}\mathrm{e}^{\mathrm{i}Ht}S^z\mathrm{e}^{-\mathrm{i}Ht}\rho_{\mathrm{pol}}\,|r\rangle\,. \tag{4.25}$$

This is the final form of $S(t)$, which is calculated in most simulations that are discussed throughout this work. N_s is typically in the range $3-5$ and only a single quantum state $|r'\rangle = \rho_{\mathrm{pol}}\,|r\rangle$ needs to be propagated for each of the N_s series elements.

4.4 Analytic Fourier transformation of the spin noise function

The experimental approach to obtain the spectral spin noise function $S(\omega)$ is to perform a real time measurement on large time scales and to perform a Fourier transformation to the obtained data. This is also a valid route for the theoretical treatment of $S(\omega)$, but since the expansion in Chebyshev polynomials features a direct analytical statement for the spectral spin noise function, the numerical evaluation of this analytical form is

preferred over the Fourier transformation of time resolved calculations. To transform $S(t)$ into the spectral regime, it is rewritten using equation (4.12) yielding

$$S(t) = \mathrm{Tr}\left[e^{iHt}S^z e^{-iHt}S^z\right] \tag{4.26}$$

$$= \sum_{n,m=0}^{\infty} \frac{2-\delta_{n,0}}{\pi}\frac{2-\delta_{m,0}}{\pi}\mathrm{Tr}\left[T_n(H')S^z T_m(H')S^z\right] \times \iint_{-1}^{1} \mathrm{d}\tilde{\omega}_1\,\mathrm{d}\tilde{\omega}_2\, e^{-i(\tilde{\omega}_1-\tilde{\omega}_2)\beta t}\frac{T_n(\tilde{\omega}_1)T_m(\tilde{\omega}_2)}{\sqrt{(1-\tilde{\omega}_1^2)(1-\tilde{\omega}_2^2)}}. \tag{4.27}$$

For simplicity the acronyms $\mu_{n,m} = \mathrm{Tr}\left[e^{iHt}S^z e^{-iHt}S^z\right]$ and $h_{n,m} = \frac{2-\delta_{n,0}}{\pi}\frac{2-\delta_{m,0}}{\pi}$ are introduced. By applying the Fourier transformation to this form of $S(t)$, one obtains

$$S(\omega) = \sum_{n,m=0}^{\infty} h_{n,m}\mu_{n,m}\iint_{-1}^{1}\mathrm{d}\tilde{\omega}_1\,\mathrm{d}\tilde{\omega}_2\frac{T_n(\tilde{\omega}_1)T_m(\tilde{\omega}_2)}{\sqrt{(1-\tilde{\omega}_1^2)(1-\tilde{\omega}_2^2)}} \times \int_{-\infty}^{\infty}\mathrm{d}t\, e^{-\mathrm{i}(\frac{\omega}{\beta}+\tilde{\omega}_1-\tilde{\omega}_2)\beta t}, \tag{4.28}$$

where the time integral can be easily evaluated. It yields a Dirac delta function of the form $\frac{2\pi}{\beta}\delta(\frac{\omega}{\beta}+\tilde{\omega}_1-\tilde{\omega}_2)$, which can be used straight forwardly to evaluate one of the remainder integrals. We arrive at the final form

$$S(\omega) = \sum_{n,m=0}^{\infty}\frac{2\pi}{\beta}h_{n,m}\mu_{n,m}\int_a^b \mathrm{d}\tilde{\omega}\frac{T_n(\tilde{\omega})T_m(\tilde{\omega}+\frac{\omega}{\beta})}{\sqrt{(1-\tilde{\omega}^2)(1-(\tilde{\omega}+\frac{\omega}{\beta})^2)}}. \tag{4.29}$$

The boundaries a and b of the occurring integral depent on the sign of the frequency ω:

$$\omega < 0: \qquad a = -1-\frac{\omega}{\beta}, \qquad b = 1 \tag{4.30}$$

$$\omega \geq 0: \qquad a = -1, \qquad b = 1-\frac{\omega}{\beta}. \tag{4.31}$$

Anyhow equation (3.31) points out that the spectral spin noise function is an even function in ω. As a consequence a restriction to $\omega \geq 0$ is well justified and will be applied in the following. There are three critical factors entering the final form (4.29) of $S(\omega)$: (i) the calculation of the momenta $\mu_{n,m}$ can be treated similarly as discussed for the occurring trace in $S(t)$. Namely a stochastical evaluation is applied and for simplicity $\mathrm{Tr}\left[T_n(H')S^z T_m(H')S^z\right]$ is rewritten as $\frac{D}{4}\mathrm{Tr}\left[\rho_{\mathrm{pol}}T_n(H')S^z T_m(H')\rho_{\mathrm{pol}}\right]$. (ii) The occurring integral features divergencies at both boundaries, making its adequate evaluation problematic. (iii) The convergence of the two infinite sums entering $S(\omega)$ is not strictly ensured, in contrast to the demonstrated behavior for $S(t)$. The two latter open challenges are discussed in the following.

4.4.1 Efficient integration method

The divergencies entering the integral in equation (4.29) stem from the denominator, while the nominator is entirely unproblematic. Figure 4.2 illustrates the behavior of the integral kernel for $n = m = 0$, where the Chebyshev polynomials are equal to 1. Apparently, its gradient is very large close to the boundaries, while it is small for a

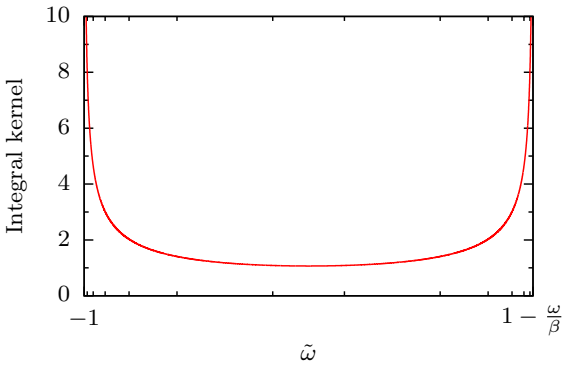

Figure 4.2: Schematical illustration of the integral kernel $((1-\tilde{\omega})(1-(\tilde{\omega}+\frac{\omega}{\beta})^2))^{-1/2}$ entering equation (4.29) for $n = m = 0$. The x-tics indicate the applied distribution of the nodes that are used to evaluate the full integral.

broad area in the middle of the relevant interval. With respect to this trend, the nodes that are used for the evaluation of the integral under study are supposed to obey a dense distribution near the integral boundaries that thins out towards the middle of the interval. To realize a distribution of this type, the distance between two considered nodes is set to increase exponentially when veering away from the boundaries, which is illustrated for 12 nodes by the x-tics in figure 4.2. Note that the discussed integral entering the spectral spin noise function $S(\omega)$ does not depend on the details of the underlying system. The only physical quantity that is crucial for the integral is the spectral width β. Therefore the result for a given grid of the frequency $\omega/\beta \in [0:2]$ and a large number N_0 of series elements can be calculated once and be stored on the hard memory of the machine. The obtained data can be applied for any numerical simulation of the Hamiltonian H and any desired number of series elements $N_c \leq N_0$, while the numerical effort for the calculation of the integral entering $S(\omega)$ has to be paid only once. As a consequence the main effort of the simulations adressing the spectral spin noise function lies in the calculation of the momenta $\mu_{n,m}$.

4.4.2 The Kernel polynomial method

As mentioned above, there is no factor entering $S(\omega)$ that ensures a strict convergence of equation (4.29) after summing up a finite number N_c of series elements. The occurence of Gibbs oscillations [112] is typical for problems of this type and to supress this unpleasant effect A. Weisse et al. [110] have discussed the kernel polynomial method (KPM). It will be briefly reviewed here, according to the review from reference

[103], to reclaim the so called Jackson Kernel [113, 114], which will be used for the suppression of Gibbs oscillations throughout this work. The basic idea of the KPM is to introduce prefactors g_n that are supposed to regulate the truncation error of infinite sums:

$$f(x) = b_0 + 2\sum_{n=1}^{\infty} b_n T_n(x) \tag{4.32}$$

$$\approx g_0 b_0 + 2\sum_{n=1}^{N_c} g_n b_n T_n(x) =: f_{\mathrm{KPM}}(x). \tag{4.33}$$

The key question of the KPM is obviously the determination of an adequate choice of the prefactors g_n. It is approached by introducing the Kernel

$$K_{N_c}(x,y) = g_0\phi_0(x)\phi_0(y) + 2\sum_{n=1}^{N_c} g_n\phi_n(x)\phi_n(y), \tag{4.34}$$

$$\phi_n(x) = \frac{T_n(x)}{\pi\sqrt{1-x^2}}, \tag{4.35}$$

which is linked to $f_{\mathrm{KPM}}(x)$ via the orthogonality relation

$$f_{\mathrm{KPM}}(x) = \left\langle K_{N_c}(x,y)|f(x)\right\rangle. \tag{4.36}$$

To classify an appropriate Kernel Weisse et al. presented three criteria: (i) the kernel is supposed to be positive definite $K_{N_c} > 0 \forall x,y \in [-1:1]$, (ii) it needs to fulfill the normalization relation $\int_{-1}^{1} \mathrm{d}x\, K_{N_c}(x,y) = \phi_0(y)$ and (iii) the second coefficient g_1 shall approach 1 for $N_c \to \infty$. To ensure that the first condition is fulfilled, the strictly positive function

$$p(\varphi) = \left|\sum_{\nu=0}^{N_c-1} a_\nu \mathrm{e}^{i\nu\varphi}\right|^2 = g_0 + 2\sum_{n=1}^{N_c-1} g_n \cos(n\varphi) \tag{4.37}$$

$$g_n = \sum_{\nu=0}^{N_c-1-n} a_\nu a_{\nu+n} \tag{4.38}$$

can be put forward, which is linked to the Chebyshev polynomials by setting $\phi = \arccos(x)$, according to their trigonometric definition (4.4). To exploit the third condition, the function

$$Q := \iint_{-1}^{1} \mathrm{d}x\mathrm{d}y\, (x-y)^2 K_{N_c}(x,y) \tag{4.39}$$

is introduced, which is a measure for the squared width of the peak of $K_{N_c}(x,y)$ occurring at $x = y$. By demanding the minimization and treating some elementary proper-

ties of Q, a system of equations is obtained that is used to determine the coefficients a_ν. One arrives at

$$a_\nu = \bar{a} \cdot \sin\left(\frac{\pi k(\nu+1)}{N_c+1}\right) \tag{4.40}$$

$$\Rightarrow \qquad g_n = \frac{(N_c - n + 1)\cos\frac{\pi n}{N_c+1} + \sin\frac{\pi n}{N_c+1}\cot\frac{\pi}{N_c+1}}{N_c+1}, \tag{4.41}$$

which are the coefficients g_n that set the Jackson kernel and will be applied to all calculations of $S(\omega)$ throughout this work. Note that the coefficients g_n are not obtained trivially [110] from the derived set of a_ν, but for simplicity the additional steps are not discussed in detail here.

4.4.3 Sum-rule

As argued above, the sum-rule (3.32) yields a valuable benchmark for the adequacy of a given numerical method. Obviously the question arises, wether the truncation of the infinite sum in equation (4.29) violates this sum-rule. Since $T_0(x) = 1$ holds, inserting the Chebyshev expansion of the spectral spin noise function into the Fourier transformation $S(t=0) = \frac{1}{2\pi}\int_{-\infty}^{\infty} \mathrm{d}\omega\, S(\omega)$ yields

$$S(t=0) = \frac{1}{2\pi}\sum_{n,m=0}^{\infty} h_{n,m}\mu_{n,m}\int_{-1}^{1}\mathrm{d}\tilde{\omega}_1\,\frac{T_n(\tilde{\omega}_1)T_0(\tilde{\omega}_1)}{\sqrt{1-\tilde{\omega}_1^2}}\int_{-1}^{1}\mathrm{d}\tilde{\omega}_2\,\frac{T_n(\tilde{\omega}_2)T_0(\tilde{\omega}_2)}{\sqrt{1-\tilde{\omega}_2^2}}$$
$$\times\int_{-\infty}^{\infty}\mathrm{d}\omega\, 2\pi\delta(\omega+\beta(\tilde{\omega}_1-\tilde{\omega}_2)) \tag{4.42}$$

$$= \sum_{n,m=0}^{\infty} h_{n,m}\mu_{n,m}\pi^2\delta_{n,0}\delta_{m,0} = \mu_{0,0} = \frac{1}{4}, \tag{4.43}$$

where the orthogonality relation of the Chebyshev polynomials has been exploited. Apparently, the spectral weight of $S(\omega)$ expanded via the CET is fully determined by the smallest order moment $\mu_{0,0}$ and the desired sum-rule is fullfilled independently of the cutoff N_c. This finding also implies that the Chebyshev polynomials of higher order only introduce a redistribution of the existing spectral weight, which is an important feature for the understanding of the spectral results obtained via the CET.

4.5 Benchmarking the Chebyshev polynomial expansion

To benchmark the CET, a simplified version of the Hamiltonian H is considered, for which a couple of exact analytical statements exist, that are useful to gain detailed insight into the convergence properties of the CET. Namely, the section at hand is

restricted to the treatment of spin-1/2 nuclei and the so called box model, which is defined by the Hamiltonian

$$H_{\text{box}} = A\vec{S} \cdot \sum_{k=1}^{N} \vec{I}_k. \tag{4.44}$$

The intrinsic time scale $T^* = (\sum_k A_k^2)^{-1/2}$ is introduced to define the dimensionless coupling constants $\tilde{A} = AT^* = 1/\sqrt{N}$. A. Khaetskii et al. [115] have put forward an analytic treatment of the CSM that is based on the conservation of the system's total spin $\mathcal{S}^z = S^z + \sum_k I_k^z$. Within their approach, a Laplace transformation of the Schrödinger equation for an arbitrary pure state with a well defined total spin $\mathcal{S}^z$ is performed. Also see the review presented in reference [103] for the details of this analytic solution. Although the exact analytic treatment of a full trace for a moderate bath size $N \sim O(10)$ is not possible in an adequate amount of time, the method provides the statement that the central spin's time evolution for an arbitrary initial condition is driven by a set of $N/2$ frequency components, which are given by

$$\Omega_{N/2-n} = \frac{\sqrt{N}}{2}\left(1 + \frac{1-2n}{N}\right), \tag{4.45}$$

where $n \in \{0, 1, ..., N/2-1\}$ holds. Thus, the spectral function $S(\omega)$ will always consist of $N/2+1$ δ-spikes (one occurring at $\omega = 0$), whose spectral weight is determined by the considered initial condition. For the real time dynamics $S(t)$ the analytical finding implies a periodic behavior, because for a finite spin bath a finite number of commensurable frequencies fully describes the time evolution. Since the recurrence time approaches infinity for an infinite number N of bath spins, it is expected to increase with the system size.

4.5.1 Benchmarks concerning $S(t)$

Figure 4.3 shows various calculations demonstrating the convergence properties of the CET applied to the real time dynamics $S(t)$ within the box model H_{box}. Note that all following statements concerning the discussed convergence properties also apply for any other model Hamiltonian, but due to its analytically accessible properties the box model is examplarily taken into account here. Panel (a) of figure 4.3 considers a spin bath of $N = 2$ nuclei. For this setup the spin noise function can easily be calculated exactly and it is given by

$$S(t) = \frac{1}{4}\left(\frac{5}{9} + \frac{4}{9}\cos\left(\frac{3t}{\sqrt{8}T^*}\right)\right). \tag{4.46}$$

According to the general analytic prediction (4.45), the spin noise function is described by a single frequency which is given by the spectral width $2\beta = 3/\sqrt{8}$. I.e. the recur-

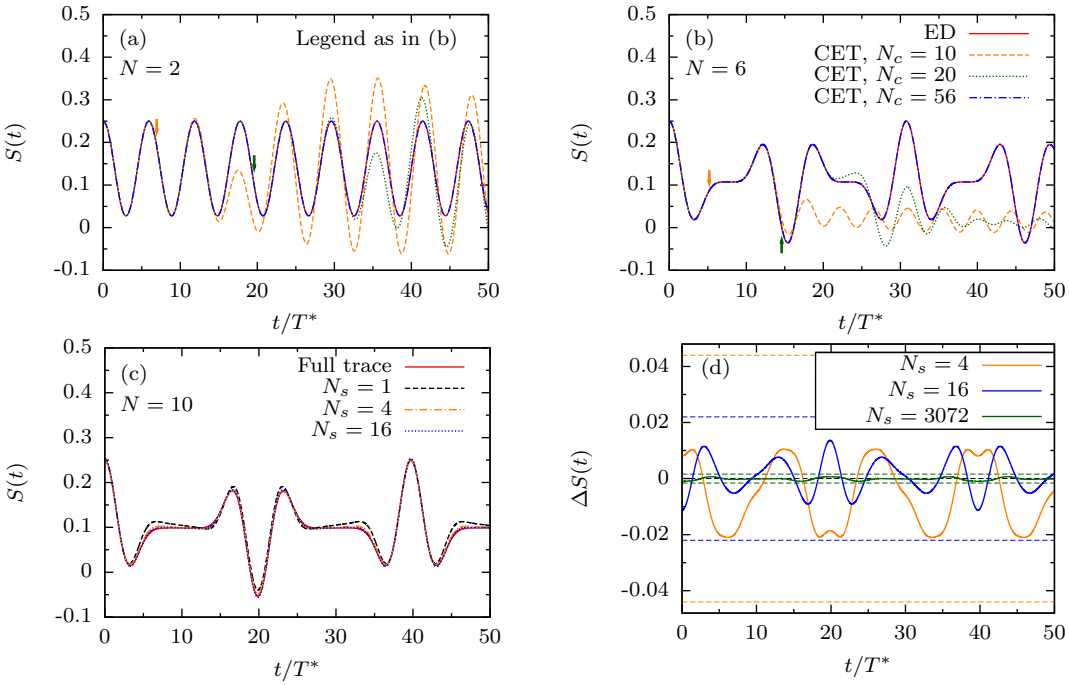

Figure 4.3: Panels (a)-(b) treat the time dependent CET's convergence for varying cutoffs N_c of the infinite sum occurring in equation (4.11). Both panels are based on the system Hamiltonian H_{box} considering N spin-1/2 nuclei. The legend of panel (b) also applies for panel (a). The arrows indicate the time when the prediction (4.15) exceeds $\epsilon = 10^{-3}$ for the order N_c of the equivalent color. Panels (c)-(d) focus on the error arising from the stochastic evaluation of the trace entering $S(t)$. The dashed lines in panel (d), which shows the relative error $\Delta S(t) = (S_{\text{ED}}(t) - S_{\text{CET}}(t))/S(0)$, indicate the estimated error for the data of the corresponding color. It is given by $1/(S(0)\sqrt{N_s D})$, where $D = 2048$ applies for all shown results. Panels (a) - (c) correspond to figure 2 from reference [97].

rence time of the periodic spin noise function $S(t)$ is given by $t_{\text{rec}}/T^* = 2\sqrt{8}\pi/3 \approx 6$. The colored arrows in panels (a)-(b) of figure 4.3 indicate where the anayltic estimate (4.15) exceeds the value $\epsilon = 10^{-3}$. For the investigated setup it yields $t_{\text{max}}/T^* = 6.95$, considering $N_c = 10$ Chebyshev polynomials and the comparison to the exact results shows a deviation of the order $O(10^{-5})$. Setting $\epsilon = 10^{-2}$ would suggest the largest reliable timescale $t_{\text{max}}/T^* = 8.75$ and an error of the order $O(10^{-4})$, which is, as will be discussed below, of the same order as the error arising from the stochastical evaluation of traces. Thus, the parameter ϵ will be set to 10^{-3} throughout this work. Turning to a larger bath of $N = 6$ nuclei, which is considered in panel (b) of figure 4.3, yields an increase of the spectral width and along with it of the largest contributing frequency to $2\beta = 7/\sqrt{24}$. As a consequence, taking $N_c = 10$ or 20 Chebyshev polynomials into account yields shorter reliable timescales than for $N = 2$. Accordingly, the obtained results from the CET develop significant deviations from the exact calculations on shorter timescales, which is most pronounced for $N_c = 20$. Setting $\epsilon = 10^{-3}$ suggests that $N_c = 56$ polynomials are adequate to guarantee reliable results for $t/T^* = 50$

and, according to our prediction, the numerical simulations performed via the CET reproduce the exact solution for $N = 2$ and 6 perfectly on the predicted timescale. As put forward in the introduction of the section at hand, the recurrence time for $N = 6$ bath spins is significantly larger than for $N = 2$, but as expected $S(t)$ is a strictly periodical function in time. Both of these observations are also stated for $N = 10$ bath spins.

Figure 4.3 (c)-(d) treats the error arising from the stochastical evaluation of the trace occurring in $S(t)$. In panel (c) its exact time evolution, obtained via exact diagonalisation (ED), for $N = 10$ is shown in comparison to CET results for various numbers N_s of randomly generated states $|r\rangle$. It turns out, that already the consideration of such a single quantum state is sufficient to reproduce the qualitative behavior of $S(t)$ and for $N_s = 16$ the accordance of the two approaches is already very good. Panel (d) quantifies this statement, by showing the relative deviation of the CET from the ED, which is defined as $\Delta S(t) = (S_{\mathrm{ED}}(t) - S_{\mathrm{CET}}(t))/S(0)$. The error estimate that has been derived by A. Weisse et al. [110] puts forward a relative error of the order $O(1/\sqrt{N_s D})$, which is indicated by the dashed lines in figure 4.3 (d) and it turns out that it overestimates the observed relative error significantly. Note that considering $N_s = 3072$ random states for $N = 10$ bath spins corresponds to the expected error of a simulation of $N = 20$ spin-1/2 nuclei taking $N_s = 3$ random states into account, which is a typical choice of parameters for the simulations that are presented thorughout this work. For such a setup the relative error is estimated to be smaller than 0.2 % and for the data shown in figure 4.3 (d) it is a factor of 2 smaller. Hence, the absolute error entering $S(t)$ is usually of the order $O(10^{-4})$, which is, as mentioned above, one order of magnitude larger than the error stemming from the CET applied to a single quantum state. Therefore the error stemming from the stochastical evaluation of traces is the main source of uncertainty that enters the simulations based on the CET. We stress that this error is not increasing with the maximum time that is simulated. This is an important statement, since it distinguishes the method at hand from most other approaches for the calculation of real time dynamics in complex quantum systems. Concerning the box model, this time-independence manifests itself in the observation that the occurring error of the simulations features the same periodicity as $S(t)$.

4.5.2 Benchmarks concerning $S(\omega)$

As argued above, there is, in contrast to the time dependent CET, no contribution to the spectral spin noise function $S(\omega)$ expanded in orders of Chebyshev polynomials, ensuring the convergence of the method in a straight forward fashion. Anyhow, it has been demonstrated that $S(t)$ is reproduced adequately up to $t_{\max} \leq 10^{-3/N_c} 2N_c/(\mathrm{e}\beta)$ (see equation (4.15)) by taking N_c polynomials into account. Inverting this statement

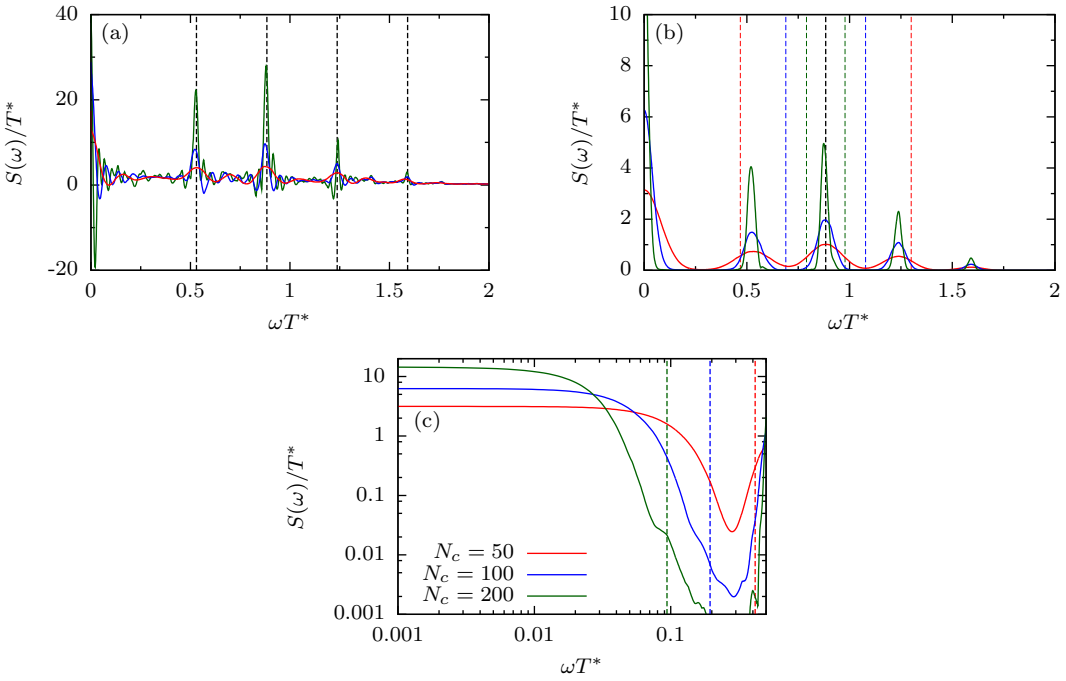

Figure 4.4: Numerical results adressing the convergence properties of the CET applied for the calculation of the spectral spin noise function $S(\omega)$. A system containing $N = 8$ spin-1/2 nuclei associated to the coupling constants $A_k = 1/\sqrt{N}$ has been considered and the legend of panel (c) applies for all shown data. For panel (a) the infinite sum occurring in equation (4.29) has been truncated without inserting the coefficients g_n. The black dashed lines indicate the positions of the frequencies $\Omega_{N/2-n}$. Panel (b) shows corresponding results, where the Jackson kernel has been added. The colored dashed lines correspond to the individual curves and indicate their reliable resolution, estimated by equation (4.47), for the δ-peak occurring at the frequency Ω_2. Panel (c) shows the same data as panel (b) on a double logarithmic scale, where the dashed lines specify the reliable resolution for the peak at zero frequency.

puts forward the estimate, that the CET applied to the spectral function $S(\omega)$ for a given number N_c of Chebyshev polynomials yields the reliable resolution

$$\omega_{\min} \geq \frac{10^{3/N_c}\pi e\beta}{N_c}. \tag{4.47}$$

This is, due to the lack of straight forward convergence properties, not necessarily a valid prediction and has to be checked numerically. Also the role of the Jackson kernel for the obtained convergence properties of the CET is unclear a priori. Figure 4.4 adresses these issues, considering a system of $N = 8$ homogeneously coupled ($A_k = 1/\sqrt{N}$) bath spins with $I = 1/2$. The $N/2 = 4$ frequencies $\Omega_{N/2-n}$, that drive the central spin dynamics for this setup, are specified by the black dashed lines in panel (a), which shows numerical results for $S(\omega)$ obtained via the CET without the introduction of convergence improving factors g_n. In contrast, figure 4.4 (b) ex-

hibits corresponding results involving the Jackson kernel (4.41). It turns out that both approaches feature maxima, where the δ-peaks of the exact spectral function are located. Also, the distribution of the total spectral weight among these individual peaks appears to be similar for both approaches. Appart from these similarities, the pronounced Gibbs-oscillations occurring in panel (a) are problematic for two reasons: (i) they feature unphysical contributions $S(\omega) < 0$ and (ii) their frequency and amplitude are increasing with the order N_c, stating that an increase of the finite order N_c does not fully solve the occurring problems. This puts forward that the introduction of convergence improving prefactors g_n is mandatory, to obtain a physically well defined spectral function $S(\omega)$ when considering a finite number of polynomials N_c.

The added dashed lines in figure 4.4 (b) and (c), mark the estimated (see equation (4.47)) reliable resolution of the peaks occurring at $\Omega_{N/2-2} = \Omega_2 = \frac{5\sqrt{2}}{8}$ (b) and $\omega T^* = 0$ (c) for the order N_c of the corresponding color. On a linear scale no violation of the analytic estimate for the reliable resolution is observed and as predicted, the numerics produce an overlap of the neighboring δ- peaks for $N_c = 50$, while they are well separated for the larger orders $N_c = 100, 200$. It also turns out, that the spectral weight of the well separated peaks is invariant for increasing N_c. Also note that the peaks calculated via the CET are not perfectly centered around the correct frequencies, but the correct spectral weight is distributed within a well defined range around it. The double logarithmic illustration of the numerical results, as presented in panel (c) of figure 4.4, reveals that a deviation of the order $S(\omega)/T^* \sim O(10^{-2})$ from the estimated reliable resolution (4.47) occurs, but due to the full amplitude of the spectral function this deviation is negligible. Therefore the introduced error estimate applied to the CET involving the Jackson kernel, is assumed to yield a valid bound for the reliably simulated interval of a given spectrum. Figure 4.4 (c) also reveals that the convergence of the CET towards an individual δ-peak is not of a strictly monotonic nature.

In section 4.4.1 an efficient method for the treatment of the integrals entering $S(\omega)$ has been introduced, that respects the problematic properties of the integral kernel. To verify that the introduced method treats these properties adequately, the demanded sum-rule (3.32) is checked by integrating the spectral functions calculated via the CET. It turns out that the occurring deviations from the sum-rule, are always of the same order as the error stemming from the stochastical evaluation of the trace entering $S(\omega)$, proving that the latter error is at least of the same order as all further uncertainties influencing $S(\omega)$.

Given that the sum-rule (3.32) is fullfilled within the introduced spectral CET, it is stressed that its convergence properties can be advantageous for the treatment of the discrete character of a finite quantum system. Since we address experiments that are applied on a large quantum system, whose spectrum is expected to be approximately continuous, it is sometimes a pleasent feature that the CET intrinsically adds a well defined broadening to the discrete frequency components of the finite system. I.e.

instead of a set of individual sharp peaks, a smooth curve can be obtained by choosing a rather small order N_c, which may account better for the experimental setup. Of course this broadening is only useful for the investigation of short time dynamics, because effects taking place on a long time scale are always associated to sharp peaks, that have to be resoluted adequately.

Chapter 5

Electron Spin Dynamics

The chapter at hand is dedicated to the study of the most prominent special case of the model Hamiltonian H, namely the isotropic central spin model (ICSM). It is given by the Hamiltonian

$$H_{\mathrm{ICSM}} = \omega_L \vec{S} \cdot \vec{n}_B + \vec{S} \cdot \sum_{k=1}^{N} A_k \vec{I}_k. \tag{5.1}$$

Since the ICSM accounts for the Fermi contact hyperfine interaction, which is the dominant interaction influencing a single electron confined in a semiconductor QD, it has been studied intensively in the past. In the following an overview of the results of numerous investigations concerning the central spin dynamics within the ICSM is presented and the virtues of the CET are exploited to gain new insights into certain aspects of the model, that are not fully understood until the present day. Hence, the main part of this chapter addresses the central spin dynamics in the absence of a magnetic field $\omega_L = 0$, which is the most challenging regime of the model, because any perturbative approach dividing the model into an easily treatable part accompanied by a small perturbation fails due to the lack of an energy hierarchy. Note that a Bethe Ansatz solution for the ICSM exists. It has been intensively studied in the past [36, 37, 33, 35], but since its treatment is quite challenging, there are still several open questions concerning the central spin dynamics within the ICSM. The discussion of the magnetic field free case is followed by the treatment of the central spin dynamics in (i) transversal ($\vec{n}_k = \vec{e}_x$) and (ii) longitudinal ($\vec{n}_k = \vec{e}_z$) magnetic fields. In large external fields the real time dynamics can be treated perturbatively [116, 117] and consequently the system dynamics are accessible for large bath sizes, while small external fields $\omega_L \lesssim A_s$ demand a non-perturbative treatment. Finally, the theoretical findings are compared to the results of recent experiments. It is stressed that the influence of quadrupolar interactions onto the electron and hole spin dynamics is postponed to chapter 8. Note that most of the discussions presented in the chapter at hand are based on the published results from references [97], [118] and [119].

5.1 Dynamics in the absence of a magnetic field

In section 3.3.2 a semi classical approach has been reviewed, that turns out to describe the short time behavior of $S(t)$ perfectly. This finding has been underlined impressively by recent DMRG investigations taking $N = 1000$ bath spins into account [39], where perfect agrement between the fully quantum mechanical and semi classical calculations was found. Hence, the semi classical result $S_{\mathrm{SCA}}(t)$ serves as a valuable benchmark for the CET concerning the obtained short time dynamics. The critical character of this benchmark is stressed by the fact that the semi classical approach (SCA) assumes an infinite spin bath, while the CET simulations are limites to $N \sim 20$ spin-1/2 nuclei. This forces the question wether the numerical simulations are able to put forward reliable statements for a system containing $O(10^5)$ bath spins at all. As sketched in section 3.1.5, we try to mimic an effectively larger bath by determining n random sets of N coupling constants and performing an individual simulation of $S(t)$ for each of these sets. Finally, the results of these individual calculations are averaged to obtain a single curve for $S(t)$, that represents a certain set of model parameters. The question wether this approach is adequate to circumvent possible occuring finite size limitations will be part of the presented studies below.

The SCA by Merkulov et al. has also been discussed concerning a prediction of the long time dynamics of the central spin. This and further estimates for $S(t)$ at large times will not be reviewed here in detail, but based on the presented numerical simulations their viability will be discussed in the corresponding section below. In this context also the influence of the system parameters r_0, d and m will by investigated in detail. The discussions will be concluded by the introduction of an analytic estimate concerning the long time behavior of $S(t)$, which has been proposed in the context of this work [119]. Its derivation will be briefly reviewed and its validity will be discussed in the final part of the section at hand.

5.1.1 Short time dynamics

As argued in section 3.3.2, the semi classical solution of the ICSM by Merkulov et al. does not contain any information about the distribution of the coupling constants A_k among the QD. Hence, the choice of the model parameters r_0, d and m, that have been introduced in section 3.1.5, is not supposed to have an impact onto the short time dynamics of $S(t)$. Figure 5.1 (c)-(d) addresses the question wether this statement is true concerning the cutoff r_0 and accordingly the remainder parameters are kept constant among the figure, choosing $d = 3$ and $m = 2$. To guarantee comparibility of the individual calculations, a set of 960 (for spin-1/2 nuclei, 480 for $I = 3/2$) coupling constants A_k has been generated for every given value of r_0 in advance. I.e. for each presented curve from figures 5.1 (a) and (b) exactly the same coupling constants have been taken into account and due to the varying bath size the number of individual

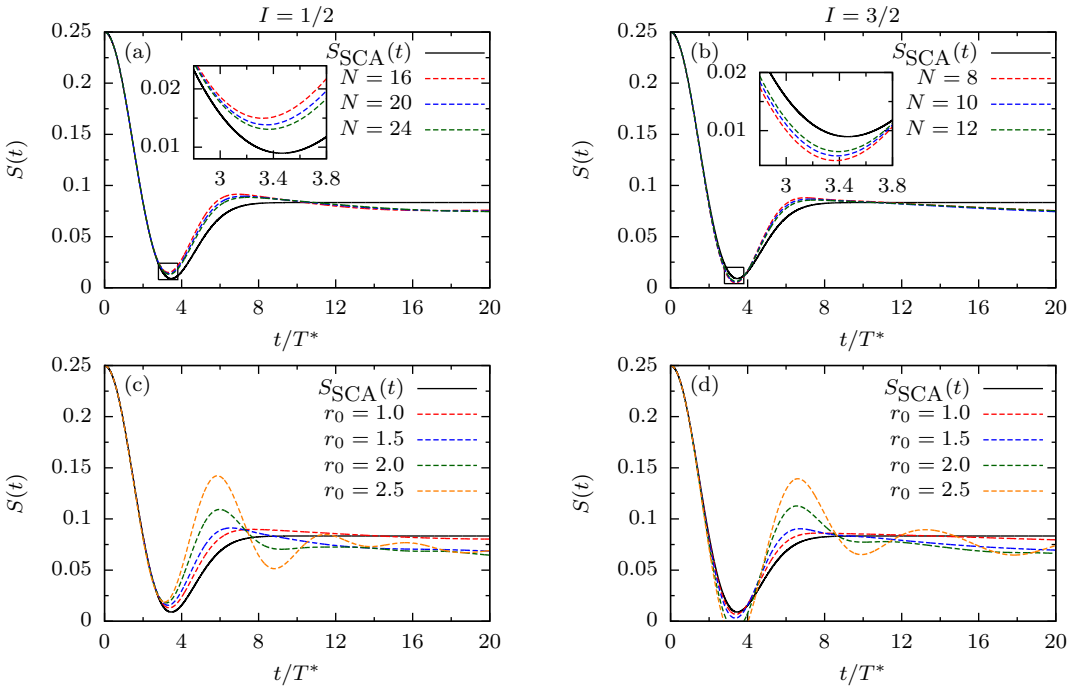

Figure 5.1: Short time dynamics of the spin noise function $S(t)$ in comparison to the semi classical prediction $S_{\mathrm{SCA}}(t)$, focusing on the role of the cutoff r_0. The left panels consider a bath of spin-1/2 nuclei, while for the right panels $I = 3/2$ holds. Panel (a)-(b) show numerical results for $r_0 = 1.2$ and a varying bath size N. The insets show a close up, which is specified by the black rectangles, of the minimum of $S(t)$. For all presented simulations the parameters $d = 3$, $m = 2$ apply and $n = 960/N$ ($I = 1/2$) or $n = 480/N$ ($I = 3/2$) randomly generated sets of coupling constants A_k have been averaged. The panels (c)-(d) treat a variation of the cutoff r_0 and are based on $N = 20$ (c) and $N = 10$ (d) bath spins, yielding an identical Hilbert space dimension $D \sim 2 \cdot 10^6$.

averaged simulations is given by $n = 960/N$ (or $n = 480/N$). E.g. all data presented in panels (c)-(d), which all consider $N = 20$ ($I = 1/2$) or $N = 10$ ($I = 3/2$) bath spins, are based on $n = 48$. In panels (a)-(b) numerical results for $S(t)$ based on various bath sizes N are shown along with the semi classical solution $S_{\mathrm{SCA}}(t)$. It turns out that the introduction of the intrinsic timescale T^* induces a collapse of all presented curves onto each other up to $t/T^* \approx 2.5$ independently of the bath size or the nuclear spin species. This finding states that T^* is indeed the crucial timescale for the short time dynamics of the spin noise function $S(t)$. After the initial collapse, the numerical results deviate from the analytic prediction: for both investigated nuclear species $S(t)$ reaches its minimum slightly earlier than predicted by $S_{\mathrm{SCA}}(t)$ and, accordingly, the ensuing increase to approximately $S(0)/3$ at $t/T^* \approx 8$ occurs faster for the numerical results. Looking into the scaling behavior of the simulations concerning the system size, it turns out that, as expected, the subsequent calculations for increasing N indicate a convergence towards the semi classical prediction up to $t/T^* \approx 8$. Also note that this convergence towards the local minimum of $S(t)$ at $t/T^* \approx 3.5$ occurs from above

for $I = 1/2$ and from below for $I = 3/2$, while the relative deviation from $S_{\mathrm{SCA}}(t)$ is comparable for both nuclear species at identical Hilbert space dimension D. In contrast, both spin-bath types feature a convergence from above at larger times. As mentioned above, D. Stanek et al. [39] were able to apply the DMRG to a spin bath of $N = 1000$ nuclei and found perfect agreement between the fully quantum mechanical calculations and $S_{\mathrm{SCA}}(t)$. The same result is expected to be found for a single simulation involving $N = 960$ bath spins associated to the coupling constants which entered figure 5.1 (a)-(b). Hence, we find that performing an average over $n = 60, 48, 40$ sets of $N = 16, 20, 24$ individual calculations, taking the same 960 coupling constants A_k into account, is not capable of reproducing the same short time dynamics as a single calculation involving all spins exactly. This finding is not surprising, because as suggested by the semi classical solution, the details of the realization of the coupling constants only influence the short time dynamics slightly. This implies that the obtained dynamics for each of the n sets of coupling constants are very similar and since a very large number of bath spins is required to reproduce $S_{\mathrm{SCA}}(t)$ in a single simulation, averaging over several smaller systems will always deviate from the analytic solution for $N \to \infty$. However, this observation states that the underestimation of the minimum of $S(t)$ for $I = 3/2$ as well as its overestimation for $I = 1/2$ is intrinsic to the two types of nuclei and not related to the random realization of the A_k.

Although the effect of statistical averaging over many individual configurations turned out to be of minor importance for the short time dynamics of $S(t)$, its central role for the present CET studies will be discussed further below. Note that the good agreement between $S_{\mathrm{SCA}}(t)$ and the numerical simulations is the central observation indicating that considering a rather small spin bath might be adequate to cover the generic dynamics of an experimental setup. Since all findings stated so far hold for arbitrary values of the parameters d and m and their variation yields very similar curves as presented for $d = 3$ and $m = 2$ in figure 5.1 (a)-(b), we renounce their further discussion in the context of the short time dynamics.

Though, the influence of the parameter r_0 for $t/T^* < 20$ is treated in figure 5.1 (c)-(d). As for $r_0 = 1.2$, all presented curves collapse onto each other for very short times, but the deviations of the numerical results from $S_{\mathrm{SCA}}(t)$ become more and more pronounced for increasing r_0. For the initial local minimum of the spin noise function this means, that the overestimate for $I = 1/2$ and the underestimate for $I = 3/2$ increase significantly. Afterwards, the simulations of $S(t)$ for $r_0 > 2$ feature significant oscillations that are not expected from the SCA. This behavior is easily understood by the distribution of coupling constants in any of the random configurations. Considering a fixed bath size N and a large cutoff r_0, the number of nuclei associated to a significant coupling constant $A_k/A_{\mathrm{max}} = O(1)$ becomes very small due to the rapidly increasing probability of finding a small coupling constant. Hence, the resulting oscillation is of a similar origin as the coherent motion shown in figure 4.3 (a), where only one or two

bath spins affect the short time behavior, and the damping is induced by the weakly coupling spins contributing to the dynamics on a longer timescale. I.e. the observed oscillations are not expected to occur in a real QD, because the distribution of coupling constants is always densely occupied and a significant number of bath spins contributing through a coupling constant $A_k/A_{\max}$ of every order is represented. In contrast the numerical limitations on the bath size only guarantee a dense distribution of the coupling constants for small cutoffs r_0 and therefore entail a limitation on the treatable cutoff, which is one of the main drawbacks of the CET. The comparison of the results for $I = 1/2$ and $I = 3/2$ yield a very similar behavior for the two bath types at times $t/T^* > 5$, while the deviations from $S_{\mathrm{SCA}}(t)$ are a lot more pronounced for $I = 3/2$ before. Due to the discussed limitations concerning the cutoff r_0, the latter observation is quite intuitive, since the number N of considered coupling constants is reduced by a factor of two for $I = 3/2$. On the other hand it is surprising that the subsequent time evolution is of a similar character for both scenarios. Besides, we find that the drop of $S(t)$ below the value $S(0)/3$ for $t/T^* > 9$ becomes more and more significant with increasing r_0 and it is not clear a priori, wether this is another finite size or a physical effect. The latter questions will be discussed further in the context of the long time dynamics below.

But for now, let us turn to the spectral spin noise function $S(\omega)$, focusing on the short time dynamics of the central spin which is treated in figure 5.2. All shown results are based on the parameters $d = 3$, $m = 2$ and $r_0 = 1.5$. The scope of panels (a)-(b), which are limited to $N = 20$ (a) or $N = 10$ (b) bath spins, is the effect of (i) averaging spectra obtained for different underlying sets of coupling constants and (ii) varying the number N_c of considered Chebyshev polynomials. For the calculation of the real time dynamics of $S(t)$ up to $t/T^* = 20$, as presented in figure 5.1, $N_c = 35$ Chebyshev polynomials are sufficient to obtain an adequate accuracy of the numerics. I.e. setting $N_c = 400$ clearly yields a higher spectral resolution than mandatory. As a consequence the obtained results for a single setup of randomly generated coupling constants (see panels (a)-(b) of figure 5.2) considering $N_c = 400$ clearly reveal the discrete character of the spectrum, which consists of several individual broadened peaks. By applying an average over $n = 50$ different sets of random couplings, the resulting spectral function $S(\omega)$ is smoothened significantly, but the discrete features are still visible, which is an unpleasant finite size feature. As indicated in section 4.5.2, this finite size effect can be eliminated by decreasing the order N_c of the CET. Correspondingly to the mandatory number $N_c = 35$ of Chebyshev polynomials for the real time calculations, spectral results for this order are added in panels (a) and (b) of figure 5.2, which yield a perfectly smooth spectral function $S(\omega)$, as it is expected to be found for $N_c \sim O(10^5)$. Note that the obtained results for $N_c = 400$ and $n = 50$ approximately reproduce the findings for $N_c = 35$ and $n = 50$ at large frequencies $\omega T^* \sim O(1)$ on average. In contrast, pronounced mismatches are found for small frequencies, where the resolution of the

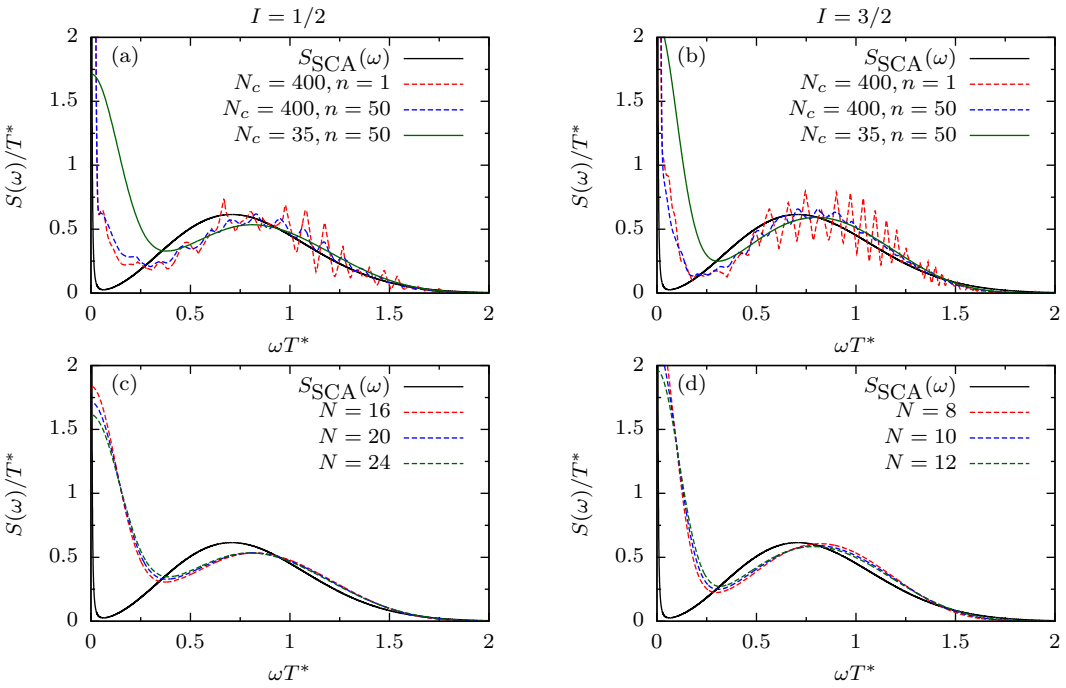

Figure 5.2: Illustration of the spectral spin noise function $S(\omega)$ for electrons, focusing on the short time dynamics. The left part of the figure addresses spin-1/2 and the right part spin-3/2 nuclei. All presented calculations are based on $d = 3$, $m = 2$ and $r_0 = 1.5$. Panels (a)-(b) address the impact of statistical averaging over various random realizations of the coupling constants A_k in conjunction with the considered number of Chebyshev polynomials N_c. Each individual underlying system involves $N = 20$ (a) or $N = 10$ (b) bath spins. Panels (c)-(d) treat the scaling behavior of $S(\omega)$ with the bath size N, where $N_c = 35$ Chebyshev polynomials have been considered and and average over $n = 50$ individual sets of coupling constants has been performed.

method for $N_c = 35$ is too rough to yield an adequate estimate for the spectral function. Strictly speaking, all spectral weight below $\omega T^* \approx 0.3$ is simply transferred into a single peak, whose detailed structure only depends on the method's convergence behavior instead of the physical details. The discussion of the spectral features occuring at $\omega T^* \to 0$ is postponed to the following section 5.1.2.

Panels (c)-(d) of figure 5.2 treat the scaling behavior of $S(\omega)$ with the bath size N, where all calculations are based on $r_0 = 1.5$, $N_c = 35$ and $n = 50$. The black reference line is given by the Fourier transformation $S_{\mathrm{SCA}}(\omega)$ of the semi classical solution. The observed behavior for the time resolved calculations is reflected in the spectral results: for both bath spin types $I = 3/2$ and $I = 1/2$ two distinct peaks occur. One is centered at $\omega = 0$ and refers to the long time behavior of the central spin, which is not resoluted reliably in the presented data. The second peak, whose maximum is arising at $\omega T^* \approx 0.8$, corresponds to the observed dip (see figure 5.1 for the time resolved calculations) on small timescales $t/T^* < 8$. For the semi classical solution, the latter peak contains $2/3$ of the full spectral weight, while the rest enters the δ-spike reflecting its finite

value $S_{\mathrm{SCA}}(t \to \infty) = S(0)/3$ at infinite times. The peaks referring to the short time behavior of the central spin are shifted to slightly larger frequencies, corresponding to smaller times, for the CET simulations, according to the time resolved case, and the general qualitative agreement between the CET and the semi classical approach is, once again, satisfactory. Also the indicated convergence towards the analytically predicted curve occurs accordingly to $S(t)$. Although the resolution of the presented calculations is too rough for a detailed analysis of the spectrum at small frequencies, it is striking that its maximum $S(\omega = 0)$ is decreasing for increasing N. There are two factors responsible for this behavior: on the one hand, all shown calculations are based on $N_c = 35$ Chebyshev polynomials, while the spectral width β is approximately 11 % larger for $N = 24$ or $N = 12$ compared to $N = 16$ or $N = 8$ bath spins, implying a worse resolution and thus a larger broadening of the zero frequency peak. On the other hand, the spectral weight of the simulated short time peak is indeed smaller than $2/3$ of the total weight and it is approaching this value slowly with the increasing system size N.

5.1.2 Long time dynamics

As demonstrated in the previous section, the semi classical analytical solution $S_{\mathrm{SCA}}(t)$ by Merkulov et al. [27] is not sensitive to the detailed realization of the coupling constants A_k, but is believed to describe the short time dynamics of a system containing a large number of bath spins correctly. Since the assumption of a frozen nuclear spin bath does obviously not hold for arbitrary timescales, the authors of reference [27] have also discussed the long time limit of their SCA. Within this picture, the central spin decays to the value $S(0)/3$ due to its precession in the frozen nuclear field and subsequently each nuclear spin precesses slowly around the direction defined by the central spin. The frequency of this precession is given by its associated coupling constant A_k for every individual nucleus. As a consequence a variation of the mean nuclear field occurs at large times, which acts back on the central spin. After inclusion of the explicit time dependence of the classically treated Overhauser field $\vec{B}_{\mathrm{eff}}(t) = B_{\mathrm{eff}}\vec{n}(t)$, the time evolution of the central spin $\vec{s}(t)$ (see section 3.3.2 and reference [97]) can be written as

$$\langle \vec{s}(t) \rangle = \langle \vec{n}(t) \cdot [\vec{n}(t) \cdot \vec{s}(t)] \rangle \,. \tag{5.2}$$

The quantity $[\vec{B}_{\mathrm{eff}}(t) \cdot \vec{s}(t)]$ accounts for the total energy of the ICSM and it is a conserved quantity. Therefore we can write $[\vec{B}_{\mathrm{eff}}(t) \cdot \vec{s}(t)] = [\vec{B}_{\mathrm{eff}}(0) \cdot \vec{s}(0)]$ and since the nuclear spin-spin correlation function is isotropic, we arrive at

$$\langle \vec{s}(t) \rangle = \frac{\vec{s}(0)}{3} \langle \vec{n}(t) \cdot \vec{n}(0) \rangle \,. \tag{5.3}$$

For the long time limit this quantity approaches a stationary value $\langle \vec{n}(t \to \infty) \cdot \vec{n}(0) \rangle =: \gamma(u)$, which is, as derived in reference [27], only dependent on the ratio $u = \langle A^2 \rangle / \langle A \rangle^2$. Namely, it is given by

$$\gamma(u) = \frac{2}{\pi} (u-1)^3 \iint_0^\infty \mathrm{d}y \, \mathrm{d}z \, \frac{(2y\cosh - \sinh(2y))^2}{yz\sinh(2y)} \exp\left[-\left(1 + (u-1)^2\right) z^2 - \frac{y^2}{z^2} \right], \tag{5.4}$$

which is a monotonically decreasing function in the interval $u \in [1 : \infty)$, with the boundary values $\gamma(1) = 1$ and $\gamma(u \to \infty) = 0$. In contrast to the short time behavior obtained from the SCA, the distribution of the coupling constants A_k enters the prediction for the long time limit through the ratio u, putting forward that u is the crucial quantity characterising the nuclear bath. Also note that the numerical evaluation of equation 5.4 is unstable for $(u-1) \to 0^+$.

Previous numerical studies concerning the ICSM, which also took the full quantum correlations of the system into account, were based on simplified assumptions for the coupling constants A_k. E.g. a statistical evaluation of the exact Bethe Ansatz equations [36] focused on the fixed set $A_k = A/N \exp[-(k-1)/(N-1)]$, where all coupling constants are of the same order of magnitude ($A_{\max}/A_{\min} = \mathrm{e}$) and $u \approx 1.082$ applies. In accordance to the discussed semi classical considerations, this study found no significant deviation from $S_{\mathrm{SCA}}(t)$ on large time scales. In the following, the coupling constants determined by equation (3.26) are investigated. In this specific scenario, the ratio between the smallest and largest coupling constant only depends on the cutoff r_0 and the form of the electron wave function, which is characterised by the parameter m: $A_{\max}/A_{\min} = \mathrm{e}^{r_0^m}$. In contrast, the ratio u is also influenced by the dimension d and therefore by all model parameters entering the hyperfine coupling constants. Thus, a variation of m and d is expected to have an impact onto the long time behavior of $S(t)$, which is one aspect that is discussed in detail on the basis of numerical simulations below.

Beside the SCA, L. Balents et al. [30] have put forward a rather intuitive argument to estimate the long time behavior of the central spin within the ICSM: for very large times the initially present total polarization within the entire system, which is given by $S(0)$, is assumed to be equally distributed over all spins within the system. Since the only energy scale applying for the k-th nucleus is given by the coupling constant A_k, the time it takes for an individual nucleus to contribute significantly to the central spin dynamics can be estimated by $t > 1/A_k$. By inserting equation (3.26) into this estimate, the radius $R(t)$ containing all nuclei contributing to $S(t)$ at a given time t is given by

$$R(t) < L_0 [\ln(A_{\max} t)]^{\frac{1}{m}} = L_0 \ln^{\frac{1}{m}}(A_{\max} t). \tag{5.5}$$

Since the short time behavior of $S(t)$ is solely governed by a number $N(R_s)$ of spins, which are found in the radius $R_s = R(T^*)$, the long time decay is expected to be of the form

$$S(t) \propto \frac{N(R_s)}{N(R(t))} \propto \ln^{-\frac{d}{m}}(A_{\max} t), \tag{5.6}$$

assuming an equal redistribution of the intitially present polarization. For an infinite system this finding puts forward a full decay of the spin noise function. But as argued above, a finite cutoff $r_0 = R/L_0$ is mandatory for the simulation of any finite system and accordingly a finite value $S_\infty := S(t \to \infty)$ will be found in any numerical simulation presented here. Still, equation (5.6) puts forward an estimate for the long time behavior of the spin noise function, which will be considered in the following discussions concerning this regime of $S(t)$.

Influence of the cutoff r_0 onto the long time dynamics

To study the qualitative impact of a variation of the cutoff r_0 onto the long time behavior of the central spin, let us, once again, focus on the fixed parameters $m = 2$ and $d = 3$ which account for a 3 dimensional QD with a Gaussian envelope wave function. Figure 5.3 shows time resolved and spectral results for the spin noise function concerning the central spin's long time behavior. Panels (a)-(b) address the according real time dynamics, where a logarithmic scale has been chosen for the t-axis, to emphasize the slowly varying behavior of $S(t)$ at large time scales. A scan of several values of the cutoff r_0 is presented, based on $n = 50$ randomly generated sets of $N = 18$ ($I = 1/2$) or $N = 9$ ($I = 3/2$) coupling constants. The effect of averaging results for several randomly determined realizations of the spin bath onto the long time dynamics will not be addressed in a separate figure here, but since the choice of the couplings is, as suggested by the results presented in figure 5.3, crucial for the long time evolution of $S(t)$, the impact of averaging multiple setups is quite intuitive: since the consideration of $N \sim O(20)$ coupling constants is far from a number of statistical significance, many more individual coupling constants have to be taken into account to obtain a *typical* spin bath realization with respect to the underlying model parameters. I.e. the obtained curves for single sets of $N = 18$ coupling constants can, due to statistical fluctuations, deviate significantly from the averaged result, which is assumed to represent the *typical* dynamics for the entering parameters. Independent of the cutoff r_0 and the nuclear spin I, all obtained results from figure 5.3 (a)-(b) feature two central aspects after experiencing the previously discussed short time evolution: (i) $S(t)$ saturates at a finite value $S_\infty := S(t \to \infty)$ after (ii) passing through a single pronounced minimum. The observed trends for increasing r_0 are also identical for $I = 1/2$ and $I = 3/2$. Namely, the saturation value S_∞ is decreasing and the relaxation time into this steady state value of $S(t)$ is increasing for larger cutoffs. The latter observation can easily be

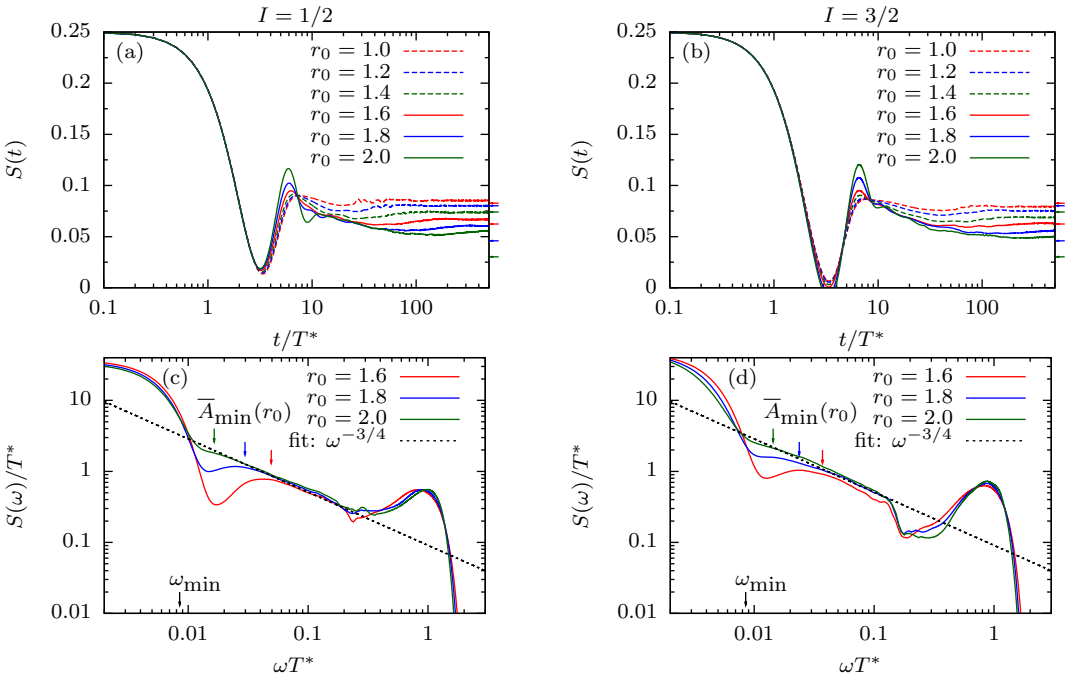

Figure 5.3: Numerical results for the electron long time dynamics in a $d = 3$ dimensional QD based on a Gaussian ($m = 2$) envelope wave function. All simulations are based on $N = 18$ (left) or $N = 9$ (right) bath spins. Panels (a)-(b) illustrate the spin noise function $S(t)$ for various cutoffs r_0, where the t-axis is scaled logarithmically. The shown results are based on $n = 50$ individual sets of coupling constants. The colored arrows indicate the estimated value $S_\infty := S(t \to \infty)$ from the SCA, which is only governed by $u = \langle A^2 \rangle / \langle A \rangle^2$. The spectral spin noise function $S(\omega)$ is treated in panels (c)-(d) on a double logarithmic scale. For all presented results $n = 200$ setups have been averaged and $N_c = 1000$ Chebyshev polynomials have been considered, yielding the indicated smallest accessible frequency ω_{min}. The black dashed line shows a power law fit $\propto \omega^{-3/4}$. The colored arrows indicate the mean value $\overline{A}_{\text{min}}(r_0)$ of the smallest coupling constant entering the corresponding simulation. Panels (a) and (c) are based on figures 4 (a) and 6 of reference [97].

traced back to the decreasing value of the smallest coupling constant that is taken into account: according to the assumption of Balents et al. [30], the inverse coupling $1/A_k$ sets the timescale at which the k-th nucleus contributes significantly to the central spin dynamics. I.e. the relaxation time of $S(t)$ is supposed to be increasing when the ratio $A_{\text{min}}/A_{\text{max}}$ is decreasing. On the other hand, the observed decrease of S_∞ is in qualitative agreement with the semi classical analysis of the long time dynamics by Merkulov et al. [27], because the ratio $u = \langle A^2 \rangle / \langle A \rangle^2$ is significantly increasing with the cutoff r_0. To check wether the semi classical result (see equations (5.3)-(5.4)) for the steady state value S_∞ also holds quantitatively, its estimate for the corresponding numerical results is indicated by the colored arrows in panels (a) and (b) of figure 5.3. Apparently the analytic estimate deviates significantly from the performed simulations. This observation is most pronounced for large values of r_0, where the semi classical pre-

diction clearly underestimates the fully quantum mechanical calculations. For small cutoffs r_0 different trends are observed depending on the nuclear species: for $I = 1/2$ the steady state value for $r_0 \in [1.0 : 1.4]$ is slightly underestimated, but approximate agreement between the two claims is found, while S_∞ is overestimated for $I = 3/2$ and $r_0 \in [1.0 : 1.4]$. Clearly there are two possible origins for the significant deviations: (i) the importance of quantum correlations for the long time behavior of $S(t)$, which are not covered by the SCA, or (ii) the inadequacy of the numerical simulations due to finite size limitations. This aspect is investigated further in figure 5.4, which will be discussed in detail below.

Figure 5.3 (c)-(d) treats the spectral spin noise function $S(\omega)$, corresponding to the time resolved results from panels (a)-(b). For all presented results $n = 200$ sets of coupling constants and $N_c = 1000$ Chebyshev polynomials have been considered. This CET order yields the smallest reliably resoluted frequency ω_{min} which is indicated on the ω-axis. As expected from the time resolved calculations, the spectral weight below ω_{min}, which represents a broadened $\delta(\omega)$ whose spectral weight corresponds to the observed finite value S_∞, is decreasing for increasing r_0. The peak occuring at $\omega T^* \approx 1$ corresponds to the initial precession of the electron spin in the frozen Overhauser field and its increasing deviation from $S_{\text{SCA}}(\omega)$ for large cutoffs has been discussed in detail in the previous section. Hence, the most interesting feature of figure 5.3 (c)-(d) occurs on the crossover scale separating the high energy energy peak from the $\delta(\omega)$ spike. The spectral function in this intermediate regime corresponds to the decay of $S(t)$ from $S(0)/3$ into S_∞. As indicated by the dashed black lines, the observed shoulder can be nicely approximated by a $\omega^{-3/4}$ fit. The regime where this fit is viable is increasing significantly with the cutoff r_0 and, in accordance to the observations from the time resolved calculations, it is shifted to slightly smaller frequencies when turning from $I = 1/2$ to $I = 3/2$. In the real time domain the observed power law suggests an equivalent decay $\propto t^{-1/4}$, which agrees nicely with the analytic claim $S(t) \propto \ln^{-3/2} t$ by Balents et al. in the intermediate regime $t/T^* \in [100, 1000]$. To establish a clear deviation form the latter estimate, a strict power law fit over more than one decade would be necessary. This is not possible due to the finite size limitations of the applied simulations. Namely, the restriction concerning the cutoff r_0 directly sets the smallest considered coupling constant A_{min} for a given simulation and as a consequence also the smallest possible energy exchange due to an individual spin flip. The colored arrows in panels (c)-(d) of figure 5.3 indicate the mean smallest coupling constant $\overline{A}_{\text{min}}$ for the underlying cutoffs r_0 and system sizes N. Apparently the shoulder $\propto \omega^{-3/4}$ begins to bend down at the frequency indicated by the smallest coupling constant, proving that it is indeed the decisive quantity for the central spin's relaxation time into the steady state value S_∞. Note that since there are obviously setups where smaller coupling constants than the mean value $\overline{A}_{\text{min}}$ are involved, the observed shoulders do

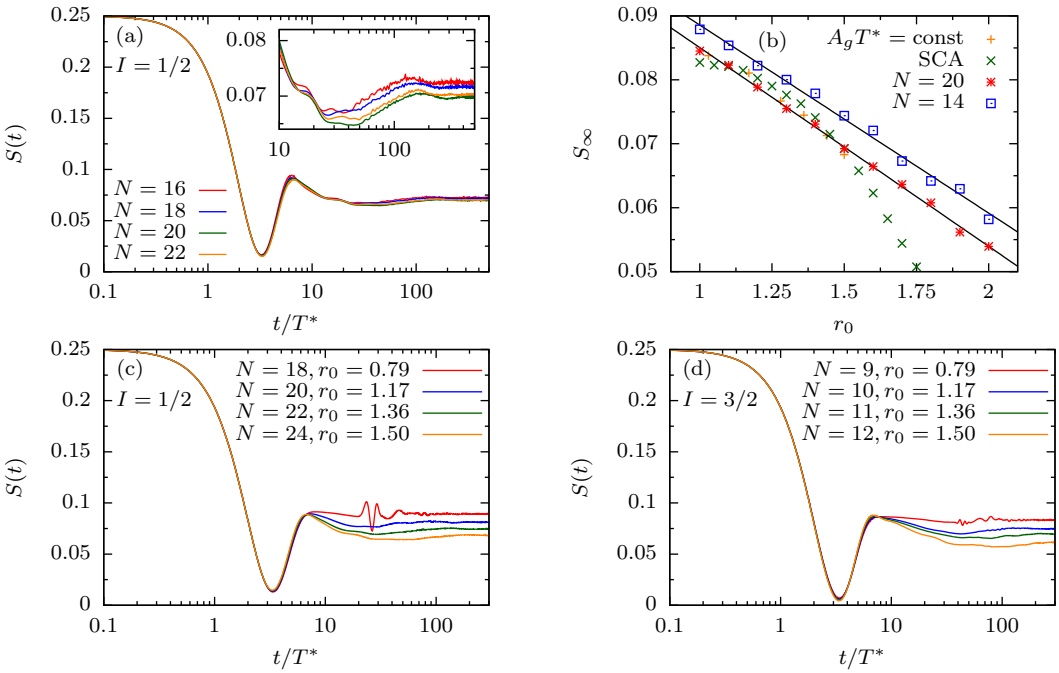

Figure 5.4: Influence of the considered spin bath size N on the long time dynamics of $S(t)$. For all presented simulations $n = 50$ individual setups have been considered for $m = 2$ and $d = 3$. Panel (a) shows a scan of the system size for a constant cutoff r_0, where the inset shows a close up of the long time dynamics $t/T^* > 10$. Panel (b) compares the SCA prediction for S_∞ based on the ratio u to a numerical r_0 scan for two different system sizes. On top of that, results obtained from panel (c) have been added. Panel (b) corresponds to figure 4 (b) of reference [97]. Panels (c)-(d) show time resolved calculations for various sets of the parameters N and r_0, where the quantity $A_g T^*$ is kept constant among the two panels. Panel (d) is the only one that is based on $I = 3/2$ instead of $I = 1/2$.

not collapse exactly at $\overline{A}_{\text{min}}$ and on top of that the finite resolution of the CET broadens the shoulder further, but apart from these deviations the stated finding is valid.

While figure 5.3 focused on the variation of the cutoff r_0 for a constant Hilbert space size $D = 2^{19}$, figure 5.4 addresses the influence of varying the system size N. This is an important benchmark for the CET's adequacy concerning its predictive power for the physical properties of large spin baths $O(10^5)$. Panel (a) shows a scan of the bath size N for a constant cutoff r_0. On the full scale $S(t) \in [0 : 0.25]$ the presented curves are very close to each other, but looking into a close up, which is shown in the inset of the panel, of the long time evolution reveals minor differences. From the semi classical estimation of S_∞ we draw the expectation that the ratio $u = \langle A^2 \rangle / \langle A \rangle^2$ is crucial for the long time dynamics. For the thermodynamic limit it is fully determined by the cutoff r_0, but since figure 5.4 (a) considers finite systems $N \in [16 : 22]$ the ratio u is varying by approximately 0.5 % among the figure, while it is 1.5 % larger for $N \to \infty$ than for $N = 16$. Based on these variations of u equation (5.4) predicts a change of the steady state value S_∞ of about 2 % when turning from $N = 16$ to $N \to \infty$. In contrast, the estimated S_∞ from the simulations already changes by approximately 4 % between

$N = 16$ and $N = 20$. Anyhow the finding for $N = 22$ indicates that the evolution of the steady state value is not necessarily monotonic with increasing system size. For this reason the SCA's prediction is not in strict disagreement with the numerical findings. For a further comparison of the two claims, figure 5.4 (b) shows cutoff scans for the saturation value S_∞, which has been determined by averaging the spin noise function $S(t)$ for $t/T^* \in [450 : 500]$, at two different system sizes along with the semi classical prediction for the thermal equilibrium case. The black lines indicate that $S_\infty(r_0)$ can be nicely fitted by a linear function, suggesting that it vanishes for large cutoffs r_0. The linear regression for $N = 20$ puts forward that this is the case for $r_0 \approx 3.7$, which would imply the ratio $A_{\max}/A_{\min} \approx 10^6$. But since the obtained r_0 varies significantly considering different system sizes, it can not be determined reliably from the CET. On top of that, the analytic estimate by the SCA yields a non-linear envelope of S_∞. This qualitative deviation might originate from the fact that an increase of r_0 at a fixed system size N also reduces the largest coupling constant taken into account and with it the energy scale A_g. The results for $S_\infty(r_0)$ obtained from the time dependent calculations, which are presented in figure 5.4 (c), are also added to panel (b). For these simulations the ratio r_0 and system size N have been determined such, that all shown results are based on a constant product $A_g T^*$. It turns out that the resulting claim for $S_\infty(r_0)$ is indeed a lot closer to the analytic estimate and even the qualitative form agrees quite nicely. I.e. the findings from the CET agree with the SCA as far as the finite size limitations allow reliable statements concerning larger systems. This finding puts forward that the ratio u may indeed be the crucial quantity for the steady state value S_∞. Note that the short time evolution of the calculations from panels (c)-(d) of figure 5.4 is invariant due to the constant energy scale A_g among the different curves. This was not the case for the results presented in figure 5.3 (a)-(b), where significant deviations occured for increasing r_0. Also note that the oscillation observed at $t/T^* \approx 30$ for $r_0 = 0.79$ originates from the small spread of considered coupling constants. In the extrem case of the box model ($A_k = A$) this feature becomes a full reoccurence of the initial polarization.

Influence of the electron wave function and the QD shape onto $S(t)$

Within the investigated modeling of the hyperfine interaction in a semiconductor QD, the electron wave function is assumed to have a Gaussian ($m = 2$) or an exponential shape ($m = 1$) and the shape of the QDs is assumed to be spherical in either two or three dimensions d. The analytic claim (5.6) by Balents et al. [30] suggests that the long time behavior of $S(t)$ is affected by the variation of either of the parameters d and m. I.e. in contrast to the short time evolution, $S(t/T^* > 10)$ depends on the detailed shape and therefore also on the growth conditions of the QD under study. Numerical results concerning the influence of the model parameters m and d onto the long time dynamics are presented in figure 5.5. Panels (a)-(b) address the real time dynamics of the spin

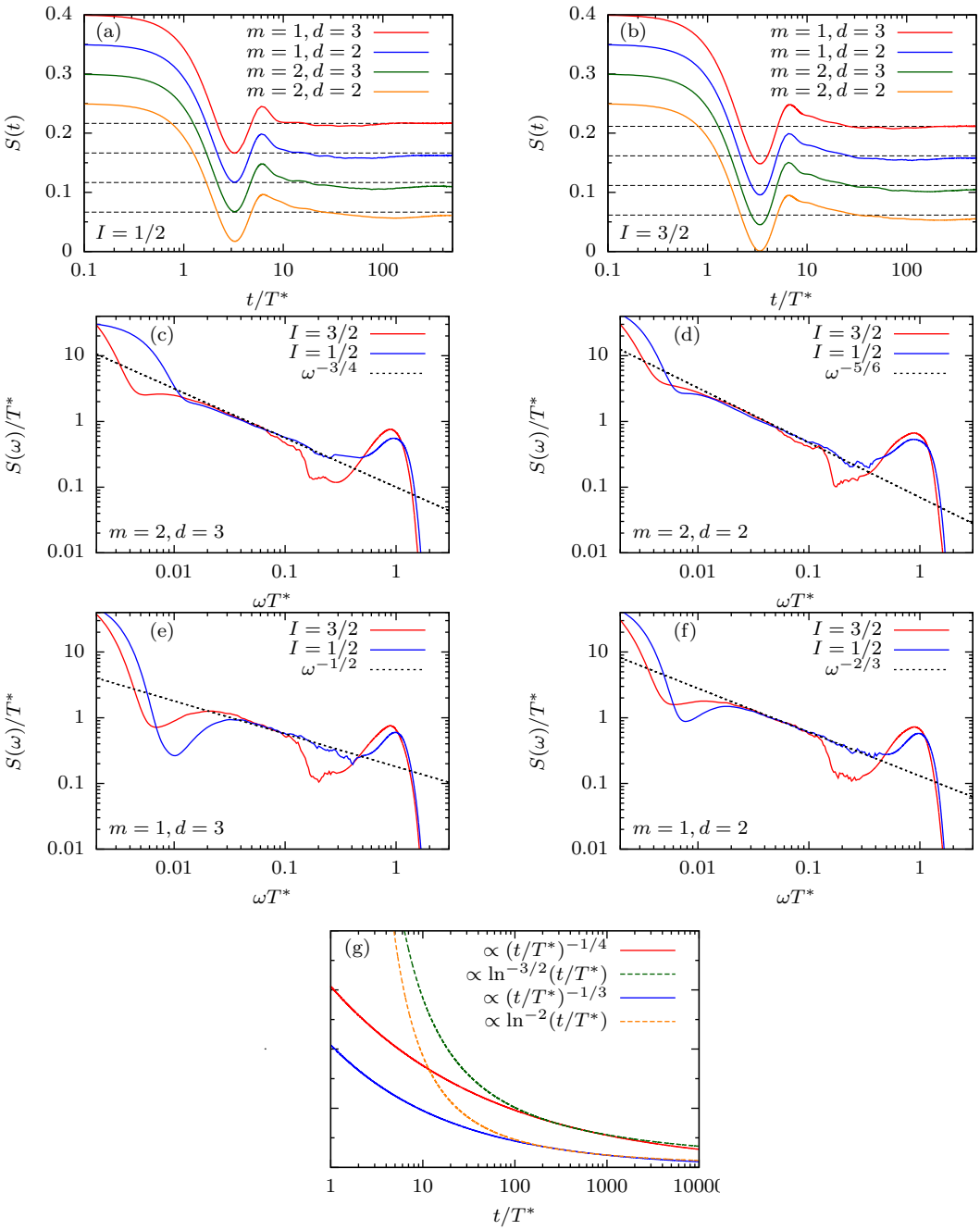

Figure 5.5: Numerical results illustrating the influence of the QD model parameters m and d onto the central spin dynamics. Panels (a)-(b) treat $S(t)$ for all considered variations of m and d, based on $N = 20$ spin-1/2 (a) or $N = 10$ spin-3/2 (b) nuclei. The cutoff has been chosen such that the ratio $A_{\text{max}}/A_{\text{min}} = \mathrm{e}^{-81/25}$ holds and all curves are based on $n = 50$ individual bath configurations. The black dashed lines are a guide to the eye. They indicate the offset that has been added to distinguish the individual curves. Panels (c)-(f) show direct comparisons of the spectral function $S(\omega)$ for the two different nuclear species. The results for $I = 1/2$ $(3/2)$ are based on $N = 18$ (9) bath spins and $n = 200$. For all calculations the CET order has been pushed to $N_c = 2000$ and the cutoff r_0 guarantees the ratio $A_{\text{max}}/A_{\text{min}} = \mathrm{e}^{-4}$. The dashed lines are power law fits with respect to the analytic prediction given in equation (5.6), which can be approximated by a power law in the intermediate time regime as demonstrated in panel (g).

noise function for the different nuclear species $I = 1/2$ and $I = 3/2$. The black dashed lines are a guide to the eye, indicating the obtained value S_∞ for $m = 1$ and $d = 3$ with respect to the added offset. While the short time dynamics is, as expected, invariant for all obtained results, two central observations on large timescales occur independently of the underlying nuclear species: First, the steady state value S_∞ is varying slightly. As discussed above, the ratio u is the prime candidate to be crucial for this observation and indeed the trends from the simulations qualitatively match the expectation from this quantity. Namely, for $N = 20$ and constant $m = 2$ it takes the almost identical values $u = 1.372$ ($d = 2$) and $u = 1.374$ ($d = 3$), which is in agreement with the observed invariance of S_∞ for the corresponding curves. For $m = 1$ a larger variation is found when turning from $d = 2$ to $d = 3$, which is again in good agreement to the predicted trend from the ratio u since $u = 1.140$ ($d = 2$) and $u = 1.100$ ($d = 3$) holds. Second, the relaxation time into S_∞ is varying significantly among the presented curves. As argued above, the smallest considered coupling constant A_{min} appears to set the largest timescale on which $S(t)$ experiences changes in its dynamics. This finding is stated by the results from figure 5.5 (a)-(b): from top to bottom the expectation value $\overline{A}_{\text{min}} T^*$ is decreasing monotonically, while the relaxation time is increasing within a comparable order of magnitude. Due to the different character of the relaxation process for the individual sets of d and m, a consistent definition of the relaxation time is problematic in this context and therefore the following, more detailed analysis of the spin noise function's decay towards S_∞ is based on $S(\omega)$ instead of $S(t)$.

Panels (c)-(f) of figure 5.5 treat the spectral function $S(\omega)$. With respect to the analytic prediction (5.6), each panel compares results for the different nuclear species at identical parameters m and d. To guarantee comparibility of the individual plots, the ratio $A_{\text{max}}/A_{\text{min}} = \mathrm{e}^{-4}$ has been kept constant. The added dashed lines correspond to power law fits, which reproduce the predicted $\ln^{-d/m}(t)$ behavior nicely in the intermediate regime $100 < t/T^* < 1000$, i.e. the exponent of the added function $\omega^{-\nu}$ depends on the model parameters d and m. The fitting procedure for the determination of the exponent ν for each individual set of d and m is illustrated in panel (g) of figure 5.5: the exponent of the shown power law curves in time $\propto t^{\nu-1}$, whose Fourier transformation yields $\omega^{-\nu}$, is determined in a trial and error procedure by comparison to $\ln^{-d/m}(t)$. Decent agreement between the numerics and the predicted decay is found over aproximately one decade for most presented results. The biggest observed deviation from the predicted power law, which is expected to hold only in the intermediate time regime, occurs for $m = 1$ and $d = 3$. Especially the simulation for $I = 3/2$ does not match the expected power law in a broad interval, but since the observed relaxation of $S(t)$ (see panels (a)-(b)) is already completed at $t/T^* = 100$, this deviation from the power law is not disproving the estimated logarithmic decay.

All in all, good agreement between the analytical estimates and the numerical data is found. For a given realization of the coupling constants A_k, the results suggest that

computing the quantities u and $A_{\min}$ is sufficient to predict the qualitative resulting behavior of $S(t)$. For this reason, the remainder discussions are restricted to $d = 3$ dimensional QDs with a Gaussian ($m = 2$) electron wave function, which is assumed to be the most adequate setup to reproduce experimental conditions. Especially note, that no fundamental differences between the induced dynamics of a spin-1/2 or spin-3/2 bath have been found. Therefore, all following discussions concerning the CSM without QCs will be restricted to $I = 1/2$ for simplicity.

5.1.3 Analytic estimate for the non-decaying fraction

Based on Mazur's inequality [120, 121], G. S. Uhrig et al. [119] have presented an analytic derivation of a rigorous lower bound S_{low} for the non-decaying fraction S_∞ that applies for a general time-independent Hamiltonian. The central ingredient of this analytic estimate is to exploit the conserved quantities of the underlying model. The derivation of S_{low} will be briefly reviewed for the special case of the ICSM in the following. Afterwards, the evaluation of the lower bound for an arbitrary set of linear independent conserved quantities will be reviewed [119] and the obtained results for one set of known conserved quantities will be compared to the CET.

Starting from equation (3.34), the Lehmann representation of $S(t)$ is given by

$$S(t) = \frac{1}{D} \sum_{i,j=1}^{D} |S^z_{i,j}|^2 \mathrm{e}^{\mathrm{i}(E_i - E_j)t}, \tag{5.7}$$

where $S^z_{i,j}$ are the matrix elements of S^z in the eigenbasis $|i\rangle$ of the Hamiltonian H. From this representation, one can deduce that the steady state value can be written as

$$S_\infty = \frac{1}{D} \sum_{i,j=1}^{D} |S^z_{i,j}|^2 \delta_{E_j, E_m} \geq 0. \tag{5.8}$$

Since the exact diagonalization of H is not feasible for a moderate bath size, a set of M constants of motion X_i, which fullfill $[X_i, H] = 0$ by definition, is considered to evaluate S_∞ instead. Let us assume that the set of linearly independent conserved quantities X_i is orthonormal with respect to the scalar product

$$(X|Y) := \left\langle X^\dagger Y \right\rangle = \frac{1}{D} \mathrm{Tr}[X^\dagger Y], \tag{5.9}$$

i.e. they fullfill $(X_i|X_j) = \delta_{i,j}$. Then, expanding the central spin operator S^z in this representation yields

$$|S^z) = |\hat{R}) + \sum_{i=1}^{M} a_i |X_i), \tag{5.10}$$

where the coefficients are given by $a_i = (X_i|S^z)$ and the operator $\hat{R}$ represents the entire operator space that is not covered by the incomplete basis $\{X_i\}$. Note that the relation $(X_i|\hat{R}) = 0$ must hold for $i \in \{1, ..., M\}$. Next, the term (5.10) is substituted into the definition $S(t) = \left\langle (S^z)^\dagger(t) S^z \right\rangle$, yielding

$$\begin{aligned} S(t) &= \left\langle \hat{R}^\dagger(t)\hat{R} \right\rangle + \sum_{i=1}^{M} \left(a_i^* \left\langle \hat{R}^\dagger(t) X_i \right\rangle + a_i \left\langle X_i^\dagger(t)\hat{R} \right\rangle \right) + \sum_{i,j=1}^{M} a_i^* a_j \left\langle X_i^\dagger(t) X_j \right\rangle \\ &= \left\langle \hat{R}^\dagger(t)\hat{R} \right\rangle + \sum_{i,j=1}^{M} a_i^* a_j \delta_{i,j} =: S^{(\hat{R})}(t) + \sum_{i=1}^{M} |a_i|^2. \end{aligned} \tag{5.11}$$

Since $[X_i, H] = 0$ holds, the time dependence of the last three terms in the first line can be eliminated and the two middle terms vanish due to $(X_i|\hat{R}) = (\hat{R}|X_i) = 0$, while the last term gives a Kronecker symbol $\delta_{i,j}$. If the set of constants of motion $\{X_i\}$ would form a basis for all conserved quantities of the Hamiltonian H, the statement $S_\infty = \sum_{i=1}^{M} |a_i|^2$ would be true (see reference [119] for further details). Anyhow, not all conserved quantities of the ICSM are known and in practice $\hat{R}$ still features a non-decaying contribution $S^{(\hat{R})}(t \to \infty) > 0$. Therefore we can only deduce Mazur's inequality

$$S_\infty \geq S_{\text{low}} = \sum_{i=1}^{M} |a_i|^2 \tag{5.12}$$

from equation (5.11). In the following, this result will be evaluated based on *one* well known set of $N+1$ conserved quantities. The first one is the total spin $\mathcal{S}^z$, which is accompanied by N constants of motion H_l, that are known from the model's Bethe Ansatz solution [29]. These are defined by

$$H_l = \sum_{k=1,\neq l}^{N} \left(\frac{1}{A_k} - \frac{1}{A_l} \right)^{-1} \vec{I}_k \cdot \vec{I}_l - A_l \vec{S} \cdot \vec{I}_l, \tag{5.13}$$

with $l \in \{1, ..., N\}$. Since these $N+1$ conserved quantities are not orthonormal with respect to the scalar product $(\cdot|\cdot)$, equation (5.12) has to be extended to non-orthonormal sets of constants of motion. For this purpose let us assume a set of $N+1$ orthonormal operators X_i was known, that spans the subspace of the known operators H_l and $\mathcal{S}^z$. Then, the lower bound (5.12) can be rewritten as

$$S_{\text{low}} = \sum_{i=1}^{M} (S^z|X_i)(X_i|S^z) \tag{5.14}$$

with respect to this set $\{X_i\}$. By introducing the vector $\vec{a}_X$, whose components are given by the scalar products $(X_i|S^z)$, the lower bound may be rewritten in the short form $S_{\text{low}} = \vec{a}_X^\dagger \cdot \vec{a}_X$. Next, the considered conserved quantities are summarized into

the operators $C_i \in \{\mathcal{S}^z, H_l\}$ and in this notation the known constants of motion can be expanded in the basis of the orthogonal ones:

$$(C_i| = \sum_{j=1}^{M} (C_i|X_j)(X_j|. \tag{5.15}$$

By introducing the matrix $\underline{\underline{M}}$ containing the elements $(C_i|X_j)$ and multiplying this equation with $|S^z)$ from the right hand side, one obtains the relation $\vec{a}_C = \underline{\underline{M}} \cdot \vec{a}_x$, where the components of $\vec{a}_C$ are given by $(C_i|S^z)$. One can easily show that the matrix product $\underline{\underline{M}} \cdot \underline{\underline{M}}^\dagger$ gives the matrix $\underline{\underline{N}}$, which is given by the overlap elements $(C_i|C_j)$ of the conserved quantities under study:

$$(\underline{\underline{M}} \cdot \underline{\underline{M}}^\dagger)_{ij} = \sum_{k=1}^{M} (C_i|X_k)(X_k|C_j) = (C_i|C_j) = \underline{\underline{N}}_{ij}, \tag{5.16}$$

since the set $\{|X_k)\}$ is assumed to form a complete basis for the subspace of the constants of motion C_i. Hence, we obtain a general form of the lower bound S_{low} for an arbitrary set of linearly independent conserved quantities:

$$S_{\text{low}} = \vec{a}_X^\dagger \cdot \vec{a}_X = \vec{a}_C^\dagger \left(\underline{\underline{M}}^{-1}\right)^\dagger \underline{\underline{M}}^{-1} \vec{a}_C = \vec{a}_C^\dagger \underline{\underline{N}}^{-1} \vec{a}_C. \tag{5.17}$$

I.e. in practice only the matrix elements $(C_i|S^z)$ and $(C_i|C_j)$ have to be calculated and an inversion of the obtained matrix $\underline{\underline{N}}$ has to be performed to obtain a rigorous lower bound for S_∞. For details concerning the mandatory matrix elements, the reader is referred to the supplemental material [122] of reference [119]. Note however, that the conserved quantities H_l need to be replaced by $H_l^z := \mathcal{S}^z H_l$ to yield a contribution to the desired matrix elements.

Besides the rigorous lower bound (5.17), Uhrig et al. [119] have also introduced an estimate based on the semi classical picture by Merkulov et al. [27]. Instead of $S(t)$ the correlation function $S^{(B)}(t) := \langle B_N^z(t) B_N^z \rangle$ is considered, where $B_N^z = A_0 S^z + \sum_k A_k I_k^z$ holds and the term $A_0 S^z$, that is added to the z-component of the Overhauser field in this expression, is used to maximize the obtained lower bound. According to the previous considerations (see section 5.1.2 concerning the long time dynamics of $S(t)$), the lower bound from the correlation function $S^{(B)}(t)$ is estimated by

$$S_{\text{low}}^{(B)} = \frac{S_\infty^{(B)}}{12 S^{(B)}(0)}. \tag{5.18}$$

Concerning the details of the additional matrix elements that need to be calculated for this claim, the reader is, once again, referred to reference [122]. In the following, the two estimates (5.17) and (5.18) are compared to numerical results obtained via the CET in regard to their general adequacy. On top of that, results from a numerical

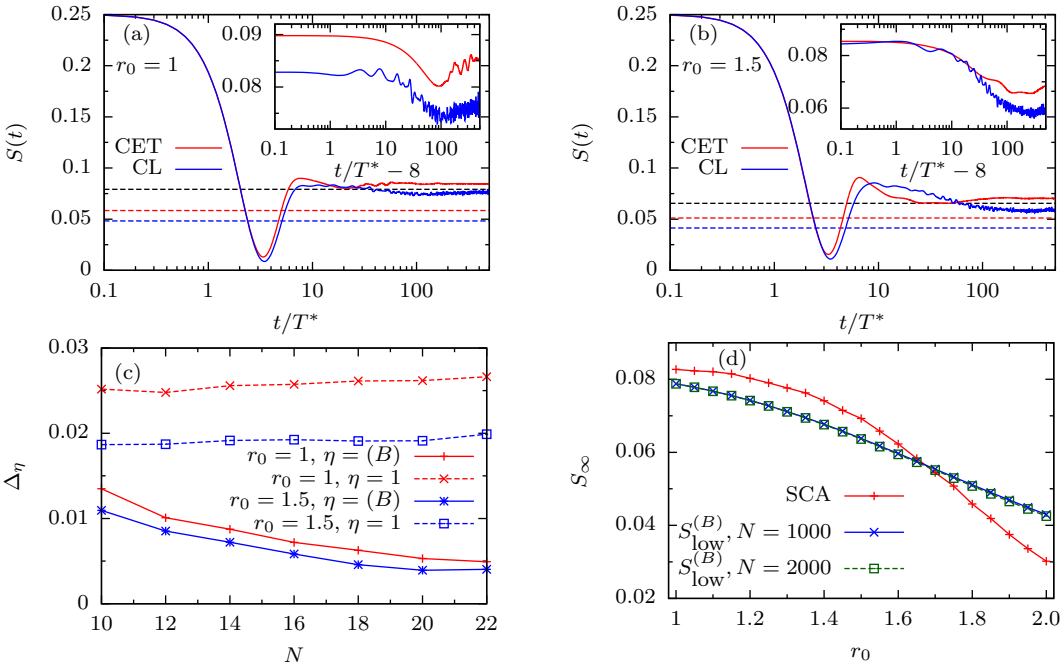

Figure 5.6: Panels (a)-(b) show a comparison of numerical results obtained via the CET and semi classical simulations (CL) that have been performed by D. Stanek [123]. For the CET $n = 50$ random configurations of $N = 20$ coupling constants have been considered using the cutoff $r_0 = 1$ (a) and $r_0 = 1.5$ (b). For the semi classical calculations the exact same coupling constants have been used in a single simulation, i.e. a bath of $N = 1000$ spin-1/2 nuclei have been taken into account at once. The black dashed lines indicate the lower bound $S^{(B)}_{\text{low}}$, which is indistinguishable for the two numerical claims, while the colored dashed lines show the rigorous bound S_{low} corresponding to the numerical data of the same color. The insets show a close up of the long time evolution, where the t-axis has been shifted to eliminate the short time decay and the CET results have been elongated by a factor of 7. Panel (c) shows the mismatch $\Delta_\eta = S_\infty - S^\eta_{\text{low}}$ between the CET and the estimated lower bounds for various system sizes. Panel (d) compares the estimated lower bounds from equations (5.3) and (5.18), where the latter one has been evaluated for $N = 1000$ and $N = 2000$.

treatment of the SCA, that has been put forward and performed by D. Stanek [49, 123], are considered and compared to the other approaches.

Comparison of numerical and analytical estimates

The mentioned semi classical model (CL) by D. Stanek et al. [49] relies on the evaluation of a system of coupled equations of motion, that respect the long time dynamics of each individual bath spin and the central spin. For details of this numerical claim see reference [123]. In figure 5.6 (a)-(b) numerical results obtained via the CET and the CL, for which the presented data have been provided by D. Stanek, are compared to the analytic estimates S_{low} and $S^{(B)}_{\text{low}}$. Note that the numerical approaches are based on the exact same randomly generated coupling constants, but the CL considered $N = 1000$ bath spins in a single simulation, while for the CET $n = 50$ results of $N = 20$

underlying nuclei have been averaged. Concerning the short time behavior, the semi classics reproduce $S_{\mathrm{SCA}}(t)$ excellently as expected, while the CET deviates slightly as discussed above. On large timescales three central observations occur. (i) The long time decay of $S(t)$ occurs slower within the CL than in the CET simulations. For a constant cutoff r_0 and an increasing bath size, the average coupling constant $\overline{A}_k T^*$ of an individual bath spin is decreasing with $\sqrt{N}$. Accordingly, an elongation of the long time decay by this factor is expected. For the presented data from figure 5.6 (a)-(b) this suggests an elongation by a factor of approximately 7 when turning from $N = 20$ to $N = 1000$. Concerning the time interval between the finished initial precession of the central spin within the Overhauser field ($t/T^* \approx 8$) and the observed local minimum at large timescales, the factor 7 reproduces the mismatch between the obtained decay times quite nicely. This is illustrated by the insets of panels (a)-(b), where the long time decay of the CET results is elongated by a factor of 7, revealing its accordance to the CL dynamics. (ii) For the semi classical numerics the correlation function $S(t)$ is accompanied by significant fluctuations on large timescales, which is a feature that is not observed within the CET for $N = 20$ and is expected to be supressed even stronger for larger spin baths. This finding reveals an inadequacy of the CL simulations, which does not necessarily imply that the obtained behavior of $S(t)$ at large times is not reproduced adequately on average. On top of this, it has been shown [123] that the quality of the SCA is improving with N and the occuring fluctuations are suppressed proceedingly. (iii) On the one hand, the fully quantum mechanical, rigorous lower bound S_{low} clearly underestimates S_∞ from both numerical simulations. This finding puts forward that the considered conserved quantities are not sufficient to yield a tight lower bound and to obtain one, further linearly independent constants of motion need to be taken into account. On the other hand, the semi classical simulations violate the phenomenological lower bound $S^{(B)}_{\mathrm{low}}$, which is not the case for the CET calculations. Since the estimate $S^{(B)}_{\mathrm{low}}$ as well as the semi classical numerics are not guaranteed to yield correct estimates for the long time evolution of $S(t)$, it remains unclear wether either of the predictions can be classified as *better* than the other.

To shed more light onto the quality of the lower bound $S^{(B)}_{\mathrm{low}}$, figure 5.6 (c) treats the scaling behavior with the system size N of the quantity $\Delta_\eta = S_\infty - S^{\eta}_{\mathrm{low}}$, where $\eta = 1$ corresponds to the rigorous lower bound S_{low} and $\eta = (B)$ to $S^{(B)}_{\mathrm{low}}$ respectively. The reference value S_∞ is determined by the CET. It turns out that the deviation Δ_η is increasing slowly with the system size for the fully quantum mechanical bound S_{low}. Given that a set of N conserved quantities H_l is known and has been taken into account to obtain S_{low}, the observed loss of accuracy for increasing N suggests, that further sets of constants of motion might exist, whose number also increases with the system size. In contrast, the deviation of the lower bound $S^{(B)}_{\mathrm{low}}$ from the CET's findings for S_∞ is decreasing with the system size and the performed scan points towards an occuring convergence for large N. Since the semi classical assumptions entering $S^{(B)}_{\mathrm{low}}$ are based

on an infinite spin bath, the observed trend is rather intuitive. But on the other hand the same conserved quantities enter the rigorous lower bound, where a decrease of the estimate's adequacy was found. Thus, the validity of $S_{\text{low}}^{(B)}$ remains unclear and can not be stated ultimately by the CET, although no deviations between the introduced bound and exact numerical calculations have been observed yet. To complete the discussion of the analytical lower bounds for S_∞, figure 5.6 (d) shows a comparison of the estimates $S_{\text{low}}^{(B)}$ and (5.3), which are both based on the considerations of Merkulov et al. [27]. It turns out that the two claims yield a significantly different shape for $S_\infty(r_0)$ and most strikingly none of them is monotonically larger or smaller than the other. The comparison of $S_{\text{low}}^{(B)}$ for two different system sizes $N = 1000$ and $N = 2000$, yielding nearly undistinguishable results, underlines that no finite size effects are expected to be responsible for the significant deviations. Since the non-rigorous estimate from Mazur's inequality reproduces the numerical findings more accurately, it is nearby to assume it is the superior claim, but all in all the CET does not allow an incontrovertible statement concerning the properties of $S(t)$ for very large systems $N \sim O(1000)$.

5.2 Dynamics within an external magnetic field

In the previous section the spin noise function $S(t)$ has been discussed in the absence of a magnetic field within the ICSM. The influence of the model parameters entering the coupling constants A_k has been discussed in detail and it has been shown that the two considered nuclear species qualitatively yield the same dynamics, both on short and long timescales. Since the effect of varying any of the mentioned factors is known from the prior discussions, the following considerations are restricted to $I = 1/2$, $m = 2$ and $d = 3$.

5.2.1 Transversal magnetic fields

Introducing a transversal magnetic field $\vec{n}_B = \vec{e}_x$ to the ICSM has two central effects. First, the conservation of the total spin $\mathcal{S}^z$ along the z-direction is not warranted anymore. Thus, the lower bound predicted by Mazur's inequality is zero and $S(t)$ is expected to approach this value within a finite time. I.e. due to the induced symmetry breaking, the value S_∞ is expected to be zero even for an infinitesimal external field. Second, the short time dynamics of $S(t)$ is governed by the timescale

$$T'^* = \left(2\omega_L^2 + (T^*)^{-2}\right)^{-1/2}, \tag{5.19}$$

which approaches T^* for $\omega_L \to 0$. According to T_λ^*, the timescale T'^* can be derived numerically by evaluating the von-Neumann equation up to second order in time. Equation (5.19) suggests that for large external magnetic fields $b = \omega_L T^* \gg 1$ the short time dynamics of $S(t)$ is solely dominated by the Larmor frequency ω_L, but since the

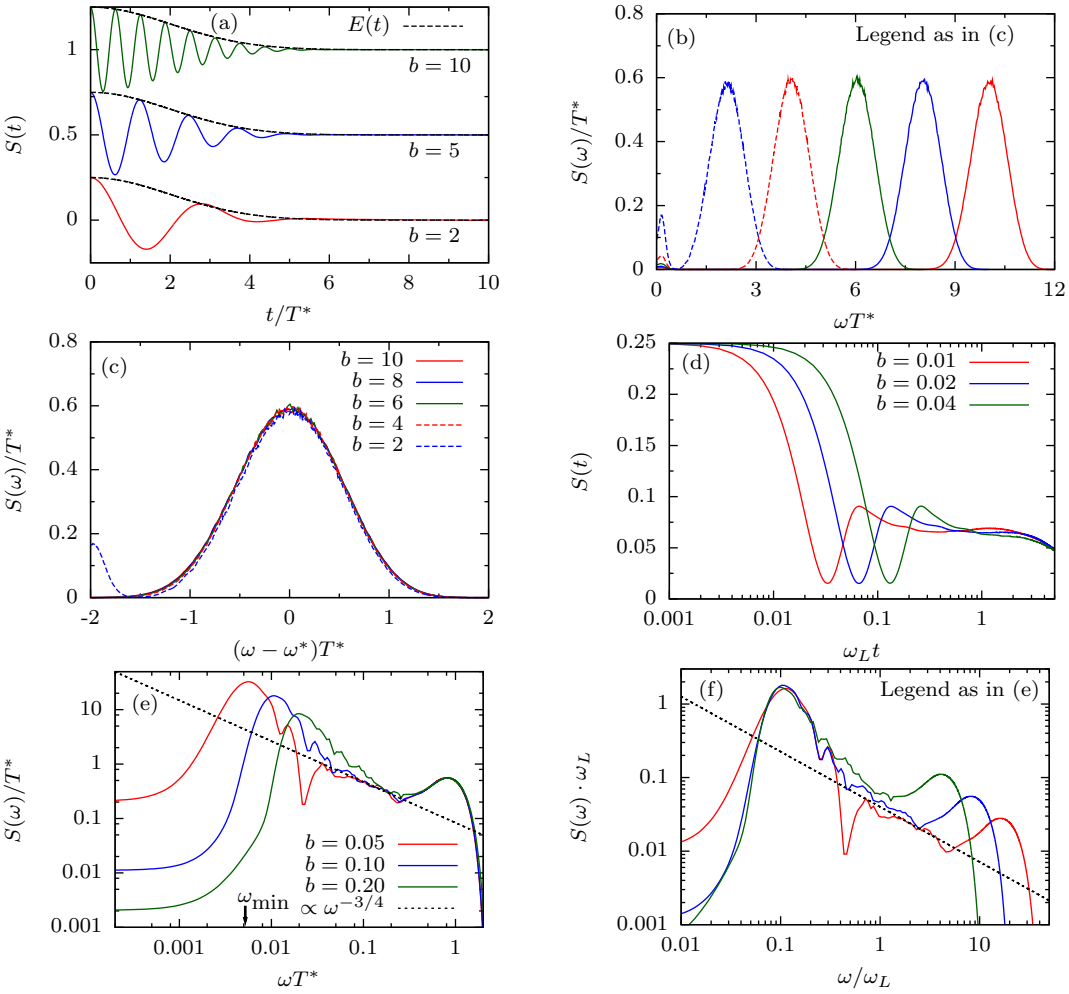

Figure 5.7: Illustration of the central spin dynamics in a transversal external magnetic field ($\vec{n}_B = \vec{e}_x$). Panel (a)-(c) treat the dynamics in a strong external field $b = \omega_L T^* > 1$. The envelope of the presented real time dynamics in panel (a) is approximated by a Gaussian function $E(t) = \frac{1}{4}\exp[-\frac{1}{2}(\frac{t}{2T^*})^2]$. An offset has been added to distinguish the curves for varying b. Panels (b) and (c) show the same set of data, which are based on $N_c = 100$ Chebyshev polynomials. Panel (c) reveals that the maximum of the approximately Gaussian peak is centered at $\omega^* = \sqrt{b^2 + 1/2}$. Panels (d)-(f) address the case of a small external field strength $b < 1$. The real time dynamics is treated in panel (d), where the time axis is scaled with $t\omega_L$ instead of t/T^* to reveal the b-dependent long time behavior of $S(t)$. This scaling is also adopted for the depiction of $S(\omega)$ in panel (f), which shows the same sets of data as panel (e). In the latter panel the smallest reliably resolved frequency $\omega_{\min} \approx 0.0052$, which stems from $N_c = 4000$ considered Chebyshev polynomials, is indicated by the black arrow. The black dashed lines in panels (e)-(f) correpsond to the power law fit from figure 5.3. All presented calculations are based on $N = 20$, $r_0 = 1.5$ and $n = 50$.

hyperfine interaction is the only source of decoherence entering the model under study, the central spin is expected to experience a decay that is still governed by the intrinsic bath fluctuations and therefore by T^*. As demonstrated in figure 5.7 (a), the expected decay occurs indeed and it can be approximated by a Gaussian envelope function

$$E(t) = \frac{1}{4} \exp\left[-\frac{1}{2}\left(\frac{t}{2T^*}\right)^2\right], \tag{5.20}$$

which is, as expected, only dependent on T^*. The spectral spin noise function for strong transversal fields is treated in panels (b)-(c) of figure 5.7. It consists of two contributions: the peak centered at the frequency $\omega^* = \sqrt{b^2 + 1/2}$, as indicated by the collapse of all five spectra in panel (c), corresponds to the short time evolution of $S(t)$ that is presented in panel (a). Corresponding to the Gaussian envelope function, the peak's shape is approximately Gaussian and its width is solely governed by T^*. Examining the addressed peaks closely shows that their spectral weight is increasing slightly with b, which is linked to the conserved sum-rule and the second observed feature near $\omega = 0$, which is vanishing quickly with increasing b. This second feature evolves continuously from the peak near zero frequency, that describes the long time dynamics and the non-decaying fraction S_∞. As stated above, the latter quantity already drops to zero for an infinitesimal external field along the x-direction. Hence, the rapidly vanishing feature at small frequencies corresponds to minor oscillations around $S(t) = 0$ on large timescales that are negligible for large field strenghts.

Panels (d)-(f) of figure 5.7 treat the central spin dynamics for small field strengths $b < 1$. Clearly the short time behavior is unaffected by the external field in this regime. Hence, the scope of the remaining panels lies on the long time evolution. Panel (d) treats the time dependent spin noise function $S(t)$. The time axis is scaled as $t\omega_L$, yielding a collapse of $S(t)$ onto one curve for varying magnetic field strength $b \in [0.01, 0.04]$ at large times $t/T^* \gtrsim 300$. This finding reveals, that the central spin's long time behavior is dictated solely by the Larmor frequency ω_L. Note that the long time decay of $S(t)$ due to the hyperfine interaction is well separated from the impact of the external field, which occurs on larger timescales in the presented regime. This is stated by the spectral results for slightly larger values of b, that are presented in panel (e): looking into the intermediate frequency regime $\omega T^* \in [0.05, 0.2]$ for $b = 0.05$, the power law fit $\propto \omega^{-3/4}$ reproduces $S(\omega)$ quite nicely and the peak occuring at smaller frequencies is well separated from the power law shoulder. For $b = 0.1$ the fit still reproduces the intermediate power law behavior of $S(\omega)$, but the separation between the two features at small frequencies is already lifted and for $b = 0.2$ they fully overlap each other. As a consequence the power law does not reproduce $S(\omega)$ anymore. The finite spectral weight, that is found for $\omega T^* \to 0$ and rapidly decreases for increasing b, occurs due to the limited resolution of the method, which is indicated by the black

arrow. According to figure 5.7 (d), panel (f) shows the exact same data for $S(\omega)$ as panel (e), but on the scale ω/ω_L instead of ωT^*. It turns out that the shape of the peak at small frequencies $\omega/\omega_L \approx 0.1$ is very similar for all presented values of b. This corresponds to the findings of recent Bethe Ansatz studies [36, 37], which reported a strictly invariant spectrum for varying b in the regime of small external fields. I.e. the Larmor frequency is indeed the crucial quantity for the long time evolution of the central spin in this regime.

5.2.2 Longitudinal magnetic fields

The main effect of introducing a longitudinal external field to the ICSM, is the suppression of spin flips of the central spin. In an arbitrarily large field $b \to \infty$, the hyperfine interaction is negligible and $S(t) = S(0)$ holds. I.e. when increasing b starting from 0, a crossover between the behavior that has been intensively discussed in section 5.1 to $S(t) = S(0)$ is expected. As depicted in figure 5.8 (a), which treats $S(t)$ for various values of b, a monotonic increase of S_∞ is observed as expected. On top of that, the minimum, which occurs due the central spin's precession in the Overhauser field, is shifted to smaller times and larger values for increasing b. As observed for transversal magnetic fields, the initial precession passes over into a precession in the external field for large field strengths. Panel (b) of figure 5.8 shows results for the spectral spin noise function $S(\omega)$ that correspond to the time resolved calculations from panel (a). The spectral weight of the peak at large frequencies is decreasing rapidly, which clearly reflects the observed increase of S_∞. The inset of panel (b) treats the steady state value S_∞ in greater detail. Since it corresponds to the spectral weight of $S(\omega = 0)$, the red solid line shows this value in dependence of b. Note that due to the limited resolution of the CET, this determination of S_∞ is not necessarily exact. Figure 5.8 (c) treats the peak at large frequencies in greater detail. For this purpose $S(\omega)$ has been rescaled by the factor b^2 and the frequency axis has been shifted by ω_L. This illustration clearly reveals two features: First, the frequency of the precession in the external field is given by ω_L instead of ω^*, which has been found for transversal fields. Second, the decrease of the peak's spectral weight is governed by b^2. From the latter finding we deduce the following estimate for the non-decaying fraction:

$$S_\infty(b) = S(0) - \frac{S(0) - S_\infty(b=0)}{1+b^2}. \tag{5.21}$$

This estimate clearly reproduces the boundary values $S_\infty(b = 0)$, which has been discussed in detail in section 5.1.2, and $S_\infty(b \to \infty) = S(0)$ and features the numerically found convergence $\propto b^{-2}$ towards $S(0)$ for large values of b. It is added to the inset of panel (b) as a black dashed line for $S_\infty(b = 0) = S(0)/3$. Apparently the claim (5.21) reproduces the numerically found result for $S_\infty(b)$ adequately. Panel (d) of figure 5.8 illustrates $S(\omega)$ for several small values of b on a double logarithmic scale. It stresses

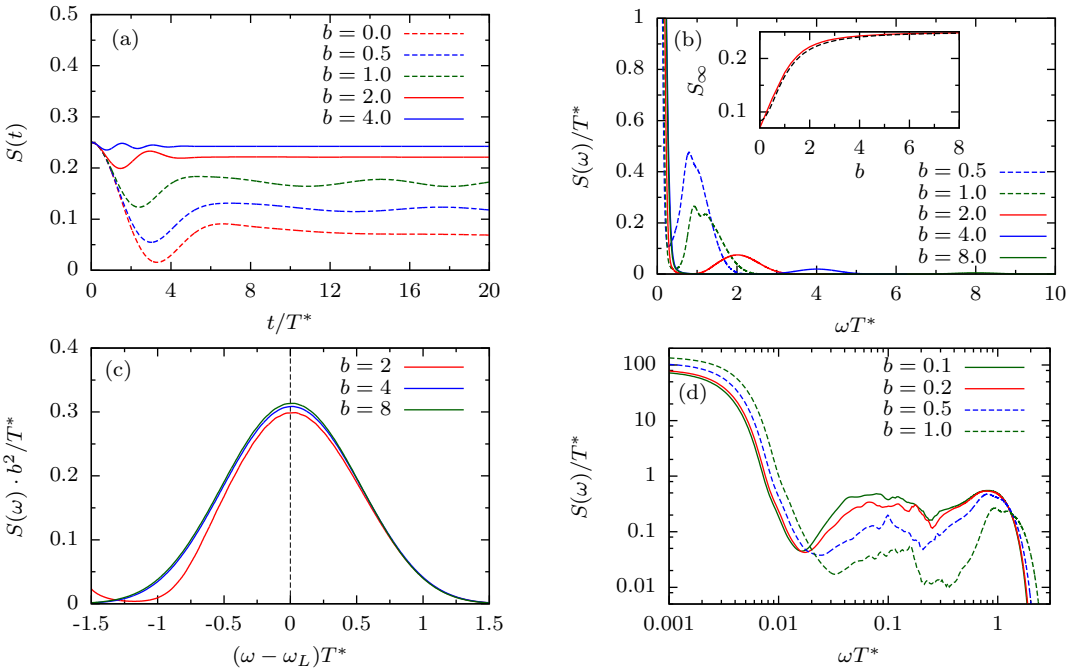

Figure 5.8: Illustration of the central spin dynamics in a longitudinal external field $\vec{n}_B \parallel z$. All panels show scans of varying field strengths b, have been calculated for $N = 20$ bath spins and $n = 50$ individual setups. The cutoff $r_0 = 1.5$ also applies for all presented data. Panel (a) addresses the time resolved correlation function $S(t)$, while the remainder panels depict results for $S(\omega)$. For panel (b) $N_c = 70$ Chebyshev polynomials have been taken into account. The inset shows two results concerning the non-decaying fraction $S_\infty(b)$: the red solid curve has been determined from the spectral weight of the peak occuring at small frequencies, i.e. from results of the CET, while the black dashed line shows the analytic estimate $S(0) \cdot \left(1 - \frac{2}{3(1+b^2)}\right)$. Panel (c) is based on the same data as panel (b), but the ω axis has been shifted by ω_L and $S(\omega)$ has been rescaled with b^2. Panel (d) shows $S(\omega)$ for various small values of b on a double logarithmic scale, where $N_c = 2000$ polynomials have been taken into account. Panels (a)-(b) correspond to figure 8 of reference [97].

the rapid suppression of the power law decay, that occurs on intermediate timescales, for increasing b. Still, some spectral features in the intermediate regime sustain for $b \sim O(1)$, whose amplitude is decreasing, in accordance to the stated increase of S_∞, with b^2 for large values of b.

5.3 Reference to recent experiments

As stated above, a recent experiment by Bechtold et al. [62] was able to measure the real time dynamics of an initially polarized, single electron spin confined in an InGaAs QD. The authors presented the first measurements that clearly show the initial decay of the electron spin within the Overhauser field, as predicted by the SCA from Merkulov et al. [27]. Comparing the CET's results from figure 5.1 to the experimental curve (see

figure 3 of reference [62]), yields perfect agreement between theory and experiment on short timescales. This comparison also puts forward that the intrinsic timescale T^* of the QD under study is very close to 1 ns, which will be assumed for the following considerations. Besides the excellent agreement on short timescales $t \leq 10$ ns, the experimentally found long time decay differs from the theoretical expectations within the ICSM. The prediction by Chen et al. [30] suggests a logarithmic decay of $S(t)$ on long timescales, which is stated by our numerical investigations for various assumptions of the dot geometry and the electron envelope wave function. In contrast, the experimentally measured signal decays faster than predicted by this theory. On top of that, a reoccurence of the signal is observed at $t \approx 1\,\mu$s. Such a feature is not involved in the theory by Chen et al., but is observed for any fully quantum mechanical simulation via the CET. I.e. it can not be excluded that the reoccurence might set in before all bath spins have contributed to the dynamics, which might supress the logarithmic decay on very large timescales. Thus, it remains unclear and rather speculative if the experimental findings can be fully understood within the ICSM or not. Anyhow, an alternate interpretation of the experimental data based on the influence of quadrupolar coupling (QC) will be presented below, which explains the non-logarithmic decay and also unifies recent measurements of holes and electrons.

In section 5.2.1 it has been demonstrated that applying a strong transversal field to the central spin yields a rapid decay of $S(t)$ that is (i) solely governed by the intrinsic timescale T^* and (ii) described by a Gaussian envelope function on timescales $t/T^* < 10$. In accordance to the above stated, excellent agreement between theory and experiment on such short timescales, the ICSM is expected to reproduce the experimentally measured electron spin dynamics in a strong transversal field correctly. Crooker et al. [59] have investigated spin noise in an ensemble of n-doped InGaAs QDs within an applied transversal field experimentally. The observed spectrum features a single peak at large frequencies, whose position is determined by the Larmor frequency. The shape of this peak turned out to be approximately given by a Lorentzian, in contrast to the expected Gaussian shape for an individual QD. I.e. an ensemble average has to be applied to the spectrum of a single dot, to compare the theory to these experimental findings. As described in section 3.4, this is realized by determining the characteristic length scale L_0 from a Gaussian distribution and inserting the obtained value into T^* with respect to equation (3.39). The average timescale $\overline{T}^*$ is set to 1 ns, as stated above. Figure 5.9 shows the obtained results, that correspond to figure 4 (a) from reference [59]. It turns out that the applied ensemble average indeed induces a change of the occuring peak from a Gaussian to a Lorentzian shape. Especially for large external fields the fits account adequately for the data, while significant deviations are found for small external fields. Both observations correspond to the experimental findings [59]. Also the position and width of the individual peaks is reproduced almost perfectly by the numerical simulations. The observed asymmetry of the peaks, mainly

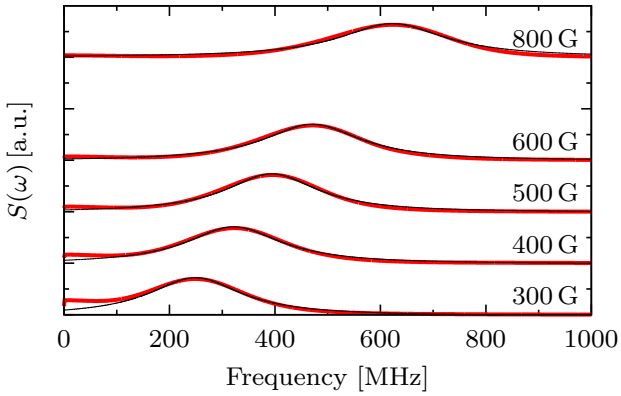

Figure 5.9: Ensemble averaged spin noise spectra for electron doped QDs at five different magnetic field strengths. The spectral function $S(\omega)$ has been calculated for $n = 100$ spin baths of $N = 20$ nuclei, a cutoff $r_0 = 1.5$ and $N_c = 15$ Chebyshev polynomials have been considered. According to reference [59], the electron g-factor $|g_e| = 0.54$ is used. Concerning the ensemble averaging, a mean intrinsic timescale $\overline{T}^* = 1\,\text{ns}$ has been assumed. The broadening of T^* results from a Gaussian distribution of the characteristic length scale L_0, which enters T^* via $L_0^{-3/2}$, with a standard deviation $\Delta L_0/L_0 = 0.2$. An offset proportional to $b = \omega_L \overline{T}^*$ has been added to distinguish the individual curves. The black lines indicate Lorentzian fits.

stems from the asymmetry of the T^* distribution arising from the $L_0^{3/2}$ term. Note that a very small number $N_c = 15$ of Chebyshev polynomials has been considered for the results of figure 5.9. This accounts for the limited resolution of the experiments on very short timescales. Due to the rough resolution, the peaks occuring at small and large frequencies feature a finite overlap, which is an artefact of the CET, for small external fields. All in all good agreement between our simulations and the experiments by Crooker et al. is found, underlining that the ICSM does describe the short time dynamics of electrons confined in InGaAs QDs adequately.

5.4 Chapter conclusion

In the precedent chapter, the isotropic central spin model (ICSM) has been discussed in detail. It has been stated that the semi classical solution $S_{\text{SCA}}(t)$ predicts the short time behavior of $S(t)$ correctly, while the adequacy of its estimate for S_∞ turned out to be questionable. Still, the qualitative prediction that the parameter $u = \langle A^2 \rangle / \langle A \rangle^2$ is crucial for the steady state value S_∞, has been stated. The timescale on which the longtime decay of the spin noise function occurs turned out to be governed by the parameter u, the ratio $A_{\text{max}}/A_{\text{min}}$ and the size of the spin bath. In contrast to the SCA, the long time decay $\propto \ln^{-d/m}(t)$, that has been proposed by Balents et al. [30], has proven to reproduce the decay of $S(t)$ for intermediate timescales adequately, but since it does not feature a reoccurence of $S(t)$ for large t, it is also not believed to cover the entire long time dynamics. It has also been shown that the investigation of

spin-1/2 nuclei qualitatively yields the same results as a bath of spin-3/2 particles. The presented rigorous lower bound for S_∞ based on Mazur's inequality has proven to be quite rough and further conserved quantities need to be taken into account to obtain a tight bound. On the other hand, the estimate $S_{\text{low}}^{(B)}$ is also not tight for arbitrary coupling constants and its general validity could not be proven and is questionable, since the semi classical simulations by D. Stanek violate it.

The central spin dynamics in large transversal magnetic fields is given by a precession with frequency $\omega^* = \sqrt{b^2 + 1/2}$ that is damped by a Gaussian envelope function which only depends on the intrinsic timescale T^*. The long time decay for small transversal fields is dictated by the Larmor frequency ω_L, while the short time behavior of $S(t)$ remains unaffected. It has been demonstrated, that the increase of the non-decaying fraction in a longitudinal field can be described by equation (5.21) when considering a fixed cutoff r_0. The short time dynamics in large longitudinal fields turned out to be governed by the Larmor frequency ω_L instead of ω^* and, according to the analytic estimate for $S_\infty(b)$, the spectral weight of $S(\omega \neq 0)$ is decreasing as b^{-2} for large external fields.

By applying an ensemble average to the results of a single QD, recent experimental results [59] for spin noise in an ensemble of n-doped InGaAs QDs within a transversal external field could be reproduced adequately. Another recent experiment [99] on a single electron spin confined in an InGaAs QD found the same short time dynamics as predicted by the SCA. Either due to the applied model's incompleteness or finite size limitations the experimental findings concerning the long time dynamics are not reproduced by the simulations considering the ICSM. This mismatch will be discussed further in section 8.

Chapter 6

TD-NRG Approach for the Isotropic Central Spin Model

The spin dynamics within the ICSM in the absence of a magnetic field has been intensively studied in the preceding chapter. We have put forward several arguments concerning the central spin's behavior on large timescales, that support the correctness of certain analytical predictions, but until the present day nobody has been able to establish a numerical procedure that is capable of treating the long time evolution for a large spin bath $N \sim O(10^3)$ on a fully quantum mechanical level. One promising candidate to achieve this goal is the time dependent numerical renormalization group (TD-NRG). It is an iterative procedure, designed to calculate time dependent expectation values of the form

$$O(t) = \langle \rho(t) O \rangle = \mathrm{Tr}\left[\mathrm{e}^{-\mathrm{i}Ht} \rho_0 \mathrm{e}^{\mathrm{i}Ht} O \right], \tag{6.1}$$

by truncating the underlying Hilbert space and performing the occuring sums appropriately. Originally [67] the NRG has been developed to study the Kondo effect [124, 125], but it can be applied to quantum impurity models in general. In the following chapter, we present first investigations concerning the realization of a TD-NRG procedure applied to the ICSM, where the central spin is the quantum impurity under study. The section at hand assumes that the reader possesses basic knowledge about the TD-NRG and does not contain a full review of the method. To take along readers who are entirely new to the NRG, the central steps of the original method are always sketched before we discuss their realisation in the CSM TD-NRG. For a detailed discussion of the original time independent NRG the reader is referred to references [67, 69], while the TD-NRG has been proposed in reference [68].

6.1 TD-NRG algorithm

For the standard NRG procedure the investigated Hamiltonian is mapped on a semi-infinite chain, where the quantum impurity (here: the central spin) is coupled to the

first site of the chain only. The algorithm relies on the fact that the coupling constants in the Wilson chain decrease exponentially with the distance from the impurity. Since mapping the ICSM onto a Wilson chain is not possible, we retain the original star-topology of the model within the NRG and assume the coupling constants A_k to be ordered as follows:

$$A_1 > A_2 > \cdots > A_N. \tag{6.2}$$

The NRG method aims towards obtaining a fixed point Hamiltonian after a large number m of iterations. To ensure that each term added in the iterative NRG procedure, which is described in detail below, is of the same order of magnitude, we introduce the rescaled coupling constants

$$\overline{A}_k = \Lambda^{k-1} A_k. \tag{6.3}$$

The selection of the so called NRG parameter Λ demands further considerations and the details on its choice will be discussed in the following section. In the central spin NRG algorithm we will start from a system consisting of the central spin coupled to the nucleus with the largest coupling constant A_1 only

$$H_1 = \overline{A}_1 \vec{S} \cdot \vec{I}_1 \tag{6.4}$$

and iteratively add the remainder bath spins to the system by using the recursion relation

$$H_{M+1} = \Lambda H_M + \overline{A}_{M+1} \vec{S} \cdot \vec{I}_{M+1}. \tag{6.5}$$

Apparently we arrive at the final Hamiltonian $H_N = \Lambda^{N-1} H$ after $N-1$ steps. As we will see below, the Hamiltonian needs to be diagonalized in each NRG step and since the Hamiltonian's Hilbert space dimension is growing exponentially with the bath size, we can only treat the full system exactly for several iterations m_0. After m_0 is exceeded we need to apply an appropriate truncation scheme selecting which states are discarded at step m and which states are kept for further iterations. With respect to the iterative construction of the Hamiltonian, we introduce the following notation for the matrix elements of an observable O at the m-th NRG iteration:

$$O_{rs}^{(m)} = \langle r, e; m | O | s, e; m \rangle, \tag{6.6}$$

where the letters r/s represent the NRG states of the central spin and those bath spins that have already been added to the Hamiltonian at step m, while e represents the states of the remainder bath spins. Since we will not consider operators acting on a bath site that has not already been added to the system up to step m, the representation (6.6) is

diagonal in e. Before we go into further detail about the used truncation schemes and the explicit calculation of time dependent expectation values, let us first slide in some considerations concerning the NRG parameter Λ and the density operator ρ.

6.1.1 Selection of the NRG parameter Λ

For the CSM the selection of the NRG parameter Λ is closely related to the selection of the coupling constants A_k, since they dictate the energy scale of the Hamiltonian (5.1) without an external field. As discussed above, we usually apply a procedure to generate random sets of coupling constants with respect to a certain distribution function, where the cutoff radius r_0 determines the ratio between the largest and smallest coupling constant taken into account. This ratio is decreasing exponentially with the square of r_0: $A_1/A_N = \mathrm{e}^{-r_0^2}$. From the definition of the rescaled couplings we can immediately see that setting

$$\Lambda^{N-1} = \frac{A_1}{A_N} \tag{6.7}$$

yields a constant ratio $\overline{A}_1/\overline{A}_N = 1$. This choice for Λ clearly fullfills our requirement, that all rescaled coupling constants added to the system are of the same order of magnitude. Anyhow, the NRG demands a strict energy hierarchy to work reliably and this condition can not be guaranteed for our randomly generated coupling constants A_k. Thus, we begin with the investigation of simplified coupling constants

$$A_k = \Lambda^{-k+1} A_1, \tag{6.8}$$

yielding $\overline{A}_k = A_1$, to check wether the NRG procedure is adequate to tackle the central spin problem in general and deal with problems that might occur for a more realistic setup later. By inserting equation (6.8) into (6.7) we see that this simplified assumption for the coupling constants allows us to choose the NRG parameter Λ freely. From the numerical point of view, a large value of Λ, yielding a pronounced energy hierarchy and therefore a reliable NRG procedure, is desirable. Anyhow this choice is contrary to the physical point of view: in a realistic QD the electron wave function varies slowly on the length scale of a unit cell and thus we wish to investigate a dense distribution of coupling constants. As a consequence we need to find a compromise between the physical and numerical demands of the underlying problem.

6.1.2 Density operator

The original TD-NRG [68] is designed to calulate the real time dynamics of a local operator after a quantum quench: the investigated system is initially in thermal equilibrium, described by the initial Hamiltonian H_i yielding the density matrix ρ_{eq} in the

basis of H_i, and then H_i is instantaneously exchanged by the final Hamiltonian H_f causing a reaction of the system. This reaction is calculated within the TD-NRG. For this type of experiment two individual NRG runs for H_i and H_f are required to compute the TD-NRG equation, vaguely speaking because ρ_{eq} has to be rotated from the initial to the final basis, which has to be constructed iteratively. I.e. the original TD-NRG demands one forward an one backward iteration. Since we are interested in the spin noise function $S(t)$ at infinite temperature, the density operator of our system is proportional to unity and therefore independent of the underlying basis. Thus, we know the exact form of the required reduced density operator in every NRG step a priori and a backward iteration is not required:

$$\rho_0 = \frac{1}{2D_N}\underline{\underline{1}}, \tag{6.9}$$

$$\implies \quad \rho_{sr}^{\mathrm{red},(m)} = \sum_e \langle s,e;m|\rho_0|r,e;m\rangle = \frac{D_{N-m}}{2D_N}\delta_{s,r}, \tag{6.10}$$

where $D_n = (2I+1)^n$ denotes the dimension of a bath containing n spins with absolute value I. I.e. the ratio $\frac{D_{N-m}}{2D_N}$ is the dimension of the system consisting of the central spin and all bath spins that have been added up to the NRG step m.

6.1.3 The ICSM TD-NRG iteration

It has been shown [68], that the expectation value of a local operator O can be written in the form

$$O(t) = \sum_{m=0}^{N} {\sum_{r,s}}' O_{rs}^{(m)} \rho_{sr}^{red,(m)}(t), \tag{6.11}$$

where the reduced sum $\sum'_{r,s}$ requires at least one of the states r and s to be discarded at step m. Also note that in the last step $m = N$ all remaining states are considered to be discarded. Since we are interested in calculating the correlation function $S(t) = \langle S^z(t)S^z\rangle$ within the ICSM, the TD-NRG equation (6.11) demands some additional consideration. As described above, we diagonalize the Hamiltonian exactly for the first m_0 iterations without discarding any states in the process, hence these NRG steps do not contribute to the TD-NRG equation due to the reduced sum. Furthermore the consideration of a correlation function as $S(t)$ demands a summation over an additional complete basis set, yielding

$$\begin{aligned} S(t) &= \sum_{m=m_0}^{N} {\sum_{r,s,t}}' S_{rs}^{z,(m)}(t) S_{st}^{z,(m)} \rho_{tr}^{\mathrm{red},(m)}, \\ &= \sum_{m=m_0}^{N} \frac{D_{N-m}}{2D_N} {\sum_{r,s}}' S_{rs}^{z,(m)}(t) S_{sr}^{z,(m)} = \sum_{m=m_0}^{N} S^{(m)}(t), \end{aligned} \tag{6.12}$$

after inserting the investigated reduced density operator (6.10). Equation (6.12) is the central equation of the CSM TD-NRG. Since the choice of an adequate truncation scheme is the key ingredient to construct an adequate NRG procedure for the central spin problem, we present two fundamentally different approaches for its realization in the following, that are based on two different truncation schemes. Note that we restrict ourselves to the case $I = 1/2$ for the remainder of this chapter.

Wilson truncation

First, we adapt the Wilson energy truncation from the original NRG [67]. Within this approach the kept NRG states entering equation (6.12) are the low energy eigenstates of the Hamiltonian. Up to step m_0 we do not truncate any states and due to the reduced sum in relation (6.12) these steps do not contribute to the spin-noise function $S(t)$. Thus, we might simply construct the Hamiltonian up to step m_0 in the eigenbasis of the operators S^z and I_k^z, i.e. the spin operators $\vec{S}$ and $\vec{I}_k$ are well known in every step. Starting at NRG iteration $m = m_0 - 1$ on the basis of Hamiltonian $\underline{\underline{H}}_{m_0-1}$ given in the basis set $|\sigma^z, I_1^z, I_2^z, \cdots, I_{m_0-1}^z, e; m\rangle = |r, e; m\rangle$, that are considered the kept states entering step $m = m_0$, we iteratively perform the following steps until arriving at $m = N$:

1. We add the m-th bath spin to the bath, forming the new basis set $|r, I_m^z, e; m\rangle$ and the Hamiltonian $\underline{\underline{H}}_m$ is constructed in this basis with respect to equation (6.5).

2. In the next step, we diagonalize $\underline{\underline{H}}_m$ and obtain its eigenstates

$$H_m|n\rangle = E_n^{(m)}|n\rangle, \tag{6.13}$$

where the degrees of freedom e of the bath that has not been added to the system have been omitted. These eigenstates are connected to the initial basis of the kept states via the unitary matrix $\underline{\underline{U}}^{(m)}$, whose elements are given by

$$|n\rangle = \sum_r U_{n;r}^{(m)}|r, I_m^z\rangle. \tag{6.14}$$

The states $|n\rangle$ are the NRG states entering equation (6.12). We consider the states corresponding to the upper half of the spectrum $|n, e; m\rangle = |l, e; m\rangle$ the discarded states and those corresponding to the lower half $|n, e; m\rangle = |k, e; m\rangle$ the kept states in the following. Note that the line between kept and discarded states is never drawn between two degenerate eigenstates and in case of a degeneracy in the middle of the spectrum we always keep all the degenerate states.

3. We use the matrix $\underline{\underline{U}}^{(m)}$ to rotate the central spin operator $\vec{S}$ into the basis $|n, e; m\rangle$ and can straight forwardly calculate the contribution of the m-th NRG step to the spin noise function:

$$S^{(m)}(t) = \frac{D_{N-m}}{2D_N} \sum_{r,s}{}' S^{z,(m)}_{rs} S^{z,(m)}_{sr} \mathrm{e}^{\mathrm{i}(E_r - E_s)t}. \tag{6.15}$$

   Next, we revisit step 1. adopting the operators H_m and $\vec{S}$ in the basis of the kept states only and setting $m = m + 1$.

As we have seen, due to the star topology of the CSM the central spin operator $\vec{S}$ enters the Hamiltonian in every iteration and its transformation into the basis spanned by the kept NRG states only is not unitary. Thus, it does not conserve the commutation relation of the components of $\vec{S}$, i.e. the central spin is also truncated in the NRG procedure and its absolute value $\left|\vec{S}\right| = 1/2$ is not conserved. Recent DMRG studies [39] have shown that this truncation is problematic in the CSM, because due to the special role of the central spin its truncation also implies an underestimation of all interactions that are added after the first truncation in the NRG procedure. This observation motivates our second approach for an adequate truncation scheme.

Central spin conserving truncation scheme

In the following we introduce a truncation scheme conserving the central spin's absolute value $\left|\vec{S}\right| = 1/2$ and the Lie-Algebra of the central spin operators S^x, S^y, S^z. To realize this, we seek to split the states of the spins that have already been added to the system up to step m into their central spin σ and bath e_r contribution: $|r, e; m\rangle \rightarrow |\sigma, e_r, e; m\rangle$. With this notation in mind, let us turn to the new CSM NRG iteration. Since we do not truncate up to step m_0, the states $|\sigma, e_r, e; m_0 - 1\rangle$, that are no eigenstates of the Hamiltonian H_{m_0-1}, are exactly known and considered the kept states entering step m_0. Accordingly all matrix elements $\langle\sigma, e_r|H_{m_0-1}|\sigma', e_r'\rangle$ forming $\underline{\underline{H}}_{m_0-1}$ are also known. Subsequently we iteratively perform the following steps starting from $m = m_0$:

1. We extend the kept basis set $|\sigma, e_r, e; m-1\rangle$ by adding another bath spin to form the new bath variable $e_r^{(m)} = (e_r^{(m-1)}, I_m^z)$ and form $|\sigma, e_r, e; m\rangle$, where one bath spin has been transferred from the environment e to the bath that is interacting with the central spin e_r. Within this new basis the Hamiltonian H_m is constructed via equation (6.5).

2. In the next step, we diagonalize H_m and obtain its eigenstates

$$H_m|n\rangle = E_n^{(m)}|n\rangle. \tag{6.16}$$

These eigenstates are connected to the initial basis of the kept states via the unitary matrix $\underline{\underline{U}}^{(m)}$, whose elements are given by

$$|n\rangle = \sum_{\sigma,e_r} U^{(m)}_{n;\sigma,e_r} |\sigma, e_r, e; m\rangle. \tag{6.17}$$

3. We use a fictitious density operator $\rho_{\mathrm{f}}^{(m)}$ and trace out the central spin to construct a reduced density matrix $\rho_{\mathrm{e}}^{(m)}$ for the bath spins only:

$$\rho_{\mathrm{f}}^{(m)} = \frac{1}{Z} \sum_n |n\rangle\langle n| \mathrm{e}^{-\beta E_n^{(m)}} \tag{6.18}$$

$$\rho_{\mathrm{e}}^{(m)} = \frac{1}{Z} \sum_\sigma \sum_n \langle\sigma|n\rangle\langle n|\sigma\rangle \mathrm{e}^{-\beta E_n^{(m)}}, \tag{6.19}$$

where $Z = \sum_n \langle n|\mathrm{e}^{-\beta E_n^{(m)}}|n\rangle = \sum_n \mathrm{e}^{-\beta E_n}$ is the partition function of the system. The parameter β is a fictitious inverse truncation temperature, differentiating the high-energy states from the low-energy states. By inserting relation (6.17) into (6.19) we obtain the matrix elements of the reduced density matrix of the spin bath

$$\rho_{\mathrm{e}}^{(m)} = \frac{1}{Z} \sum_n \sum_\sigma \sum_{e_r,e_r'} |e_r, e; m\rangle\langle e_r', e'; m| U^{(m)}_{n;\sigma,e_r} \left(U^{(m)}_{\sigma,e_r',n}\right)^* \mathrm{e}^{-\beta E_n^{(m)}} \tag{6.20}$$

$$\Longrightarrow \quad \left(\rho_{\mathrm{e}}^{(m)}\right)_{e_r,e_r'} = \frac{1}{Z} \sum_n \mathrm{e}^{-\beta E_n^{(m)}} \left(U^{(m)}_{n;\uparrow,e_r} \left(U^{(m)}_{\uparrow,e_r',n}\right)^* + U^{(m)}_{n;\downarrow,e_r} \left(U^{(m)}_{\downarrow,e_r',n}\right)^*\right). \tag{6.21}$$

Now we diagonalize $\rho_{\mathrm{e}}^{(m)}$ obtaining its eigenstates $|\tilde{e}_r\rangle$, that are connected to the original bath states via

$$|\tilde{e}_r, e; m\rangle = \sum_{e_r} S^{(m)}_{\tilde{e}_r,e_r} |e_r, e; m\rangle, \tag{6.22}$$

where the matrix $\underline{\underline{S}}^{(m)}$ transforms $\rho_{\mathrm{e}}^{(m)}$ into its diagonal form.

4. We consider those eigenstates $|\tilde{e}_k, e; m\rangle$ that correspond to the larger half of absolute eigenvalues the new kept states and the remainder eigenstates $|\tilde{e}_l, e; m\rangle$ discarded states. In case of degenerate states in the middle of the spectrum, the same rules as above apply. Now we add the central spin back to the system, obtaining the states $|\sigma, \tilde{e}_k, e; m\rangle$ and $|\sigma, \tilde{e}_l, e; m\rangle$ that are the basis states entering the TD-NRG equation (6.12). For the time-dependency, we need to expand the kept and discarded states in the eigenstates of the Hamiltonian

$$|\sigma, \tilde{e}_r, e; m\rangle = \sum_{e_r} S^{(m)}_{\tilde{e}_r;e_r} |\sigma, e_r, e; m\rangle = \sum_{e_r} \sum_n S^{(m)}_{\tilde{e}_r;e_r} \left(U^{(m)}_{\sigma,e_r;n}\right)^* |n\rangle \tag{6.23}$$

and obtain their time dependency

$$\mathrm{e}^{-\mathrm{i}Ht}|\sigma,\tilde{e}_r,e;m\rangle = \sum_n \tilde{U}^{(m)}_{\tilde{e}_r;n}[\sigma]\mathrm{e}^{-\mathrm{i}E_n t}|n\rangle \tag{6.24}$$

after defining the matrix $\tilde{U}^{(m)}$

$$\underline{\underline{\tilde{U}}}^{(m)}[\sigma] = \underline{\underline{S}}^{(m)}\left(\underline{\underline{U}}^{(m)}[\sigma]\right)^{\dagger}. \tag{6.25}$$

5. Finally, we calculate the contribution of NRG step m to the spin noise function

$$\begin{aligned} S^{(m)}(t) = \frac{D_{N-m}}{2D_N}\sum_{\sigma,\sigma'}{\sum_{\tilde{e}_r,\tilde{e}_s}}' \langle\sigma,\tilde{e}_r;m|\mathrm{e}^{\mathrm{i}Ht}S^z\mathrm{e}^{-\mathrm{i}Ht}|\sigma',\tilde{e}_s;m\rangle\times \\ \times\langle\sigma',\tilde{e}_s;m|S^z|\sigma,\tilde{e}_r;m\rangle, \end{aligned} \tag{6.26}$$

where the reduced sum demands that at least one of the states $\tilde{e}_r$ and $\tilde{e}_s$ is a discarded state. Now we use the fact that S^z is diagonal in the underlying basis $\langle\sigma',\tilde{e}_s;m|S^z|\sigma,\tilde{e}_r;m\rangle = \frac{\sigma}{2}\delta_{\sigma,\sigma'}\delta_{\tilde{e}_s,\tilde{e}_r}$, with $\sigma = +$ for spin up and $\sigma = -$ for spin down, and insert relation (6.24) to arrive at

$$\begin{aligned} S^{(m)}(t) &= \frac{D_{N-m}}{2D_N}\sum_{\sigma}\sum_{\tilde{e}_l}\sum_{n,n'}\frac{\sigma}{2}\langle n|\left(\tilde{U}^{(m)}_{n;\tilde{e}_l}[\sigma]\right)^*S^z\tilde{U}^{(m)}_{\tilde{e}_l;n'}[\sigma]|n'\rangle\mathrm{e}^{-\mathrm{i}(E_{n'}-E_n)t} \\ &= \frac{D_{N-m}}{4D_N}\sum_{n,n'}\mathrm{e}^{-\mathrm{i}(E_{n'}-E_n)t}\langle n|S^z|n'\rangle\sum_{\tilde{e}_l}\times \\ &\times\left[\left(\tilde{U}^{(m)}_{n;\tilde{e}_l}[\uparrow]\right)^*\tilde{U}^{(m)}_{\tilde{e}_l;n'}[\uparrow] - \left(\tilde{U}^{(m)}_{n;\tilde{e}_l}[\downarrow]\right)^*\tilde{U}^{(m)}_{\tilde{e}_l;n'}[\downarrow]\right] \end{aligned} \tag{6.27}$$

Note that all states are considered discarded states in the last NRG step $m = N$. After calculating equation (6.27) step 1. is revisited for $m = m+1$ and the states $|\sigma,\tilde{e}_k,e;m\rangle$ as new kept states.

6.2 Results

Let us now turn to the discussion of the results obtained via the two approaches for a CSM TD-NRG procedure, that have been introduced in the previous section. Beside the comparison of exact calculations to corresponding NRG calculations of the spin noise function $S(t)$, we will discuss the NRG energy flow of the investigated Hamiltonian (5.1), i.e. the behavior of the Hamiltonian's energy spectrum in the proceeding NRG steps.

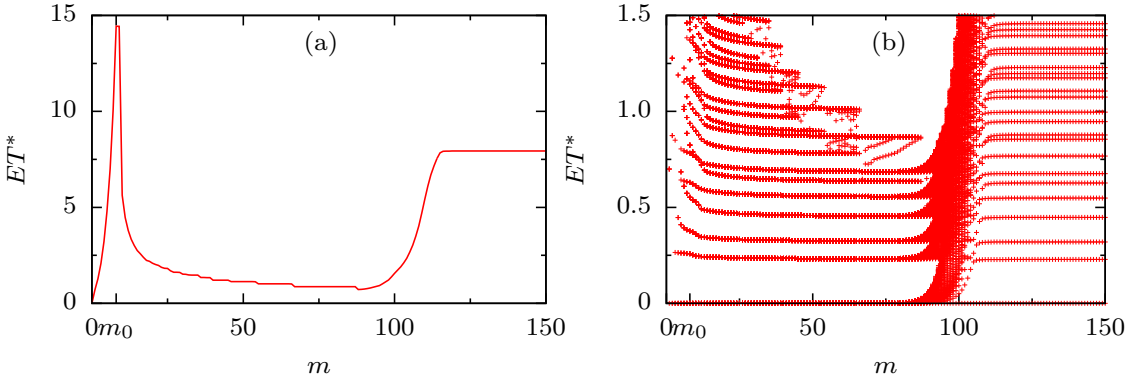

Figure 6.1: Energy flow of the Hamiltonian (5.1) for the Wilson energy truncation, $\Lambda = 1.4$ and simplified coupling constants $A_k = \lambda^{1-k} A_1$. The lowest eigen energy E_{min} is always set to 0 and panel (a) only depicts the flow of the largest energy level E_{max}. Panel (b) depicts the energy flow of the low lying eigen energies and each energy level is represented by an individual red dot. The first truncation was applied at $m_0 = 8$ corresponding to keeping $N_k = 256$ states in every NRG step.

6.2.1 Wilson truncation

Before we go into detail on the calculations concerning the spin noise function $S(t)$, let us discuss the energy flow of the underlying Hamiltonian, that is shown in figure 6.1 for one representative setup. Panel (a) demonstrates how the width of the spectrum is growing exponentially until arriving at iteration $m_0 = 8$, where the first truncation is applied. From this point forward we observe a rapid decay of the spectral width, which is not expected in a usual NRG procedure since the coupling constants are chosen such that the terms added to the Hamiltonian yield a contribution of the same order of magnitude in every NRG step. After $m \approx 100$ iterations the monotonous decrease of the spectral width is turning into a rapid increase. After $m \approx 120$ iterations we arrive at a fixed point Hamiltonian, i.e. a Hamiltonian with an invariant spectrum for $m > 120$. This invariance is underlined by the detailed extract of the low energy spectrum shown in panel (b) and its occurrence is a positive precursor indicating that the realization of a working TD-NRG procedure for the central spin problem might be possible. Anyhow the rapid decrease of the spectral width during the first couple of applied truncations is unusual, especially due to the simplified choice of coupling constants. Hence, the truncation of the central spin operators within the Wilson energy truncation is the most likely source for this unusual behavior. Note that the energy flow for varying Λ always looks similar to the case shown in figure 6.1. The only major change for decreasing Λ is an increase of the NRG steps m that have to be performed to obtain a fixed point Hamiltonian. Let us now turn to the discussion of the time dependent data obtained within the Wilson apporach of the ICSM TD-NRG realization.

Figure 6.2 (a) compares ICSM TD-NRG results, based on varying values of the NRG parameter λ, for the spin noise function $S(t)$ to results obtained via exact diagonalization (ED) for $N = 12$ bath spins. For the presented data we set $m_0 = 11$, i.e. only

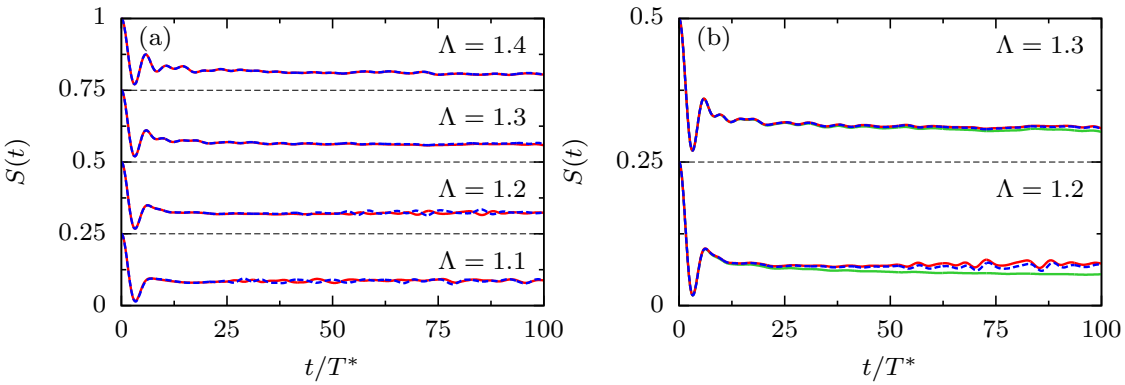

Figure 6.2: Time dependence of the correlation function $S(t)$ for different values of the NRG parameter Λ. To distinguish between its different values, offsets have been added that are indicated by the black dashed lines. The underlying coupling constants are chosen as discussed above: $A_k = \lambda^{1-k} A_1$, where A_1 is adjusted such that $T^* = 1$ is fullfilled. Panel (a) shows a comparison between results obtained via ED (red solid lines) and the ICSM TD-NRG (blue dashed lines), where all calculations are based on $N = 12$ bath spins and the number of kept NRG states has been set to $N_k = 2048$, i.e. only one truncation was applied in the procedure. In panel (b) this limitation is exceeded: the solid green lines have been obtained using the CET for $N = 20$ bath spins, while the dashed blue lines show NRG calculations for the same system size and $N_k = 4096$. The red curves in panel (b) are the same as in panel (a) for the corresponding values of Λ.

one truncation of the energy spectrum was applied in the NRG procedure. Of course the goal of a final TD-NRG for the central spin problem is to reproduce exact results adequately for a large number of bath spins N after many truncations $O(N)$, but being able to adequately reproduce exact results for a single truncation is clearly the first step to approach this final goal. We observe good agreement for all values of the NRG parameter Λ on short time scales $t/T^* < 20$. On top of that, the NRG reproduces the ED nicely on the whole shown timescale for $\Lambda = 1.4$, but for a decreasing NRG parameter the deviations on long timescales are increasing drastically. This finding meets the expectation we put forward in section 6.1.1: since a large value of Λ induces a clear separation of energy scales, the NRG works less accurate the smaller the NRG parameter is. Panel (b) of figure 6.2 shows CSM TD-NRG results, where more than just a single truncation has been applied, in comparison to exact results obtained via the CET for $N = 20$. For $\Lambda = 1.2$ we find that the deviation between the exact and NRG results is a lot larger than it was found in panel (a). This once more underlines the fact that the NRG does not work reliably for small values of Λ. On top of that the similarity of the NRG data for $N = 20$ and the exact data for $N = 12$ in panel (b) is striking. Bearing in mind that setting $N_k = 4096$ is equivalent to $m_0 = 12$ and therefore the two sets of data both include the same exact eigenstates, this observation points out that the contribution of the NRG steps after the first truncation is only a small correction on top of the exact results. We trace this finding back to the truncation of the central spin operators, resulting in an underestimation of all coupling constants that are

added after the first truncation. The data from figure 6.2 (b) for $\Lambda = 1.3$ show a very similar behavior for all three considered cases. This underlines the physical limitation on the NRG parameter: the fact that the exact results for $N = 12$ and $N = 20$ only deviate slightly from each other points out that the dynamics is heavily dominated by a small number of large coupling constants and thus the good agreement of the NRG calculations, that take the heavily dominant coupling constants exactly into account, is not surprising. On top of that the lack of a dense distribution of couplings prohibits the description of a realistic quantum dot and for this reason the investigation of large values of Λ is of limited interest. All in all the approach for a CSM TD-NRG based on the Wilson energy truncation seems not to be a promising candidate to tackle setups that are of experimental interest.

6.2.2 Central spin conserving truncation scheme

Panel (a) of figure 6.3 shows a small extract of the Hamiltonian's energy flow in a typical NRG run based on the central spin conserving truncation scheme. We restrain ourselves to a small number of kept states here, to be able to distinguish the individual energy levels with the bare eye, but in principle all discussed observations remain the same for a much larger number of kept states. Starting from the exact eigenstates of an untruncated Hamiltonian at $m = 7$, the Hamiltonian is first rotated into the subspaces of the kept and discarded states only, yielding new approximate eigenenergies that are also depicted in the figure. On the one hand, we find that most of the original eigenstates are reproduced appropiately and only a few pronounced deviations are observed. An unpleasant feature in the context of this finding is that most of the occuring deviations are found in the low energy regime, which is crucial for an adequately working TD-NRG procedure. On the other hand, it is striking that the central spin conserving truncation scheme always produces the same number of high and low energy states that are considered kept states, while all the discarded states lie in the middle of the spectrum. This finding is problematic for two reasons: (i) the NRG relies on the fact that the low energy states are the ones mainly driving the dynamics of a quantum system, i.e. the kept high energy states are mainly unnecessary baggage slowing down the procedure, and (ii) the spectral width is increasing exponentially with m, causing severe numerical problems for large spin baths.

The lower panels of figure 6.3 treat the calculations concerning $S(t)$, where we only took a single truncation of the Hamiltonian into account. We observe that none of the shown NRG runs yields an appropriate approximation for the exact central spin dynamics. As observed for the Wilson truncation scheme, panel (b) shows that the quality of the NRG calculations is slightly increasing for increasing Λ, but as discussed before this effect might be trivial, because $S(t)$ is heavily dominated by a small amount of bath spins in this regime that are treated exactly in the NRG. On top of that panel (c) reveals that even a pronounced increase of the truncation parameter β does not improve

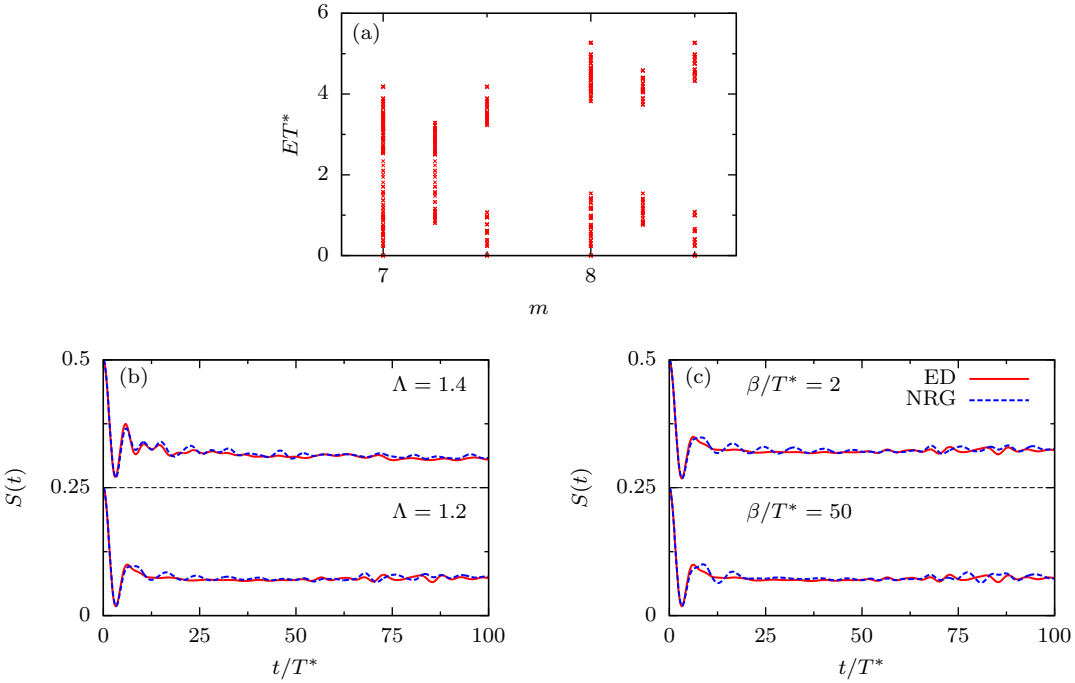

Figure 6.3: Data for the central spin conserving truncation scheme. We used the same choice for the coupling constants as in figure 6.2 for all calculations. Panel (a) shows a small extract of the energy flow for $\Lambda = 1.2$, $\beta/T^* = 10$ and $N_k = 128$. The first and second applied truncations are shown, where the points at $m = 7$ and $m = 8$ show the energy levels of the Hamiltonian right after a new spin has been added to the system and the shifted data points are the corresponding energy levels after rotating the Hamiltonian into either the subspace of the kept (at $m + 0.5$) or discarded (at $m + 0.25$) states. The lower panels show the time dependence of the correlation function $S(t)$ for the central spin conserving truncation scheme, where the solid red curves show results obtained by exact diagonalization (ED) and the blue dashed lines have been calculated using the NRG. For all TD-NRG runs $N_k = 2048$ was used, i.e. the Hamiltonian was only truncated once. The lower panels show a comparison between (b) two different values of the NRG parameter Λ based on $\beta/T^* = 10$ and (c) two different values of the truncation temperature β based on $\Lambda = 1.2$. As in figure 6.2 an offset has been added to distinguish the different calculations.

the obtained results noticeably. In conclusion, the central spin conserving truncation scheme significantly fails to reproduce $S(t)$ already for a single truncation. Since the eigenenergies of the Hamiltonian are crucial for the time evolution of any observable, the failure of the method most likely originates from the fact that the exact eigenstates are not sufficiently reproduced in the subspaces of the kept and discarded states. We conclude that if we were able to find a truncation scheme that fixes this problem and at the same time conserves the central spin, the realisation of an appropriate CSM TD-NRG might be possible. Anyhow we failed to find such a scheme until the present day.

Chapter 7

Hole Spin Dynamics

As argued in section 3.1.2, the spin dynamics of holes confined in semiconductor QDs is mainly driven by a dipole-dipole type interaction instead of the Fermi contact hyperfine interaction. The resulting Hamiltonian, that will be studied in the chapter at hand, is referred to as the anisotropic CSM and it is given by equation (3.14). In contrast to the ICSM, the anisotropic version has not been subject of numerous studies in the past. The publication that introduced the anisotropic CSM [56], also included the evaluation of the resulting central spin dynamics within a semi classical picture, according to the approach by Merkulov et al. [27]. Thus, the published analytical results are expected to be valid for the short time dynamics. The first section of the chapter at hand treats the Ising limit of the anisotropic CSM, which accounts for heavy holes. As discussed below, the Hamiltonian of this special case can easily be diagonalized analytically. Hence, the Ising limit will serve as reference to understand the central spin dynamics for the transition from the ICSM to the anisotropic CSM. The remainder of the chapter is structured similar as the preceding one: First, the hole spin dynamics in the absence of a magnetic field is discussed with respect to the anisotropy parameter λ. Second, the effect of an externally applied transversal magnetic field is investigated in detail. Since the effect of an externally applied longitudinal field is almost the same for holes as for electrons, this special case will only be briefly discussed. Finally, a comparison of the numerical findings within the anisotropic central spin model to recent experiments is discussed. As stated above, the numerical findings for spin-1/2 and 3/2 are qualitatively the same and also the variation of the model parameters m and d, that account for the QD geometry, yields no fundamentally new insight into the model's properties. As a consequence this chapter is restricted to spin-1/2 nuclei and the parameters $m = 2$ and $d = 3$. The majority of the results that will be presented within the chapter below have already been published in reference [97].

7.1 The Ising limit of the CSM

For the description of heavy hole spins in semiconductor QDs, the Ising limit of the CSM applies. It is given by the Hamiltonian

$$H_{\text{Ising}} = \omega_L \vec{n}_B \cdot \vec{S} + \sum_{k=1}^{N} A_k S^z I_k^z. \tag{7.1}$$

The dynamics of heavy holes confined in semiconductor QDs has been previously studied in references [31] and [54] for instance. In the following, we will first discuss the Ising limit of the CSM based on analytical arguments and will back the discussion up with numerical simulations afterwards.

7.1.1 Analytical treatment

Clearly, the central spin operator S^z is conserved within this model for $\vec{n}_B = \vec{e}_z$ or $\omega_L = 0$ and in these cases the spin noise function is trivially given by $S(t) = S(0)$. Hence, only the case $\vec{n}_B = \vec{e}_x$ needs to be treated in the following. Since the interaction term between the central spin and the bath spins does not introduce any spin flips of the nuclei, each nuclear operator I_k^z is a conserved quantity. I.e. the nuclear bath is static and fully determined by the configuration $\{m_k\}$ of the bath spin operators' eigenvalues. The eigenvalues of the Hamiltonian (7.1) for $\omega_L = 0$ can be written as

$$E^*(\sigma, \{m_k\}) = \sigma \sum_k A_k m_k = \sigma E^*(\{m_k\}), \tag{7.2}$$

where σ denotes the eigenvalue of S^z. Due to the conservation of I_k^z, the Hamiltonian matrix H_{Ising}, containing an added transversal field, decomposes into 2×2 subblocks for each configuration $\{m_k\}$. Diagonalizing these blocks yields the eigenvalues

$$E_\pm(\{m_k\}) = \pm \frac{\sqrt{\omega_L^2 + [E^*(\{m_k\})]^2}}{2}, \tag{7.3}$$

which correspond to the precession of the central spin in the effective magnetic field $\vec{B}_{\text{eff}} = (\omega_L, 0, E^*(\{m_k\}))^T$. The knowledge of the Hamiltonian's exact eigenenergies enables us to write down an exact analytical form for $S(t) = \langle S^z(t) \rangle_{\rho_{\text{pol}}}/2$. Therefor the initial polarized state $|\uparrow, \{m_k\}\rangle$ is expanded using the exact eigenstates $|\pm, \{m_k\}\rangle$ for a given configuration $\{m_k\}$:

$$|\pm, \{m_k\}\rangle = c_+(|\pm, \{m_k\}\rangle)\, |+, \{m_k\}\rangle + c_-\, |-, \{m_k\}\rangle\,. \tag{7.4}$$

The excitation energies of the system are given by $\Delta E(\{m_k\}) = \sqrt{\omega_L^2 + [E^*(\{m_k\})]^2}$ and averaging over these yields the time evolution

$$S(t) = S_\infty + \sum_{\{m_k\}} c_+^2 c_-^2 \cos(\Delta E(\{m_k\})t), \tag{7.5}$$

$$S_\infty = \sum_{\{m_k\}} \frac{1}{4}(c_+^2 - c_-)^2. \tag{7.6}$$

Since the number of elements in the occuring sum equals the Hilbert space dimension D, the evaluation of this result can not be realized for arbitrarily large systems, but for spin baths of the order $N \sim 20$ it is evaluated in a few seconds using a standard workstation without parallelization.

The semi classical estimate (5.3) for the non-decaying fraction S_∞ can also be applied to the Ising limit of the CSM, where the effective magnetic field is given by $\vec{B}_{\text{eff}} = (\omega_L, 0, E^*(\{m_k\}))^T$. For a spin initially polarized along the z-direction, an average over all nuclear configurations $\{m_k\}$ has to be applied to the z-component of the nonprecessing contribution $(\vec{e}_z \cdot \vec{n}_{B_{\text{eff}}})^2 S(0)$, yielding

$$\left\langle (\vec{e}_z \cdot \vec{n}_{B_{\text{eff}}})^2 \right\rangle_{\{m_k\}} = \left\langle \frac{[E^*(\{m_k\})]^2}{\omega_L^2 + [E^*(\{m_k\})]^2} \right\rangle_{\{m_k\}}. \tag{7.7}$$

For large magnetic fields this term approaches the value $1/4b^2$, while in zero magnetic field $\langle (\vec{e}_z \cdot \vec{n}_{B_{\text{eff}}})^2 \rangle_{\{m_k\}} = 1$ is obtained. As mentioned above, Testelin et al. [56] have extended the SCA to the anisotropic CSM and in the limit of strong external fields the result

$$E_z(\tau) = \frac{1}{4}\left[\frac{\cos(4b^2\tau + \frac{1}{2}\arctan(\tau))}{(1+\tau^2)^{1/4}} + \frac{1}{4b^2}\left(1 - \frac{\cos(4b^2\tau + \frac{3}{2}\arctan(\tau))}{(1+\tau^2)^{3/4}}\right)\right] \tag{7.8}$$

is obtained for the Ising limit $\lambda \to \infty$, where the timescale $\tau := t/4bT^*$ has been introduced. This estimate is clearly in good agreement with the claim $S_\infty = S(0)/4b^2$ from equation (7.7). The analytical result consists of two oscillatory contributions governed by the Larmor frequency ($4b^2\tau = \omega_L t$) accompanied by a phase shift term and two envelope functions $\propto (1+\tau^2)^{-1/4}$ and $\propto (1+\tau^2)^{-3/4}$. The power law form of the spin noise functions' decay can also be derived by averaging the central spin's precession for one given nuclear state $\{m_k\}$ over all possible configurations, using a Gaussian distribution of the nuclear field [54]. Note that equation (7.8) implies an increase of the coherence time for increasing b. Since no decay of $S(t)$ occurs at all for $b = 0$ this is not a necessarily intuitive finding, but it can be understood from the suppression of the nuclear field fluctuations for large external fields.

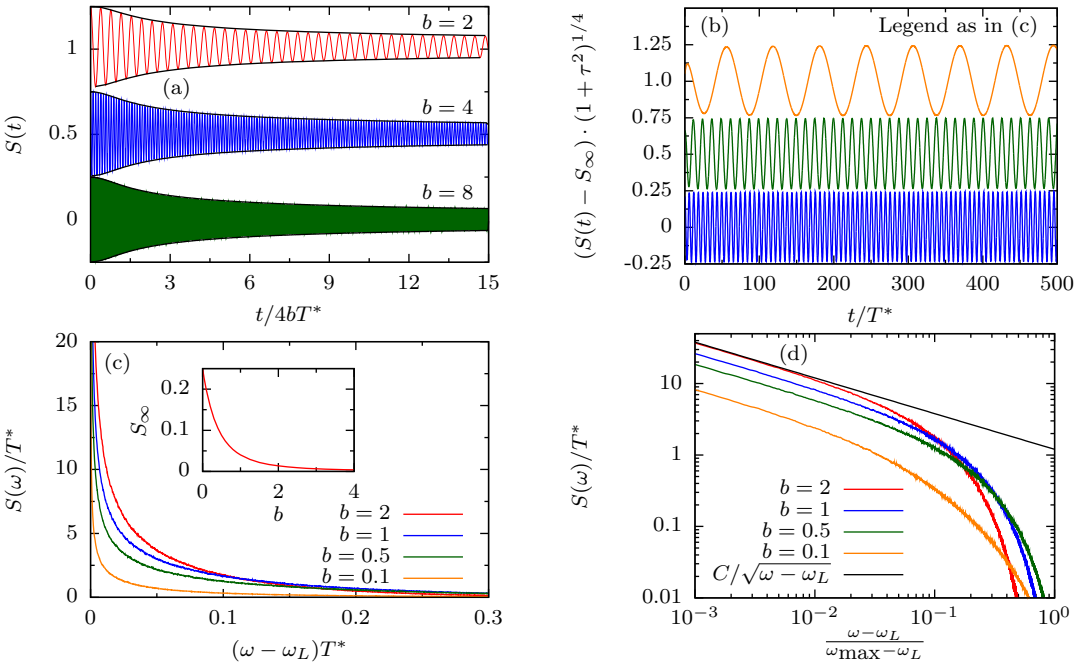

Figure 7.1: Illustration of the spin noise function for the Ising limit $\lambda \to \infty$ of the CSM. $N = 18$ bath spins have been considered for each presented curves and the cutoff $r_0 = 1.5$ has been used. Panel (a)-(b) show $S(t)$, based on $n = 20$ sets of coupling constants, for various values b of the external magnetic field, where the dimensionless timescale $\tau := t/4bT^*$ has been introduced. The black lines in panel (a) indicate the envelope of the analytical prediction $E_z(\tau)$ as defined in equation (7.8). Panel (b) reveals that the power law decay $\propto (1+\tau^2)^{1/4}$ also holds for small external fields. An offset of 0.5 has been added to distinguish the individual curves. Panel (c)-(d) treat the spectral function $S(\omega)$, where the frequency axis is shifted by ω_L. Both panels show the same results, which have been obtained from an exact Fourier transformation of equation (7.5). The inset of panel (c) shows the spectral weight S_∞ of the δ-peak occuring at $\omega = 0$, which is not included in the illustration of $S(\omega)$. Panel (a) corresponds to figure 9, panel (c) to figure 10 of reference [97].

7.1.2 Numerical discussion

Figure 7.1 presents numerical results for the spin noise function in the real time and the spectral regime within the Ising limit of the CSM. Panel (a) shows $S(t)$ in the regime of large external fields $b > 1$. The added black lines depict the envelope of the analytically estimated function $E_z(\tau)$, which reproduces the decay of the numerical results excellently. I.e. the simulations state a power law decay $\propto t^{-1/2}$ of $S(t)$ in the regime of large external fields, that is fully governed by the timescale $\tau = t/4bT^*$. Our findings also imply, that the SCA describes both the short and long time dynamics of the central spin correctly within the Ising limit. Panel (b) of figure 7.1 addresses the long time behavior of the central spin for small external fields $b \leq 1$, for which no closed expression of $S(t)$ within the SCA exists. The presented numerical results are rescaled by the factor $(1+\tau)^{1/4}$ to reveal that the predicted power law for the long time

decay also holds in the limit of small external fields, but we stress that the prediction (7.8) does not reproduce the exact shape of $S(t)$ for $b \ll 1$ anymore.

From the above introduced excitation energies of the Hamiltonian H_{Ising}, which are given by $\Delta E(\{m_k\}) = \sqrt{\omega_L^2 + [E^*(\{m_k\})]^2}$, we can immediately deduce central properties of $S(\omega)$: (i) apart from the contribution at $\omega = 0$, there is a finite threshold frequency ω_{th} for which $S(0 < \omega < \omega_{\text{th}}) = 0$ holds, (ii) due to the definition of $E^*(\{m_k\})$ the limit $\lim_{N\to\infty} \omega_{\text{th}} = \omega_L$ must hold and (iii) since the largest excitation frequency is fiven by $\omega_{\text{max}} = \sqrt{\omega_L^2 + A_s^2/4}$, the statement $S(\omega_{\text{max}} > 0) = 0$ must hold. It is stressed that the occuring gap in the spectral function prevails in the thermodynamic limit and its width is solely set by the Larmor frequency. Panels (c)-(d) of figure 7.1 treat the spectral spin noise function $S(\omega)$ and both include the exact same sets of data depicted on (a) a linear and (b) a double logarithmic scale. The numerical results are shifted by the Larmor frequency to stress the threshold behavior of $S(t)$. The spectral weight of the δ-peak occuring at 0 frequency, which is not included in the frequency range of the figure, is depicted in the inset of panel (c). The added black line in panel (d) shows a fit $\propto 1/\sqrt{\omega - \omega_L}$. Apparently the spectral function near the threshold frequency can be approximated nicely by such a power law, although the accuracy of the fit decreases for $b \to 0$. This loss of accuracy stems from the fact that $S(\omega)$ is dominated by the non-decaying fraction in this regime and accordingly only a small portion of the spectral weight occurs at finite frequencies. The applied $1/\sqrt{\omega - \omega_L}$ fit corresponds to a long time decay proportional to $1/\sqrt{t}$ [97], which corresponds to the prediction of $E_z(\tau)$, but is found independently of the external field strength.

7.2 Dynamics in the absence of a magnetic field

So far the spin dynamics of heavy holes ($\lambda \to \infty$) and electrons ($\lambda = 1$) have been discussed in detail. In contrast to the Ising limmit of the CSM, the case of light holes ($\lambda = 1/2$) does not include comparable unique features and therefore it is discussed along with the general case of light and heavy hole mixing in the following. In the absence of a magnetic field, the decay of $S(t)$ is solely induced by the flip-flop term, whose magnitude in the general Hamiltonian (3.14) is scaling with $1/\lambda$. I.e. the decay of the spin noise function is expected to occur slower for increasing λ, which is in accordance to the definition of the intrinsic timescale T_λ^*. Since $S(t) = S(0)$ holds in the Ising limit of the CSM, also the steady state value S_∞ is expected to increase monotonically with λ, because a crossover behavior from the real time dynamics for $\lambda = 1$ to those for $\lambda \to \infty$ is expected. Figure 7.2 (a) shows $S(t)$ for various values of the anisotropy parameter λ. Apparently, the location of the minimum occuring at $t/T_\lambda^* \approx 4$ remains almost invariant, although its characteristic form, as described by $S_{\text{SCA}}(t)$, vanishes for large λ. The expected increase of $S(t)$ on all timescales is also clearly observed. In general the obtained curves basically interpolate between the limit

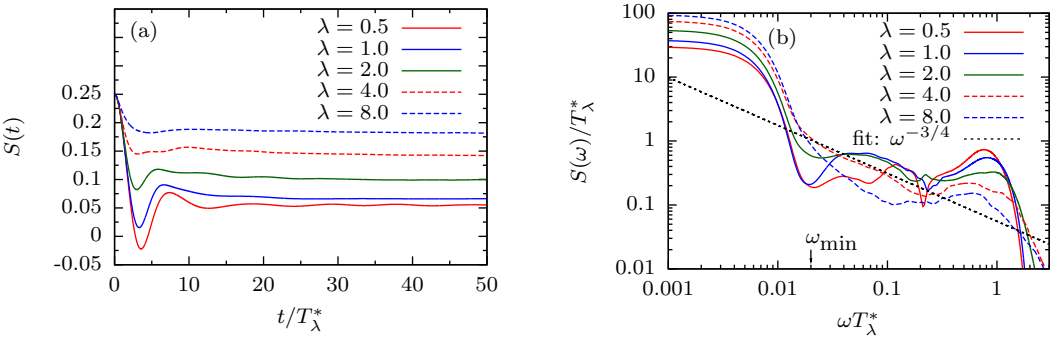

Figure 7.2: Impact of the anisotropy factor λ onto the spin noise function without an externally applied field. Panel (a) shows a λ scan addressing the real time dynamics $S(t)$. Panel (b) shows the spectral spin noise function on a double logarithmic scale. The smallest reliably resoluted frequency ω_{min} is indicated on the ω-axis. E.g. for $\lambda = 8$ this resolution implies considering $N_c = 6113$ polynomials in a single simulation. The black dashed line represents a power law fit $\propto \omega^{-3/4}$. All shown simulations are based on $n = 50$, $N = 18$ and $r_0 = 1.5$.

of light and heavy holes. Figure 7.2 (b) shows the corresponding spectral spin noise function $S(\omega)$ focusing on the real time dynamics in the intermediate regime. Corresponding to the observed increase of S_∞, the spectral weight of the short time peak occuring at $\omega T^*_\lambda \approx 1$ is decreasing rapidly with an increase of λ and, as observed for the time resolved calculations, its shape is broadened for large anisotropy. Due to the conserved sum-rule, that applies for all calculated spectra, it is clear that the decreasing spectral weight at large frequencies must be shifted to smaller frequencies, but it is not clear wether it is only transferred into the δ-peak at $\omega = 0$ or also an increase of the total spectral weight in the intermediate regime is obtained. In panel (b) of figure 7.2, where the reliable resolution of the CET is given by $\omega T^*_\lambda = 0.02$ for all presented calculations, a clear gap between the resolution-broadened peak at zero frequency and the shoulder at $0.03 \leq \omega T^*_\lambda \leq 0.2$ is observed for $\lambda = 1/2$ and $\lambda = 1$. For larger values of λ this gap is filled increasingly and, within the warranted resolution, for $\lambda \geq 4$ the zero and intermediate frequency features are merging such that no gap can be identified anymore. At the same time, the amplitude of the shoulder is decreasing between the high frequency peak and the position of the gap. This finding implies that the suppression of the spin-flip terms in the anisotropic CSM pushes the long time decay of $S(t)$ to larger times than implied by the intrinsic timescale T^*_λ. I.e. the linear elongation of the central spin dynamics only holds on short timescales and the longtime decay is suppressed even stronger than linearly. This can be understood within the semi classical picture: the initial decay of $S(t)$ is fully described by the central spin's interaction with a frozen spin bath, while the long time decay is influenced by the slow dynamics of the bath spins that acts back onto the electron. This indirect process clearly only contributes in higher orders of the hyperfine interaction and is therefore governed by higher orders of λ. This is also in accordance with the rapid drop of the intermediate

frequency shoulder for $\lambda = 1/2$ compared to $\lambda = 1$. Still, it is noticeable that a power law fit $\propto \omega^{-3/4}$ appears to describe the intermediate regime of $S(\omega)$ adequately up to $\lambda = 4$, which is in accordance to the argument by Chen et al. [30] that only relies on the distribution of the coupling constants A_k. It is unclear wether the observed deviation from this estimate for $\lambda = 8$ is a physical effect or if it stems from the limited resolution. I.e. the expected power law might occur on smaller frequencies, which are beyond the resolution of the applied method.

7.3 Dynamics within an external magnetic field

Before going into detail on the hole spin dynamics in an external magnetic field, a word concerning the field strength parameter $b = \omega_L T_1^*$ is in order. As demonstrated in the preceding section, the influence of the hyperfine interaction onto the decay of the spin noise function $S(t)$ is governed by T_λ^*. When the CSM Hamiltonian is rescaled by this timescale, one obtains

$$H_{\mathrm{CSM}} T_\lambda^* = \lambda b \vec{S} \cdot \vec{n}_B + \sum_{k=1}^{N} A_k T^* \left(\lambda S^z I_k^z + (S^x I_k^x + S^y I_k^y) \right). \tag{7.9}$$

Hence, the discussion wether the external field is weak or strong compared to the hyperfine interaction, depends on the orientation vector $\vec{n}_B$. For a longitudinal external field b must be compared to $A_s T^*$, as for the isotropic case, and for transversal fields the product λb needs to be considered instead. Thus, in the latter case, we speak of a strong external field, when $\lambda b > 1$ holds and the weak field limit is defined accordingly. Since the effect of an externally applied longitudinal field is independent of the parameter λ and its main impact is, as for the isotropic CSM, to preserve the spin noise function from decaying, no new physics is found for the case $\vec{n}_B = \vec{e}_z$ and consequently it is not discussed further in the following. Instead, we limit ourselves to the treatment of transversal magnetic fields in the remainder of this section.

7.3.1 Transversal external fields

Testelin and coworkers [56] have presented an analytical estimate for the central spin dynamics within the SCA, that is supposed to apply for large external fields $b \gg 1$. It reads

$$\begin{aligned} E_{xy}(t) = \frac{1}{16b^2} + \left(1 - \frac{1}{4b^2} + \frac{\lambda^{-4} + 2\lambda^{-2} - 3}{4b^2} \left(\frac{t}{2T^*}\right)^2\right) \cos(\omega_L t) \exp\left[-\frac{1}{2}\left(\frac{t}{2T_\lambda^*}\right)^2\right] \\ - \frac{\lambda^{-2} + 1}{8b} \frac{t}{T^*} \sin(\omega_L t) \exp\left[-\frac{1}{2}\left(\frac{t}{2T_\lambda^*}\right)^2\right]. \end{aligned} \tag{7.10}$$

The time dependent part of this estimate is clearly damped by a Gaussian envelope function that corresponds to equation (5.20), where only T^* is replaced by T^*_λ. I.e. for the limit of large external fields, which is, as discussed above, realized if the condition $\lambda b > 1$ is fullfilled, this analytical estimate suggests a decay of the central spin that is identical to the isotropic case and the anisotropy parameter λ only influences the timescale of the occuring Gaussian decay. In section 7.1 it has been demonstrated that the Ising limit of the CSM features a significantly different decay $\propto t^{-1/2}$ of $S(t)$ than predicted by equation (7.10), for which Testelin et al. accounted by the introduction of the estimate (7.8), that only holds for the Ising limit. Within this semi classical picture of the central spin dynamics, no crossover regime between the Ising limit and the isotropic case arises. Panel (a) of figure 7.3 shows a direct comparison between results obtained via the CET and the analytical prediction from equation (7.10). Among the panel the magnetic field $b = 10$ is kept constant, while the anisotropy parameter takes the values $\lambda = 2$ and $\lambda = 10$. Both sets of parameters clearly fullfill the introduced condition for a large external field. Nevertheless we find good agreement between the two claims for $\lambda = 2$, while the semi classical estimate deviates significantly from the numerical results for $\lambda = 10$. This finding indicates that the estimate (7.10) does not hold for large external fields in general, but it also puts forward that the magnitude of the ratio b/λ might be relevant for $S(t)$. Figure 7.3 (b)-(c) addresses the impact of this ratio onto the envelope of $S(t)$ in greater detail. In panel (b) the magnetic field strength b is varied keeping the anisotropy parameter $\lambda = 10$ constant and in panel (c) a λ-scan is applied for fixed $b = 4$. The added Gaussian envelope functions $\propto \exp[-(t/T^*_\lambda)^2/8]$ serve as reference for the spin decay in the isotropic CSM. Clearly the Gaussian envelope describes the decay of $S(t)$ adequately for $b/\lambda \geq 1$, while the deviations from it increase with decreasing ratio $b/\lambda < 1$. For its smallest presented value $b/\lambda = 1/25$ the deviations are very pronounced. Namely, the initial decay of the spin noise function occurs much faster than suggested by the Gaussian decay, but on large timescales its lifetime is increased significantly. The observed dependency of the central spin dynamics on the ratio b/λ can be understood within a very intuitive physical picture: if a very large magnetic field along the x-direction is applied, the contribution of the model Hamiltonian along the z-direction is suppressed. As a consequence the central spin does not feel the presence of anisotropy and behaves as in the ICSM, but since the impact of the spin operators acting in the $x-y$-plane is decreasing linearly with λ, the required magnitude b of the magnetic field, that is mandatory to suppress the anisotropy, increases with λ.

Although it is not demonstrated in a separate panel here, note that the envelope of $S(t)$ is truly fully governed by the ratio b/λ. E.g. panel (b) of figure 7.3 involves numerical results for $b = 2$, $\lambda = 10$, while panel (c) features data for $b = 4$, $\lambda = 20$ and both obtained curves feature the exact same envelope function. To illustrate the crossover from large to small values of the ratios b/λ further, panel (d) of figure 7.3

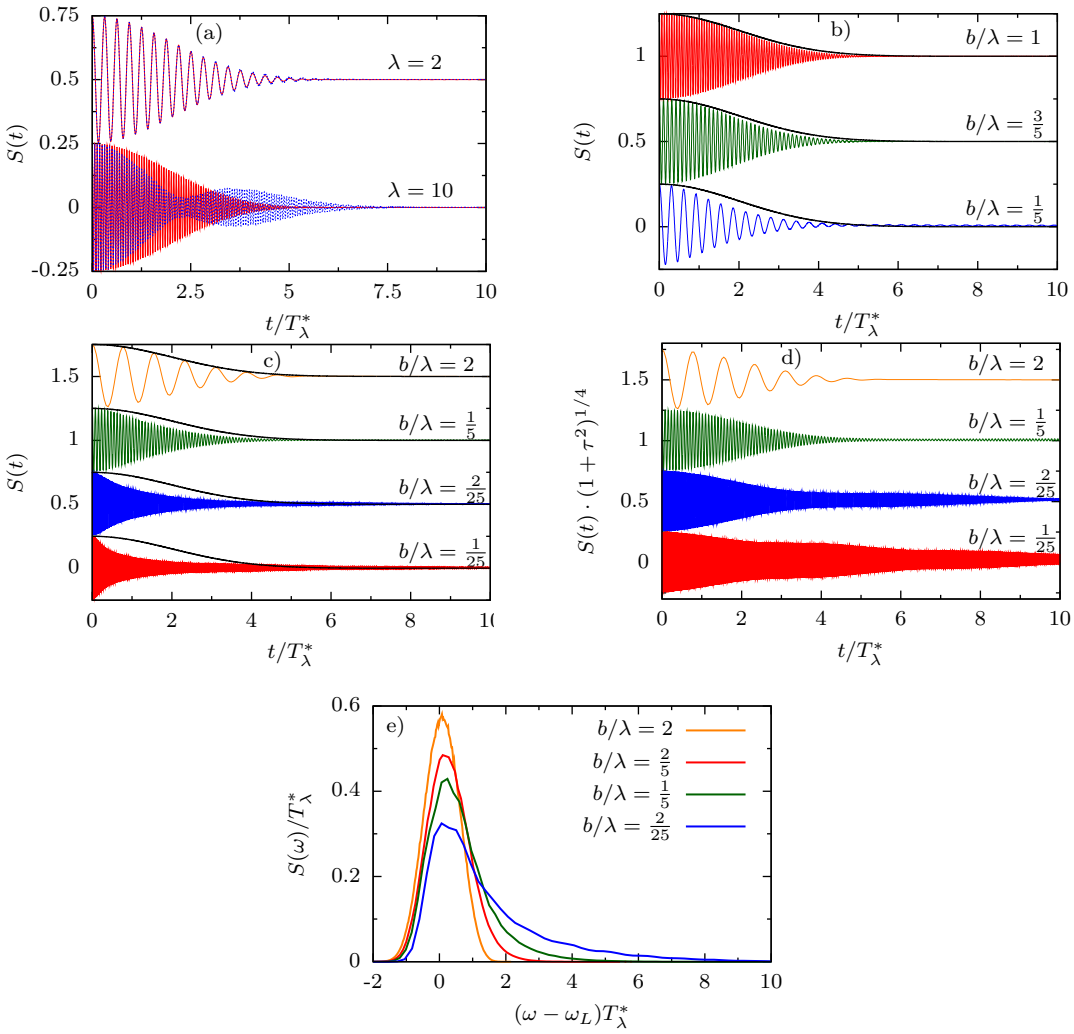

Figure 7.3: Illustration of the hole spin dynamics in the presence of a transversal magnetic field. The parameters $n = 50$, $N = 18$ and $r_0 = 1.5$ hold for all presented results. An offset of 0.5 has been added to distinguish between neighbouring curves in panels (a)-(d). Panel (a) shows a comparison between the analytical prediction of equation (26c) of reference [56] (blue) and numerical results obtained via the CET (red) for $S(t)$. The field strength $b = 10$ applies for all curves, while the anisotropy parameter λ is varied. Panels (b)-(c) also depict numerical results concerning $S(t)$ for a variation of the ratio b/λ, where in panel (b) $\lambda = 10$ and in panel (c) $b = 4$ is kept constant. The envelope function $\frac{1}{4}\exp[-(t/T^*_\lambda)^2/8]$ has been added to the individual curves to reveal the occuring deviations from the observed spin dynamics in the ICSM. Panel (e) shows the spectral spin noise function $S(\omega - \omega_L)$ also for constant $b = 4$. The number of considered Chebyshev polynomials has been determined such that the same resolution is guaranteed for all shown curves. All panels are based on figures 12-14 of reference [97].

presents the rescaled spin noise function $S(t) \cdot (1+\tau^2)^{1/4}$ for the exact same set of data as panel (c), a depiction of $S(t)$ that corresponds to panel (b) of figure 7.1, where the rescaled fluctuation function has been found to remain invariant for large times. Considering this invariant behavior and the Guassian envelope function from the ICSM as reference, the crossover from the isotropic to the anisotropic case is clearly revealed and we find three different regimes of the occuring decay: (i) for large ratios $b/\lambda \geq 1$ the envelope of $S(t)$ is clearly given by the Gaussian function. (ii) For small values $b/\lambda \ll 1$, corresponding to the Ising regime, a power law decay $\propto t^{-1/2}$ dominates the central spin dynamics on large timescales and (iii) in the intermediate regime $b/\lambda \sim O(0.1)$ the short time decay deviates from the Gaussian envelope function, which still describes the long time tail of $S(t)$ adequately. Note that concerning the analytical prediction (7.10) our findings suggest that it is not valid for the limit of large external fields $b \gg 1$ as stated in reference [56], but for the limit of large ratios $b/\lambda \gg 1$ instead.

The results for the spectral spin noise function, that are depicted in figure 7.3 (e), clearly reflect the observed crossover from the isotropic to the anisotropic limit. Since the latter extreme case features a strict threshold, which is given by the Larmor frequency, behavior that also holds in the thermodynamic limit, the presented spectra are shifted by ω_L. As demonstrated for the ICSM, the Gaussian peak that occurs for $b/\lambda = 2$ is centered at $\omega^* = \sqrt{b^2 + 1/2}$ instead of ω_L. While the position of the peak's maximum remains approximately invariant for all depicted results, the spectral weight left of the Larmor frequency is decreasing monotonically with b/λ and, according to the expected threshold behavior for $\lambda \to \infty$, it is shifted to the right side of ω_L. I.e. the symmetric form of $S(\omega)$ for $b/\lambda > 1$ is replaced by the fully asymmetric threshold shape step by step. It is stressed that $\lambda = 100$ holds for the smallest presented ratio $b/\lambda = 2/25$ and depicting $S(\omega)$ versus ωT^* instead of ωT^*_λ yields a very sharp peak near the threshold ω_L corresponding to a very large lifetime of the central spin in the anisotropic limit.

So far the dynamics in a strong $\lambda b > 1$ transversal field have been discussed in detail. In the opposite scenario of a small transversal field, characterized by the condition $\lambda b \ll 1$, the central spin already experiences decoherence induced by the spin bath before a whole Larmor precession occurs. Hence, the short time dynamics of the central spin in this regime is identical to the magnetic field free case, that has been presented in figure 7.2. After the characteristic initial decay on the timescale T^*_λ, $S(t)$ will approach zero on a large time interval that is governed by ω_L/λ. This long time evolution is analogous to the decay of $S(t)$ in the ICSM and has been demonstrated in panel (d) of figure 5.7. Consequently combining the observed effects from figures 7.2 (a) and 5.7 (d) fully describes the long and short time behavior of $S(t)$ in the weak field limit of the anisotropic CSM. Thus no results concerning this regime are presented here.

7.4 Reference to recent experiments

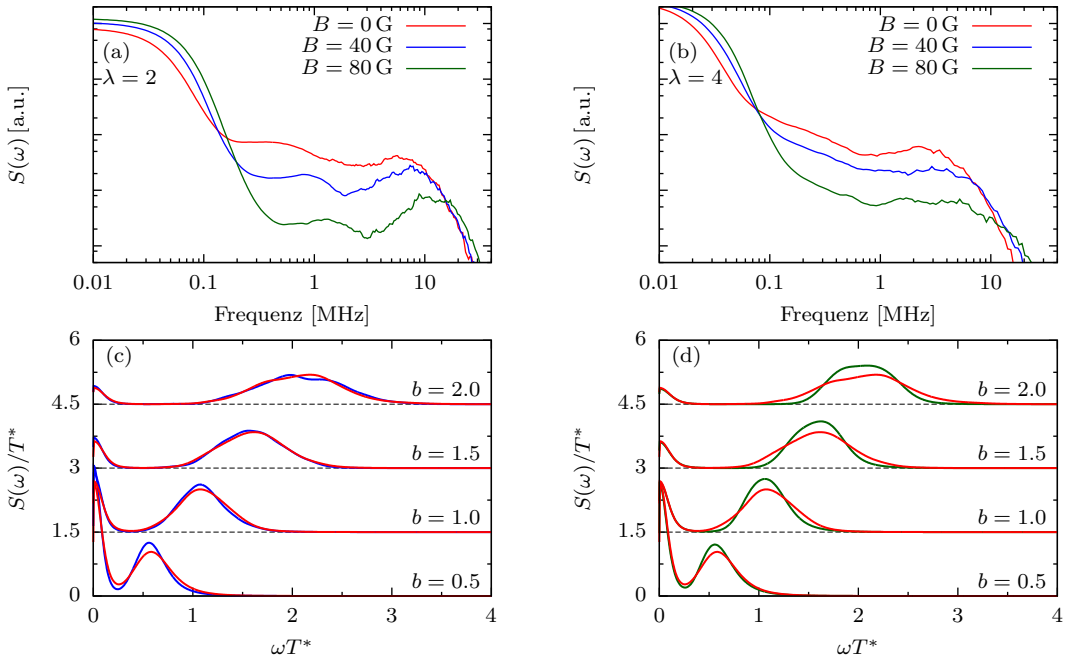

Figure 7.4: Illustration of the ensemble averaged spectral spin noise function $S(\omega)$ based on simulations within the anisotropic CSM in the experimtally relevant regime. Concerning the timescale T^*, the same procedure for the ensemble average has been applied as described in figure 5.9. Panels (a)-(b) depict numerical results for various longitudinal external fields on a double logarithmic scale, where (a) $\lambda = 2$, $N_c = 2000$ or (b) $\lambda = 4$, $N_c = 4000$ has been considered and results of $n = 100$ individual setups have been averaged. The average intrinsic hole spin fluctuation timescale has been assumed to be given by $\overline{T}^* = 10\,\mathrm{ns}$. As for panel (c), the spread of g-factors is modeled by a Gaussian probability distribution with the standard deviation $\Delta g/g = 0.2$ and the average hole g-factor $\overline{g}_h = 0.15$. Panels (c)-(d) treat the case of transversal external fields, where $N_c = 50$ and $n = 500$ applies for all presented curves. The solid red curves are identical in both panels and are based on $\lambda = 5$. In panel (c) these results are compared to calculations for $\lambda = 50$ (solid blue), while for the solid green curves also $\lambda = 5$ has been assumed, but the underlying g-factor spread is obtained from a uniform probability distribution $g_i/g \in [0.8, 1.2]$. For panels (c)-(d) an offset of 1.5 has been added to distinguish the individual curves. Further parameters: $d = 3$, $m = 2$, $r_0 = 1.5$ and $N = 18$. Panels (c)-(d) are based on figure 16 from reference [97], but show different sets of data.

To bridge between the findings of the preceding chapter and recent experiments on ensembles of p-doped QDs, the occuring variation of the intrinsic timescale T^*, which enters the performed simulations as described in section 5.3, and the hole g-factors in ensembles of QDs is considered in the following. The g-factor spread is assumed to obey a Gaussian probability distribution with the standard deviation $\Delta g/g = 0.2$. Panels (a)-(b) of figure 7.4 address the central spin dynamics in zero and longitudinal magnetic fields for two different choices of the anisotropy parameter λ. For the

average intrinsic timescale we assume $\overline{T}^* = 10\,\text{ns}$ and the average hole g-factor is set to $\overline{g}_h = 0.15$. When turning from $\lambda = 2$ to $\lambda = 4$ the entire spectrum is shifted to smaller frequencies, indicating an enhancement of the central spin coherence time for increasing λ as also suggested by the definition of the intrinsic timescale T^*_λ. According to the findings for electron spins in longitudinal magnetic fields, the spectral weight of $S(\omega)$ at large frequencies is clearly decreasing faster than linearly and a corresponding increase of the peak at zero frequency is found. Comparing the results from panels (a)-(b) to recent measurements on an ensemble of hole doped InGaAs QDs [64] reveals striking deviations between the experimental and numerical results. Namely figure 7.4 corresponds to figure 3 (b) of reference [64], where an approximately Lorentzian lineshape of the spin noise function is found for $b = 0$, that transforms into a $1/f$ behavior in the intermediate frequency regime with increasing longitudinal field strength. We stress that the experimentally found behavior of $S(\omega)$ is not reproduced by the applied simulations in any fashion. This pronounced mismatch between numerics and experiment points toward an incompleteness of the considered theory, which will be enhanced by the quadupole Hamiltonian in the chapter below.

Figure 7.4 (c)-(d) addresses the hole spin noise within a transversal external field. Due to the spread of the hole g-factors, the width of the peak occuring near the Larmor frequency is, in contrast to the case of n-doping, increasing with the field strength b. This effect is rather trivial and was also observed in recent experimental measurements [59]. In section 7.3.1 it has been demonstrated that an increase of λ at constant b induces a crossover from a symmetric Gaussian peak to an asymmetric threshold behavior at the Larmor frequency. Also the width of these peaks is decreasing for increasing λ if the results are depicted on the scale ωT^*. The direct comparison of numerical data for $\lambda = 5$ and $\lambda = 50$ in figure 7.4 (c) demonstrates, that the pronounced asymmetry and decreasing width of the underlying spectra of the individual QDs are smoothened out by the applied ensemble average. Of course this effect is strongest for large values of b, while the signature of the individual spectra is still visible for $b \leq 1$. This observation puts foward that the measurement of hole spin noise on an ensemble of QDs in a transversal field, primarily yields information on the distribution of the g-factor spread of the sample instead of the properties of the confined particles. To underline this statement, figure 7.4 (d) compares spin noise spectra for two different assumptions concerning the spread of the hole g-factors: the red lines, that are identical to panel (c), are based on a Gaussian spread and the green lines on a uniform probability distribution in the interval $g_i/g \in [0.8, 1.2]$. Apart from these assumptions the compared sets of parameters are identical. The direct comparison reveals that the spin noise function for $b \gg 1$ is expected to be solely governed by the underlying distribution function of the g-factor spread, that also affects the obtained spectra for small external fields, which still mirror some basic properties of the underlying individual QDs. I.e. the measurement of spin noise in the absence of an external field reveals

most information on the physical properties of an individual hole spin confined in a semiconductor QD.

7.5 Chapter conclusion

In the preceding chapter it has been demonstrated that the short time dynamics of hole spins confined in semiconductor QDs in the absence of a magnetic field is governed by the timescale T_λ^* and the long-term decay, which appears to be of a logarithmic form as for the isotropic case, of $S(t)$ is enhanced stronger than linearly in λ. Also the Ising limit, accounting for heavy holes, of the CSM model has been discussed in detail, for which the spin noise function is trivial if no transversal magnetic field is applied. In this limit the eigenvalues of the Hamiltonian are known a priori, a power law $\propto t^{-1/2}$ holds for the long time evolution of $S(t)$ and the spectral spin noise function features a threshold behavior.

We have argued that a longitudinal as well as a weak transversal external field does not introduce new physical effects compared to the ICSM. For $\vec{n}_B = \vec{e}_x$ the parameter λb distinguishes wether an external field is strong or weak compared to the influence of the hyperfine interaction onto the central spin. In the limit of large external fields the envelope of $S(t)$ is dictated by the ratio b/λ and a crossover between a Gaussian, which also accounts for electrons, to a power law decay, which accounts for heavy holes, is observed. The results of recent experiments [64] on an ensemble of hole doped InGaAs QDs in zero and a longitudinal external field can not be reproduced within the anisotropic CSM. Due to the large spread of the hole g-factors and the large lifetime of hole spins within the CSM, the measurement of hole spin noise on an ensemble of QDs in a transversal field is expected to primarily yield information about the distribution of the g-factors.

Chapter 8

Influence of the Quadrupole Interaction onto the Confined Spins

Due to the mismatch between the predictions of the anisotropic CSM and recent experimental findings, the influence of EFGs coupling to the quadrupole moment of the nuclei is investigated in the chapter below. The importance of this interaction has been put forward by Sinitsyn and coworkers [63], who also applied a semi classical treatment of the model to demonstrate the qualitative effect of the quadrupolar couplings (QCs). In this context they introduced an effective model, replacing the quadrupole Hamiltonian (3.29), that also applies for nuclei with spin-1/2. The focus of the chapter at hand is to treat the quadrupolar interaction in detail and for this purpose it can be notionally split into two parts. The first one contains a detailed discussion of the influence onto $S(t)$ of all the system parameters entering the quadrupole interaction. In this context also a comparison between the effective and the original model for the QCs is discussed. In the second part of the chapter we bridge towards the results of recent experiments, discuss realistic values of the model parameters and how they are influenced by the structure of the underlying QDs. This part of the chapter grants detailed insight into the findings of various experiments and unifies some findings that seem to contradict each other on first sight. Some of the following results have already been published in reference [65].

8.1 Effective model for spin-1/2

As mentioned in the introduction, Sinitsyn et al. [63] introduced an effective model that allows a treatment of the quadrupole interaction considering spin-1/2 nuclei, giving access to larger spin baths in numerical calculations. The authors claimed that the effective Hamiltonian is capable of reproducing the central spin dynamics which is

obtained by taking the full quadrupole Hamiltonian (3.29) into account. The effective quadrupole Hamiltonian reads

$$H_{Q,\text{eff}} = \sum_{k=1}^{N} q_k \vec{I}_k \cdot \vec{n}_k, \tag{8.1}$$

where the quadrupolar term is mimiced by magnetic fields applied to each nuclear spin individually and the asymmetry parameter η is set to zero. The purpose of the section at hand is twofold: (i) We discuss the viability of the effective Hamiltonian $H_{Q,\text{eff}}$ by putting forward analytical arguments and comparing numerical results. (ii) Since the quadrupolar orientation vector $\vec{n}_k$ will turn out to play an important role in the comparison of the Hamiltonians (3.29) and (8.1), we investigate its influence on the central spin dynamics in detail in this context. With respect to reference [63] we will also restrict ourselves to the case $\eta = 0$ in this section.

8.1.1 Analytical discussion

In the previous chapters we discussed the correlation function $S(t)$ within the CSM intensively. Now we study the influence of an additional term that is added to the Hamiltonian, namely H_Q or $H_{Q,\text{eff}}$ respectively. One of the most common ways to approach such a modification is to set up a perturbation theory, that might grant insight into the dynamics for a small parameter Q_r on both an analytical and numerical level. Such a perturbation theory relies on an exactly solved Hamiltonian, that is enhanced by a complex interaction term. In our case this precondition is not fullfilled, because there is no closed form for an exact solution of the CSM. Thus we take a different route to gain an intuition concerning the influence of H_Q and $H_{Q,\text{eff}}$. Namely, we exploit the series expansion of the time evolution operators in $\langle S^z(t)S^z\rangle = \left\langle e^{iHt}S^z e^{-iHt}S^z\right\rangle$ as demonstrated in equation (3.37). To explicitly calculate higher order commutators of the form $\langle [H,S^z]_n S^z\rangle$, we need to specify the orientation vectors $\vec{n}_k$. For simplicity we restrict ourselves to a system where all quadrupolar moments are fixed along the z-direction for the moment. Evaluating equation (3.37) for the simplified case $\vec{n}_k = \vec{e}_z$ and the usual density operator $\rho_0 = \frac{1}{D}\underline{\underline{1}}$ up to fourth order in time yields

$$H_{Q,\text{eff}}: \quad S(t) = \frac{1}{4} - \frac{1}{16}\left(\frac{t}{T^*}\right)^2 + \frac{5}{768}\left(\frac{t}{T^*}\right)^4 + \frac{t^4}{192}\sum_k q_k^2 A_k^2 \tag{8.2}$$

$$H_{Q}: \quad S(t) = \frac{1}{4} - \frac{1}{16}\left(\frac{t}{T^*}\right)^2 + \frac{5}{768}\left(\frac{t}{T^*}\right)^4 + \frac{t^4}{16}\sum_k (q_k^2 A_k^2 - q_k A_k^3), \tag{8.3}$$

where we neglected contributions proportional to $\sum_k A_k^4$, because for large systems they are small compared to the competing terms proportional to $(T^*)^{-4}$. Note that the first three terms, that are identical for H_Q and $H_{Q,\text{eff}}$, reproduce the Taylor series of the

analytical solution by Merkulov et al. [27] up to fourth order. On top of that we find that both analytical predictions feature additive contributions proportional to $\sum_k q_k^2 A_k^2$, while only for the latter case the subtractive term $\sum_k q_k A_k^3$ occurs, i.e. the effective model tends only to protect the central spin's polarisation while the usual model also features a destructive term for $\vec{n}_k \parallel \vec{e}_z$. This finding is in good agreement with a rather intuitive argument: writing down the operators I_k^z and $(I_k^z)^2$ in their eigenbasis for spin-3/2

$$I_k^z = \begin{pmatrix} 3/2 & 0 & 0 & 0 \\ 0 & 1/2 & 0 & 0 \\ 0 & 0 & -1/2 & 0 \\ 0 & 0 & 0 & -3/2 \end{pmatrix} \qquad (I_k^z)^2 - \frac{I(I+1)}{3} = \begin{pmatrix} 1 & 0 & 0 & 0 \\ 0 & -1 & 0 & 0 \\ 0 & 0 & -1 & 0 \\ 0 & 0 & 0 & 1 \end{pmatrix} \tag{8.4}$$

points out that the quadrupolar contribution in the effective Hamiltonian sets a preferred orientation for each nuclear spin, e.g. spin flips of the bath spins and in consequence also of the central spin are proceedingly suppressed for an increasing value of Q_r. For H_Q this is not the case, since the only preference indicated by $(I_k^z)^2$ is in favor of the states $|1/2\rangle$ and $|-1/2\rangle$ over $|3/2\rangle$ and $|-3/2\rangle$. The fact that the substractive term in equation (8.3) contributes linearly in the quadrupole couplings of the nuclei, while the additive term contributes in second order, suggests that the former will dominate for small values of the parameter Q_r while the latter should dominate for large values. All in all we expect a fundamental difference for the behavior of the noise function $S(t)$, that should be most striking in the intermediate regime $Q_r \approx 1$, based on wether we take H_Q or $H_{Q,\text{eff}}$ into account. We postpone the discussion of the influence of varying orientation vectors $\vec{n}_k$ to the following section, restricting ourselves to numerical results in that context.

8.1.2 Numerical results

Figure 8.1 shows the time evolution of the spin noise function $S(t)$ obtained via the CET corresponding to the analytical predictions (8.2)-(8.3), i.e. all quadrupolar orientation vectors are aligned along the $z-$direction. In the upper panel, showing calculations for the effective model $H_{Q,\text{eff}}$ and $I = 1/2$, a monotonic increase of the correlation function for all times $t/T^* \gtrsim 1$ is observed, a finding that is in good agreement with the intuitive argument given in the previous section: since the quadrupole interaction is mimiced by magnetic fields applied to each individual bath spin, the occuring Zeeman splitting suppresses spin flips within the bath and in direct consequence also for the central spin. It is also noticable that the monotonic increase of $S(t)$ in the effective model $H_{Q,\text{eff}}$ only sets in significantly at moderate ratios of $Q_r \gtrsim 1$, what can be traced back to the term $\sum_k q_k^2 A_k^2$ from equation (8.2) that is negligible compared to $(T^*)^{-4}$ for small

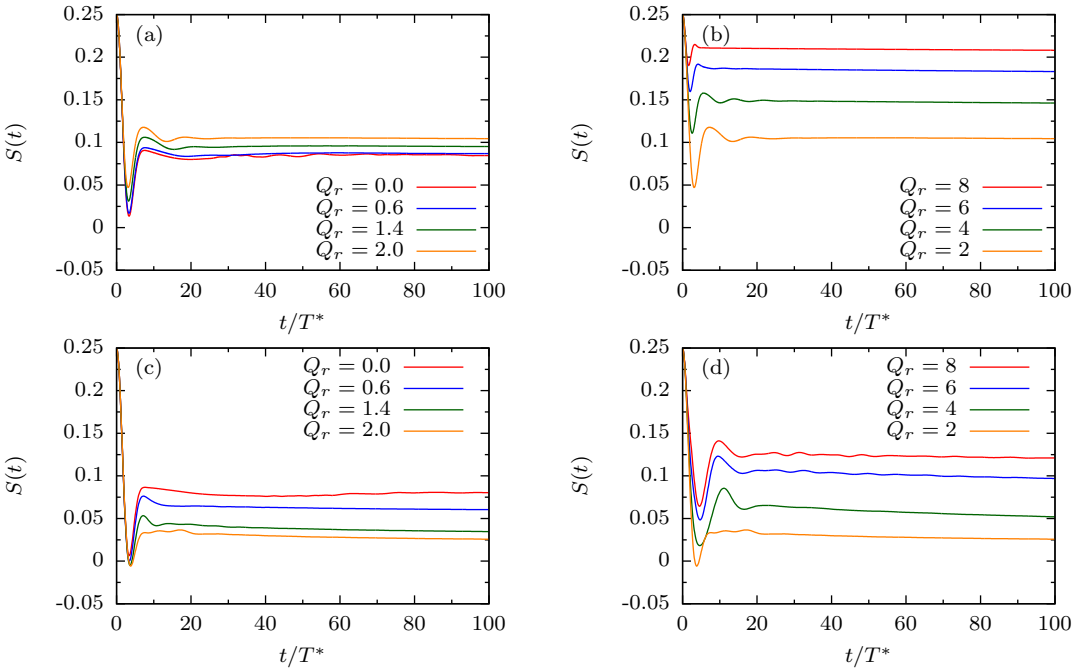

Figure 8.1: The correlation function $S(t)$ calculated for the isotropic CSM $\lambda = 1$ without external magnetic field and all quadrupole moments oriented along the $z-$direction $\vec{n}_k = \vec{e}_z$. Each curve has been averaged over $n = 50$ randomly generated sets of coupling constants A_k and q_k, as described above. The cutoff for the random generation of the hyperfine coupling constants is set to $r_0 = 1$. Panels (a)-(b) show results for $N = 18$ bath spins with spin $I = 1/2$ taking the effective quadrupolar hamiltonian $H_{Q,\text{eff}}$ into account, while panels (c)-(d) have been calculated for $N = 9$ nuclei with spin $I = 3/2$ based on H_Q. I.e. all calculations are based on a Hilbert space with $D = 2^{19}$ dimensions. The asymmetry paramter is set to $\eta = 0$.

Q_r. According to the analytical prediction, the quadrupolar interaction clearly tends to protect the central spin's coherence in the scenario at hand.

The observed behavior changes drastically for the model hamiltonian H_Q and $I = 3/2$, as shown in the lower panel of figure 8.1. In this case we find a decrease of the correlation function $S(t)$ for small values of the ratio $Q_r \in [0 : 2]$ at times $t/T^* > 3$. The short time evolution remains unchanged in this regime. For $Q_r > 2$ a reversal of this trend is observed: the minimum $S(t)$ passes through at short times is shifted to slightly larger times and the value of $S(t)$ is increasing on all time scales. Thus the dynamics in the original model H_Q is twofold: for small and intermediate values of Q_r a decrease of S_∞ is observed, which is in correspondence to the dominance of the term that is linear in the QC in equation (8.3). For large values of Q_r a change of the trend in favour of spin coherence is observed, which once again is in agreement to the additive term in (8.3) that is quadratic in q_k and will dominate over the linear term in this regime. It is also important to note, that we do not observe a decay of the spin correlation towards $S(t) = 0$ for large times. Although the analytical estimates from section 8.1.1 are restricted to the fourth order in time and the long time evolution of $S(t)$

is clearly influenced by higher orders, all presented numerical findings for $\vec{n}_k = \vec{e}_z$ are in perfect agreement with the qualitative prediction of equation (8.3). This suggests that the higher orders in the series expansion of $S(t)$ are expected to feature only additive contributions with even exponents of the couplings q_k, A_k and subtractive contributions with odd exponents, where linear terms in the hyperfine couplings are not expected. Due to the lack of these two competing effects, the dynamics obtained from the effective model $H_{Q,\text{eff}}$ overestimate the effect of the QCs in protecting the spin noise function $S(t)$ from decaying, but underestimate the contribution to the possible occurence of decoherence. Anyhow we expect the two models to feature similar dynamics in the limit of a large ratio Q_r, while in the intermediate regime $A_s \approx A_q$ and for small Q_r fundamental differences are observed for $\vec{n}_k = \vec{e}_z$.

There is also an intuitive argument that can be put forward to explain the observed twofold dynamics. Without QCs the preferred orientation of the nuclei only depends on the orientation of the central spin and to minimize the total energy all nuclei seek the same state, which is usually oriented opposite to the central spin and from a purely classical point of view has the largest possible absolute value $|I_k^z| = 3/2$. Adding the terms $(I_k^z)^2$ to the Hamiltonian introduces an energy splitting to each individual nucleus, such that the states $\pm 1/2$ are energetically beneficial compared to $\pm 3/2$. As a consequence certain nuclear spin flips are energetically less suppressed allowing a larger variety of central spin flips in favor of a decrease of $S(t)$.

Figure 8.2 treats the central spin correlation function for two different setups of the orientation vectors $\vec{n}_k$. For the upper panels (a)-(b) $S(t)$ has been calculated for fixed orientations $\vec{n}_k = \vec{e}_x$. Given the fact that figure 8.2 is restricted to the isotropic CSM with no applied magnetic field, the only physically defined direction without considering the QCs is, due to the definition of $S(t)$, the $z-$direction. I.e. the choice of the quadrupolar vectors at hand is representative for all possible orientations within the $x-y-$plane, which is the opposite extreme to setting $\vec{n}_k = \vec{e}_z$ as treated before. The obtained numerical results for (a) the effective model $H_{Q,\text{eff}}$ and (b) the original model H_Q, once again, reveal striking differences in the spin noise function $S(t)$. While the short time behavior $t/T^* < 4$ is similar for both setups, the calculations for the effective model develop pronounced damped oscillations around $S(t) = 0$ on large timescales, whose amplitude is $\sim S(0)/5$. With an increase of Q_r the relaxation of these oscillations occurs more and more rapidly. The results for the original model H_Q do not feature this type of long time oscillations. The difference is most pronounced for small values $Q_r < 1$: after passing through the usual minimum due to the precession in the Overhauser field, a monotonic decay to $S(t \to \infty) = 0$ is observed as examplary shown for $Q_r = 0.5$ in figure 8.2 (b). Apart from that, we also observe occuring oscillations within the original model for larger values of Q_r, whose amplitude is a lot smaller and their decay sets in a lot faster than for the effective model. It is also noticable that the oscillations for the effective model are almost symmetric around the time axis, while

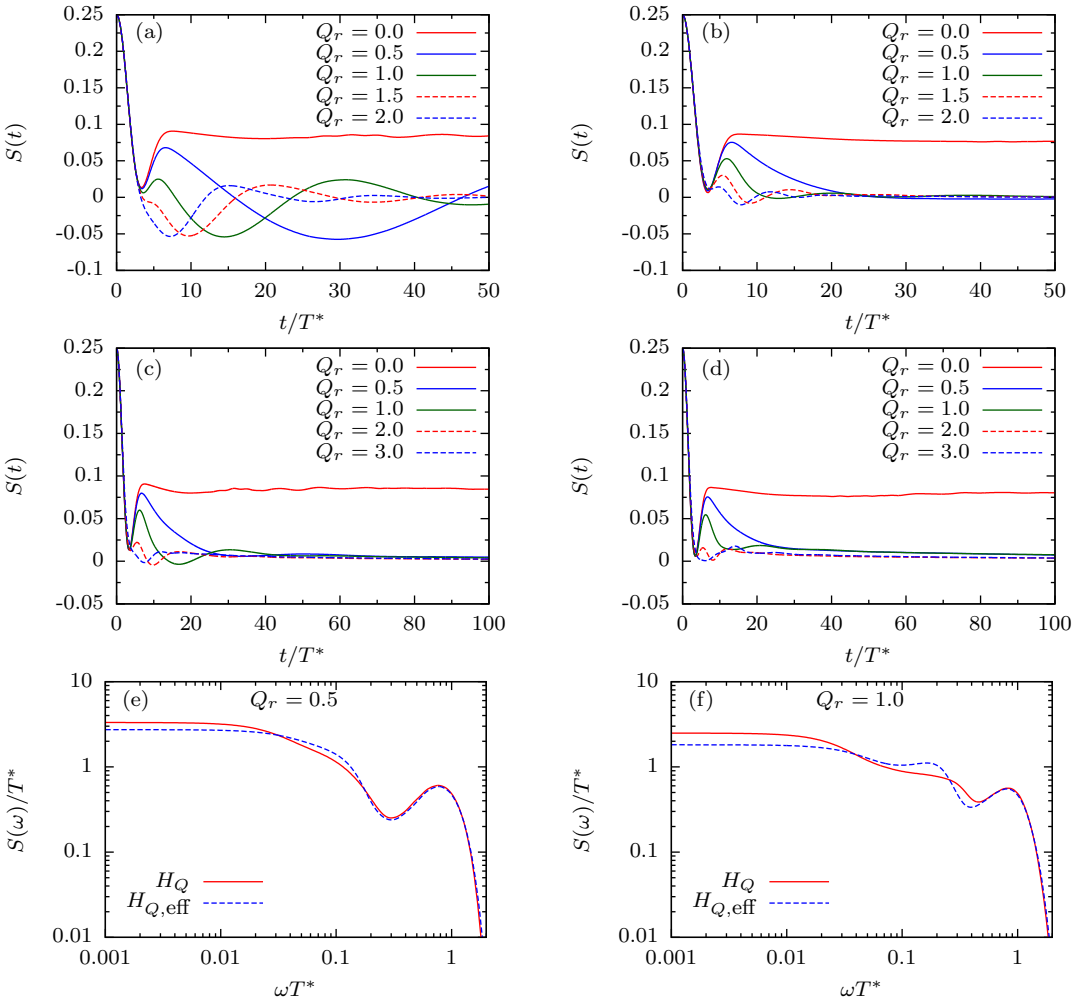

Figure 8.2: Numerical results for $S(t)$ and $S(\omega)$ considering two different choices of the quadrupolar orientation vectors $\vec{n}_k$. For the upper panels (a)-(b) all vectors are fixed along the $x-$axis $\vec{n}_k = \vec{e}_x$, while the lower panels (c)-(f) are based on isotropically randomly oriented quadrupole moments. The calculations for panels (a) and (c) use the effective model $H_{Q,\mathrm{eff}}$ and nuclear spin $I = 1/2$, while H_Q and $I = 3/2$ enter the calculations for panels (b) and (d). The lower panels (e) and (f) show a comparison of the spectral correlation function $S(\omega)$ for the two competing models, where the solid red lines are dedicated to H_Q and the dashed blue lines to $H_{Q,\mathrm{eff}}$. For panel (e) $N_c = 325$ Chebyshev polynomials have been used and to guarantee the same spectral resolution for all shown data we set $N_c = 450$ for panel (f). All further parameters have been chosen as described in figure 8.1.

the original model prefers positive values for $S(t)$. Summarized we find a similar trend for the two extreme choices of the vectors $\vec{n}_k$, namely that the dynamics obtained from the two models are fundamentally different for small and intermediate values of Q_r and seem to approach each other for large values.

We have seen that fixing the nuclear quadrupole moments along either the z- or x-axes results in drastically different results for the correlation function $S(t)$ when either H_Q or $H_{Q,\text{eff}}$ is taken into account. The authors of reference [63] however only discussed the case of isotropically randomly oriented quadrupole moments and found qualitatively good agreement between the two models. For the results shown in panels (c)-(f) of figure 8.2 we adapted this approach by isotropically determining a random vector $\vec{n}_k$ on the surface of the unit sphere. The time resolved data in panels (c)-(d) suggest that this scenario, in contrast to the results for fixed vectors $\vec{n}_k$, yields *similar* results for the correlation function $S(t)$ for both models. The most surprising similarity is the good agreement between the curves for $Q_r = 0.5$ that are representative for small values of the ratio Q_r, because in this regime the most striking differences were found for fixed $\vec{n}_k$ as discussed above. With the preceding discussions in mind, the qualitative accordance between the models for large values of Q_r as well as the occurence of the biggest disagreement for $Q_r = 1$ are less surprising. Since we are mainly adressing recent experimental measurements of spin noise in this chapter, our highest interest is gaining insight into the long time evolution of the spin noise function. Figure 8.2 (e)-(f) shows results for spectral spin noise function for the same setup as panels (c)-(d), comparing results for the two different Hamiltonians H_Q and $H_{Q,\text{eff}}$ again. $S(\omega)$ is presented on a double logarithmic scale to set the focus of the figure on the intermediate frequency regime, which corresponds to the evolution of $S(t)$ after the initial decay. We observe that the short time dynamics, i.e. the spectral peak occuring around $\omega T^* \approx 1$, is reproduced execellently by the effective model. This is not surprising, since for the shown values of Q_r the contribution of the quadrupole moments significantly sets in after the initial precession of the central spin in the Overhauser field has already been performed. In the intermediate time regime, where the central spin dynamics is influenced by the quadrupole interaction, the spectra corresponding to the two models differ significantly. For $Q_r = 1$ the spectral correlation functions deviate massively for all values $\omega T^* < 0.4$, stressing that the long and intermediate time evolution obtained for the two compared hamiltonians is fundamentally different. For $Q_r = 0.5$ similar, but less stressed deviations occur for $\omega T^* < 0.2$. Since we are primarily interested in the central spin's long time dynamics, these results point out that the effective model is not sufficient to be taken into account for further investigations. Although averaging over all possible orientations of the quadrupole orientation vectors $\vec{n}_k$ turned out to qualitatively reproduce the real time dynamics of the central spin correlation function, it has been demonstrated that the effective model is not reliable for arbitrary setups and even when averaging isotropic orientation vectors it yields deviating re-

sults when looking into the details. On top of the discussion of the effective model $H_{Q,\text{eff}}$ the preceding section has shed some light on the influence of the alignment of the quadrupolar orientation vectors $\vec{n}_k$: aligning them parallel to the $z-$axis, that is set by the definition of the correlation function $S(t)$, tends to feature a protective effect concerning the central spin's coherence and the orthogonal alignment strictly supports decoherence. Isotropically generating random vectors for $Q_r \leq 3$ turned out to yield similar dynamics as the alignment along the x-axis, a finding that is not necessarily correct in all regimes of Q_r. Besides, an analysis of the corresponding spectral function $S(\omega)$ might also reveal interesting differences that are not visible on first sight from the time resolved calculations. Anyhow we will set this analysis aside for now and postpone it to upcoming sections.

8.2 Discussion of the system parameters

In context of the comparison between the effective and the full model Hamiltonian, the selection of the orientation vectors $\vec{n}_k$ has turned out to be crucial for the physics of the spin noise function $S(t)$. The following section is dedicated to the general discussion of the further system parameters entering H_Q. First, the validity of the common approximation of axial symmetry, yielding $\eta = 0$, will be discussed and second, the impact onto $S(t)$ of three different assumptions concerning the distribution of the quadrupolar coupling constants q_k will be compared to each other.

8.2.1 Axial asymmetry of the electric field gradients

In the previous section we have seen that aligning the quadrupole orientation vectors $\vec{n}_k$ along the growth direction, which is set to be parallel to the z-direction and is also entering the definintion of $S(t)$, tends to protect the coherence of the central spin. In contrast, setting $\vec{n}_k = \vec{e}_x$ supports rapid decoherence. Since the vectors $\vec{n}_k^{x/y}$ entering the asymmetry term in (3.29) are always orthogonal to the symmetry axis $\vec{n}_k$, the former observations provide the intuition that increasing η from zero to a finite value will support the occuring decoherence. This is obvious for the scenario $\vec{n}_k = \vec{e}_z$, where the asymmetry term only consists of components orthogonal to the growth direction. For $\vec{n}_k = \vec{e}_x$ either $\vec{n}_k^x$ or $\vec{n}_k^y$ is rotated into the z-direction, suggesting that a protection of the central spin's coherence due to the asymmetry term might occur, but we will always find a competing term that is necessarily of the same order of magnitude and destroys the coherence.

The upper panels of figure 8.3 show results for the two extreme cases of fixed alignment $\vec{n}_k = \vec{e}_{z/x}$ and various values of the asymmetry parameter η. As expected, an increase of η induces a faster occuring decay of $S(t)$ in both scenarios. When comparing the results for $\eta = 0$ and $\eta = 0.25$, it is noticeable that the observed effect sets in more pronounced for the case $\vec{n}_k = \vec{e}_x$, while the opposite observation applies for the

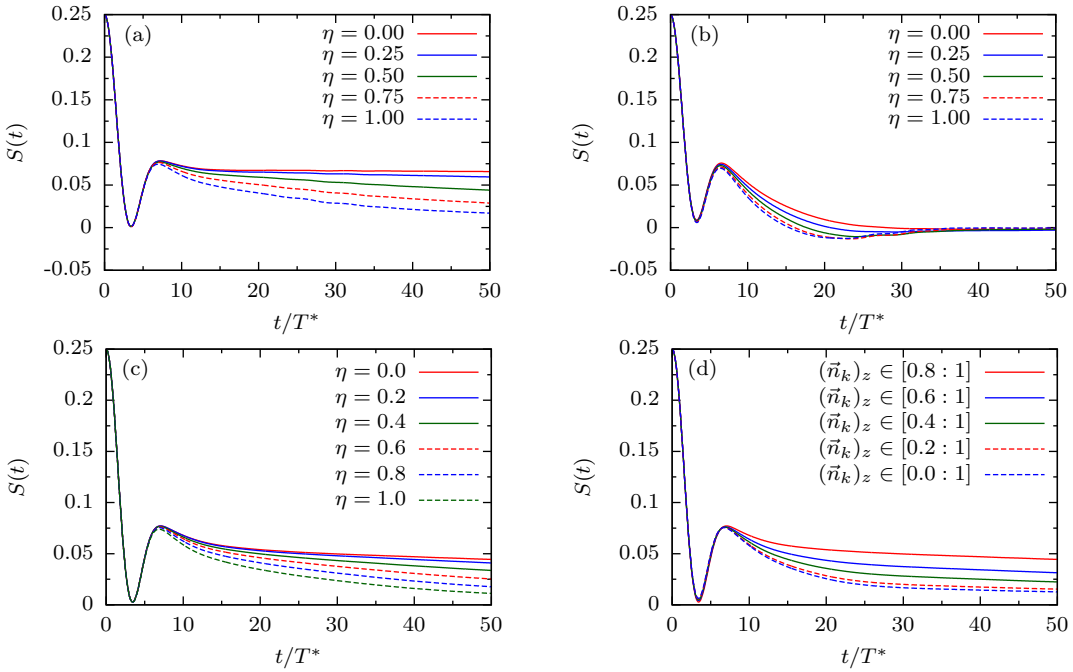

Figure 8.3: Influence of the asymmetry parameter η on the spin noise function $S(t)$. In the upper panels the orientation vectors $\vec{n}_k$ are aligned along (a) the z- and (b) the x-direction. For the lower panels the vectors have been determined randomly. Panel (c) shows a scan of the asymmetry parameter η, where the z-component of the orientation vector fullfills $(\vec{n}_k)_z \in [0.8 : 1]$. In panel (d) the allowed values for $(\vec{n}_k)_z$ are increased proceedingly, while $\eta = 0$ is kept constant. All calculations concern the isotropic CSM, involving $N = 10$ spin$-3/2$ nuclei and the cutoff for the coupling constants is set to $r_0 = 1$. The quadrupole couplings q_k are determined randomly out of a uniform distribution in the interval $[0.5 : 1]$ and $Q_r = 0.5$ holds. Results for $n = 50$ individual setups have been averaged.

increase of η from 0.75 to 1. The combination of these observations suggests that the impact of the Hamiltonian terms $\propto (I_k^{(x/y)})^2$ is larger for small values of Q_r, while the terms $\propto (I_k^z)^2$ dominate when Q_r is large.

For an arbitrary orientation vector $\vec{n}_k$ the asymmetry term, governed by η, and the general quadrupole interaction term, governed by the coupling constants q_k, both feature the same operators. Hence, it is intuitive to assume that it might be possible to circumvent the introduction of the asymmetry term by applying an adequate distribution of the orientation vectors $\vec{n}_k$ instead. The lower panels of figure 8.3 address the question wether a variation of the orientation vectors can indeed mimic the asymmetry term. For this sake, random orientation vectors are determined isotropically within a certain dome of the unit sphere, which is specified by the z-component of $\vec{n}_k$. In panel (c) this distribution is kept invariant for $(\vec{n}_k)_z \in [0.8 : 1]$ and η is varied, while panel (d) presents results for $\eta = 0$ and varying size of the considered dome. On first sight, the obtained results are very similar as one would intuitively expect. Just as an increase of η, the growing variation of $(\vec{n}_k)_z$ entails a faster decay of $S(t)$ towards zero, but when looking into the details important differences are revealed. The lowest lying curve from

panel (c) and the one from panel (d) both feature a very similar value $S(t/T^* = 50)$, but their relaxation behavior for $7 < t/T^* < 50$ is significantly different. For $\eta = 0$ and $(\vec{n}_k)_z \in [0:1]$ the spin noise function decays rapidly up to $t/T^* = 30$ and is almost constant afterwards, while the asymmetry induced decay is more steady. These trends are found throughout panels (c)-(d) of figure 8.3 and the observed behavior is mainly traced back to the energy hierarchy in the Hamiltonian (3.29): when the asymmetry term is not taken into account, all considered contributions are necessarily of the same order of magnitude and solely governed by the coupling constants q_k. Since the asymmetry term enters the Hamiltonian with $\eta/3$, it introduces a second energy scale to the system that is, roughly speaking, one order of magnitude smaller than the QCs themselves. Accordingly, a decoherence mechanism is introduced that occurs slower than induced by averaging over different directions of the same orientation vector. On top of the missing energy hierarchy, finding an adequate distribution for the vectors $\vec{n}_k$ that reproduces the impact of the asymmetry term for arbitrary η is challenging, while involving the term is more accurate and implies less effort.

8.2.2 Distribution of the quadrupole coupling constants q_k

Aside from prefactors, the coupling constants q_k are governed by the EFGs among the QD that arise due to the occuring strain in their growth process. In the literature[102, 126] often only the strain along a single axis within a dot is discussed, while we are interested in its distribution among the entire QD. In references [70, 71] a three dimensional treatment of the strain within InGaAs QDs is presented. It has been found that the strain does not necessarily reflect the symmetry of the dot: while a uniform distribution among the $x-y-$plane at the bottom of the dot, where the largest strain-values occur, was found, the strain varies unsteadily in the remainder of the QD. On top of that the observed strain in the close environment of the dot, where the coupling constants A_k from the anisotropic CSM are small, is of the same order of magnitude as within the QD. I.e. the quadrupolar splitting of the corresponding nuclei might be a lot larger than its hyperfine coupling, suppressing the contribution to the central spin dynamics of the nuclei out of the dot. This effect supports the adequacy of our finite size limitation to a small cutoff r_0 in the context of the influence of quadrupole couplings onto the central spin dynamics. In the following we will dicuss three different choices for the quadrupole coupling constants q_k: (i) according to reference [63] we generate a random number for each q_k from a uniform distribution in the interval $[0.5:1]$, which respects the reported [70] unsteady behavior of the strain in InGaAs QDs. (ii) To account for the large strain at the bottom of the QDs, where the coupling constants A_k are expected to be rather small, we generate a linear set of coupling constants $q_k = 0.5 + k/2N$ such that the largest hyperfine coupling A_k is associated to the smallest quadrupole coupling constant and so on. (iii) For simplicity we compare the

latter setups to identical couplings $q_k = q$. For all three distributions we rescale the coupling constants to ensure $Q_r = A_q / A_s$.

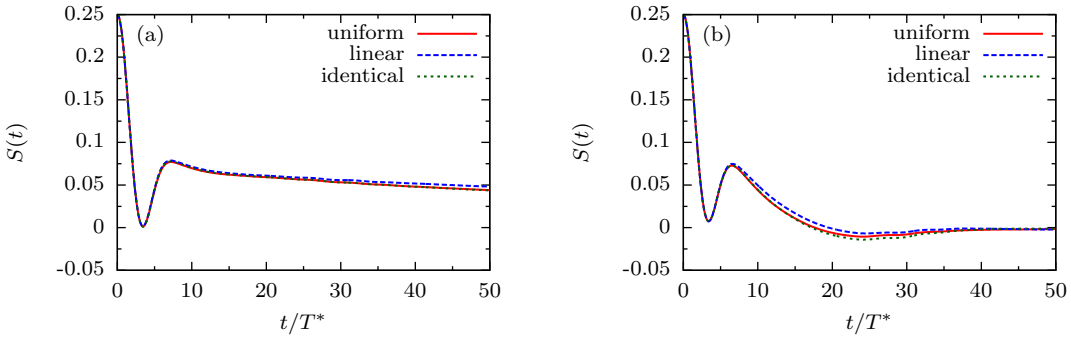

Figure 8.4: Results for $S(t)$ concerning three different claims to model the quadrupole coupling constants q_k: (i) the red solid lines are based on randomly generated q_k drawn from a uniform probability distribution in the interval $[0.5 : 1]$, (ii) for the blue solid lines the couplings q_k are linearly increasing from $q_1 = 0.5$ to $q_N = 1$ where A_1 refers to the largest and A_N to the smallest hyperfine coupling constant, (iii) finally the green dashed lines treat a setup where all quadrupole couplings are identical $q_k = q$. The quadrupole parameters are $\eta = 0.5$ and $Q_r = 0.5$. Panel (a) treats $\vec{n}_k = \vec{e}_z$ and for panel (b) $\vec{n}_k = \vec{e}_x$ holds. All further system parameters are correspond to the setup discussed in figure 8.3.

Figure 8.4 shows numerical results for these three different distributions of the coupling constants q_k. The calculations for $\vec{n}_k = \vec{e}_z$ shown in panel (a) exhibit no visible difference between the results for identical and randomly generated coupling constants, while the impact of the quadrupole interaction on the central spin dynamics appears to be weaker for the linear set of coupling constants. The latter observation also holds for the results from panel (b) for $\vec{n}_k = \vec{e}_x$. This finding can be justified by a rather intuitive argument: since the interaction between the nuclei and the central spin is always mediated by the couplings A_k and, for the linearly increasing sets of coupling constants q_k, the small QCs are associated to the large hyperfine couplings, the total impact on the central spin dynamics must be smaller than for the evenly distributed sets of q_k. Bearing this simple argument in mind, it is also intuitive that taking the randomly generated and the identical couplings into account has on average a very similar effect on $S(t)$. Although slight deviations are observed for these two assumptions in panel (b), the only difference in the obtained dynamics from the different distributions is that the impact of the quadrupolar interactions for a given value of Q_r is effectively larger if the large q_k are associated to nuclei with a large coupling to the central spin and vice versa. To summarize the current section we obtained two central results concerning the model Hamiltonian at hand: (i) taking a possible axial asymmetry of the EFGs into account corresponds to the introduction of a term to the Hamiltonian that is an additional source of decoherence for arbitrary orientations of the nuclear symmetry axes. (ii) Introducing a certain distribution of the quadrupolar coupling constants q_k does not yield fundamentally new effects in terms of the central spin dynamics and the

impact of the quadrupole interaction on $S(t)$ can always be predicted by considering how the quadrupole couplings q_k are correlated with the central spin couplings A_k. This statement does not necessarily hold for unrealistic distributions like $q_j = Q_r$ and $q_k = 0$ for $k \neq j$ for instance, but since we focus our investigations on rather realistic setups we will not consider such cases in the present work.

8.3 Spin noise in InGaAs quantum dots

After the general investigation of the various system parameters entering the quadrupole Hamiltonian (3.29), we now turn to the discussion of recent experiments. As mentioned above, the focus of the present work is on various measurements on InGaAs QDs and with respect to the findings of references [70, 71] we concentrate the further investigations on the set of system parameters that constitutes a realistic model for this type of QDs: (i) the quadrupole coupling constants q_k are determined randomly from a uniform distribution in the interval $[0.5 : 1]$, (ii) the considered orientation vectors $\vec{n}_k$ are also generated randomly and all end on a dome of the unit sphere, whose size is chosen such that the average angle between the z-axis and $\vec{n}_k$ is 30°. (iii) The asymmetry parameter is set to $\eta = 0.5$. (iv) We assume a Gaussian shape ($m = 2$) for the electron (or hole) wave function and investigate a $d = 3$ dimensional dot. This set of parameters enters every calculation that is discussed in the remainder of this chapter.

Note that the intention of restricting the following investigations to InGaAs QDs, is to demonstrate the accordance of our numerical findings and various experimental results. From the knowledge of certain physical properties, such as the built in strain, the orientation of the nuclear symmetry axes and the EFG's asymmetry, the real time dynamics of an electron or hole confined in most other semiconductor QDs can also be predicted from our theory. E.g. the finding that the life time of hole spins is significantly larger in InAs QDs [127] than in InGaAs QDs, is in perfect agreement with the results from the previous sections, once again taking the findings of reference [70] into account: (i) in InAs the symmetry axes of the nuclei tend to be aligned along the growth direction of the dot, i.e. the system is close to the extreme case $\vec{n}_k = \vec{e}_z$ that tends to conserve the central spin's coherence and (ii) the asymmetry parameter η, which is an additional source of decoherence, is significantly smaller in InAs than in InGaAs.

We proceed as follows: first, the influence of the ratio $Q_r = A_q / A_s$ onto the dynamics of a single electron spin (setting $\lambda = 1$) confined in an InGaAs QD is investigated in general. Second, for electron spins the crucial theory parameters T^* and Q_r are gauged towards corresponding measurements from a recent experiment [62]. On this basis we advance to the treatment of hole doped QDs in general and demonstrate the comparibility between the obtained theoretical and recent experimental results [64], where the determined system parameters from the electron doped case are taken into

account. Afterwards, further experimental measurements are discussed, which have been performed here in Dortmund by Glasenapp et al. [65] and constitute the only set of original experimental data that is available to us. All in all, our theoretical treatment of spin noise in semiconductor QDs will shed light on the comparable coherence times of electron and hole spins, which is, according to the findings of the preceding chapters, a priori not an intuitive result. On top of that, the general validity of our theory grants an in-depth insight into the desired properties of a QD that conserves the confined spin's coherence ideally.

8.3.1 Electron spin dynamics

Figure 8.5 treats the central spin dynamics for a single, electron doped InGaAs QD for a variation of the system parameter Q_r, where all further model parameters have been set to reproduce the realistic properties of an InGaAs QD. The time resolved data shown in panels (a)-(b) correspond to the spectral functions shown in panels (c)-(d) and the resolution of the presented spectra $S(\omega)$ corresponds to the largest shown timescale $t/T^* = 100$. As demonstrated in panel (a), the short time dynamics up to $t/T^* \approx 4$ remains invariant for intermediate ratios $0.25 \leq Q_r \leq 1.0$, i.e. the impact of the quadrupole interaction is not strong enough to influence the initial decay of the central spin. Anyhow its full initial evolution due to the frozen Overhauser field does not occur for $Q_r > 0.5$. Namely the usual reoccurrence to the value $S(t) = S(0)/3$ at $t/T^* \approx 8$ is not observed, because a decay of $S(t)$ due to the quadrupole interaction sets in earlier. It is noticeable that $S(t)$ does not decay to 0 on the depicted time scale, although an intuitive prediction from the obtained results for $Q_r = 0.25$ and 0.5 would suggest such a decay. In contrast, the value $S(t = 100T^*)$ is almost indistinguishable for a broad variety of ratios Q_r. The corresponding spectra for intermediate values of Q_r, that are shown in figure 8.5 (c), reflect the time resolved results: due to the consideration of QCs the high frequency peak is only altered at its left shoulder. The height of the observed peak at small frequencies, which contains all the spectral weight that is beyond the resolution of the shown calculations, is decreasing monotonically. The occurence of this peak does not necessarily imply that the spin noise function approaches a finite value $S(t \to \infty)$, but that the long time evolution of the central spin occurs on a larger time scale than it is resoluted in figure 8.5. In the intermediate frequency regime $0.063 \leq \omega T^* < 1$ the observed spectral weight in panel (c) is monotonically increasing with Q_r. The occuring gap between the peaks at $\omega T^* \approx 1$ and at small frequencies, that is very pronounced for $Q_r = 0.25$, is filled and for $Q_r = 1.5$ a relatively even spectrum is found. Accordingly, the gradient of $S(\omega)$ in the transition regime from small to intermediate frequencies is decreasing with increasing Q_r. Turning to scenarios where the total quadrupole coupling $A_q = \sum_k q_k$ is dominant compared to the total hyperfine interaction $A_s = \sum_k A_k$, a change of the observed trend sets in (see panels (b) and (d) of figure 8.5): on the one hand a significant effect on the initial precession of the cen-

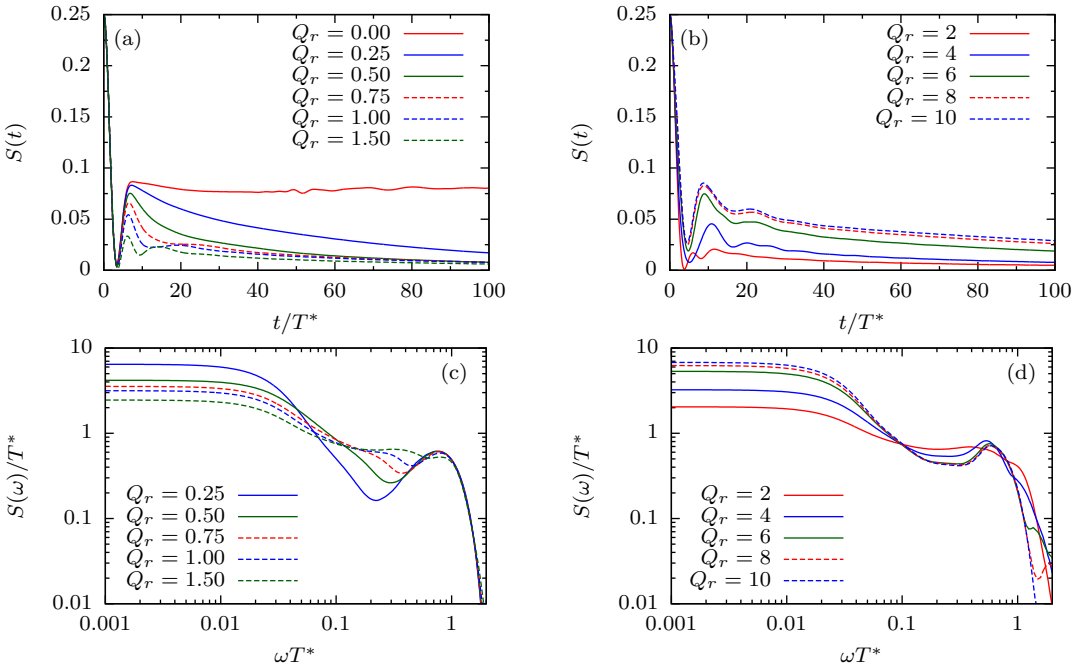

Figure 8.5: Impact of the varying ratio Q_r on the spin noise function in the time and frequency domain for intermediate and large values. All results consider electron doped QDs ($\lambda = 1$) and the model parameters $r_0 = 1$, $d = 3$ and $m = 2$. The orientation vectors $\vec{n}_k$ are determined randomly and reproduce the average deviation angle 30° from the growth direction of the dot. The q_k are determined from a uniform probability distribution in the interval $[0.5 : 1]$. The number of Chebyshev polynomials N_c taken into account for the results in panel (c) and (d) is chosen such, that the reliable resolution of the spectral function $S(\omega)$ is $\omega_{\text{min}} T^* \approx 0.063$, which corresponds to the time scale that is shown in panels (a) and (b). $N = 9$ bath spins have been taken into account and results for $n = 50$ setups have been averaged.

tral spin is now observed and on the other hand the occuring decay for intermediate timescales is less pronounced for very large ratios Q_r. Both observations have in common that they provide a longer life time of the electron spin, since the initial decay is shifted to larger times. Interestingly the central spin dynamics for very large values of Q_r is, apart from a shift to smaller frequencies, similar to that for rather small values and only in the intermediate regime a significant deviation is observed. In the latter case the results for $S(\omega)$ shown in panels (b) and (d) feature significantly more spectral weight at intermediate frequencies, while in the other scenarios a clear gap between the peak due to the initial spin precession and the one that describes the long time decay is observed. Qualitatively the same behavior was also observed for the simplified cases discussed in section 8.1 and it can be traced back to the finding of equation (8.3), suggesting that the highest order term in the quadrupole coupling constants q_k is always an additive term. On top of this it is rather intuitive that the mediation of a nuclear spin flip due to the hyperfine interaction is very unlikely when the interaction of the nuclear spin with an external field is significantly larger than the hyperfine cou-

plings. The finding that quadrupole interactions are in principle capable of increasing the coherence of the central spin, is in good agreement with recent predictions [99, 128]. Anyhow we do not believe that the magnitude of the quadrupole coupling constants q_k in a common InGaAs QD is large enough to realise such a protection of the electron spin coherence, as will be discussed in the following.

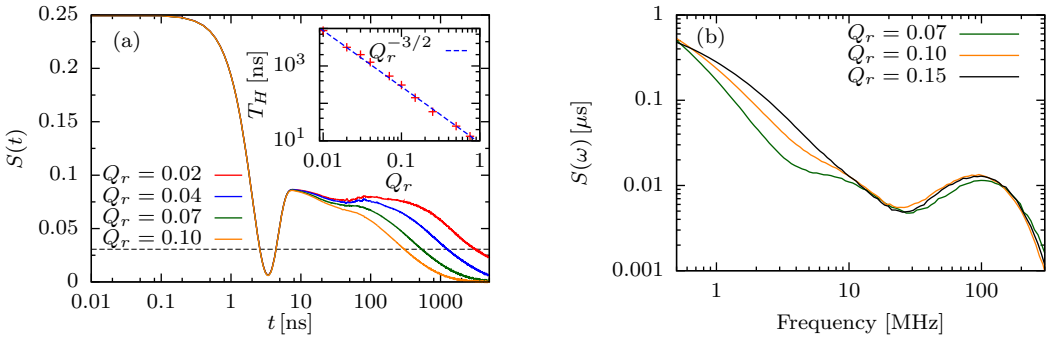

Figure 8.6: Panel (a) depicts real time CET results, considering $n = 20$ setups of $N = 18$ bath spins, for various small values of the ratio $Q_r \leq 0.1$, addressing the core result of reference [62]. The crossover of $S(t)$ and the black dashed line at $t/T^* > 7$ defines the timescale T_H, which measures the decay of the spin noise function to the value $S(t/T^* = 7)/\mathrm{e}$. The inset of panel (a) shows the dependence of this timescale on the parameter Q_r. As indicated by the blue dashed line, $T_H(Q_r)$ can be approximated by a power law fit $\propto Q_r^{-3/2}$. Panel (b) presents corresponding results for $S(\omega)$ calculated for $N_c = 6000$, $n = 50$ and $N = 18$. Further parameters: $r_0 = 1.2$ and $\lambda = 1$. Panel (a) corresponds to figure 1 (a) and panel (b) to figure 2 (a) of reference [65].

Comparison to an experiment on a single n-doped InGaAs QD

Let us now turn to the direct comparison of our theory to recent measurements [62] on a single n-doped InGaAs QD. Looking into the core result (figure 2 (a) of reference [62]) of this experiment, it turns out that a realistic choice of the system parameter Q_r must be significantly smaller than the considered values from figure 8.5, because the observed decay of the elctron spin polarisation, after its initial precession in the Overhauser field, sets in a lot slower than in our findings for $Q_r > 0.2$. To compare our theory to the experiment, figure 8.6 treats the electron spin dynamics for small values of Q_r up to times $t/T^* = 5000$. The resulting short time dynamics of the central spin reproduces the experiment excellently, pointing out that the theory of Merkulov et al. [27] describes the initial electron spin decay adequately. The comparison of the time scale of figure 8.6 (a) to the experimental result reveals that the intrinsic time scale T^* is very close to 1 ns for the InGaAs QD under study, which will be assumed from now on.

As demonstrated in section 5.1.2, the electron spin's long time evolution within the ICSM is expected to be governed by a logarithmic decay, which is not in agreement to the experimental results. In contrast, figure 8.5 (a) indicates that the influence of the

quadrupole interaction for $Q_r \approx 0.07$ reproduces the central spin dynamics found in the experiment up to $t \approx 800\,\mathrm{ns}$ quite nicely, while the following increase of $S(t)$ to approximately $S(0)/9$ after roughly $1\,\mu\mathrm{s}$ is not reproduced by the simulations. This deviation might stem from several sources: (i) since we can not take nuclei with arbitrarily small coupling constants A_k into account, contributions from the hyperfine interaction at large times are neglected. Although these contributions are expected to be suppressed by the quadrupolar splitting, we can not exclude that they might have a major impact on $S(t)$ on large timescales. (ii) There are interactions our model does not take into account that might contribute after $1\,\mu\mathrm{s}$, like the dipole-dipole interaction between the nuclei for instance. Note that Bechtold et al. [62] also introduced a semi classical model for the central spin dynamics. It takes the quadrupole interaction on basis of the effective model by Sinitsyn et al. [63] into account and features a reoccurrence of $S(t)$ after approximately $1\,\mu\mathrm{s}$. Beside the above stated lack of reliability of the effective model for the QC, their presented numerical results seem questionable for a second reason: from figure 8.5 we draw the expectation that the short time evolution of $S(t)$ is altered significantly compared to $S_{\mathrm{SCA}}(t)$ when the parameter Q_r is larger than 1. This effect has not been measured in the experiment and does not occur in the presented simulations of reference [62] although $Q_r = 2$ has been considered. All in all this leaves the origin of the occuring reoccurrence as an open question.

The inset of figure 8.6 (a) shows the dependency of the newly introduced timescale T_H on the ratio Q_r. T_H denotes the time it takes until the spin noise function has dropped to $1/\mathrm{e}$ of its initial value due to the influence of the quadrupole interaction. For its determination the initial value of $S(t)$ is not defined at $t = 0$ but at $t/T^* = 7$ instead, because the initial decay of the spin noise function to one third of its initial value occurs due to the central spin's precession in the Overhauser field and is not significantly influenced by the quadrupole couplings for $Q_r < 0.1$. The black dashed line in figure 8.6 (a) indicates the value $S(t)$ has to take to set T_H. The purpose of the inset is to construct a prediction concerning the influence of the quadrupole interaction for the case of hole doped QDs. Since the coupling constants A_k are one order of magnitude smaller for holes than for electrons and the strain within a QD is indpendent of its doping, we assume that the model parameter Q_r has to be set about a factor of 10 larger for holes to obtain a realistic description. As demonstrated in figure 8.6 (a), the function $T_H(Q_r)$ can be approximated by a power law $\propto x^{-3/2}$, i.e. we expect that an increase of Q_r by a factor of 10 will reduce the central spin's coherence time by a factor of approximately 30. On the other hand one also has to bear in mind that the underlying timescale T^* is also about 10 times larger for holes due to the small coupling constants A_k and on top of that the anisotropy parameter λ enters T^*_λ linearly, which also yields an increase of the coherence time. Combining these three factors, we expect the increase of the coherence time due to the change of parameters within the CSM and its decrease due to the quadrupole interaction to even out each

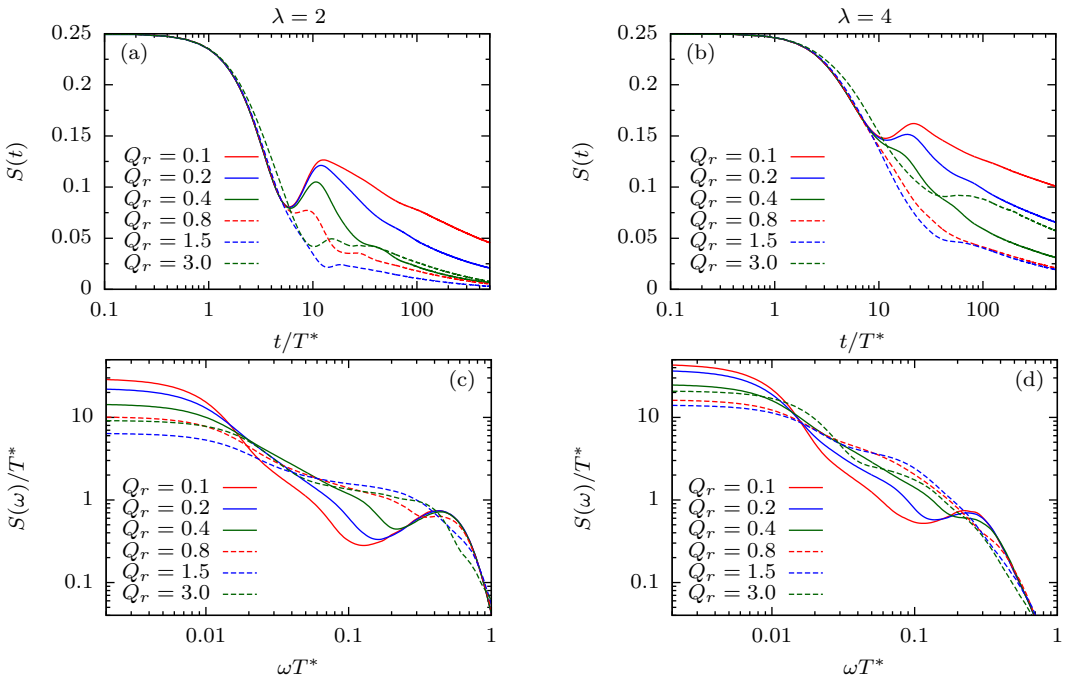

Figure 8.7: Influence of the ratio Q_r onto the hole spin dynamics within a single InGaAs QD for $\lambda = 2$ (left) and $\lambda = 4$ (right). For all presented calculations $d = 3$, $m = 2$, $r_0 = 1.2$, $n = 50$ and $D = 2^{19} = 2 \cdot I^N_{\text{dim}}$ applies. The resolution of the shown spectra in panels (c) and (d) has been adjusted to $\omega T^* = 0.013$, corresponding to the depicted timescale from panels (a) and (b). Note that the timescale T^* is used instead of T^*_λ, to warrant a better intuition concerning the effects of varying λ and Q_r in an experimental setup.

other approximately. We will recall this prediction within the discussion of hole spin dynamics in the following section.

Panel (b) of figure 8.6 presents CET results for the spectral spin noise function for small values of Q_r. A clear separation of the spin noise function's decay due to the hyperfine interaction ($10 \lesssim \nu \lesssim 30\,\text{MHz}$) and the QCs ($\nu \lesssim 5\,\text{MHz}$) is observed for $Q_r = 0.07$, which is lifted proceedingly with an increase of Q_r. This clear separation stems from the limited considered cutoff r_0 and is not expected to be observed in an experimental measurement of the spectral function $S(\omega)$, but still a smoothened kink, similar to the one observed for $Q_r = 0.1$, in the crossover regime from the hyperfine to the quadrupolar mediated decay might occur in $S(\omega)$ in an experiment where $Q_r \approx 0.07$ applies.

8.3.2 Hole spin dynamics

Figure 8.7 treats the impact of the quadrupole interaction onto the hole spin dynamics in a single InGaAs QD. For this purpose, scans of the ratio Q_r for two different values of the anisotropy parameter λ are presented in the real time and spectral domain. Within the general discussion of the anisotropic CSM it has been demonstrated that the

timescale T_λ^* induces an invariant short time dynamics for a variation of the anisotropy parameter. This clearly implies a linear increase of the initial spin decay time with λ, which is supposed to be observed in the experiments. Since the mixing of light and heavy holes for a given sample is generally not known a priori, the comparison of experimental and theoretical results might shed some light onto this property of the QDs under study.

As observed for the case of electrons, an increase of Q_r from 0 to approximately 2 precedingly induces a faster decay of the spin noise function $S(t)$ and also the value $S(t/T^* = 500)$ decreases monotonically in this regime. When the energy scale of the quadrupole interaction exceeds the hyperfine interaction significantly ($Q_r > 2$), flips of the central spin are suppressed and a protection of the spin's coherence sets in. Comparing the real time results from panels (a)-(b) of figure 8.7 for the two different values of λ at fixed Q_r reveals several interesting features. For the two smallest ratios $Q_r = 0.1, 0.2$ and both considered anisotropy parameters the central spin's reoccurrence due to its precession in the static nuclear field is observed. This is also the case for $\lambda = 2$ and $Q_r = 0.4$, but considering the same magnitude of the QCs the reoccurrence is already suppressed for $\lambda = 4$, where a monotonic decrease of the spin noise function is observed. In figure 8.6 it has been demonstrated, for $Q_r < 0.2$, that an increase of Q_r impacts the electron spin dynamics stronger than linearly, while the decoherence driving flip-flop terms from the CSM are suppressed linearly with λ. Thus, it is intuitive to assume that the impact of the QCs onto $S(t)$ is not qualitatively the same for a constant value λQ_r, but instead the hole spin evolution through the hyperfine interaction is suppressed stronger if λ is large. This intuition is stated by comparing the numerical results for $\lambda = 2$, $Q_r = 0.8$ and $\lambda = 4$, $Q_r = 0.4$: in the latter scenario the initial precession in the frozen bath is fully suppressed, which is not the case in the first scenario. For large $Q_r > 1$ this comparison does not hold anymore, but since the prediction from figure 8.6 only holds for $Q_r < 0.25$, the presented argument is only supposed to by valid for small ratios Q_r.

The comparison of the spectral functions $S(\omega)$ for varying Q_r, as presented in figure 8.7 (c)-(d), underlines the strong dependence of the spin noise function's shape on the underlying parameters λ and Q_r. Combining the observations from (i) the general discussion of the anisotropic CSM and (ii) the influence of Q_r in the electronic case, fully covers the qualitative behavior for hole spins. Namely, an increase of λ shifts the entire spectrum to smaller frequencies, corresponding to a linear slow-down of the short time dynamics and occuring long time effects on a timescale that is increased more than linearly. The increase of Q_r yields a suppression of the characterisitc initial precession and a shift of spectral weight to the intermediate frequency regime, which entails a decrease of the gradient of $S(\omega)$ in this regime.

Comparison to an experiment on a p-doped ensemble of InGaAs QDs

Panel (a) of figure 8.8 treats the real time evolution of a single hole spin confined in an InGaAs QD. The simulations were calculated via the CET for various combinations of the parameters Q_r and λ. As stated above, the parameter Q_r is assumed to be one order of magnitude larger for holes than for electrons, where $Q_r \approx 0.07$ turned out to reproduce the experimental findings by Bechtold et al. [62] adequately. To point out the occurence of comparable lifetimes when investigating n- or p-doped QDs, the following discussion of the experiments by Li et al. [64] is entirely based on the assumption that the QDs investigated in the two experimental studies feature an identical strain tensor. Note that this assumption is not necessarily true, because, with respect to the performed measurements, the underlying nano-device in the experiment by Bechtold and coworkers features a significantly different design than usual samples of InGaAs QDs.

The three presented parameter sets that are considered in figure 8.8 (a) all feature a similar lineshape of $S(t)$. It does not feature the characteristic dip due to the central spin's precession in the Overhauser field. As argued at the beginning of this section, the initial precession is suppressed due to the interplay of the QCs and the anisotropic hyperfine interaction. Note that the decay time T_H is varying significantly among the different curves due to two factors: the anisotropy factor is increased and Q_r is decreased proceedingly. Since the Fourier transformation of a Lorentzian peak at zero frequency is given by an exponential decay in time, we have added the function $S(0)\exp(-t/T_H)$ for comparison. In contrast to the case of electrons, the horizontal black dashed line, whose crossover with $S(t)$ defines the lifetime T_H, indicates the value $S(t) = S(0)/\mathrm{e}$, since for hole spins the decay due to the quadrupole interaction can not be clearly separated from the decay due to the hyperfine interaction. Li et al. [64] reported a hole spin lifetime of 400 ns, while we find the lifetimes $T_H = 176$ ns for $\lambda = 4$, $T_H = 399$ ns for $\lambda = 6$ and $T_H = 738$ ns for $\lambda = 8$. I.e. our finding for $\lambda = 6$ and $Q_r = 0.8$ is in very good agreement to the experiment. On top of that, the obtained lifetime for $Q_r = 0.07$ in the electronic case was $T_H = 536$ ns and thus of the same order of magnitude as the hole lifetime. This finding agrees to our initially stated prediction that the influence of QCs counters the enhanced lifetime of hole spins that is expected from the bare anisotropic CSM and represents one of the central results of this work. Approximating $S(t)$ by a purely exponential decay does work to some extent: on short and intermediate timescales qualitative agreement is found, while the exponential decay fails to reproduce the long time tail of the spin noise function, which does not decay to zero on the presented timescale.

Figure 8.8 (b) is related to recent spin noise measurements by Li et al. [64], where we focus on the presented results in zero and longitudinal external fields. The authors of the experimental publication claimed that the hole noise spectrum in zero magnetic field can be nicely approximated by a Lorentzian fit and with an increasing longitudinal

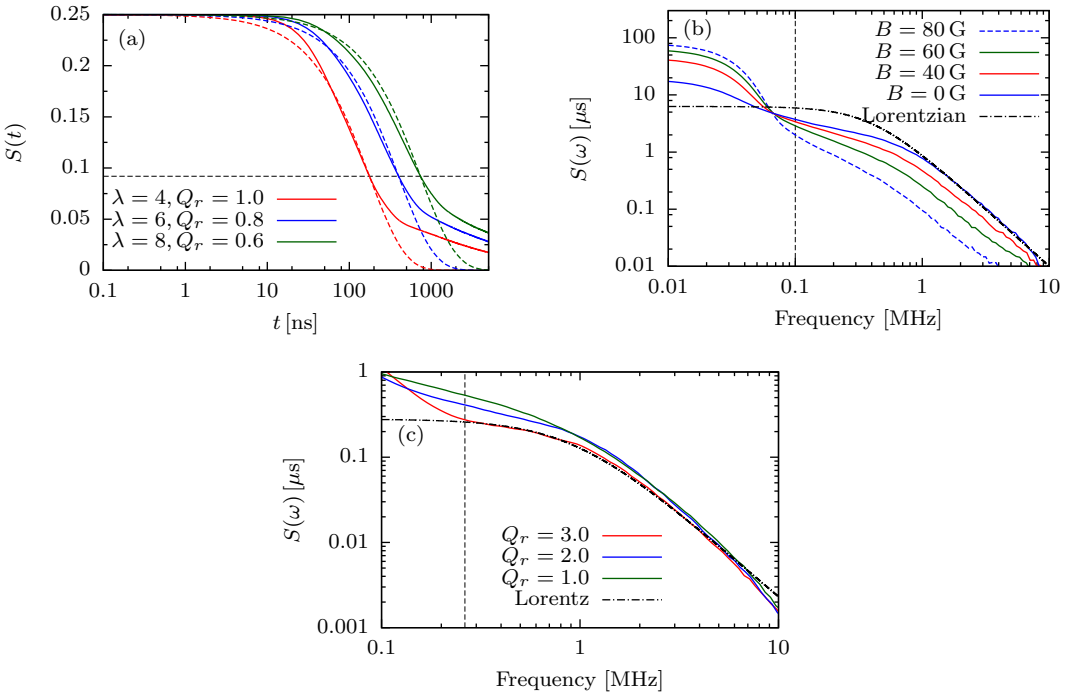

Figure 8.8: Illustration of hole spin noise results for InGaAs QDs in experimentally relevant parameter regimes. The solid lines in panel (a) show real time calculations for three combinations of the parameters λ and Q_r. The dashed lines of the corresponding color indicate a bare exponential decay of the form $S(0)\exp(-t/T_H)$, where T_H is determined by the crossover of $S(t)$ and the black dashed line. Panel (b) depicts spectral results for a varying external field $\vec{n}_B \parallel z$ at fixed parameters $Q_r = 0.8$ and $\lambda = 6$. A Lorentzian peak that corresponds to the red dashed line from panel (a) is added. Panel (c) presents spectral results for $\lambda = 6$ and various values of Q_r. $S(\omega)$ is nicely approximated by a Lorentzian fir for $Q_r = 3.0$. All spectra have been calculated for $N_c = 6000$ Chebyshev polynomials and the vertical black dashed lines indicate the roughest spectral resolution of the depicted curves. We assumed the intrinsic timescale $T^* = 10$ ns to be a factor of 10 larger than for electrons and the hole g-factor was set to $g_h = 0.15$ [64]. All further parameters have been chosen as in figure 8.6 and the ensemble average has been performed as described in figure 7.4.

field the Lorentzian proceedingly turns into a $1/f$ behavior. Both findings have in common that they feature a monotonous decrease of the spectral spin noise function and no shoulder, which is always observed for n-doping, occurs at large frequencies.

To substantiate the stated agreement between our theory and the experiment by Li and coworkers, numerical results for $S(\omega)$ are presented in panel (b) of figure 8.8. From the comparison to the measurements on a single electron by Bechtold et al. [62], we obtained the intrinsic timescale $T_e^* = 1$ ns, which is expected to be enhanced approximately by a factor of 10 for hole spins due to the smaller magnitude of their hyperfine coupling constants. Based on this assumption, we find decent agreement between experiment and theory. Namely, the frequency scale on which the spin noise function is varying is reproduced adequately by the simulations and the added Lorentzian

fit, which corresponds to the exponential decay from panel (a), accounts correctly for $S(\omega)$ at large frequencies. According to our observations in the real time domain, pronounced deviations between the added Lorentzian lineshape and $S(\omega)$ occur for small frequencies. These deviations stem from two origins: (i) as demonstrated in reference [65], renouncing the norm of the Lorentzian fit and focusing it on the reliably resoluted part of the spectrum, yields a significantly better approximation of $S(\omega)$ that does not account for the peak beyond the numerical resolution. (ii) With respect to the finite size limitations of the applied theory, slightly different theoretical results concerning the long time behavior of the spin noise function are expected compared to the experiment. Figure 8.8 (b) also includes spectral results within an external longitudinal field. As discussed above, the suppression of central spin flips due to the magnetic field trivially shifts the entire spectral weight to smaller frequencies. The simulations demonstrate how this shift induces a variation of the spectral function's gradient to smaller values at large frequencies and consequently the observed $1/\omega^2$ behavior for $b = 0$ vanishes. Due to the increase of spectral weight in the intermediate regime and at small frequencies, the gradient of $S(\omega)$ rises on the frequency scales where it flattened out for $b = 0$. Li et al. referred to the combination of these two effects as a crossover from a Lorentzian to a $1/f$ noise. Our theory points out that both observations only hold approximately and the detailed lineshapes are closely related to the QDs under study. For different materials and even for InGaAs/GaAs QDs grown under different conditions the obtained spectral functions might vary significantly. Note that we are unable to resolve the experimentally observed crossover of the individual curves from figure 8.8 (b) at small frequencies due to numerical limitations, but since the sum-rule 3.32 must hold in any case, it is ensured to occur beyond the numerical resolution. All in all we find decent agreement between our theory and the experimental results.

Panel (c) of figure 8.8 demonstrates that the above discussed results are qualitatively reproduced for $b = 0$ when increasing Q_r from 0.8 to 3.0 at constant $\lambda = 6$. While the approximately Lorentzian shape of $S(\omega)$ at $b = 0$ is not reproduced for $Q_r = 1.0$ and $Q_r = 2.0$, it is reclaimed for $Q_r = 3.0$. The observed similar shape of the spectral spin noise function for two different values of the ratio Q_r stems from the above stated crossover behavior of the QC's impact onto $S(\omega)$: the quadrupolar interaction has a destructive effect onto the central spin's coherence for small ratios Q_r, while the coherence is enhanced for large Q_r and consequently a comparable lineshape can be obtained at two different magnitudes of the QCs. Therefore it remains unclear, wether the QD sample under study is described adequately by $Q_r = 0.8$ or $Q_r = 3.0$ and while starting from the experimental results by Bechtold et al. [62] the first option appears more realistic, the latter choice for Q_r is in better agreement with the below treated measurements that have been performed in Dortmund.

8.3.3 Mixture of electrons and holes

The section at hand addresses experimental measurements by Glasenapp et al. [65], that have been performed on ensembles of InGaAs QDs grown by the group of A.D. Wieck in Bochum [79, 129]. Yet unpublished results on the samples under study put forward that the doping of the underlying sample is not necessarily ideal: in the n-doped QD ensemble approximately 20 % of the QDs turned out to feature a resident hole instead of the desired electron. This statement is based on measurements in a finite transversal field, where the obtained spectral function turned out to feature two peaks centered around the Larmor frequency (i) of holes and (ii) of electrons (based on the g-factors $g_\mathrm{h} \approx 0.15$ and $g_\mathrm{e} \approx 0.54$). For the, ideally, p-doped QD ensemble the admixture of electrons has been found to be less pronounced, but is not necessarily negligible. With respect to these experimental observations, a mixture of spectral functions of electrons and holes is considered and compared to the experimental spectra in the following section.

It is stressed that the considered QDs have been grown under different conditions than the samples from the above treated experiments [62, 64] and as a consequence the model parameters T^*, Q_r and λ might vary compared to the above stated results. From internal discussions with M. Bayer, it is known that the QDs grown in the group of A. D. Wieck have been found to be larger than the ones in the investigated sample from reference [64]. Along with the diameter of the considered QDs, the spread of the confined particle's wavefunction is increasing. According to equation (3.39) this entails an increase of T^*, but at the same time the magnitude of an individual hyperfine coupling constant is decreasing and therefore the ratio Q_r is expected to be increasing for the QD samples that are investigated in Dortmund.

Figure 8.9 presents a direct comparison of experimental and theoretical results for spin noise in (a) an n-doped and (b) a p-doped ensemble of InGaAs QDs. In the experiments, performed by P. Glasenapp, two different detectors granting access to different frequency regimes have been used. While the measurements by Bechtold et al. [62] clearly reflect the electron's initial precession in the Overhauser field which is separated from the remainder spin decay, the presented electron spin noise spectrum from figure 8.9 (a) features a significantly less pronounced shoulder at 100 MHz and no clear gap between the large and small frequency features is observed. There are three decisive factors inducing this behavior. (i) Performing an ensemble average slightly broadens the peak due to the precession in the Overhauser field. (ii) As stated above, the underlying sample features approximately 20 % resident holes instead of electrons and according to the results from the preceding section, the peak at large frequencies is suppressed for holes. (iii) As indicated in figure 8.5, the same effect occurs for electrons if Q_r is of the order $O(1)$. Since the first two arguments are not sufficient to justify the experimentally measured shoulder at large frequencies, it indicates that the influence

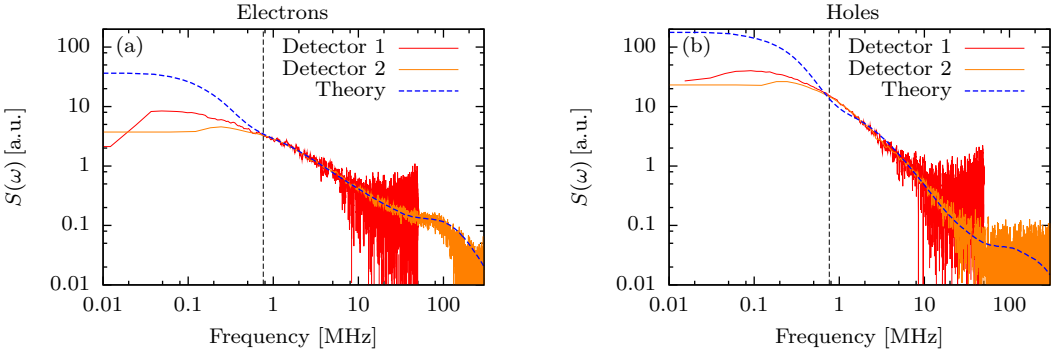

Figure 8.9: Direct comparison of experimentally measured InGaAs spin noise spectra, which have been provided by P. Glasenapp, and results for $S(\omega)$ obtained via the CET. In the experiment two different detectors that are sensitive in different frequency ranges have been used. Panel (a) shows results for an electron doped sample, where a hole spin admixture of 20 % and $Q_r = 0.6$ has been assumed for the simulations. In panel (b) corresponding results for p-doped QDs are presented, which are based on $Q_r = 6.0$, $\lambda = 5$ and an electron spin admixture of 15 %. For electrons the intrinsic timescale $T_\mathrm{e}^* = 1\,\mathrm{ns}$ and for holes $T_\mathrm{h}^* = 7\,\mathrm{ns}$ has been assumed. The vertical dashed lines indicate the reliable resolution of the CET calculations. The ensemble average has been performed as described in figure 5.9. Further parameters: $N = 9$, $n = 100$ and $r_0 = 1.5$. The experimental spectra have been published in reference [65].

of QCs is a lot larger in the sample under study than in the experiment by Bechtold et al. [62].

With respect to this observation, the theoretical curve in figure 8.9 (a) is based on a rather large ratio $Q_r = 0.6$ applying for resident electrons. Accordingly $Q_r = 6.0$ is assumed for resident hole spins and the anisotropy parameter has been set to $\lambda = 5$. Note that the ratio $Q_r = 3.0$ has been found to describe the measured spin noise spectra from reference [64] adequately and, as discussed above, due to the larger size of the investigated QDs the assumption $Q_r = 6.0$ appears valid. A mixture of 80 % electron and 20 % hole spins enters the simulations that are presented in figure 8.9 (a). The choice of the intrinsic timescale $T_\mathrm{e}^* = 1\,\mathrm{ns}$ will be discussed with respect to the QD size below. Also note that the intrinsic timescale of hole spins has not been set a factor of 10 larger, but instead $T_\mathrm{h}^* = 7\,\mathrm{ns}$ has been assumed. This choice is well justified within the applied model as described in chapter 3. The vertical line indicates the reliably resoluted frequency of the simulations and especially in the intermediate frequency regime ($\approx 1 - 30\,\mathrm{MHz}$) excellent agreement between theory and experiment is found. As discussed intensively throughout this work, the exact gradient of $S(\omega)$ in this regime is heavily dependent on the details of the hyperfine coupling constants A_k and the quadrupole parameters Q_r, η and $\vec{n}_k^z$. Due to the finite size limitations of the applied method and the simplifcations that are linked to it, this excellent agreement is surprising. The slight deviations of the different curves at large frequencies stem from the mentioned model limitations: by choosing a slighlty larger intrinsic timescale T_e^*, which is in accordance to the expected increase of T^* when turning to larger QDs, per-

fect agreement between the different results is found at $\approx 100\,\mathrm{MHz}$, but the obtained spectra would differ in the intermediate regime. This deviation is expected to be lifted if $N \sim O(1000)$ nuclei could be considered in a single simulation. In such a scenario a more realistic choice of the model parameters might also pay off and with the results of section 5.1.2 in mind, taking into account that In carries nuclear spin $I = 9/2$ instead of $I = 3/2$ might also have an impact onto the details of the spectrum.

Apparently, the considered magnitude of the ratio $Q_r = 6.0$ for hole spins is already within the parameter range, where the central spin lifetime is enhanced compared to the intermediate values $Q_r \approx 1.5$. Thus, the above stated argument that increasing the ratio Q_r by a factor of 10 counters the enhanced hole spin lifetime, as it is expected from the anisotropic CSM, does not hold anymore. Although the QCs still have a destructive effect onto the central spin's coherence, the determined similar lifetimes of electrons and holes also stem from the non-ideally doped samples that have been studied in the experiment at hand and the investigated hole spins indeed feature a larger lifetime than the electrons. Still, we stress that the lifetime enhancement is significantly smaller than implied by the bare anisotropic CSM.

Due to the assumed admixture of hole spins in the electronic spectra, turning from an n-doped to a p-doped ensemble of InGaAs QDs only induces a change in the percentages with which the particles contribute to the theoretical results. With respect to the above stated, yet unpublished measurements, we assumed a portion of 15 % resident electrons to contribute to the measured hole spin noise. Based on this assumption, we find decent agreement between theory and experiment in the frequency range above 5 MHz. The observed deviations for smaller frequencies, corresponding to large timescales, are not surprising with respect to the simplicity of the applied model. On top of the already discussed finite size limitations, we also assumed a factor of 10 between the ratio Q_r for electrons and holes for simplicity, which is clearly a further approximation.

With all the limiting factors of the studied finite size model in mind, the good agreement between our theory and the different spin noise spectra from recent experiments is remarkable. We are able to describe the experimentally realized spin dynamics adequately and obtain correct estimates independently of the spin species.

8.4 Chapter conclusion

The preceding chapter is dedicated to the study of the influence of strain induced EFGs onto the spin dynamics of holes and electrons confined in semiconductor QDs. Using both analytical and numerical tools, we have pointed out significant insufficiencies of an effective model accounting for the quadrupole interaction, that has been put forward by Sinitsyn et al. [63]. In this context it has been demonstrated that a variation of the quadrupolar orientation vectors $\vec{n}_k$ has a major impact onto the central spin

dynamics, which is not reproduced adequately by the effective model. An alignment of the orientation vectors along the dot's growth direction tends to protect the central spin's coherence compared to a perpendicular alignment. Introducing an anisotropy of the EFGs near the nuclei tends to enhance the occurrence of decoherence in any case. Nevertheless, if the quadrupolar splitting of each nucleus is significantly larger, which appears not to be realized in semiconductor QDs, than its hyperfine coupling to the confined particle, flips of the central spin are suppressed for any orientation of the vectors $\vec{n}_k$.

For the comparison of the developed theory to recent experiments, we focused on the special case of InGaAs QDs, basing the considered model parameters on the microscopic studies of these QDs by Bulutay [70, 71]. Within the finite size limitations of the presented studies, we found excellent agreement between the theoretical and experimental results for measurements of n- and p-doped QDs. While the detailed shape of the spin noise spectra of semiconductor QDs has been demonstrated to be very sensitive to all the factors influencing the QCs (i.e. the orientation vectors $\vec{n}_k$, their relative magnitude Q_r and the local asymmetry governed by η), one general statement concerning n- and p-doped QDs has been put forward as a central finding: we pointed out that the lifetime of hole and electron spins confined in InGaAs QDs are of the same order of magnitude due to the interplay of the hyperfine and quadrupole interaction: due to the decreasing magnitude and the anisotropy of the hyperfine interaction for holes, the spin's lifetime is enhanced, which is countered by the increasing impact of the EFGs relatively to the hyperfine interaction.

Chapter 9

Conclusion

As the central result of this work, we have demonstrated that the fully quantum mechanical treatment of the introduced enhanced CSM is capable of reproducing the results of various experiments on n- or p-doped InGaAs QDs. Due to the intensive study of the impact onto the central spin dynamics that stems from every individual model parameter, we have been able to gain a more detailed insight into the role of the studied sample's material properties than ever before. From a detailed analysis of the magnitude of the hyperfine interaction, the linked strain distribution and orientation of the nuclear quadrupole momenta we are able to predict the lifetime of the confined spins and the qualitative shape of their experimentally measured spin noise function in the spectral and real time regime. This achievement represents a very valuable enhancement of the knowledge concerning the spin dynamics of electrons or holes confined in semiconductor QDs.

To facilitate the above stated core result, several steps towards an accurate numerical treatment of spin noise in semiconductor QDs were in order. First, we have revisited the anisotropic central spin model, that accounts for the hyperfine interaction influencing hole and electron spins, and introduced a claim for a realistic distribution of the coupling constants A_k, that is based on the shape of the underlying QD and the envelope wave function of the confined particle. Second, we have enhanced the CSM by the quadrupole interaction and considered a recent detailed analysis of the strain tensor in In(Ga)As QDs, to deduce realistic choices of the corresponding model parameters. Third, an ensemble average of the spin noise function for an individual QD has been applied with respect to the varying physical properties of the QDs within an ensemble. Finally, we have enhanced the Chebyshev polynomial expansion technique to be able to evaluate traces, whose occurence is unevitable when considering a high temperature limit, and to gain direct access to the spectral spin noise function $S(\omega)$. Besides, an approach concerning the realisation of a time dependent NRG procedure for the isotropic CSM has been presented, that turned out to be inappropriate for the treatment of the central spin problem at hand, mainly due to the truncation of the central spin operators. The introduced claim to circumvent this truncation also failed,

because the crucial low energy eigenstates could not be reproduced adequately along with the central spin's Lie algebra.

The central spin dynamics within the isotropic CSM has been intensively discussed, with respect to various prior works. The quantum mechanical simulations stated the validity of a semi classical treatment on short timescales, where the time evolution of the central spin is only governed by the intrinsic fluctuation scale T^* and independent of the detailed QD properties. On large timescales a numerical, semi classical treatment of the ICSM also appears viable. We have stated that a logarithmic decay, whose form respects the QD geometry, of the spin noise function is likely to be the correct prediction for the long time decay of $S(t)$ and introduced a rigorous lower bound for the non-decaying fraction S_∞ that only relies on the conserved quantities of the CSM and leaves a lot of possible research for the future. Combined with an ensemble average, the ICSM is perfectly capable of reproducing the experimentally measured electron spin dynamics within strong transversal fields, stating that it describes the physics of the largest energy scale acting on the electron spins confined in semiconductor QDs. For zero or longitudinal fields the pure ICSM is insufficient to reproduce experimental measurements, because the influence of the quadrupolar interactions has a significant impact onto the electron spin dynamics in these cases. In this context we have demonstrated that our theory is capable of reproducing the results of two different experiments on samples of n-doped QDs, which have been grown under different conditions.

The description of the hole spin dynamics within the anisotropic CSM, which tends to enhance the lifetime of the confined particles, turned out to describe the measured hole spin noise from recent experiments inadequately. Even more the expected basic features of the spectral spin noise function $S(\omega)$ for a single QD have not been observed in experiments on ensembles of QDs. Namely, a transversal magnetic field induces an asymmetric spectral function around the Larmor frequency, that develops into a strict threshold behavior for the case of heavy holes, and a narrowing of this peak is expected from the anisotropic CSM. The energy scale of the hyperfine interaction is, due to its dipole-dipole nature for p-doped QDs, approximately one order of magnitude smaller for holes than for electrons and therefore the role of the quadrupole interaction is more central in the p-doped than in the n-doped case. The induced decoherence from the quadrupole interaction turns out to counter the occuring lifetime enhancement from the anisotropic CSM and finally the lifetime of hole and electron spins confined in semiconductor QDs is of the same order of magnitude. This finding constitutes one central result of this work.

In general the theory that has been established within this work granted us a deeper insight into the details of the role the quadrupole interaction plays when it is involved in the CSM, while prior studies were limited to more superficial and qualitative statements. While the strain of the discussed samples of InGaAs QDs induces a quadrupole

interaction that is weak compared to the Fermi contact interaction and therefore tends to destroy the confined spin's coherence, a *very* large strain tensor might protect it. We have also demonstrated that a parallel alignment (with respect to the QD's growth direction) of the nuclear orientation vectors and a weak asymmetry of the EFGs near the individual nuclei are in favor of the confined particle's spin coherence. All in all our findings put forward that pushing microscopic studies concerning the detailed strain and quadrupole moment distribution within a large variety of QD-types, represents a worthwhile field of investigations.

We have achieved significant progress in understanding the spin dynamics of electrons and holes confined in semiconductor QDs, but of course there are still many open questions left for future research. Due to the finite size character of the presented studies, we are unable to resolve the experimentally observed reoccurrence of $S(t)$ at large times. We have argued that the semi classical treatment of the enhanced CSM introduced by Bechtold et al. [62], which is based on an effective Hamiltonian accounting for the QCs and features a reoccurrence of the central spin polarisation, clearly fails to reproduce elementary features of the spin dynamics. Thus, an adequate method for the treatment of the enhanced CSM involving large spin baths on long timescales is desirable, but extremely challenging at the same time. A quantum mechanical treatment of the model might be possible using an innovative renormalization group approach, but the most promising tool appears to be a numerical evaluation of the semi classical picture. Of course there are further interactions, beside the hyperfine and quadrupolar interaction, that might contribute significantly to the central spin dynamics on long time scales, like the dipole-dipole interaction between the nuclei for instance. All of the preceding studies are based on the limit of infinite temperature, which is clearly an approximation and considering the effects of introducing a finite temperature is also an interesting subject for studies in the future. On top of that, the investigation of higher order correlation functions, for which the CET's runtime rapidly exceeds considerable efforts, might reveal additional interesting information on the system properties.

Bibliography

[1] Richard P. Feynman. Simulating physics with computers. *International Journal of Theoretical Physics*, 21(6-7):467–488, 1982.

[2] Ethan Bernstein and Umesh Vazirani. Quantum complexity theory. In *Proceedings of the Twenty-fifth Annual ACM Symposium on Theory of Computing*, STOC '93, pages 11–20, New York, NY, USA, 1993. ACM.

[3] D. Deutsch. Quantum theory, the Church-Turing principle and the universal quantum computer. *Proceedings of the Royal Society of London A: Mathematical, Physical and Engineering Sciences*, 400(1818):97–117, 1985.

[4] David Deutsch and Richard Jozsa. Rapid solution of problems by quantum computation. *Proceedings of the Royal Society of London A: Mathematical, Physical and Engineering Sciences*, 439(1907):553–558, 1992.

[5] D. Coppersmith. An approximate fourier transform useful in quantum factoring. *ArXiv e-prints*, January 2002.

[6] P. W. Shor. Algorithms for quantum computation: Discrete logarithms and factoring. In *Proceedings of the 35th Annual Symposium on Foundations of Computer Science*, SFCS '94, pages 124–134, Washington, DC, USA, 1994. IEEE Computer Society.

[7] Peter W. Shor. Polynomial-time algorithms for prime factorization and discrete logarithms on a quantum computer. *SIAM Journal on Computing*, 26(5):1484–1509, 1997.

[8] D. Suter and J. Stolze. *Quantum computing*. Wiley-VCH, Weinheim, 2004.

[9] David P. DiVincenzo. The physical implementation of quantum computation. *Fortschritte der Physik*, 48(9-11):771–783, 2000.

[10] F. Jelezko, T. Gaebel, I. Popa, M. Domhan, A. Gruber, and J. Wrachtrup. Observation of coherent oscillation of a single nuclear spin and realization of a two-qubit conditional quantum gate. *Phys. Rev. Lett.*, 93:130501, Sep 2004.

[11] R. Hanson, V. V. Dobrovitski, A. E. Feiguin, O. Gywat, and D. D. Awschalom. Coherent dynamics of a single spin interacting with an adjustable spin bath. *Science*, 320(5874):352–355, 2008.

[12] L. M. K. Vandersypen and I. L. Chuang. NMR techniques for quantum control and computation. *Rev. Mod. Phys.*, 76:1037–1069, Jan 2005.

[13] Jonathan A. Jones. Quantum computing with NMR. *Progress in Nuclear Magnetic Resonance Spectroscopy*, 59(2):91 – 120, 2011.

[14] B. E. Kane. A silicon-based nuclear spin quantum computer. *Nature*, 393(6681):133, 1998.

[15] Yuriy Makhlin, Gerd Schön, and Alexander Shnirman. Quantum-state engineering with Josephson-junction devices. *Rev. Mod. Phys.*, 73:357–400, May 2001.

[16] M. A. Sillanpää, J. I. Park, and R. W. Simmonds. Coherent quantum state storage and transfer between two phase qubits via a resonant cavity. *Nature*, 449:438–442, 2007.

[17] A. A. Houck, H. E. Tuereci, and Jens Koch. On-chip quantum simulation with superconducting circuits. *Nature Physics*, 8:292, 2012.

[18] Daniel Loss and David P. DiVincenzo. Quantum computation with quantum dots. *Phys. Rev. A*, 57:120–126, Jan 1998.

[19] J. Schliemann, A. Khaetskii, D. Loss. Electron spin dynamics in quantum dots and related nanostructures due to hyperfine interaction with nuclei. *J. Phys.: Condens. Matter*, 81:R1809 – R1833, 2003.

[20] R. Hanson, L. P. Kouwenhoven, J. R. Petta, S. Tarucha, and L. M. K. Vandersypen. Spins in few-electron quantum dots. *Rev. Mod. Phys.*, 79:1217–1265, Oct 2007.

[21] J. M. Elzerman, R. Hanson, L. H. Willems van Beveeren, B. Witkamp, L. M. K. Vandersypen, and L. P. Kouvenhoven. Single-shot read-out of an individual electron spin in a quantum dot. *Nature*, 430:431, 2004.

[22] N. H. Bonadeo, J. Erland, D. Gammon, D. Park, D. S. Katzer, and D. G. Steel. Coherent optical control of the quantum state of a single quantum dot. *Science*, 282(5393):1473–1476, 1998.

[23] A. Greilich, A. Shabaev, D. R. Yakovlev, Al. L. Efros, I. A. Yugova, D. Reuter, A. D. Wieck, and M. Bayer. Nuclei-induced frequency focusing of electron spin coherence. *Science*, 317(5846):1896–1899, 2007.

[24] L. V. Fokina, I. A. Yugova, D. R. Yakovlev, M. M. Glazov, I. A. Akimov, A. Greilich, D. Reuter, A. D. Wieck, and M. Bayer. Spin dynamics of electrons and holes in InGaAs/GaAs quantum wells at millikelvin temperatures. *Phys. Rev. B*, 81:195304, May 2010.

[25] S. Spatzek, A. Greilich, Sophia E. Economou, S. Varwig, A. Schwan, D. R. Yakovlev, D. Reuter, A. D. Wieck, T. L. Reinecke, and M. Bayer. Optical control of coherent interactions between electron spins in InGaAs quantum dots. *Phys. Rev. Lett.*, 107:137402, Sep 2011.

[26] E. Fermi. Über die magnetischen Momente der Atomkerne. *Z. Phys.*, 60:320, 1930.

[27] I. Merkulov, Al. Efros, and M. Rosen. Electron spin relaxation by nuclei in semiconductor quantum dots. *Phys. Rev. B*, 65:205309, Apr 2002.

[28] Seungwon Lee, Paul von Allmen, Fabiano Oyafuso, Gerhard Klimeck, and K. Birgitta Whaley. Effect of electron-nuclear spin interactions for electron-spin qubits localized in InGaAs self-assembled quantum dots. *Journal of Applied Physics*, 97(4):–, 2005.

[29] M. Gaudin. Diagonalisation d'une classe d'hamiltoniens de spin. *J. Phys. France*, 37:1087 – 1098, 1976.

[30] Gang Chen, Doron L. Bergman, and Leon Balents. Semiclassical dynamics and long-time asymptotics of the central-spin problem in a quantum dot. *Phys. Rev. B*, 76:045312, Jul 2007.

[31] Wenxian Zhang, V. V. Dobrovitski, K. A. Al-Hassanieh, E. Dagotto, and B. N. Harmon. Hyperfine interaction induced decoherence of electron spins in quantum dots. *Phys. Rev. B*, 74:205313, Nov 2006.

[32] Michael Bortz and Joachim Stolze. Spin and entanglement dynamics in the central-spin model with homogeneous couplings. *Journal of Statistical Mechanics: Theory and Experiment*, 2007(06):P06018, 2007.

[33] Michael Bortz and Joachim Stolze. Exact dynamics in the inhomogeneous central-spin model. *Phys. Rev. B*, 76:014304, Jul 2007.

[34] Michael Bortz, Sebastian Eggert, and Joachim Stolze. Spectrum and screening cloud in the central spin model. *Phys. Rev. B*, 81:035315, Jan 2010.

[35] Michael Bortz, Sebastian Eggert, Christian Schneider, Robert Stübner, and Joachim Stolze. Dynamics and decoherence in the central spin model using exact methods. *Phys. Rev. B*, 82:161308, Oct 2010.

[36] Alexandre Faribault and Dirk Schuricht. Integrability-based analysis of the hyperfine-interaction-induced decoherence in quantum dots. *Phys. Rev. Lett.*, 110:040405, Jan 2013.

[37] Alexandre Faribault and Dirk Schuricht. Spin decoherence due to a randomly fluctuating spin bath. *Phys. Rev. B*, 88:085323, Aug 2013.

[38] Andreas Friedrich. *Time-dependent Properties of one-dimensional Spin-Systems: a DMRG-Study*. PhD thesis, RWTH Aachen, 2006.

[39] Daniel Stanek, Carsten Raas, and Götz S. Uhrig. Dynamics and decoherence in the central spin model in the low-field limit. *Phys. Rev. B*, 88:155305, Oct 2013.

[40] B. Erbe and J. Schliemann. Perturbative regimes in central spin models. *Phys. Rev. B*, 85:235423, Jun 2012.

[41] W. A. Coish and Daniel Loss. Hyperfine interaction in a quantum dot: Non-Markovian electron spin dynamics. *Phys. Rev. B*, 70:195340, 2004.

[42] Jan Fischer and Heinz-Peter Breuer. Correlated projection operator approach to non-markovian dynamics in spin baths. *Phys. Rev. A*, 76:052119, Nov 2007.

[43] E. Ferraro, H.-P. Breuer, A. Napoli, M. A. Jivulescu, and A. Messina. Non-markovian dynamics of a single electron spin coupled to a nuclear spin bath. *Phys. Rev. B*, 78:064309, Aug 2008.

[44] Sigurdur I. Erlingsson and Yuli V. Nazarov. Hyperfine-mediated transitions between a Zeeman split doublet in GaAs quantum dots: The role of the internal field. *Phys. Rev. B*, 66:155327, Oct 2002.

[45] Sigurdur I. Erlingsson and Yuli V. Nazarov. Evolution of localized electron spin in a nuclear spin environment. *Phys. Rev. B*, 70:205327, Nov 2004.

[46] F. M. Cucchietti, J. P. Paz, and W. H. Zurek. Decoherence from spin environments. *Phys. Rev. A*, 72:052113, Nov 2005.

[47] I. A. Merkulov, G. Alvarez, D. R. Yakovlev, and T. C. Schulthess. Long-term dynamics of the electron-nuclear spin system of a semiconductor quantum dot. *Phys. Rev. B*, 81:115107, Mar 2010.

[48] K. A. Al-Hassanieh, V. V. Dobrovitski, E. Dagotto, and B. N. Harmon. Numerical modeling of the central spin problem using the spin-coherent-state p representation. *Phys. Rev. Lett.*, 97:037204, Jul 2006.

[49] Daniel Stanek, Carsten Raas, and Götz S. Uhrig. From quantum-mechanical to classical dynamics in the central-spin model. *Phys. Rev. B*, 90:064301, Aug 2014.

[50] W. M. Witzel, Rogerio de Sousa, and S. Das Sarma. Quantum theory of spectral-diffusion-induced electron spin decoherence. *Phys. Rev. B*, 72:161306, Oct 2005.

[51] W. M. Witzel and S. Das Sarma. Quantum theory for electron spin decoherence induced by nuclear spin dynamics in semiconductor quantum computer architectures: Spectral diffusion of localized electron spins in the nuclear solid-state environment. *Phys. Rev. B*, 74:035322, Jul 2006.

[52] Lukasz Cywinski, V. V. Dobrovitski, and S. Das Sarma. Spin echo decay at low magnetic fields in a nuclear spin bath. *Phys. Rev. B*, 82:035315, Jul 2010.

[53] Wayne M. Witzel, Malcolm S. Carroll, Łukasz Cywiński, and S. Das Sarma. Quantum decoherence of the central spin in a sparse system of dipolar coupled spins. *Phys. Rev. B*, 86:035452, Jul 2012.

[54] Jan Fischer, W. A. Coish, D. V. Bulaev, and Daniel Loss. Spin decoherence of a heavy hole coupled to nuclear spins in a quantum dot. *Phys. Rev. B*, 78:155329, Oct 2008.

[55] Mircea Trif, Pascal Simon, and Daniel Loss. Relaxation of hole spins in quantum dots via two-phonon processes. *Phys. Rev. Lett.*, 103:106601, Sep 2009.

[56] C. Testelin, F. Bernardot, B. Eble, and M. Chamarro. Hole-spin dephasing time associated with hyperfine interaction in quantum dots. *Phys. Rev. B*, 79:195440, May 2009.

[57] M. M. Glazov and E. L. Ivchenko. Spin noise in quantum dot ensembles. *Phys. Rev. B*, 86:115308, Sep 2012.

[58] D. Press, K. De Greve, P. L. McMahon, T. D. Ladd, B. Friess, C. Schneider, M. Kamp, S. Höfling, A. Forchel, and Y. Yamamoto. Ultrafast optical spin echo in a single quantum dot. *Nature Photonics*, 4:367 – 370, 2010.

[59] S. A. Crooker, J. Brandt, C. Sandfort, A. Greilich, D. R. Yakovlev, D. Reuter, A. D. Wieck, and M. Bayer. Spin noise of electrons and holes in self-assembled quantum dots. *Phys. Rev. Lett.*, 104:036601, Jan 2010.

[60] K. De Greve, P. L. McMahon, D. Press, T. D. Ladd, D. Bisping, C. Schneider, M. Kamp, L. Worschesch, S. Höfling, A. Forchel, and Y. Yamamoto. Ultrafast coherent control and suppressed nuclear feedback of a single quantum dot hole qubit. *Nature Physics*, 7:872 – 878, 2011.

[61] S. Varwig, A. Schwan, D. Barmscheid, C. Müller, A. Greilich, I. A. Yugova, D. R. Yakovlev, D. Reuter, A. D. Wieck, and M. Bayer. Hole spin precession in a (In,Ga)As quantum dot ensemble: From resonant spin amplification to spin mode locking. *Phys. Rev. B*, 86:075321, Aug 2012.

[62] A. Bechtold, D. Rauch, T. Simmet, P.-L. Ardelt, A. Regler, K. Müller, and J. J. Finley. Hyperfine mediated electron spin relaxation in a single InGaAs quantum dot at low magnetic fields. *ArXiv e-prints*, October 2014.

[63] N. A. Sinitsyn, Yan Li, S. A. Crooker, A. Saxena, and D. L. Smith. Role of nuclear quadrupole coupling on decoherence and relaxation of central spins in quantum dots. *Phys. Rev. Lett.*, 109:166605, Oct 2012.

[64] Yan Li, N. Sinitsyn, D. L. Smith, D. Reuter, A. D. Wieck, D. R. Yakovlev, M. Bayer, and S. A. Crooker. Intrinsic spin fluctuations reveal the dynamical response function of holes coupled to nuclear spin baths in (In,Ga)As quantum dots. *Phys. Rev. Lett.*, 108:186603, May 2012.

[65] J. Hackmann, F. B. Anders, P. Glasenapp, A. Greilich, and M. Bayer. Influcence of the nuclear electric quadrupolar interaction on the coherence time of hole- and electron-spins confined in semiconductor quantum dots. *ArXiv e-prints*, April 2015.

[66] H. Tal-Ezer, R. Kosloff. An accurate and efficient scheme for propagating the time dependent Schrödinger equation. *J. Chem. Phys.*, 81:3967 – 3969, 1984.

[67] Kenneth Wilson. The renormalization group: Critical phenomena and the Kondo problem. *Rev. Mod. Phys.*, 47:773–840, Oct 1975.

[68] Frithjof Anders and Avraham Schiller. Real-time dynamics in quantum-impurity systems: A time-dependent numerical renormalization-group approach. *Phys. Rev. Lett.*, 95:196801, Oct 2005.

[69] Ralf Bulla, Theo Costi, and Thomas Pruschke. Numerical renormalization group method for quantum impurity systems. *Rev. Mod. Phys.*, 80:395–450, Apr 2008.

[70] Ceyhun Bulutay. Quadrupolar spectra of nuclear spins in strained $In_xGa_{1-x}As$ quantum dots. *Phys. Rev. B*, 85:115313, Mar 2012.

[71] Ceyhun Bulutay, E. A. Chekhovich, and A. I. Tartakovskii. Nuclear magnetic resonance inverse spectra of InGaAs quantum dots: Atomistic level structural information. *Phys. Rev. B*, 90:205425, Nov 2014.

[72] I. N. Stranski and L. V. Krastanow. Abhandlungen d. mathematisch-naturwissenschaftlichen Klasse. 146, 1939.

[73] L. Goldstein, F. Glas, J. Y. Marzin, M. N. Charasse, and G. Le Roux. Growth by molecular beam epitaxy and characterization of InAs/GaAs strained layer superlattices. *Applied Physics Letters*, 47(10):1099–1101, 1985.

[74] I.L. Krestnikov, N.N. Ledentsov, A. Hoffmann, and D. Bimberg. Arrays of two-dimensional islands formed by submonolayer insertions: Growth, properties, devices. *physica status solidi (a)*, 183(2):207–233, 2001.

[75] Dissertation: T. Auer. *The Electron-Nuclear Spin System in (In,Ga)As Quantum Dots*. TU-Dortmund, Lehrstuhl für experimentelle Physik 2, 2008.

[76] Juan Marquez, Lutz Geelhaar, and Karl Jacobi. Atomically resolved structure of InAs quantum dots. *Applied Physics Letters*, 78(16):2309–2311, 2001.

[77] Toshiba. https://www.toshiba-europe.com/research/crl/qig/quantumdots.html, Jun. 2015.

[78] N. W. Ashcroft and D. N. Mermin. *Festkörperphysik*. Oldenbourg Wissenschaftsverlag, Germany, 2001.

[79] W. Langbein, P. Borri, U. Woggon, V. Stavarache, D. Reuter, and A. D. Wieck. Control of fine-structure splitting and biexciton binding in $In_xGa_{1-x}As$ quantum dots by annealing. *Phys. Rev. B*, 69:161301, Apr 2004.

[80] M. Yu. Petrov, I. V. Ignatiev, S. V. Poltavtsev, A. Greilich, A. Bauschulte, D. R. Yakovlev, and M. Bayer. Effect of thermal annealing on the hyperfine interaction in InAs/GaAs quantum dots. *Phys. Rev. B*, 78:045315, Jul 2008.

[81] S. Cortez, O. Krebs, S. Laurent, M. Senes, X. Marie, P. Voisin, R. Ferreira, G. Bastard, J-M. Gérard, and T. Amand. Optically driven spin memory in *n*-doped InAs-GaAs quantum dots. *Phys. Rev. Lett.*, 89:207401, Oct 2002.

[82] J. S. Colton, T. A. Kennedy, A. S. Bracker, and D. Gammon. Microsecond spin-flip times in $n-$GaAs measured by time-resolved polarization of photoluminescence. *Phys. Rev. B*, 69:121307, Mar 2004.

[83] Michio Ikezawa, Bipul Pal, Yasuaki Masumoto, Ivan V. Ignatiev, Sergey Yu. Verbin, and Il'ya Ya. Gerlovin. Submillisecond electron spin relaxation in InP quantum dots. *Phys. Rev. B*, 72:153302, Oct 2005.

[84] F. Fras, B. Eble, P. Desfonds, F. Bernardot, C. Testelin, M. Chamarro, A. Miard, and A. Lemaître. Hole-spin initialization and relaxation times in InAs/GaAs quantum dots. *Phys. Rev. B*, 84:125431, Sep 2011.

[85] A. Greilich, R. Oulton, E. A. Zhukov, I. A. Yugova, D. R. Yakovlev, M. Bayer, A. Shabaev, Al. L. Efros, I. A. Merkulov, V. Stavarache, D. Reuter, and A. Wieck. Optical control of spin coherence in singly charged $(In,Ga)As/GaAs$ quantum dots. *Phys. Rev. Lett.*, 96:227401, Jun 2006.

[86] A. Greilich, D. R. Yakovlev, A. Shabaev, Al. L. Efros, I. A. Yugova, R. Oulton, V. Stavarache, D. Reuter, A. Wieck, and M. Bayer. Mode locking of electron spin coherences in singly charged quantum dots. *Science*, 313(5785):341–345, 2006.

[87] A. Greilich, M. Wiemann, F. G. G. Hernandez, D. R. Yakovlev, I. A. Yugova, M. Bayer, A. Shabaev, Al. L. Efros, D. Reuter, and A. D. Wieck. Robust manipulation of electron spin coherence in an ensemble of singly charged quantum dots. *Phys. Rev. B*, 75:233301, Jun 2007.

[88] A. Greilich, S. Spatzek, I. A. Yugova, I. A. Akimov, D. R. Yakovlev, Al. L. Efros, D. Reuter, A. D. Wieck, and M. Bayer. Collective single-mode precession of electron spins in an ensemble of singly charged (In,Ga)As/GaAs quantum dots. *Phys. Rev. B*, 79:201305, May 2009.

[89] M. Oestreich, R. Dahbashi, F. Berski, and J. Hübner. Spin noise spectroscopy: hole spin dynamics in semiconductor quantum dots. *Proc. SPIE*, 8461:846105–846105–6, 2012.

[90] Ramin Dahbashi, Jens Hübner, Fabian Berski, Klaus Pierz, and Michael Oestreich. Optical spin noise of a single hole spin localized in an (InGa)As quantum dot. *Phys. Rev. Lett.*, 112:156601, Apr 2014.

[91] J. Hübner, R. Dahbashi, F. Berski, J. Wiegand, H. Kuhn, J. Lonnemann, and M. Oestreich. Spin noise spectroscopy in semiconductors: from a billion down to single spins. *Proc. SPIE*, 9167:91672R–91672R–8, 2014.

[92] Lucio Claudio Andreani, Giovanna Panzarini, and Jean-Michel Gérard. Strong-coupling regime for quantum boxes in pillar microcavities: Theory. *Phys. Rev. B*, 60:13276–13279, Nov 1999.

[93] Lehrstuhl für experimentelle Physik E2a. http://www.e2.physik.tu-dortmund.de/cms/index.php/research-menu/researchgroupse2a-menu/cohspindyn-menu, Jun. 2015.

[94] Diploma thesis: M. Wiemann. *Kohärente Spinkontrolle in (In,Ga)As/GaAs Quantenpunkten und Quantenschichten*. TU-Dortmund, Lehrstuhl für experimentelle Physik 2, 2007.

[95] Dissertation: S. Spatzek. *Kohärente Kontrolle und Wechselwirkung von Elektronenspins in einem (In,Ga)As/GaAs Quantenpunktensemble*. TU-Dortmund, Lehrstuhl für experimentelle Physik 2, 2011.

[96] A. Abragam. *Principles of Nuclear Magnetism*. Oxford University Press, 1994. S. 170 ff.

[97] Johannes Hackmann and Frithjof B. Anders. Spin noise in the anisotropic central spin model. *Phys. Rev. B*, 89:045317, Jan 2014.

[98] C. P. Slichter. *Principles of Magnetic Resonance*. Springer-Verlag, Tiergartenstrasse 17, D-69121 Heidelberg, Germany, 1996. Corrected 3rd Printing.

[99] E. Welander, E. Chekhovich, A. Tartakovskii, and G. Burkard. Influence of nuclear quadrupole moments on electron spin coherence in semiconductor quantum dots. *ArXiv e-prints*, May 2014.

[100] O. Stier, M. Grundmann, and D. Bimberg. Electronic and optical properties of strained quantum dots modeled by 8-band k·p theory. *Phys. Rev. B*, 59:5688–5701, Feb 1999.

[101] S. Schulz and G. Czycholl. Tight-binding model for semiconductor nanostructures. *Phys. Rev. B*, 72:165317, Oct 2005.

[102] S. Schulz and E. P. O'Reilly. Theory of reduced built-in polarization field in nitride-based quantum dots. *Phys. Rev. B*, 82:033411, Jul 2010.

[103] J. Hackmann. *Chebyshev-Polynomentwicklung zur Beschreibung von Dephasierung im Zentralspinmodell*. TU-Dortmund, Otto-Hahn-Strasse 4, D-44227 Dortmund, Germany, 2012. Master thesis.

[104] Ken-ichi Shiramine, Shunichi Muto, Tamaki Shibayama, Norihito Sakaguchi, Hideki Ichinose, Tamotsu Kozaki, Seichi Sato, Yoshiaki Nakata, Naoki Yokoyama, and Masafumi Taniwaki. Tip artifact in atomic force microscopy observations of InAs quantum dots grown in Stranski–Krastanow mode. *Journal of Applied Physics*, 101(3):–, 2007.

[105] Nist digital library of mathematical functions. http://dlmf.nist.gov/, Release 1.0.9 of 2014-08-29. Online companion to [106].

[106] F. W. J. Olver, D. W. Lozier, R. F. Boisvert, and C. W. Clark, editors. *NIST Handbook of Mathematical Functions*. Cambridge University Press, New York, NY, 2010. Print companion to [105].

[107] M. Abramowitz, I. A. Stegun. *Handbook of Mathematical Functions*. New York: Dover, 1972. S. 771-802.

[108] Charles R. Johnson and Roger A. Horn, editors. *Matrix analysis*. Cambridge University Press, Cambridge, 1990.

[109] J. H. Wilkinson, editor. *The Algebraic Eigenvalue Problem*. Oxford University Press, Inc., New York, NY, USA, 1988.

[110] A. Weiße, G. Wellein, A. Alvermann, H. Fehske. The kernel polynomial method. *Rev. Mod. Phys.*, 78:279–280, Mar 2006.

[111] G. E. P. Box and Mervin E. Muller. A note on the generation of random normal deviates. *Ann. Math. Statist.*, 29(2):610–611, 06 1958.

[112] Edwin Hewitt and RobertE. Hewitt. The Gibbs-Wilbraham phenomenon: An episode in fourier analysis. *Archive for History of Exact Sciences*, 21(2):129–160, 1979.

[113] D. Jackson. *Ueber die Genauigkeit der Annaeherung stetiger Funktionen durch ganze rationale Funktionen gegebenen Grades und trigonometrische Summen gegebener Ordnung*. Georg-August-Universitaet Goettingen, 1911. Ph.D. thesis.

[114] D. Jackson. On the degree of convergence of the development of a continuous function according to Legendre's polynomials. *Trans. Amer. Math. Soc.*, 13, 1912.

[115] Alexander Khaetskii, Daniel Loss, and Leonid Glazman. Electron spin evolution induced by interaction with nuclei in a quantum dot. *Phys. Rev. B*, 67:195329, May 2003.

[116] Alexander V. Khaetskii, Daniel Loss, and Leonid Glazman. Electron spin decoherence in quantum dots due to interaction with nuclei. *Phys. Rev. Lett.*, 88:186802, Apr 2002.

[117] D. Klauser, W. A. Coish, and Daniel Loss. Nuclear spin dynamics and Zeno effect in quantum dots and defect centers. *Phys. Rev. B*, 78:205301, Nov 2008.

[118] Johannes Hackmann, Dmitry S. Smirnov, Mikhail M. Glazov, and Frithjof B. Anders. Spin noise in a quantum dot ensemble: From a quantum mechanical to a semi-classical description. *physica status solidi (b)*, 251(6):1270–1275, 2014.

[119] Götz S. Uhrig, Johannes Hackmann, Daniel Stanek, Joachim Stolze, and Frithjof B. Anders. Conservation laws protect dynamic spin correlations from decay: Limited role of integrability in the central spin model. *Phys. Rev. B*, 90:060301, Aug 2014.

[120] P. Mazur. Non-ergodicity of phase functions in certain systems. *Physica*, 43(4):533 – 545, 1969.

[121] M. Suzuki. Ergodicity, constants of motion, and bounds for susceptibilities. *Physica*, 51(2):277 – 291, 1971.

[122] http://link.aps.org/supplemental/10.1103/PhysRevB.90.060301. *Supplemental material to PRB 90, 060301 (R)*. PRB, 2014.

[123] D. Stanek. *Dynamics and Decoherence in the Central Spin Model: From a Quantum Mechanical to a Classical Description*. TU-Dortmund, Otto-Hahn-Strasse 4, D-44227 Dortmund, Germany, 2013. Dissertation.

[124] Jun Kondo. Resistance minimum in dilute magnetic alloys. *Progress of Theoretical Physics*, 32(1):37–49, 1964.

[125] A. C. Hewson. *The Kondo Problem to Heavy Fermions*. Cambridge University Press, 1997.

[126] S. Schulz and G. Czycholl. Tight-binding model for semiconductor nanostructures. *Phys. Rev. B*, 72:165317, Oct 2005.

[127] F. Fras, B. Eble, P. Desfonds, F. Bernardot, C. Testelin, M. Chamarro, A. Miard, and A. Lemaitre. Two-phonon process and hyperfine interaction limiting slow hole-spin relaxation time in InAs/GaAs quantum dots. *Phys. Rev. B*, 86:045306, Jul 2012.

[128] R. I. Dzhioev and V. L. Korenev. Stabilization of the electron-nuclear spin orientation in quantum dots by the nuclear quadrupole interaction. *Phys. Rev. Lett.*, 99:037401, Jul 2007.

[129] D Reuter, P Schafmeister, J Koch, K Schmidt, and A.D Wieck. Growth of InAs quantum dots on focussed ion beam implanted GaAs(100). *Materials Science and Engineering: B*, 88(2–3):230 – 233, 2002.

Acknowledgements

Zunächst möchte ich mich bei Frithjof Anders bedanken, der meine Arbeit beaufsichtigt hat, immer für Rückfragen zur Verfügung stand und mir viele hilfreiche Anregungen gegeben hat.
Zudem bedanke ich mich bei Götz Uhrig, dass er sich bereit erklärt hat als zweiter Gutachter meiner Arbeit zu fungieren.
Ganz besonders möchte ich mich bei meiner Freundin und wohl besten Frau der Welt Ann-Kristin Graf bedanken, die mir während der vergangenen acht Jahre großen Rückhalt gegeben hat und auch in sehr stressigen Phasen immer Verständnis und Geduld mit mir hatte.
Ich bedanke mich bei meinen Eltern für ihre menschliche und finanzielle Unterstützung, sowohl während meines Studiums als auch davor.
Darüber hinaus möchte ich mich bei all meinen Freunden sowohl aus Dortmund als auch Bergkamen bedanken, mit denen ich immer gute Zeiten und einen entsprechenden Ausgleich neben der Arbeit hatte.
Zuletzt möchte ich mich bei all meinen Arbeitskollegen, besonders aber bei meinen Bürokollegen Christian Kleine und Benedikt Lechtenberg, bedanken, da durch sie stets ein sehr positives und angenehmes Arbeitsklima gewährleistet war.